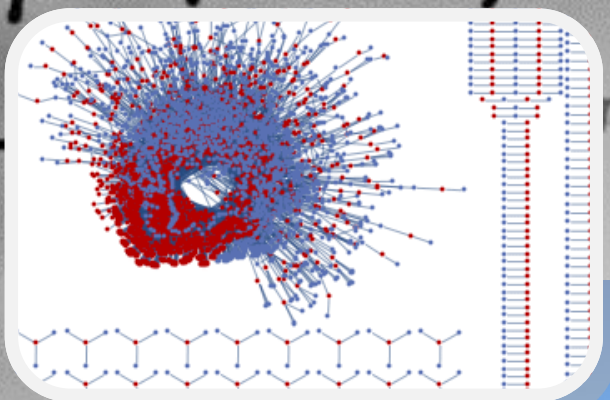


MODELLING FOR ENGINEERING AND HUMAN BEHAVIOUR

2017

Instituto Universitario de Matemática Multidisciplinar



L. Jódar, J. C. Cortés and L. Acedo (Editors)

Instituto Universitario de
Matemática Multidisciplinar

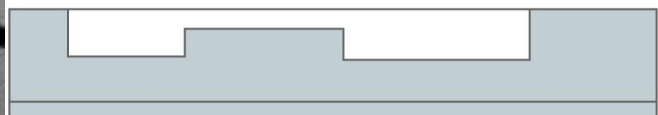
im²

Instituto de Matemática Multidisciplinar



UNIVERSITAT
POLITÈCNICA
DE VALÈNCIA

Ciudad Politécnica de la Innovación



MODELLING FOR ENGINEERING, & HUMAN BEHAVIOUR 2017

Instituto Universitario de Matemática Multidisciplinar

Universitat Politècnica de València

Valencia 46022, SPAIN

Edited by

Lucas Jódar, Juan Carlos Cortés and Luis Acedo

Instituto Universitario de Matemática Multidisciplinar

Universitat Politècnica de València

I.S.B.N.: 978-84-697-8505-8

CONTENTS

1. **A comparative study of the local convergence radius of iterative methods for multiple roots**, by D. Alarcón, F. Cevallos, J. Hueso, and E. Martínez Pag: 1-6
2. **Mathematical modelling of the value of technology brands**, by M. A. Alcaide, E. de la Poza, and N. Guadalajara Pag: 7-12
3. **Methylphenidate and the self-regulation therapy: a systemic mathematical model**, by S. Amigó, J. C. Micó, and A. Caselles Pag: 13-18
4. **Jacobian-free iterative schemes to solve nonlinear systems**, by A. R. Amiri, A. Cordero, M. T. Darvishi, and J. R. Torregrosa Pag: 19-24
5. **Optimal Control of Counter-Terrorism Tactics**, by L. Bayón, P. Fortuny, P. J. García-Nieto, J. M. Grau, and M. M. Ruiz Pag: 25-30
6. **Calculation of the adjoint flux of the neutron diffusion equation**, by A. Bernal, J. E. Roman, R. Miró, and G. Verdú Pag: 31-36
7. **Uncertainty quantification for meningococcus W carriers prediction**, by L. Acedo, C. Burgos, J. C. Cortés, D. Martínez, and R. J. Villanueva Pag: 37-42
8. **Some awkward issues on pairwise comparison matrices**, by J. Benítez, S. Carpitella, A. Certa, A. Ilaya-Ayza, and J. Izquierdo Pag: 43-48
9. **Block iterative methods to compute the λ -modes of a nuclear power reactor**, by A. Carreño, A. Vidal, D. Ginestar, and G. Verdú Pag: 49-55
10. **Constructive analytic-numerical solution of random parabolic problems in a one-dimensional random medium by a mean square Fourier integral method**, by M. C. Casabán, J. C. Cortés, and L. Jódar Pag: 56-62
11. **A genetic algorithm to calibrate systems: a case in psychology**, by A. Caselles, J. C. Micó, and S. Amigó Pag: 63-67
12. **Two algorithms for computing the matrix cosine based on new Hermite approximations**, by E. Defez, J. Ibáñez, J. Peinado, J. Sastre, and P. Alonso Pag: 68-77
13. **Wildland fire propagation modelling**, by V. Egorova, G. Pagnini, and A. Trucchia Pag: 78-83
14. **Efficient three time level numerical scheme for option pricing Heston-Hull-White model**, by M. Fakharany, R. Company, and L. Jódar Pag: 84-88

15. **Modeling eutrophication using the hybrid ABC-SVM-based approach, multilayer perceptron neural network and M5 model tree in the Pozón de la Dolores lake (Northern Spain)**, by P. J. Garía-Nieto, E. García-Gonzalo, J. R. Alonso, and C. Díaz
Pag: 89-98
16. **Efficient class of iterative schemes with memory for solving nonlinear problems**, by A. Cordero, N. Garrido, E. Gómez, and J. R. TorregrosaPag: 99-105
17. **A methodology for the detection of rail irregularities and defects based on the vehicle dynamic response**, by B. Baydal, M. Labrado, C. Masanet, and C. Zamorano Pag: 106-111
18. **Application of a modified concrete for vibration attenuation in railway infrastructures**, by A. J. Pérez, T. Real, F. Ribes, and J. Real 112-117
19. **Attenuation performance of track stiffness transitions under different vehicle speeds**, by F. Roca, J. del Pozo, T. Real, and J. Real Pag: 118-123
20. **Detection of earthquake-induced soil liquefaction in harbours based on changes of the structure vibration modes**, by P. Moscoso, F. Ribes, V. Ramos, and J. Real Pag: 124-129
21. **Development of a high precision algorithm for predictive maintenance of industrial belt conveyors**, by M. Labrado, C. Masanet, F. Roca, and J. L. Velarte Pag: 130-135
22. **Effect of mixture gradation and thickness on the cooling process of hot mix asphalts**, by J. Real, B. Baydal, M. Labrado, and A. Zornoza Pag: 136-141
23. **Numerical modelling of flying ballast phenomenon on high speed lines. Part A: Analysis of the train-track aerodynamic interaction by means of field data and a CFD model**, by C. Masanet, F. Roca, J. del Pozo, and J. Real Pag: 142-148
24. **Numerical modelling of flying ballast phenomenon on high speed lines. Part B: Analysis of the stability of the ballast layer by means of a DEM model**, by T. Real, J. Peset, E. Colomer, and J. Real Pag: 149-154
25. **Predictive maintenance of tunnels based on real-time acceleration registers on the concrete revetment**, by F. Ribes, C. Zamorano, B. Baydal, and J. L. Velarte... Pag: 155-160
26. **Stability of parametric family of iterative methods for root-finding**, by A. Cordero, L. Guasp, and J. R. Torregrosa Pag: 161-166
27. **Network analysis for inferring spatio-temporal predictive models in water demand consumption**, by C. Navarrete, M. Herrera, B. M. Brentan, E. Luvizotto Jr., and J. Izquierdo Pag: 167-170
28. **A Procedure of Generation of Directed Graphs for the Comparative Study of Algorithms for the Detection of Communities**, by J. M. Montañana, A. Hervás, and P. P. Soriano Pag: 171-176

29. **A discontinuous Galerkin framework for option pricing problems with stochastic volatilities**, by J. Hozman, and T. Tychý Pag: 177-182
30. **Exponential methods for solving non-autonomous linear wave equations**, by P. Bader, S. Blanes, F. Casas, and N. Kopylov Pag: 183-188
31. **Glucose model optimization for specific patients**, by C. Burgos, J. C. Cortés, J. I. Hidalgo, D. Martínez, and R. J. Villanueva Pag: 189-195
32. **Semilocal convergence study under omega continuity condition**, by S. Singh, E. Martínez, D. K. Gupta, and A. Kumar Pag: 196-201
33. **Mathematical model based on the diffusion of electronic commerce in Spain**, by I. C. Lombana, C. Burgos, J. C. Cortés, D. Martínez, and R. J. Villanueva ... Pag: 202-207
34. **A New Content Location and Data Retrieval Algorithm for Peer to Peer in Smart Microgrids**, by S. Marzal, R. Salas, R. González, G. Garcera, and E. Figueres Pag: 208-213
35. **A mathematical invariance principle to study the body-mind problem**, by J. C. Micó, S. Amigó, and A. Caselles Pag: 214-218
36. **An approach to assess the competitiveness in Logistics Centers through the analysis of its effectiveness**, by V. Muerza, E. Larrodé, C. García Pag: 219-222
37. **Mathematical Modelling of Shafts in Drives**, by T. Náhlík, P. Hrubý, and D. Smetanová Pag: 223-228
38. **The Randomized Non-Autonomous Scaled Logistic Differential Equation: Theory and Applications**, by J. C. Cortés, A. Navarro, J. V. Romero, and M. D. Roselló Pag: 229-233
39. **Proposal of a graphic model for solving delay time model inspection cases of repairable machinery**, by F. Pascual, E. Larrodé, and V. Muerza Pag: 234-237
40. **New insights on multiplex PageRank**, by F. Pedroche, R. Criado, E. García, and M. Romance Pag: 238-243
41. **Simultaneous Smoothing and Sharpening of colour images**, by C. Pérez, J. Alberto Conejero, C. Jordán, and S. Morillas Pag: 244-249
42. **Numerical solution of nonlinear moving boundary problems for carbonation in reinforced concrete structures**, by M. A. Piqueras, R. Company, and L. Jódar Pag: 250-255
43. **Modeling the depreciation rate of construction machinery. An ordinary least-squares approach and quantile regression approach**, by D. Postiguillo, A. Blasco, and F. J. Ribal Pag: 256-263

44. **Mathematical modeling of the suicidal risk in Spain**, by E. de la Poza, L. Jódar, and D. Durá Pag: 264-269
45. **Coupling internal nozzle flow turbulence features to DNS of sprays primary atomization**, by F. J. Salvador, M. Crialesi-Esposito, J. V. Romero, and M. D. Roselló Pag: 270-276
46. **Numerical mode matching for sound propagation in silencers with granular material**, by E. M. Sánchez-Orgaz, F. D. Denia, L. Baeza, and R. Kirby Pag: 277-283
47. **Modal Method for the Efficient Analysis and Design of Microwave Filters based on Multiple Discontinuities**, by J. R. Sánchez, C. Bachiller, M. Juliá, and H. Esteban Pag: 284-289
48. **Introducing Covariates in Reliability Models by Markovian Arrival Processes**, by C. Santamaría, B. García-Mora, and G. Rubio Pag: 290-295
49. **Including a human happiness index in a social well-being model**, by J. C. Micó, D. Soler, M. T. Sanz, and A. Caselles Pag: 296-300
50. **Numerical solution of the Burgers' equation by splitting methods using Crank-Nicolson schemes**, by M. Seydaoğlu, and S. Blanes Pag: 301-306
51. **Infectious Disease Expansion: a discrete approach to the Kermack and McKendrick model**, by M. T. Signes, H. Mora, and A. Cortés Pag: 307-311
52. **On Legendre Transformation for Hamiltonian Systems Corresponding to Second Order Lagrangians**, by D. Smetanová Pag: 312-317
53. **Using Integer Linear Programming to study the relationship between the main variables involved in the construction of an external wall**, by A. Salandin, D. Soler, and J. C. Micó Pag: 318-322
54. **Metamaterial Acoustics on the $(2 + 1)D$ Schwarzschild Plane**, by M. M. Tung, and E. W. Weinmüller Pag: 323-334
55. **On the solution of different eigenvalue problems associated with the neutron transport using the nite element method**, by A. Vidal, S. González-Pintor, D. Ginestar, G. Verdú, and C. Demazière Pag: 335-340
56. **Finding multiple roots of nonlinear equations using eighth-order optimal iterative methods**, by F. Zafar, A. Cordero, S. Sultana, and J. R. Torregrosa Pag: 341-346
57. **Spatial modelling of diabetes patients in the region of Valencia**, by J. Díaz, D. Vivas, N. Guadalajara, and V. Caballer Pag: 347-351

58. **Modeling Plant Virus Propagation with Seasonality**, by M. Jackson, and B. Charpentier Pag:
352-357

A comparative study of the local convergence radius of iterative methods for multiple roots

D. Alarcón^b *; F. Cevallos[†], J. Hueso[‡]
and E. Martínez[‡]

(b) Departamento de Matemática Aplicada. Universitat Politècnica de València,

(†) Facultad de Ciencias Económicas. Universidad Laica Eloy Alfaro de Manabí,

(‡) Instituto Universitario de Matemática Multidisciplinar. Universitat Politècnica de València,

November 30, 2017

1 Introduction

In the last years some of the studies concerning on iterative methods for approximating roots of nonlinear equations have focused on multiple roots. That is, to find a multiple zero α of multiplicity m of a nonlinear equation $f(x) = 0$, $f : D \subseteq \mathbb{R} \rightarrow \mathbb{R}$, it is a special case where some particular aspects must be taken into account. In this sense different iterative methods for this particular case have been recently published see [1]-[6] and the references therein.

Given an iterative method, We say that r is the radius of the local convergence ball if the sequence x_n generated by this iterative method, starting from any initial point in the open ball $B(\alpha, r)$ converges to α and remains in the ball.

First of all, we have studied the local convergence of Dong's method (1). This method has two steps and because of that some variations must be taken into account.

$$y_n = x_n - \sqrt{m} \frac{f(x_n)}{f'(x_n)}, \quad (1)$$

$$x_{n+1} = y_n - m \left(1 - \frac{1}{\sqrt{m}}\right)^{(1-m)} \frac{f(y_n)}{f'(x_n)}. \quad (2)$$

Previous papers studied the local convergence of this method when the involved function satisfies Hlder continuity conditions, that is, $\forall x, y \in D$, $p \in]0, 1]$ and K_0, K_m positive real numbers,

$$\left| f^{(m)}(x^*)^{-1} (f^{(m+1)}(x) - f^{(m+1)}(y)) \right| \leq K_0 |x - y|^p, \quad (3)$$

$$\left| f^{(m)}(x^*)^{-1} f^{(m+1)}(x) \right| \leq K_m. \quad (4)$$

*e-mail: dielacor@doctor.upv.es

In this work we give a simple alternative to obtain this local convergence without using sophisticated properties of divided differences operators. In this case we will use the following bound conditions:

$$|f^{(m)}(\alpha)^{-1}f^{(m+1)}(x)| \leq k_1, \quad \forall x \in D, \quad k_1 > 0. \quad (5)$$

and in case the method uses second derivative we need a second assumption as follows:

$$|f^{(m)}(\alpha)^{-1}f^{(m+2)}(x)| \leq k_2, \quad \forall x \in D, \quad k_2 > 0. \quad (6)$$

2 Preliminaries

Lemma 1 *If α is a multiple zero of multiplicity m with $m > 1$, of a nonlinear equation $f(x) = 0$, where $f : D \rightarrow R$ is a sufficiently differentiable function in a open interval D , then the function $f(x)$ can be expressed as*

$$f(x) = (x - \alpha)^m h(x), \quad h(\alpha) \neq 0, \quad (7)$$

where

$$h(x) = \frac{f^{(m)}(\alpha)}{m!} + \frac{1}{(m-1)!} \int_0^1 [f^{(m)}(\alpha + \theta(x-\alpha)) - f^{(m)}(\alpha)](1-\theta)^{m-1} d\theta, \quad (8)$$

Lemma 2 *Let $f(x)$ be a function satisfying conditions (5) and (6) for all $x_0 \in]\alpha - r_0, \alpha + r_0[= I_0$ where $r_0 = \frac{m+1}{k_1}$ and $e_0 = x_0 - \alpha$. Then, function $h(x)$ defined by (8) verifies the following bounds:*

$$\begin{aligned} (B_1) \quad & |h(\alpha)^{-1}h(x_0)| \leq \frac{m+1+k_1|e_0|}{m+1} \\ (B_2) \quad & |h(\alpha)^{-1}h'(x_0)| \leq \frac{k_1}{m+1} \\ (B_3) \quad & |h(x_0)^{-1}h(\alpha)| \leq \frac{m+1}{m+1-k_1|e_0|} \\ (B_4) \quad & |h(x_0)^{-1}h'(x_0)| \leq \frac{k_1}{m+1-k_1|e_0|} \\ (B_5) \quad & |h(x_0)^{-1}h''(x_0)| \leq \frac{2k_2}{(m+2)(m+1-k_1|e_0|)}. \end{aligned}$$

3 Local convergence results

We start the study with the first step that we can write:

$$\hat{e}_0 = y_0 - \alpha = x_0 - \alpha - m^{\frac{1}{2}} \frac{f(x_0)}{f'(x_0)} = \frac{h'(x_0)e_0 + m^{\frac{1}{2}}(m^{\frac{1}{2}} - 1)h(x_0)}{h'(x_0)e_0 + mh(x_0)} e_0,$$

First, we bound upperly the numerator (\hat{A}_0) using the mean value theorem and the bounding conditions. Then, we use Banach Lemma to bound the denominator (\hat{B}_0). So we have:

$$|\hat{A}_0| \leq \frac{k_1|e_0| + m^{\frac{1}{2}}(m^{\frac{1}{2}} - 1)(m + 1 + k_1|e_0|)}{m(m + 1)}$$

$$|\hat{B}_0^{-1}| = \frac{m}{m - k_1|e_0|}.$$

It is important to notice that for bounding the denominator it appears a new restriction, so we have to take now $|e_0| < \frac{m}{k_1} = r_1$. Turning to the error equation we have:

$$|\hat{e}_0| \leq \frac{k_1|e_0| + m^{\frac{1}{2}}(m^{\frac{1}{2}} - 1)(m + 1 + k_1|e_0|)}{(m + 1)(m - k_1|e_0|)}|e_0| = g_1(|e_0|)|e_0|,$$

verifying $\exists r_2 \in]0, r_1[\ / \ 0 \leq g_1(t) < 1 \ \forall t \in]0, r_2[$. Now, we proceed to analyze the second step. In a similar reasoning as before we get:

$$|\hat{e}_1| \leq \frac{\varphi(|e_0|)}{(m + 1)(m - k_1|e_0|)} = g_2(|e_0|)|e_0|$$

verifying $\exists r_3 \in]0, r_2[\ / \ 0 \leq g_2(t) < 1 \ \forall t \in]0, r_3[$. The same process holds starting from x_1 and getting x_2 and by an inductive procedure and by taking limits in the infinite we have proved that the iterative sequence is well-defined and tends to α .

4 Numerical results

In this section, first we give the local convergence radius for the previous method. For that, we use some equations taken from [3] and [5].

Exercise	α	m	$k_1 = k_m$	k_2	k_0	p
$f_1(x) = \cos(x) - 1$	0	2	1	1	1	1
$f_2(x) = (x^{5/2} - 1)^2$	1	2	$\frac{54}{5} - \frac{1}{10}\sqrt{6}$	$\frac{72}{5} + \frac{1}{30}\sqrt{6}$	$\frac{72}{5} - \frac{3}{30}\sqrt{2}$	$\frac{1}{2}$
$f_3(x) = x^2(x^2 - 1)$	0	2	12	12	12	1
$f_4(x) = \int_0^x G(x)dx,$ $G(x) = \int_0^x (x + \cos(\pi x^2))dx$	0	2	$1 + 2\pi$	$2\pi(1 + 2\pi)$	2π	1
$f_5(x) = (\frac{1}{10}x - \frac{1}{15}x^{3/2})^2$	$\frac{9}{4}$	2	2.56	0.43	6.32	$\frac{1}{2}$
$f_6(x) = x^5 - 8x^4 + 24x^3 - 34x^2 + 23x - 6$	1	3	4	10	10	1

Table 1: Nonlinear examples.

In table 2 we can see the different values of $r_i, i = 0, 1, 2, 3$ described in our theoretical results for Dong's iterative method (1). As it can be observed, the minimum value for the radio is always r_3 .

Dong's method					
<i>Examples</i>	r_0	r_1	r_2	r_3	r
f_1	3	2.0000	0.9252	0.2167	0.2167
f_2	0.2842	0.1895	0.0877	0.0205	0.0205
f_3	0.2500	0.1667	0.0771	0.0181	0.0181
f_4	0.4119	0.2746	0.1270	0.0298	0.0298
f_5	1.1719	0.7813	0.3614	0.0846	0.0846
f_6	1.0000	0.7500	0.2763	0.0230	0.0230

Table 2: Numerical values of local convergence radii for examples given in Table (1).

5 Case of unknown multiplicity

Now the goal is to analyze the behavior of some iterative methods for multiple roots when the value of the multiplicity, m is unknown. Our aim in this section is to check if the formulas proposed in [7] for approximating the multiplicity. Finally, some examples are shown to demonstrate their application.

For this section, we use the modified Newton method, Osada's method and an optimum method of fourth order (M4), see [2] defined as

$$y_n = x_n - b \frac{f(x_n)}{f'(x_n)},$$

$$x_{n+1} = x_n - (s_1 + s_2h(y_n, x_n) + s_3h(x_n, y_n) + s_4h(y_n, x_n)^2) \frac{f(x_n)}{f'(x_n)}.$$

Additionally, to meet the objective, we have the following procedures to estimate the multiplicity m of the root given in [7].

We have defined three different strategies to approximate the multiplicity. First, without rounding the estimation. Second, rounding the estimation to the nearest integer and last one if we get to consecutive values of the estimation equal we work with this value and stop the estimation of the multiplicity. These 3 strategies have been applied to example f_2 of Section 4.

In order to compare the performance of the different strategies, we count the number of functional evaluations of the whole procedure per each case.

Table 3 shows, for each method and multiplicity estimation procedure, the number of iterations needed to converge, the approximated computational order of convergence obtained according to the absolute value of the difference between the last two iterates, the absolute value of the function at the last iterate, the multiplicity estimations used in each iteration, and the total cost of the iterations, in terms of the total number of evaluations of the function and its derivatives along the iterations of each method.

Although the methods for estimating the multiplicity give a good approximation to the multiplicity, using these estimations limit the convergence order

Method	Aprox.	iter	ρ	incr	$f(x_n)$	mul	EF
M. Newton	Ost ₁	6	2.00	7.42e-36	2.66e-141	[1.03, 1.96, 1.99, 1.99, 1.99, 1.99]	24
	Ost ₂	6	2.00	6.81e-26	7.58e-101	[1, 2, 2, 2, 2, 2]	24
	Ost ₃	6	2.00	6.81e-26	7.58e-101	[1, 2, 2]	18
	Scho ₁	7	2.00	3.88e-22	8.00e-86	[0.52, 1.21, 1.82, 1.99, 1.99, 1.99, 1.99]	21
	Scho ₂	6	2.00	6.81e-26	7.58e-101	[1, 2, 2, 2, 2, 2]	18
	Scho ₃	6	2.00	6.81e-26	7.58e-101	[1, 2, 2]	15
	Trau ₁	24	1.02	6.03e-22	2.56e-45	[..., 1.93]	48
	Trau ₂	9	2.00	4.06e-23	9.58e-90	[1, 1, 1, 1, 1, 2, 2, 2, 2]	18
	Trau ₃	30	1.00	6.06e-11	2.29e-20	[1, 1]	60
	Stra ₁	5	2.42	5.58e-35	4.80e-117	[1.03, 1.96, 1.99, 1.99, 1.99]	20
	Stra ₂	6	2.00	6.81e-26	7.58e-101	[1, 2, 2, 2, 2, 2]	24
	Stra ₃	5	2.00	6.54e-36	6.45e-141	[1, 2, 2]	16
	known	8	2.00	1.95e-38	5.13e-151	2	16
Osada	Ost ₁	6	2.00	6.61e-40	3.78e-157	[1.03, 1.98, 1.99, 1.99, 1.99, 1.99]	30
	Ost ₂	5	3.00	2.06e-35	2.18e-207	[1, 2, 2, 2, 2]	25
	Ost ₃	5	3.00	2.06e-35	2.18e-207	[1, 2, 2]	21
	Scho ₁	7	2.00	3.88e-22	8.01e-86	[0.52, 1.21, 1.82, 1.99, 1.99, 1.99, 1.99]	21
	Scho ₂	5	3.00	2.06e-35	2.18e-207	[1, 2, 2, 2, 2]	15
	Scho ₃	5	3.00	2.06e-35	2.18e-207	[1, 2, 2]	15
	Trau ₁	21	1.03	7.82e-21	1.33e-43	[..., 1.93]	63
	Trau ₂	8	3.00	1.28e-23	1.29e-136	[1, 1, 1, 1, 1, 2, 2, 2]	24
	Trau ₃	30	1.00	6.06e-11	2.29e-20	[1, 1]	90
	Stra ₁	5	2.43	3.13e-37	1.88e-125	[1.03, 1.96, 1.99, 1.99, 1.99]	25
	Stra ₂	5	3.00	2.06e-35	2.18e-207	[1, 2, 2, 2, 2]	25
	Stra ₃	4	2.39	3.15e-36	2.75e-212	[1, 2, 2]	21
	known	7	2.99	4.83e-42	3.61e-247	2	21
M4	Ost ₁	6	2.00	1.92e-33	5.57e-132	[1.03, 1.93, 1.99, 1.99, 1.99, 1.99]	30
	Ost ₂	4	4.01	1.10e-22	1.08e-175	[1, 2, 2, 2]	20
	Ost ₃	4	4.01	1.10e-22	1.07e-175	[1, 2, 2]	18
	Scho ₁	7	2.00	1.28e-36	1.95e-144	[0.52, 1.42, 1.95, 1.99, 1.99, 1.99, 1.99]	21
	Scho ₂	4	4.01	1.10e-22	1.08e-175	[1, 2, 2, 2]	12
	Scho ₃	4	4.01	1.10e-22	1.08e-175	[1, 2, 2]	12
	Trau ₁	16	1.03	6.41e-22	1.63e-46	[..., 1.93]	48
	Trau ₂	6	4.00	6.61e-41	1.80e-321	[1, 1, 1, 2, 2, 2]	18
	Trau ₃	30	1.00	1.08e-17	1.13e-34	[1, 1]	90
	Stra ₁	5	2.42	2.46e-45	6.00e-154	[1.03, 1.98, 1.99, 1.99, 1.99]	25
	Stra ₂	4	4.01	1.10e-22	1.08e-175	[1, 2, 2, 2]	20
	Stra ₃	4	3.43	2.43e-76	6.05e-605	[1, 2, 2]	18
	known	6	3.99	7.51e-28	4.95e-217	2	18

Table 3: $f_2(x) = (x^{5/2} - 1)^2$, $x_0 = 0.5$, $\alpha = 1$, $m = 2$

to about 2, in spite of the method’s theoretical convergence order, as seen in the tables at the rows where the method’s name has subindex 1. This convergence order can be reached by rounding the multiplicity estimations, as show the rows with subindexes 2 and 3.

An additional reduction of the cost can be obtained if one ceases estimating the multiplicity when it stabilizes. So, rows with subindex 3 have lower cost than the ones with subindex 2.

The Schroeder’s method for estimating the multiplicities gives in general the bests results, whereas Traub’s method fails sometimes in estimating the multiplicity and converging.

The cost increment due to the multiplicity estimation is quite moderated. In general, it is less than two times the cost of the same method with known multiplicity.

References

[1] I. Argyros, On the convergence and application of Newton’s method under weak Hlder continuity assumptions, Int. J. Comput. Math. 80 (2003) 767-780.

- [2] Jose L. Hueso, Eulalia Martnez, Carles Teruel, Determination of multiple roots of nonlinear equations and applications, *J. Math. Chem.* (2015) 880-892.
- [3] W. Bi, H. Ren, Q. Wu, Convergence of the modified Halley's method for multiple zeros under Hlder continuous derivative, *Numer. Algorithms* 58 (2011) 497-512.
- [4] Xiaojian Zhou, Xin Chen, Yongzhong Song, On the convergence radius of the modified Newton method for multiple roots under the center-Hlder condition, *Numer. Algor.* 65 (2014) 221-232.
- [5] Xiaojian Zhou, Yongzhong Son, Convergence radius of Osada's method under center-Hlder continuous condition, *Applied Mathematics and Computation* 243 (2014) 809-816.
- [6] C. Dong, A basic theorem of constructing an iterative formula of the higher order for computing multiple roots of an equation, *Mathematica Numerica Sinica*, vol. 11, pp. 445-450, (1982).
- [7] J.M. McNamee, A comparison of methods for accelerating convergence of Newton's method for multiple polynomial roots, *ACM SIGNUM Newsletter*, vol 33, pp. 17-22 (1998)

Mathematical modelling of the value of technology brands

Alcaide González, M^a Ángeles^a; De la Poza Plaza, Elena^a and Guadalajara Olmeda, Natividad^a

^aFaculty of Business and Management. Center of Economic Engineering, Universitat Politècnica de València, Spain.

*Corresponding author e-mail: manalgon@upv.es

Abstract

Nowadays there are a lot of methods to value brands, however there is not a consensus about the most convenient methodology to be used in accordance to the purpose of the valuation. For this reason, the most common methods are the mixed methods. This fact produced that international consultancy companies have developed rankings to value brands using its own mixed methods, but these consultancy companies also diverge in their results when ranking companies by their estimated brand value.

This paper deals with developing mathematical models that explain the value of brand rankings in the sector of new technologies based on economic-financial and stock market information from 2000 to 2016.

The linear regression analysis shows that economic-financial information is useful for explaining the brand value of technological companies; specifically, the *net results* is the most significant driver in the three selected rankings. Its explanatory power oscillates in the interval [45.7%, 61.8%]. Also, other common significant quantitative variables are: *financial expenses*, *number of employees* and *account receivables*. Furthermore, among 71.30% and 89% of the value of the brand is explained by economic-financial variables, while the remaining proportion [11%, 28.7%] is explained by the driver brand strength. Finally, our results show that some consultancy companies value brands over others consistently; in concrete Millward Brown values are the highest, while Brand Finance values are lower than the other two selected consultancy companies.

Keywords

Valuation, economic-financial information, technology brands, models, rankings.

1. Introduction

In recent years, brands have taken a significant relevance in the creation of value of the companies (Bonet, 2003). Nevertheless, due to the component of immateriality and subjectivity of brands, there is no consensus on the most appropriate valuation method and numerous valuation methods have been developed. These methods can be classified into two main groups: methods based on economic-financial information (Aaker, 1991; Damodaran, 1994, 2007; Fernández, 2005; Simon & Sullivan, 1993), and methods based on consumer perception (Kapferer, 1992, 2004; Keller, 1993, 2007; Ratnatunga & Ewings, 2009).

While methods based on marketing perspective or consumer perception provide an index of the value of the brand and they use qualitative variables, methods based on economic-financial perspective provides a quantitative value of the brand through economic-financial variables.

At the same time, within the economic-financial approach to brand valuation are distinguished three methods, based on costs, market and results. However, through the study of the literature (Majerova & Kliestik, 2015; Salinas & Ambler, 2009) it is observed that the vast majority of researches do not use a pure method, but a combination of them, mixing qualitative and quantitative variables, and those are called the mixed methods.

Due to this lack of consensus in methodologies and since there isn't a single method to value brands, the most used methods are the mixed methods. And this fact produced that international consultancy firms, such as Interbrand, Brand Finance, and Millward Brown, have developed rankings to value brands using mixed methods, but this consultancy companies only publish the top 100 brands of their rankings. Moreover, they diverge results in their annual rankings, since the position of brands in the rankings are different between them, and this is due to the different methodology and variables considered for valuing the brand.

The aim of this paper is to develop mathematical models that explain the value of brand rankings in the sector of new technologies based on economic-financial and stock market information.

2. Method

a. Information sources

Data was obtained from secondary sources of information, in particular from the annual rankings of brands estimated by 3 consultancy firms during the period from 2000 to 2016, but also from the annual income statements of the brand's companies. Our population of study was composed by those brands that had been ranked in the top 100 of at least two of the three consultancy firms Interbrand, Millard Brown and Brand Finance but also the companies must belong to the technology sector. Then, the economic-financial information of the companies was obtained from the firms' publicly reported income statements.

With these requirements, the population of study is composed by 13 technology brands. Those are Apple, Cisco, Google, HP, IBM, Intel, Microsoft, Oracle, Samsung, SAP, Sony, Accenture, and Facebook.

b. Mathematical model

The methodology used is a multivariate linear regression analysis using the next expression:

$$Y = a + b_1 X_1 + b_2 X_2 + \dots + b_n X_n + \varepsilon$$

The parameters used are:

Y: Dependent variable,

a: Constant term,

b_i: Coefficients of the explanatory variables. Estimated by Ordinary Least Squares.

X_i: Explanatory variables,

ε: Random disturbance term,

However, to satisfy the hypotheses of normality, heterogeneity, and linearity, dependent variable has been transformed in logarithmic form. The model is expressed as follows:

$$\ln Y = a + b_1 X_1 + b_2 X_2 + \dots + b_n X_n + \varepsilon$$

Dependent variables are the value of the brands estimated by the 3 consultancy firms selected. According with these criteria, 8 models have been built, where dependent variables in each model are:

Model 1 and 2 → V_{Imn} : Interbrand value (\$) of brand m in period n,

Model 3 and 4 → V_{Bmn} : Brand Finance value (\$) of brand m in period n,

Model 5 and 6 → V_{Mmn} : Millward Brown value (\$) of brand m in period n,

Model 7 and 8 → V_{mn} : Value of the three firms (\$) of brand m in period n,

And there are 17 explanatory variables expressing the economic-financial information of the companies. Those variables are: *accounts receivables, capital, current assets, current liabilities, dividends, dividends per share, financial expenses, net equity, net result, number of employees, number of shares, operating income, research and development, sales, tax rate, total assets, and total liabilities.*

3. Results

Results of regression analysis are compiled in Table 1.

Table 1. Models generated by regression analysis for each ranking.

EXPLANATORY VARIABLES	DEPENDENT VARIABLES					
	Ln V _{Imm}		Ln V _{Bmm}		Ln V _{Mmm}	
	MODEL 1	MODEL 2	MODEL 3	MODEL 4	MODEL 5	MODEL 6
CONSTANT	9.475	9.014	9.523	9.095	9.712	9.777
NET RESULT	7.12	9.104	5.243	2.698	6.778	2.562
R&D		7.951				-5.545
EMPLOYEES		1.24		3.267		3.932
FINANCIAL EXPENSES		-1.525		-1.293		-2.919
DVND. PER SHARE		-0.04				-0.04
ACCOUNT RECEIVABLES		1.837		3.053		4.231
NUM. SHARES				1.264		
TOTAL LIABILITIES						-7.645
N	201		104		137	
Adjusted R ²	58.80%	89.00%	61.80%	79.00%	45.70%	71.30%
F	234.687	190.508	154.907	60.702	103.748	38.885

As table I shows, the goodness of fit of models 1, 3 and 5 varies among the interval [45.7%, 61.80%]; for those models *net results* was the only explanatory variable. However, models 2, 4 and 6, reached a better goodness of fit by including additional explanatory variables (Table 1), resulting in a higher goodness of fit. Thus, Interbrand values reached a of 89% explanatory power, while Brand finance was 79% and Millward Brown was 71.30%.

Model number 2 reached the best goodness of fit (89%) explained by quantitative variables, thus the remained percentage, 11%, could be explained by qualitative variables or brand strength.

Table 2. Models generated by regression analysis for the three rankings jointly.

EXPLANATORY VARIABLES	DEPENDENT VARIABLE: Ln V _{mm}		
	MODEL 7	MODEL 8	
CONSTANT	9,15	9.212	
NET RESULT	6.085	1.858	
CURRENT ASSETS		3.162	
EMPLOYEES		4.166	
NUM. SHARES		9.838	
ACCOUNT RECEIVABLES		3.04	
TOTAL LIABILITIES		-4.156	
FINANCIAL EXPENSES		-18	
D.INTERBRAND		0.213	Δ +23.70%
D.MILLWARD BROWN		0.412	Δ +50.98%
N	312		
Adjusted R ²	51.10%	74.50%	
F	383,083	94,911	

Table 2 shows results of models 7 and 8, where dependent variable are the values of three rankings jointly in logarithmic form, from period 2007 to 2016. Then, the number of observation is 312. Moreover, we have introduced dummy variables of the 3 rankings in those two models.

We observe that model 7 is only explained by *net results*, where its goodness of fit is 51.10%. However, model 8 is explained by quantitative variables (see Table 2). Model 8 is better than model 7, because its goodness of fit is 74.50%.

Therefore, Brand Finance adds less value in comparison with Interbrand and Millward Brown valuations. In particular, Millward Brown increase the values by approximately 51% in relation to Brand Finance, and Interbrand's does by 23.70%.

4. Conclusions

The paper presents models to value brands of technology sector considering quantitative variables, such as the economic financial information of companies but also the value of brands estimated by international consultancy companies.

On the one hand, the main result obtained is that economic-financial information is useful for estimating the brand value of technological companies. Specifically, results show that *net result* is the most significant driver in the three rankings, its explanatory power ranges in the interval [45.7%, 61.8%]. Other common significant quantitative variables are: *financial expenses*, *number of employees* and *account receivables*. In addition, among 71.30% and 89% of the value of the brand is explained by economic-financial variables, while the remaining 11-28.7% by brand strength.

On the other hand, results show that some consultancy companies value higher than others, in concrete Millward Brown values higher, while Brand Finance value lower than the other two companies.

References

- Aaker, DA. (1991). Managing brand equity. Capitalizing on the value of a brand name. *Editorial the Free Press*.
- Abratt, R. & Bick, G. (2003). Valuing brands and brand equity: Pitfalls and processes. *Journal of Applied Management and Entrepreneurship*, 8, 21-39.
- Bonet, J. (2003). The importance of brands for the company. Valuation criteria. *Judicial Studies*, 49, 305.
- Chu, S. & Keh, H.T. (2006). Brand value creation: Analysis of the Interbrand-Business Week brand value rankings. *Springer Science*, 17, 323-331.
- Damodaran, A. (1994). Damodaran on valuation. *John Wiley and Sons*. New York.

- Damodaran, A. (2007). Valuation approaches and metrics: A survey of the theory and evidence. *Foundations and Trends in Finance*, 1(8), 693-784.
- Fernández, P. (2005). Valuation of companies: How to measure and manage the creation of value. *Editions Management 2000*.
- Guadalajara, N. & Barrachina, I. (2013). Application of simultaneous equation models to temporary disability prescriptions in primary healthcare centres. *International Journal of Computer Mathematics*, 91(2), 252-260.
- Gujarati, D.N. (2003). *Econometrics*. Mc Graw-Hill Companies, Mexico.
- Kapferer, J.N. (1992). The brand, capital of the company: Principles and control of its management. *Editions Deusto*.
- Kapferer, J.N. & Schuiling, I. (2004). Executive insights: Real differences between local and international brands: Strategic implications for international marketers. *Journal of International Marketing*, winter 2004, 12(4), 97-112.
- Keller, K.L. (1993). Conceptualizing, measuring and managing customer-based brand equity. *Journal of Marketing*, 57, 1-22.
- Keller, K.L. (2007). *Strategic Brand Management*. Praha: *Grada Publishing*, 796.
- Majerova, J. & Kliestik, T. (2015). Brand valuation as immanent component of brand value building and managing. *4th World Conference on Business, Economics and Management, WCBWM*, 26, 546-552.
- Ratnatunga, J. & Ewing, M.T. (2009). An ex-ante approach to brand capability valuation. *Journal of Business Research*, 62(3), 323-331.
- Salinas, G. & Ambler, T. (2009). A taxonomy of brand valuation practice: Methodologies and purposes. *Journal of Brand Management*, September, 17(1), 39-61.
- Schendel, D. & Patton, G.R. (1978). A simultaneous equation model of corporate strategy. *Management Science*, 24(15), 1611-1621.
- Simon, J. & Sullivan, M. (1993). The measurement and determinants of brand equity: A financial approach. *Marketing Science*, 1(12), 28-52
- Timoteo, J., Matías, G., Buxaderas, E. & Ferruz, S. (2015). Intangibles in the value of companies. The business of Faust. *Editions Díaz de Santos*.

Methylphenidate and the self-regulation therapy: a systemic mathematical model

Salvador Amigó^{*1}, Joan C. Micó^{**}, Antonio Caselles^{***}

(*) Departament de Personalitat, Avaluació i Tractaments Psicològics.
Universitat de València,

Av. Blasco Ibáñez 21, 46010, ciutat de València, Spain.

(**) Institut Universitari de Matemàtica Multidisciplinar.
Universitat Politècnica de València.

Camí de Vera s/n., 46022, ciutat de Valencia, Spain.

(***) Departament de Matemàtica Aplicada.
Universitat de València.

Dr. Moliner 50, 46100 Burjassot, Spain.

1. Introduction

The Self-Regulation Therapy (SRT) is a psychological procedure based on learning and suggestion that has been specially designed to facilitate reproducing effects of drugs, imitation and re-experimenting effects of drugs. For a review of the theoretical foundations and experimental results, see Amigó (2016). This article deals with reproducing the effects of a stimulating drug, methylphenidate (MP).

The SRT can be used to remember the effects of a drug taken in the past, or to re-experiment the effects of a recently taken drug when a detailed account of its effects is still remembered. In the latter case, the procedure consists in two sessions: 1) a drug-taking session by experiencing real effects and scoring them with subjective scales of the effects and with instruments to measure physiological variables; 2) reproducing effects of a drug “mentally” by next using the SRT (2 or 3 days later).

To compare the effects, former research has statistically compared the subjective and physiological scores obtained at the most intense point of the effects of a drug, or what is known as the drug’s *high* (and rush). In this way, the similarity between the drug’s high and that achieved with the SRT is verified. This is precisely what was achieved for MP and the SRT (Amigó, 1997, 2005, Amigó, Caselles, Micó & García, 2009).

Comparing the dynamic effects of a drug and the SRT is most interesting to verify whether the evolution of the subjective and objective scores corresponds. The main tool employed to date for this purpose has been a visual inspection, which verifies the similarity between the effect of MP and the SRT as far as the course of the effects curve is concerned, although the duration of the effect with the SRT is shorter than it is with the drug (Amigó, Caselles & Micó, 2013; Micó, Amigó & Caselles, 2012). Nonetheless, the mathematical analysis is more complex for two reasons; on the one hand, scores present serial dependence; on the other hand, and as previously mentioned, a visual inspection reveals differences in the type of effects curve. For instance, the duration of the effect of the SRT is shorter than it is with the drug and, moreover, the effect starts earlier, is more intense and also ends earlier with the SRT than with the drug. Thus determining a direct correspondence between the effects curve obtained with MP and the SRT is not the most suitable approach.

This article proposes dealing with this matter, that of comparing the effects curves of MP and the SRT, with a voluntary participant using a single-case experimental design.

Participant, design and procedure

¹ E-mail: salvador.amigo@uv.es

The participant was a 46-year-old man who was a University of Valencia staff member. A single-case experimental ABC design was used. In phase A, the participant received no treatment. At the start of phase B, the participant took 20 mg of MP. In phase C, he underwent the SRT to reproduce the effects of MP, but did not take this drug. In phases A and B, the participant filled in a sheet of adjectives every 15 minutes over a 4-hour period. In phase C, the participant filled in the list for 2 hours as previous studies have indicated visibly shorter effects than that of the drug. These adjectives measure the General Factor of Personality, which represents the organism's general activation. It is a Five-Adjective Scale of the General Factor of Personality (GFP-FAS, Amigó, Mico & Caselles, 2009), and the five adjectives are: adventurous, daring, enthusiastic, merry and bored. For the mathematical analysis, the response model was applied as an integro-differential equation, whose usefulness has been shown to model the dynamic effect of a stimulant drug (Amigó, Caselles & Micó, 2008; Caselles, Micó & Amigó, 2010, 2011). The model is as follows:

$$\left. \begin{aligned} \frac{dy(t)}{dt} &= a(b - y(t)) + \frac{p}{b}s(t) - b \cdot q \cdot \int_0^t e^{-\frac{x-t}{\tau}} \cdot s(x) \cdot y(x) dx \\ y(0) &= y_0 \end{aligned} \right\} \quad (1)$$

In (1), $s(t)$ represents the stimulus, $y(t)$ represents the GFP-FAS, and b e y_0 are respectively their tonic level and initial value. The other parameters are a , p , q and τ , which are respectively called the power of the homeostatic effect, the power of the excitement effect, the power of the inhibitor effect and the delay in the inhibitor effect. The stimulus was calculated as:

$$s(t) = \begin{cases} \frac{\alpha \cdot M}{\beta - \alpha} (\exp(-\alpha \cdot t) - \exp(-\beta \cdot t)) : \alpha \neq \beta \\ \alpha \cdot M \cdot t \cdot \exp(-\alpha \cdot t) : \alpha = \beta \end{cases} \quad (2)$$

In (2), it is assumed that the organism is completely free of MP before it is administered. M is the quantity of MP taken, α is the assimilation rate and β is the distribution rate.

Results

Figure 1 depicts the GFP dynamics during the 4-hour period of Phase A without treatment. We observe mass data dispersion. Figure 2 shows the GFP dynamics caused by 20 mg of MP in Phase B, with an inverted U, which has been obtained in the studies cited in the previous section. The GFP dynamics also takes an inverted U, obtained after reproducing the effects of MP with the SRT in Phase C (see Figure 3). However, the Phase C duration lasts half the time of the other two phase durations (because the effect of the SRT is known to last less than that of MP). The GFP recovers in the end.

Tables 1 and 2 provide the value of the model parameters that correspond to Phases B (with MP) and C (with the SRT). We can see that some parameters considerably differ. Indeed in Phase C, both the excitement and inhibitor effects are greater than in Phase B, as is the assimilation rate, while the delay in the inhibitor effect is shorter. On the whole, we can conclude that the effect becomes more intense with the SRT than with MP itself, but the MP dose is 20 mg (M1) and the SRT "dose" is 7.67 (M2), which seems a contradiction. However, as already mentioned, the SRT effect duration is approximately half that of the MP.

Discussion

Now it is important to reflect on the apparent contradictions that we have just pointed out. The duration of the effect is shorter with the SRT than it is with MP. Hence we can conclude that the suggested SRT "dose" (7.67 mg) is lower than the MP one (20 mg) and, to a point, it is proportional to the duration of the effect.

So, why is it that when reading the parameters in Tables 1 and 2 we think that the SRT effect is more intense despite lasting less? Let's remember that the excitement and inhibitory

effects, and the assimilation rate, are greater. The response is found in the shape of the curve. The curve produced by MP is flatter than that produced by the SRT, and the latter curve presents an initially more pronounced slope and also a quicker drop. Nonetheless in the two phases, the participant experiences a high at the same level with both MP and the SRT, with a score of 24 out of 25. So why then is the SRT “dose” considerably smaller than that of MP?

The response that best includes these apparently different and contradictory results is to consider the hypothesis that the SRT reflects the effect of the drug, but the drug is administered differently. We know that as opposed to being taken orally, snorting causes subjective effects more quickly, with a more intense “rush” in stimulants like d-amphetamine or methamphetamine (e.g., Hart et al., 2008; Lile et al., 2011). The hypothesis that stems from this article is that the SRT reproduces the effect of MP, but not when taken orally, rather when it is snorted or taken intravenously. Following intravenous dosing, uptake in the brain is very fast for methylphenidate (6–10 minutes) and the onset of the perceived “high” parallels the fast uptake of the drugs in the striatum, with the peak for the “high” reported at about the same time as the peak striatal concentration. But, however, the “high” returned to baseline even while the striatal levels of methylphenidate remained high (80% of peak). “Behavioral/reinforcing half life” of intravenous methylphenidate is much shorter than its pharmacokinetic half life (Volkow and Swanson, 2003; pp. 1912-1913). Thus we could consider that the SRT “dose” of 7.67 mg (M2) is the equivalent of MP being snorted or taken intravenously, which corresponds to an oral 20 mg dose (M1) in the $M1/M2=2.6$, proportion, as seen in Table 2.

The consequences would be most significant if this were indeed the case. With the mathematical response model that was used herein, and which we mentioned earlier, we could calculate the proportional doses of a given drug according to how it is administered, which would extend its application in the pharmacology domain and in the study of drugs, and also with therapeutic consequences. Thus if someone is capable of applying the SRT to him/herself to experiment the rush of a drug by snorting or by taking it intravenously, and without having to take the drug, or by remembering its effects when orally taken, it would be feasible to follow this procedure to reduce, or to even eliminate, real drug use. Evidence exists that the SRT can reduce drug craving (see Amigó, 1996, for a review).

Although what is currently a hypothesis needs to be empirically confirmed, and repeating this study with more participants is also necessary, it is true that we have established a reasonable criterion to mathematically compare the real effect of a drug and the conditioned effect which, in this case, is done by the SRT. Thus it is a matter of mathematically studying the invariance of real effects with “mental” or psychological ones. This also opens up a new perspective on the path that we have been following to study the mind-body problem (Micó, Caselles, Amigó, Cotolí & Sanz, 2013).

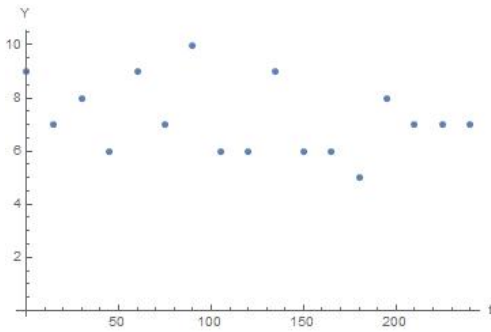


Figure 1: Dynamics of the *GFP*(Y) versus time (t) in minutes, for Phase A

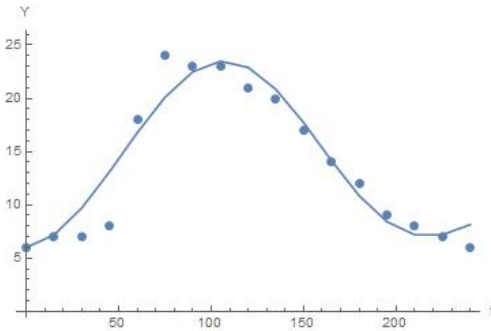


Figure 2: Dynamics of the *GFP* (Y), measured by the *GFP-FAS*, versus time (t) in minutes, for Phase B. The dots represent the experimental values and the curve the theoretical values. $R^2=0.91$.

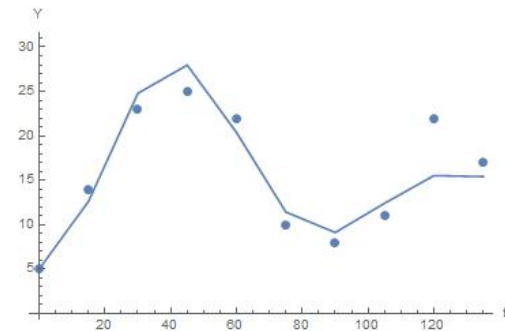


Figure 3: Dynamics of the *GFP* (Y), measured by the *GFP-FAS*, versus time (t) in minutes, for Phase C. The dots represent the experimental values and the curve the theoretical values. $R^2=0.81$.

Parameter symbol	Name	Optimal value
$M1$	Methylphenidate dose	20.0
τ	Inhibitor effect delay	102.1278972923755600
α	Assimilation rate	0.0032860666513443
β	Distribution rate	0.0008838047437323
a	Homeostatic control power	0.0049064028928751
b	Tonic level	10.9240722656250000
p	Excitation effect power	1.3321752324700356
q	Inhibitor effect power	0.0000126763916016
p/b	Excitation effect intensity	0.1219485920705610
$q.b$	Inhibitor effect intensity	0.0001384778179232

Table 1: optimal values of the model parameters 2, Phase B, corresponding to the *GFP* dynamics (Y).

Parameter symbol	Name	Optimal value
$M2$	Dose without Methylphenidate	7.6786547899246216

τ	Inhibitor effect delay	26.8286811240000200
α	Assimilation rate	0.0374856430099922
β	Distribution rate	0.0001013970502164
a	Homeostatic control power	0.0010036492012055
b	Tonic level	16.6801452636718750
p	Excitation effect power	5.1046919459528768
q	Inhibitor effect power	0.0000507841074228
p/b	Excitation effect intensity	0.3060340222018650
$q.b$	Inhibitor effect intensity	0.0008470862888982
$M1/M2$	Dose proportion	2.6046228860610500

Table 2: optimal values of the model parameters, Phase C, corresponding to the *GFP* dynamics (Y).

References

- Amigó, S. (1996). Vencer el deseo de la droga: un tratamiento alternativo. En Amigó (Ed.), II Jornadas sobre Drogodependencias. Valencia: Servicio de Publicaciones de la Universidad Politécnica de Valencia. (pp. 91-116).
- Amigó S. (1997). Uso potencial de metilfenidato y la sugestión en el tratamiento psicológico y en el aumento de las potencialidades humanas: Un estudio de caso [Potential use of methylphenidate and suggestion in the psychological treatment and in the increase of human potentialities: A case study]. *Análisis y Modificación de Conducta*, 23, 863–890.
- Amigó, S. (2005). *La teoría del rasgo único de personalidad. Hacia una teoría unificada del cerebro y la conducta* (The Unique Personality Trait Theory. Towards a unified theory of brain and behavior). Editorial de la Universitat Politècnica de València. Valencia, Spain.
- Amigó, S. (2016). Sugar Pills To Experience Cocaine and Other Drug Effects: The Self-Regulation Therapy As a Placebo Without Deception. *EC Neurology*, 3.1, 320-331.
- Amigó, S., Caselles, A. & Micó, J.C. (2008). A dynamic extraversion model: the brain's response to a single dose of a stimulant drug. *British Journal of Mathematical and Statistical Psychology*, 61, 211–231.
- Amigó S., Caselles A. & Micó J. C. (2013). Self-regulation therapy to reproduce drug effects: A suggestion technique to change personality and DRD3 gene expression. *The International Journal of Clinical and Experimental Hypnosis*, 61, 282–304.
- Amigó, S., Caselles, A., Micó, J.C. & García, J.M. (2009). Dynamics of the unique trait of personality: blood's glutamate in response to methylphenidate and conditioning. *Revista Internacional de Sistemas*, 16, 35-40.
- Amigó, S., Micó, J.C. & Caselles, A. (2009). Five adjectives to explain the whole personality: a brief scale of personality. *Revista Internacional de Sistemas*, 16, 41-43.
- Caselles, A., Micó, J. C., & Amigó, S. (2010). Cocaine addiction and personality: A mathematical model. *British Journal of Mathematical and Statistical Psychology*, 63, 449–480.
- Caselles, A., Micó, C., & Amigó, S. (2011). Dynamics of the General Factor of Personality in response to single dose of caffeine. *The Spanish Journal of Psychology*, 14, 675–692.
- Hart, C.L., Gunderson, E.W., Perez, A., Kirkpatrick, M.G., Thurmond, A., Comer, S.D. et al (2008). Acute physiological and behavioral effects of intranasal methamphetamine in humans. *Neuropsychopharmacology*, 33, 1847–1855.
- Lile, J.A., Babalonis, S., Emurian, C., Martin, C.A., Wermeling, D.P. & Kelly TH. (2011). Comparison of the behavioral and cardiovascular effects of intranasal and oral d-

- amphetamine in healthy human subjects. *Journal of Clinical Pharmacology*, 51, 888–898.
- Micó, J.C., Amigó S. & Caselles, A. (2012). Changing the General Factor of Personality and the c-fos expression with methylphenidate and Self-Regulation Therapy. *The Spanish Journal of Psychology*, 15(2): 850-867.
 - Micó, J.C., Caselles, A., Amigó, S., Cotoí, A. & Sanz, M.T. (2013). A mathematical approach to the body-mind problem from a System Personality theory. *Systems Research and Behavioral Science*, 30, 735–749.
 - Volkow, N.D. & Swanson, J.M. (2003). Variables that affect the clinical use and abuse of methylphenidate in the treatment of ADHD. *American Journal of Psychiatry*, 160, 1909–1918.

Jacobian-free iterative schemes to solve nonlinear systems

A. R. Amiri^{b,*}, A. Cordero[†], M. T. Darvishi^b, and J. R. Torregrosa[†]

(b) Department of Mathematics, Razi University, Iran

Tazeh Abad, Kermanshah, 67149-67346, Kermanshah Province, Iran

(†) Instituto de Matemáticas Multidisciplinar, Universitat Politècnica de València

Camí de Vera, s/n, 46022 València

November 30, 2017

1 Introduction

One of the most important and challenging problems in scientific computing is to find efficiently the real roots of nonlinear systems. Let us consider the system of nonlinear equations of the form

$$G(x) = Ax - \varphi(x) = 0, \quad (1)$$

where $A \in \mathbb{C}^{m \times m}$ and $\varphi(x) : \mathbb{D} \subseteq \mathbb{C}^m \rightarrow \mathbb{C}^m$. This kind of nonlinear equations arise in many areas of scientific computing and engineering applications. In this paper, we try to find the solution of these nonlinear equations, when A is a large, sparse, positive definite matrix and $\varphi(x)$ is a continuously differentiable function. The most common root-finding method for nonlinear systems is Newton's scheme

$$x^{(n+1)} = x^{(n)} - [G'(x^{(n)})]^{-1}G(x^{(n)}), \quad n = 0, 1, 2, \dots$$

*e-mail: amiriabdolreza@gmail.com, acordero@mat.upv.es, darvishimt@yahoo.com, jr-torre@mat.upv.es

Besides, many high order schemes in recent decades have been introduced to improve the order of convergence of Newton method. Most of these methods need to compute or approximate Jacobian matrix at one or several points at each iteration, which is a very time-consuming process. Therefore, introducing any scheme which does not need Jacobian matrices is welcome. Based on the separability and strong dominance between the linear term Ax and the nonlinear term $\varphi(x)$ (weakly nonlinear system), one can use the Picard iteration method as (see [1])

$$Ax^{n+1} = \varphi(x^n). \quad (2)$$

By applying (2), one must solve a linear system such as $Ax = b$. Usually an iterative method is used to solve this linear system that arises at each step of the Picard iteration. We call these iterative methods inner iterations. Some of the most famous inner iteration methods are Jacobi, Gauss-Siedel, successive overrelaxation (SOR), accelerated overrelaxation (AOR) and Krylov subspace methods. They are based on splitting of the coefficient matrix A as $A = M - N$.

In this paper, we present two new Jacobian-free methods to solve nonlinear systems. In the next section we introduce the new algorithms and in Section 3 some numerical tests are performed.

2 New algorithm

In this section, we propose a new iterative method to solve nonlinear systems which is based on HSS scheme [2]. Let us consider the system of linear equations $Ax = b$ and suppose that H and S are the Hermitian and skew-Hermitian parts of A , respectively, that is, $A = H + S$ with $H = \frac{1}{2}(A + A^*)$ and $S = \frac{1}{2}(A - A^*)$. Now, for an initial guess $x_0 \in \mathbb{C}^m$, and positive constants α and tol , in HSS scheme, one computes x_l for $l = 1, 2, \dots$ by

$$\begin{cases} (\alpha I + H)x_{l+\frac{1}{2}} = (\alpha I - S)x_l + b, \\ (\alpha I + S)x_{l+1} = (\alpha I - H)x_{l+\frac{1}{2}} + b, \end{cases} \quad (3)$$

where α is a given positive constant and I denotes the identity matrix. Stopping criteria for relations (3) is $\|b - Ax_l\| \leq \text{tol}\|b - Ax_0\|$, for an initial guess x_0 and a given tolerance tol .

When the the system of nonlinear equations (1) is weakly nonlinear, Picard-HSS is a Jacobian-free method for solving nonlinear problems.

Usually a modified form of Picard scheme called nonlinear Picard is used to avoid the computing of the stopping criteria at each step of Picard iteration. However, this variant is still too costly.

In order to solve (1), without using Jacobian matrices we construct a new algorithm that not only, like Picard and non-linear Picard, is good for solving weakly nonlinear problems, but also it can solve wider range of nonlinear problems. First, let us change (1) as

$$Ax^{(n+1)} - Ax^{(n)} = -Ax^{(n)} + \varphi(x^{(n)}). \tag{4}$$

For known $x^{(n)}$, we define $b^{(n)} = \varphi(x^{(n)})$ and $G_n(x) = b^{(n)} - Ax$. Next, by intermediate iterations we obtain $x^{(n+1)}$ as follows:
 Let $x_0^{(n)} = x^{(n)}$ and until $\|G(x_k^{(n)})\| \leq \text{tol}_n \|G(x_0^{(n)})\|$ do

$$As_k^{(n)} = G(x_k^{(n)}), \tag{5}$$

where $s_k^{(n)} = x_{k+1}^{(n)} - x_k^{(n)}$. Note that to solve (5) we can use any inner solver, here we use HSS scheme. Then for initial value $x_0^{(n)}$ and $k = 1, 2, \dots, k_n - 1$ until $\|G_n(x_k^{(n)})\| \leq \text{tol}_n \|G_n(x_0^{(n)})\|$, we apply HSS algorithm as follows:

- 1) Set $s_{k,0}^{(n)} = 0$.
- 2) For $l = 0, 1, 2, \dots, l_{k_n} - 1$, apply algorithm HSS:

$$\begin{cases} (\alpha I + H)s_{k,l+\frac{1}{2}}^{(n)} = (\alpha I - S)s_{k,l}^{(n)} + G_n(x_k^{(n)}) \\ (\alpha I + S)s_{k,l+1}^{(n)} = (\alpha I - H)s_{k,l+\frac{1}{2}}^{(n)} + G_n(x_k^{(n)}) \end{cases} \tag{6}$$

and obtain $s_{k,l_{k_n}}^{(n)}$ such that

$$\|G_n(x_k^{(n)}) - As_{k,l_{k_n}}^{(n)}\| \leq \eta_k^n \|G_n(x_k^{(n)})\| \quad \eta_k^n \in [0, 1]. \tag{7}$$

- 3) Set $x_{k+1}^{(n)} = x_k^{(n)} + s_{k,l_{k_n}}^{(n)}$.

Finally, set $x_0^{(n+1)} = x_{k_n}^{(n)}$, $b^{(n+1)} = \varphi(x_0^{(n+1)})$ and $G_{n+1}(x) = b^{(n+1)} - Ax$ and again we apply the previous steps until the following stopping criteria holds

$$\|Ax^{(n)} - \varphi(x^{(n)})\| \leq \text{tol} \| Ax^{(0)} - \varphi(x^{(0)}) \| .$$

At the end of this procedure we set $x^{(n+1)} = x_{k_{n+1}}^{(n)}$. This algorithm is a Jacobian-free one, because we don't compute any Jacobian matrix. Also, since in this algorithm we use the HSS method thus in fact, we have a Jacobian-free HSS scheme. In it there are three kinds of iterations. The outermost iteration which yields $x^{(n)}$, is used to generate new $b^{(n)} = \varphi(x^{(n)})$ and $G_n(x) = b^{(n)} - Ax$. The intermediate iteration that we call it Newton-like iteration scheme, because it is similar to Newton-HSS scheme (see [5]). However in this intermediate iteration, Jacobian matrix is not used. The other iteration, which is used in this algorithm is the innermost iteration, which applies HSS scheme to solve linear equations that are obtained in each iteration of our Newton-like scheme. We call this new method as JFHSS (Jacobian free HSS) algorithm.

Since JFHSS scheme uses many HSS splittings based on HSS algorithm, hence we can use another splitting methods instead of the HSS one. In the next section we use the JFHSS scheme to solve a system of nonlinear equations.

3 Numerical tests

In this section, we apply JFHSS method to solve a system of nonlinear equations. This example shows that JFHSS method perform better than Nonlinear HSS-like and Picard-HSS. Consider the following two-dimensional nonlinear convection-diffusion equation [3]

$$\begin{aligned} -(u_{xx} + u_{yy}) + qe^{x+y}(xu_x + yu_y) &= ue^u + \sin(\sqrt{1 + u_x^2 + u_y^2}), & (x, y) \in \Omega \\ u(x, y) &= 0, & (x, y) \in \partial\Omega \end{aligned}$$

where $\Omega = (0, 1) \times (0, 1)$, $\partial\Omega$ is its boundary and q is a positive constant for measuring magnitude of the convection term. By applying the upwind finite difference scheme on the equidistant discretization grid with the stepsize $h = \frac{1}{N+1}$ and the central difference scheme to the convective term, we

obtain a system of nonlinear equations of the form

$$F(x) = Mx - h^2\psi(x). \tag{8}$$

The initial guess is chosen as $u^{(0)} = 0 = (0, 0, \dots, 0)^T$. The stopping criterion for the outer iteration in this example for all methods, is

$$\frac{\|Mu^{(n)} + h^2\psi(u^{(n)})\|}{\|Mu^{(0)} + h^2\psi(u^{(0)})\|} \leq 10^{-12}.$$

q			50	100	200	400	1200	2000
<i>N</i> = 48	JFHSS	α_{opt}	0.8	1.4	2.6	4.8	13	20.5
		CPU	5.25	5.31	5.5	5.93	6.21	6.28
		IT_{out}	12	12	12	12	12	12
		IT_{int}	12	12	12	12	12	12
		IT_{inn}	13.66	14.58	15.083	16.08	17.34	17.58
	Nonlinear HSS-like	$\ F(\mathbf{x})\ $	2.42,-14	6.04,-15	6.36,-15	1.96,-14	6.15,-15	8.60,-15
		CPU	8.87	11.828	10.02	10.31	11.28	11.85
		IT	161	209	178	186	201	207
		$\ F(\mathbf{x})\ $	1.5,-14	1.59,-14	1.46,-14	1.57,-14	1.615,-14	1.46,-14
		CPU	50.81	50.01	51.85	53.34	56.32	59.95
	Picard-HSS	IT_{out}	12	12	12	12	12	12
		IT_{inn}	177.16	179.1	183.50	189.34	202.75	213.25
		$\ F(\mathbf{x})\ $	7.7,-15	9.67,-15	1.11,-14	1.23,-14	1.22,-14	1.26,-14
<i>N</i> = 64	JFHSS	α_{opt}	0.7	1	1.8	3.3	8.9	14.2
		CPU	21.68	18.23	18.65	19.156	20.53	21.39
		IT_{out}	12	12	12	12	12	12
		IT_{int}	12	12	12	12	12	12
		IT_{inn}	21	17.39	18.17	18.75	19.91	20.84
	Nonlinear HSS-like	$\ F(\mathbf{x})\ $	1.61,-14	6.73,-15	9.15,-15	8.39,-15	7.7,-15	4.71,-15
		CPU	38.57	31.78	33.50	34.65	36.56	37.70
		IT	246	206	213	221	235	242
		$\ F(\mathbf{x})\ $	1.17,-14	1.26,-14	1.26,-14	1.16,-14	1.19,-14	1.22,-14
		CPU	219.54	217.45	266.83	225.37	228.60	248.35
	Picard-HSS	IT_{out}	12	12	12	12	12	12
		IT_{inn}	219.54	248.58	230.75	252	258.75	264.50
		$\ F(\mathbf{x})\ $	6.12,-15	7.7,-15	8.9,-15	1.0,-14	1.1,-14	1.1,-14

Table 1: Numerical results of JFHSS, Nonlinear HSS-like and Picard-HSS methods for system (8) ($\eta = tol = 0.1$).

Table 1 show CPU-time in JFHSS is much better than CPU-time in Picard-HSS and Nonlinear HSS-like algorithms. Also we adopt the experimentally optimal parameters α to obtain the least CPU times for these

iterative methods. These optimal values are listed in Table 1. One can see the number of outer iteration in both Picard-HSS and JFHSS are the same, but there are big difference between their CPU-time.

4 Conclusion

In this paper, a Jacobian-free iterative method based on HSS scheme has been proposed. It is a combination of inexact Newton method, Hermitian and skew-Hermitian splittings and Jacobian-free Newton-Krylov algorithms. The advantage of this method over the Newton and the Newton-HSS iteration schemes is that they do not need explicit construction and accurate computation of Jacobian matrices. Hence, computation workloads and computer memory may be saved in actual implantations. Numerical implementations show that JFHSS method is effective, robust, and feasible nonlinear solver for the class of nonlinear and weakly nonlinear systems. Application of this algorithm is found to be simple, accurate, fast, flexible, convenient and has small computation cost.

References

- [1] M.Z. Zhu. On asymmetric Hermitian and skew-Hermitian splitting iteration methods for weakly nonlinear systems, *J. Comput. Anal. Appl.*, 14: 1321–1331, 2011.
- [2] Z.Z. Bai, G.H. Golub and M.K. Ng. Hermitian and skew-Hermitian splitting methods for non-Hermitian positive definite linear systems, *SIAM J. Matrix Anal. Appl.*, 24(3): 603–626, 2003.
- [3] Z.Z. Bai and X. Yang. On HSS-based iteration methods for weakly nonlinear systems, *Appl. Numer. Math.*, 59(12): 2923–2936, 2009.
- [4] X. Li and Y.J. Wu. Accelerated Newton-GPSS method for systems of nonlinear equations, *J. Comput. Anal. Appl.*, 17: 245–254, 2014.
- [5] X.P. Guo and I.S. Duff. Semilocal and global convergence of the Newton-HSS method for systems of nonlinear equations, *Linear Algebra Appl.*, 18: 299–315, 2010.

Optimal Control of Counter-Terrorism Tactics

L. Bayón*, P. Fortuny Ayuso,
P.J. García-Nieto, J.M. Grau, and M.M. Ruiz

Department of Mathematics, University of Oviedo, Spain

November 30, 2017

1 Introduction

Modeling a “stock” of terrorists, is not common, but has precedents, especially after September 11, 2001 [1]. In this sense [2] presents an intelligent ecological metaphor to analyze actions by Governments and citizens against terror. In [3] a model for the transmission dynamics of extreme ideologies in vulnerable populations is presented. In [4] the authors propose a terror-stock model that treats the suicide bombing attacks in Israel. In other countries like, for example, Spain or Ireland, the problem has also been analyzed.

Several papers develop dynamical models of terrorism. In [5] the authors incorporate the effects of both military/police and nonviolent/persuasive intervention to reduce the terrorist population. This idea is widely developed in [6] where the controls are two types of counter-terror tactics: “water” and “fire”, which is the model we shall consider in this paper.

In this context we present in this work a new approach to analyze the efficacy of counter-terrorism tactics. We state an optimal control problem that attempts to minimize the total cost of terrorism. An excellent summary of optimal control application in terrorism issues can be consulted in [7].

The optimization criterion is to minimize the discounted damages created by terror attacks plus the costs of counterterror efforts. The underlying mathematical problem is complicated. It constitutes a multi-dimensional,

*e-mail: bayon@uniovi.es

constrained problem where the optimization interval is infinite. An important feature is that the time t is not explicitly present in the problem (hence, it is a time-autonomous problem), except in the discount factor. Using the Minimum Principle of Pontryagin, the shooting method and the cyclic descent of coordinates we develop an optimization algorithm. We also present a method (based upon [8]) for computing the optimal steady-state in multi-control, infinite-horizon, autonomous models. This method does not require the solution of the dynamic optimization problem. Using it, we can choose parameters that reach a desirable steady-state solution.

2 Mathematical Model

In this work we use the excellent model provided by [6], which classifies counter-terrorism tactics into two categories:

- “Fire” strategies are tactics that involve significant collateral damage. They include, for example, the killing of terrorists through drones, the use of indiscriminate checkpoints or the aggressive blockade of roads.
- “Water” strategies, on the other hand, are counter-measures that do not affect innocent people, like intelligence arrests against suspects individuals.

The fire and water strategies will be denoted by the control variables $v(t)$ and $u(t)$, respectively. Both controls have their advantages, and their drawbacks. For example $v(t)$ have the direct benefit of eliminating current terrorists but the undesirable indirect effect of stimulating recruitment rates (and the possible harm to innocent bystanders). On the other hand, $u(t)$ is more expensive and more difficult to be applied than $v(t)$.

The strength or size of the terrorists is represented by the state variable $x(t)$. This includes not only the number of active terrorists, but also the organization’s total resources including financial resources, weapons, etc. [2]. Its value changes over time and we distinguish two inflows and three outflows in it:

$$\dot{x} = \tau + I(v, x) - O_1(x) - O_2(u, x) - O_3(v, x) \quad (1)$$

We include first of all a small constant recruitment term τ , accounting for a small constant recruitment rate. Second, following [3], the model considers

that new terrorists are recruited by existing terrorists. So the inflow $I(v, x)$ is increasing in proportion to the current number of terrorists x . But this growth is bounded and should also slow down. Moreover, the aggressive control v , also increases recruitment. In summary the form of the model is:

$$I(v, x) = (1 + \rho v)kx^\alpha \tag{2}$$

with $\tau, \rho \geq 0, k > 0$ and $0 \leq \alpha \leq 1$.

On the other hand, we consider three outflows: The first one, $O_1(x)$, represents the rate at which people leave the organization by several reasons not related with the controls. This natural outflow is assumed linear in x :

$$O_1(x) = \mu x \tag{3}$$

with $\mu > 0$. The second outflow, $O_2(u, x)$, reflects the effects of water strategies. This outflow is assumed to be concave in x because there is a limited number of units that conduct water operations:

$$O_2(u, x) = \beta(u)x^\theta \tag{4}$$

with $\theta \leq 1$. The third outflow $O_3(v, x)$ is due to fire strategies. This is modeled as linear in x , because the methods are perceived to be “direct attack”:

$$O_3(v, x) = \gamma(v)x \tag{5}$$

The functions $\beta(u)$ and $\gamma(v)$ should be concave; Culkins [6] uses the same functional form for both: a logarithmic function. The water function is pre-multiplied by a constant β smaller than the corresponding constant γ for fire operations. These two constants reflect the “efficiency” of the two types of operations.

Finally, the costs of terrorism are assumed to be linear in the number of terrorists, that is, of the form cx . We also model the control cost function as separable, and the costs of employing the water and fire strategies are modeled as quadratic. Over a infinite planning horizon, the objective is to minimize the sum of both costs (terrorism and counter-terror operations). We also assume that outcomes are discounted by a constant rate r . In brief, the control problem we pose can be written as:

$$\min_{u,v \geq 0} J = \min_{u,v \geq 0} \int_0^\infty (cx + u^2 + v^2)e^{-rt} dt \tag{6}$$

$$\dot{x} = \tau + (1 + \rho v)kx^\alpha - \mu x - \beta \ln(1 + u)x^\theta - \gamma \ln(1 + v)x; \quad x(0) = x_0$$

$$u(t) \geq 0; \quad v(t) \geq 0$$

where x_0 is the initial stock level and we impose also control constraints.

3 Optimization Algorithm

The above problem (6), is an Optimal Control Problem (OCP) where the total costs have to be minimized, given the state dynamics and the constraints on the controls. Denoting $\mathbf{u}(t) = (u(t), v(t)) = (u_1(t), u_2(t))$, we wish to compute:

$$\min_{\mathbf{u}(t)} J = \int_0^\infty F(t, x(t), \mathbf{u}(t)) dt \tag{7}$$

subject to satisfying:

$$\dot{x}(t) = f(t, x(t), \mathbf{u}(t)), \quad 0 \leq t \leq \infty; \quad x(0) = x_0 \tag{8}$$

$$\mathbf{u}(t) \in \mathbf{U}(t), \quad 0 \leq t \leq \infty \tag{9}$$

The problem presents several noteworthy features. First, the optimization interval is infinite. Second, the time t is not explicitly present in the problem (it is a time-autonomous problem), except in the discount factor. Third, we impose constraints on the control and finally, it constitutes a multi-dimensional problem.

To solve the multi-control variational problem, we propose a numerical algorithm which uses a particular strategy related to the cyclic coordinate descent (CCD) method [9]. The classic CCD method minimizes a function of n variables cyclically with respect to the coordinates. With our method, the problem can be solved like a sequence of problems whose error functional converges to zero. The algorithm (with $i = 1, 2$) carries out several iterations and at each j -th iteration it calculates 2 stages, one for each i . At each stage, it computes the optimal of $u_i(t)$, assuming the other variable is fixed.

Beginning with some admissible \mathbf{u}^0 , we construct a sequence of (\mathbf{u}^j) and the algorithm will search:

$$\lim_{j \rightarrow \infty} \mathbf{u}^j \tag{10}$$

It is easy to justify the convergence of the algorithm taking into account Zangwill's global convergence Theorem [10].

Based on the above, we present the solution for the unidimensional case, using Pontryagin's Minimum Principle (PMP) [11]. Our integrand takes the form:

$$F(x(t), u(t), t) = G(x(t), u(t), t)e^{-rt} \tag{11}$$

where r is the positive rate of discount, and G is a function bounded from above. Under these conditions, the integral is found to be convergent for each admissible control. Let H be the associated Hamiltonian:

$$H(t, x, u, \lambda) = F(t, x, u) + \lambda \cdot f(t, x, u) \tag{12}$$

where λ is the costate variable. Using PMP, the optimal solution can be obtained from a two-point boundary value problem. In order for $u^* \in U$ to be optimal, a nontrivial function λ must exist, such that for almost every $t \in [0, \infty)$:

$$\dot{x} = H_\lambda = f; \quad x(0) = x_0 \tag{13}$$

$$\dot{\lambda} = -H_x; \quad \lim_{t \rightarrow \infty} \lambda(t) = 0 \tag{14}$$

$$H(t, x, u^*, \lambda) = \min_{u(t) \in U} H(t, x, u, \lambda) \tag{15}$$

Due to the nonlinearity of the system dynamics, the optimal solution can only be computed numerically. In this paper we propose an efficient method which adapts the shooting method, Euler’s method, and numerical integration. All the calculations are carried out in the Mathematica environment.

4 Steady-state Solution

In [8] a method for computing the optimal steady-state in infinite-horizon one-dimensional problems is presented which does not require the solution of the dynamic optimization problem, in which the bounds $U(t)$ do not play any role. Tsur considers:

$$\min_{u(t)} J = \int_0^\infty G(x(t), u(t)) e^{-rt} dt \tag{16}$$

$$\dot{x}(t) = f(x(t), u(t)), \quad x(0) = x_0 \tag{17}$$

For the steady-state solution, $u = R(x)$, the *evolution function* is defined by:

$$L(x) = r \left(\frac{G_u(x, R(x))}{f_u(x, R(x))} + W(x) \right) \quad \text{with } W(x) = \frac{1}{r} G(x, R(x)) \tag{18}$$

The function $L(x)$ allows to formulate the following necessary condition for the optimal steady state x_s :

$$L(x_s) = 0 \tag{19}$$

We also extend the method to multi-dimensional problems.

References

- [1] P. Heymann, Dealing with terrorism after september 11, 2001: An overview. In *Countering terrorism: Dimensions of preparedness*, MIT Press, 57-72, 2003.
- [2] N.O. Keohane, R.J. Zeckhauser, The Ecology of Terror Defense. *Journal of Risk and Uncertainty* 26, 201-229, 2003.
- [3] C. Castillo-Chavez, B. Song, Models for the transmission dynamics of fanatical behaviors. In *Bioterrorism: Mathematical Modeling Applications in Homeland Security*, SIAM, Philadelphia, 155-172, 2003.
- [4] E.H. Kaplan, A. Mintz, S. Mishal, C. Samban, What happened to suicide bombings in Israel? Insights from a terror stock model. *Studies in Conflict and Terrorism* 28, 225-235, 2005.
- [5] F. Udawadia, G. Leitmann, L. Lambertini, A dynamical model of terrorism. *Discrete Dynamics in Nature and Society*, 1-32, 2006.
- [6] J.P. Caulkins, D. Grass, G. Feichtinger, G. Tragler, Optimizing counter-terror operations: Should one fight fire with “fire” or “water”? *Computers & Operations Research* 35, 1874-1885, 2008.
- [7] D. Grass, J.P. Caulkins, G. Feichtinger, G. Tragler, D.A. Behrens, *Optimal Control of Nonlinear Processes: With Applications in Drugs, Corruption and Terror*. Springer-Verlag, Berlin, 2008.
- [8] Y. Tsur and A. Zemel, The infinite horizon dynamic optimization problem revisited: A simple method to determine equilibrium states, *European Journal of Operational Research* 131(3), 482-490, 2001.
- [9] Z.Q. Luo and P. Tseng, On the convergence of the coordinate descent method for convex differentiable minimization, *J. Optim. Theory Appl.* 72(1), 7-35, 1992.
- [10] W.L. Zangwill, *Nonlinear Programming: A Unified Approach*, Prentice Hall, Nueva Jersey, 1969.
- [11] A. Chiang, *Elements of Dynamic Optimization*. Waveland Press, 2000.

Calculation of the adjoint flux of the neutron diffusion equation

A. Bernal^b *; J. E. Roman[†], R. Miró^b, and G. Verdú^b

(^b) Institute for Industrial, Radiophysical and Environmental Safety, Universitat Politècnica de València
Camí de Vera s/n, 46022, Valencia (Spain),

([†]) Department of Information Systems and Computation, Universitat Politècnica de València
Camí de Vera s/n, 46022, Valencia (Spain)

November 30, 2017

1 Introduction

The aim of this work is to perform a fast calculation of the adjoint flux of the neutron diffusion equation. The neutron diffusion equation is the easiest way of calculating the neutron distribution inside nuclear reactors. It is a partial differential equation, which contains spatial and time differential terms. Time differential terms are set to zero for considering the steady state of the neutron diffusion equation, which is an eigenvalue problem and the eigenvector is the neutron flux [1]. Spatial differential terms are discretized by using numerical methods in a discretized geometry.

The adjoint flux is the adjoint operator of the neutron diffusion equation, which is important and useful in several applications, such as transient calculations and the generalized perturbation theory [1]. In these applications, both forward and adjoint neutron flux are needed, which can be calculated by solving both eigenvalue problems, forward and adjoint.

These eigenvalue calculations might be computationally costly for large matrices. So, it would be desirable to calculate only one of them and calculate the other from the first one.

*e-mail: abernal@iqn.upv.es

There are some methods for estimating the adjoint eigenvectors from the forward ones, such as that developed in [2]. In this method, the adjoint eigenvectors are calculated by using a combination of the forward eigenvectors, whose coefficients are determined by solving a reduced eigenvalue problem. This method is fast, but it might be inaccurate for some cases.

In this work, the authors proposed a simpler and more accurate method, based on the product of the forward eigenvectors and the adjoint system matrix. In addition, the method includes a reorthogonalization for conserving the biorthogonal relationship of the forward and adjoint eigenvectors. Several tests are performed and compared with the method developed in [2] and with the adjoint eigenvalue calculation, which shows the capability of the method.

The outline of this paper is as follows. Section 2 describes briefly the method. Section 3 defines the validation cases and shows the results. This section is subdivided into two subsections, one for each reactor used for the validation. Section 4 summarizes the conclusions.

2 Method

Eq.1 shows the adjoint eigenvalue problem of the neutron diffusion equation, where Φ^* is the adjoint eigenvector and \mathbf{k} is the eigenvalue. This method estimates the adjoint eigenvector as shown in Eq.2, where U is a matrix calculated as expressed in Eq.3. This calculation of U guarantees the accomplishment of the biorthogonal relationship, as shown in Eq.4, where I is the identity matrix.

$$L^T \Phi^* = \frac{1}{\mathbf{k}} M^T \Phi^* \quad (1)$$

$$\Phi^* = \frac{1}{\mathbf{k}} (L^T)^{-1} M^T \Phi^* \approx \frac{1}{\mathbf{k}} (L^T)^{-1} M^T \Phi U \quad (2)$$

$$U = (\Phi^T M^T \Phi)^{-1} \quad (3)$$

$$\langle \Phi^*, M \Phi \rangle = \langle \Phi U, M \Phi \rangle = I \quad (4)$$

Table 1: Cross sections of the homogeneous reactor

D_1 (cm)	D_2 (cm)	$\Sigma_{a,1}$ (cm ⁻¹)	$\Sigma_{a,2}$ (cm ⁻¹)	$\nu\Sigma_{f,1}$ (cm ⁻¹)	$\nu\Sigma_{f,2}$ (cm ⁻¹)	$\Sigma_{s,1\rightarrow 2}$ (cm ⁻¹)
1.28205128205	0.666667	0.01	0.1	0.01	0.109017634020268	0.075

3 Results

The authors applied this method and that proposed by Döring and Kalkkuhl to two reactors: a homogeneous reactor and Langenbuch reactor.

The validation is based on the accomplishment of two equations. First, the biorthogonal property, which is expressed in Eq.5, where $\delta_{i,j}$ is the Kronecker delta. Second, the adjoint eigenvalue problem, which is evaluated with the error shown in Eq.6.

$$\langle \Phi_i^*, L\Phi_j \rangle = \delta_{i,j} \tag{5}$$

$$E_i = \langle L^T \Phi_i^* \mathbf{k}_i - M^T \Phi_i^*, L^T \Phi_i^* \mathbf{k}_i - M^T \Phi_i^* \rangle \tag{6}$$

The authors calculated 5 adjoint eigenpairs and checked the biorthogonal property with 10 forward eigenvectors. In addition, the authors used the Nodal Collocation Method (order 2) to discretize the spatial derivatives.

3.1 Homogeneous reactor

This reactor is a parallelepiped with the following dimensions: 99cm x 60cm x 180cm. It is composed of only one material with the cross section defined in Table 1. The boundary conditions were zero flux.

The method proposed in this work and that developed by Döring and Kalkkuhl provide the same results. Errors (E_i) are zero for the five eigenpairs. The biorthogonal property is also accomplished for the 10 forward eigenvectors, as shown in Table 2. One can conclude that the results are excellent.

Table 2: Biorthogonal property for the homogeneous reactor

		$L\Phi_j$								
Φ_i^*		-995.20	0.0	0.0	0.0	0.0	0.0	0.0	0.0	0.0
		0.0	1003.58	0.0	0.0	0.0	0.0	0.0	0.0	0.0
		0.0	0.0	-1017.22	0.0	0.0	0.0	0.0	0.0	0.0
		0.0	0.0	0.0	1021.44	0.0	0.0	0.0	0.0	0.0
		0.0	0.0	0.0	0.0	-1029.48	0.0	0.0	0.0	0.0

Table 3: Cross sections of Langenbuch reactor

Material	D_1 (cm)	D_2 (cm)	$\Sigma_{a,1}$ (cm^{-1})	$\Sigma_{a,2}$ (cm^{-1})	$\Sigma_{s,1 \rightarrow 2}$ (cm^{-1})	$\nu\Sigma_{f,1}$ (cm^{-1})	$\nu\Sigma_{f,2}$ (cm^{-1})
Comb.1	1.423913	0.356306	0.01040206	0.08766217	0.0175555	0.006477691	0.1127328
Comb.2	1.425611	0.350574	0.01099263	0.09925634	0.01717768	0.007503284	0.1378004
Absorbent	1.423913	0.356306	0.01095206	0.09146217	0.0175555	0.006477691	0.11273228
Reflector	1.634227	0.264002	0.002660573	0.04936351	0.02759693	0.0	0.0

3.2 Langenbuch reactor

Langenbuch reactor is a heterogeneous reactor composed of 4 materials, whose cross sections are defined in Table 3. Fig.1 shows the geometry of this reactor. The boundary conditions were zero flux for all boundaries, except for boundaries -X and -Y, which were reflective.

As regards the results obtained with the method of Döring and Kalkkuhl, Table 4 displays the errors (E_i) and Table 5 shows the biorthogonal property. One might draw two conclusions from these tables. First, E_i are not close to zero. Second, there are some values of the biorthogonal property which are clearly not zero, such as $i = 2, j = 6$ and $i = 5, j = 9$; thus, one cannot conclude that the biorthogonal property is accomplished.

One can see the results for this method in Tables 6 and 7. Table 6 displays the errors (E_i), which are close to zero. Table 7 shows the biorthogonal property, in which one can appreciate that there are some values slightly higher than zero. However, these values are almost zero and they are about three order of magnitude lower than non-zero values. Thus, one concludes that the biorthogonal property is accomplished. In conclusion, the method proposed by Döring and Kalkkuhl might provide wrong results for heterogeneous results, whereas the method of this work provides accurate results.

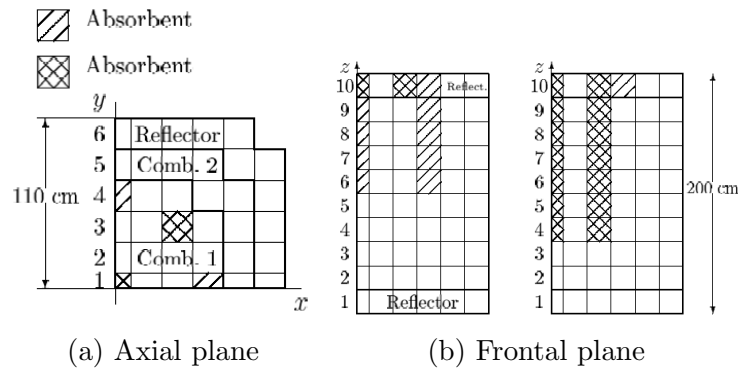


Figure 1: Langenbuch reactor

Table 4: Errors for Langenbuch reactor and the method of Döring and Kalkkuhl

Eigenpair	1	2	3	4	5
E_i	320.81	305.05	323.80	256.74	274.24

Table 5: Biorthogonal property for Langenbuch reactor and the method of Döring and Kalkkuhl

		$L\Phi_j$									
Φ_i^*		-92.78	0.0	0.0	0.0	-0.31	0.0	-6.29	0.0	-0.36	0.0
		0.0	-86.17	0.0	0.0	0.0	-19.44	0.0	-0.39	-0.33	0.0
		0.0	0.0	97.52	0.0	0.0	0.0	-0.41	0.0	0.0	-0.16
		0.0	0.0	0.0	81.94	0.0	0.74	0.0	-17.69	0.33	0.0
		0.0	0.0	0.0	0.0	-88.25	0.07	0.0	0.20	-19.92	0.0

Table 6: Errors for Langenbuch reactor and the method of this work

Eigenpair	1	2	3	4	5
E_i	0.69	0.70	1.37	1.13	0.72

Table 7: Biorthogonal property for Langenbuch reactor and the method of this work

		$L\Phi_j$								
Φ_i^*	101.08	0.0	0.0	0.0	0.0	-0.00	0.0	-0.01	0.00	0.0
	0.0	102.88	0.0	0.0	0.0	-0.28	0.0	-0.00	0.00	0.0
	0.0	0.0	106.33	0.0	0.0	0.0	0.00	0.0	0.0	0.00
	0.0	0.0	0.0	99.32	0.0	-0.01	0.0	0.19	-0.01	0.0
	0.0	0.0	0.0	0.0	105.76	0.01	0.0	-0.00	-0.31	0.0

4 Conclusions

This work shows a simple method to estimate the adjoint eigenvectors of the neutron diffusion equation from the forward ones. The method is based on the product of the forward eigenvectors by the adjoint system matrix.

The authors validated the method in two reactors: a homogeneous reactor and Langenbuch reactor. The results were compared with the method proposed by Döring and Kalkkuhl. One draws two conclusions from the results of this method. First, the biorthogonal relationship is accomplished. Second, errors are lower in comparison with the method proposed by Döring and Kalkkuhl.

As regards future work, the authors would like to perform better estimations of the initial adjoint flux, which will be based on a linear combination of the forward ones.

References

- [1] W. M. Stacey, Nuclear Reactor Physics. New York, John Wiley & Sons, 2001.
- [2] M.G. Döring, J.C. Kalkkuhl, and W. Schröder. Subspace Iteration for Nonsymmetric Eigenvalue Problems Applied to the λ -Eigenvalue Problem, *Nuclear Science and Engineering*, 115(3):244–252, 1993.

Uncertainty quantification for meningococcus W carriers prediction

L. Acedo ^(a) * ; C. Burgos ^(a) †

J.C. Cortés ^(a) ‡ ; D. Martínez-Rodríguez ^(a) § ; R.-J. Villanueva ^(a) ¶

^(a) Instituto Universitario de Matemática Multidisciplinar, Universitat Politècnica de València

November 30, 2017

1 Introduction

The aim to this work is to study the dynamics of carriers of Men W. We have proposed a susceptible-carrier-susceptible (SCS) epidemiological model, in order to determine the percentage of carriers in the population, together with a fractional Lotka- Volterra competition model due to describe the evolution of the meningococcal genogroups in Spain among the carriers.

Using data available from the amount of carriers of Meningococcus of each genogroup in Spain in 2011 and 2012, we find the model parameters that best fit our data.

This paper is organized as follows. In Section 2, two mathematical epidemiological models will be described in order to study the dynamics of Men W. In Section 3 a probabilistic study in order to fit the carriers of Men W in Spain is shown. Finally in Section 4 all the conclusions are written.

*e-mail: luiacrod@imm.upv.es

†e-mail: clabursi@posgrado.upv.es

‡e-mail: jccortes@imm.upv.es

§e-mail: damarro3@etsii.upv.es

¶e-mail: rjvillan@imm.upv.es

2 Mathematical models

In this section the two mathematical models required to describe the dynamics of Men W among the total population are introduced. First a susceptible-carrier-susceptible (SCS) model, in order to study the evolution of the carrier individuals, is constructed. Second a Lotka-Volterra competition model is described due to study the dynamics of meningococcus genogroup over the time. The real data available for this study is collected in Table 1, which is supplied by the Reference Laboratory for Meningococci of the Spanish Institute of Health Carlos III, corresponding to December, 2011 and December, 2012.

Year	$t_1 = 2011$	$t_2 = 2012$
Sample size	$n_1 = 3000$	$n_2 = 500$
Susceptible population	2626 (87.53%)	409 (81.8%)
Carrier population of any meningococcus	374 (12.47%)	91 (18.2%)
Genotype Men W	16 (4.3%)	358 (95.7%)
Other genotypes	5 (5.5%)	86 (94.5%)

Table 1: Sample size. Number and percentage of susceptible/carriers of any meningococcus. Percentage of carriers of the genotype Men W and the rest of genotype meningococcus in Spain corresponding to Dec 2011 and Dec 2012.

Working with percentages and using a discrete SIS type-epidemiological model recalling the “infected” population with carrier of Meningococcus, the transmission dynamics of all the meningococci over the time is modeled. In fact, this model is named as the SCS-model. Let β be the transmission rate of meningococci and γ the recovery rate, the dynamics of C_t can be described using a classical discrete SCS-type epidemiological model by the following difference equation

$$C_{t+1} = (1 + \beta - \gamma)C_t - \beta C_t^2, \quad \beta, \gamma > 0. \quad (1)$$

As we will work in percentages the susceptible population at the time instant t , S_t , is given by $S_t = 1 - C_t$

Once we have modelled the dynamics of susceptible and carrier population, we need to describe the carrier of meningococci W among the total amount of carrier. It is well known that the meningococci genogroups are in competition. The competition dynamics may reinforce certain genogroups

by DNA recombination or mutations and this would depend on the other genogroups coexisting with them as well as the time this coexistence lasts and their populations. In this spirit, we will extend the original Lotka-Volterra competition model to a generalized one in which ordinary derivatives are replaced by fractional derivatives. It is well known that fractional differential equations could get these memory effects as they are usually applied to visco-elastic materials and subdiffusive processes, given that the historic of a function is considered with non-integer derivatives, see [1, 4].

In order to motivate the formulation of that fractional model, let us first consider the classical Lotka-Volterra model

$$\begin{cases} X_1'(t) = r_1 X_1(t)(K_1 - X_1(t)) - \alpha_{1,2} X_1(t) X_2(t), \\ X_2'(t) = r_2 X_2(t)(K_2 - X_2(t)) - \alpha_{2,1} X_2(t) X_1(t), \end{cases} \quad (2)$$

where $i = 1$ corresponds to Men W genogroup, $i = 2$ corresponds to non-Men W genogroup, and

- $X_i(t)$, $1 \leq i \leq 2$, denotes the total amount of the genotype i meningococcus bacteria at the time instant t (in months),
- $r_i > 0$ is the growth rate of the genotype i meningococcus bacteria,
- $K_i > 0$ is the carrying capacity of the genotype i meningococcus bacteria,
- $\alpha_{i,j} > 0$ is the effect of the genotype j bacteria on the growth of the genotype i bacteria, $1 \leq j \leq 2$, $j \neq i$.

Data available in Table 1 is in percentages. Thus, in order to apply this data with the SCS model (1), the scaling of the model (2) is indispensable. With this aim the following change of variable is introduced

$$x_i(t) = \frac{X_i(t)}{K_i}, \quad i = 1, 2,$$

representy the percentatge of ecosystems occupied by the i -th-genogroup. As $x_1(t) + x_2(t) = 1$, we can recast the first equation of model (2) as follows.

$$x_1'(t) = N_1 x_1(t)(1 - x_1(t)), \quad (3)$$

where $N_1 = H_1 - M_1$ and $H_1 = r_1 K_1 > 0$, and $M_1 = \alpha_{1,2} K_2 > 0$. Proceeding with the same approach we can obtain the differential equation from $x_2(t)$. Once we have scaled the model, the first derivative, $x_1'(t)$ in (3), is substituted by the fractional Caputo derivative, ${}^C D^\alpha x_1(t) := \frac{1}{\Gamma(1-\alpha)} \int_0^t x_1'(s)(t-s)^{-\alpha} ds$, [5]. This leads to the fractional Lotka-Volterra model

$${}^C D^\alpha x_1(t) = N_1 x_1(t)(1 - x_1(t)). \tag{4}$$

This continuous model does not admit a closed-form solution, so we need to discretizate it. To this aim, let us consider the following discrete scheme for the Caputo operator named as Caputo like-delta-difference operator, see [6].

$$(\Delta_*^\alpha x_1)(t) = \frac{1}{\Gamma(1-\alpha)} \sum_{s=0}^{t-n+\alpha} \frac{\Gamma(t-s)}{\Gamma(t-s+1)} (\Delta x_1)(s), \tag{5}$$

where $t \in \mathbb{N}_{1-\alpha} := \{1-\alpha, 2-\alpha, \dots\}$ and $(\Delta x_1)(t)$ is the discretization of the first derivative of $x_1(s)$ in discrete time, i.e.,

$$(\Delta x_1)(s) = x_1(s) - x_1(s-1). \tag{6}$$

Substituting the Caputo like-delta-difference operator in the model, we obtain

$$(\Delta_*^\alpha x_1)(t) = N_1 x_1(t)(1 - x_1(t)). \tag{7}$$

Putting $x_1(t) = x_t$, changing the index from $t \in \mathbb{N}_{1-\alpha}$ to $t \in \mathbb{N}$, and isolating x_t , the fractional Lotka-Volterra model in discrete time can be rewritten as

$$x_t = x_0 + \frac{N_1}{\Gamma(\alpha)} \sum_{k=1}^t \frac{\Gamma(t-k+\alpha)}{\Gamma(t-k+1)} x_{k-1}(1 - x_{k-1}), \tag{8}$$

where N_1 and α are the model parameters to be determined and t is the time in months.

3 Results

Applying the probabilistic technique developed in [3] in the two different scaled models, we can obtain on the one hand a confidence interval of the carrier percentage of meningococcus (without distinction of group) among the total population. On the other hand the percentage of carrier of Men

W among the total population of carriers is obtained. Combining all two models we can get a confidence interval with the percentage of carriers of MenW among the total population which is shown in Figure 1.

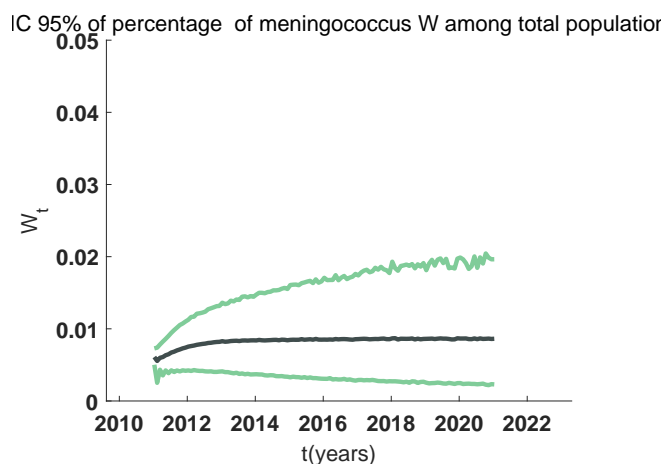


Figure 1: The light line represents the 95% CI of the solution stochastic process of the percentage of carriers given by model (8) for each month, t , from Dec 2011 until Dec 2021. The dark green line represents the mean of the process.

4 Conclusions

In this work we have used seroepidemiological data corresponding to the prevalence of genogroup W and other meningococci genogroups in Spain. Our model consists of two coupled systems. First, we consider the transmission of the disease among the human population in terms of a SCS model. Then, applying a fractional Lotka-Volterra competition model we can study the dynamics of the carriers of Men W among the total amount of carriers. Mixing both models we have established the equivalence between the carriers of Men W among the total population.

Acknowledgements

This work has been partially supported by the Ministerio de Economía y Competitividad grant MTM2013-41765-P and the FIS grant PI13/01459. We also acknowledge Dr. Julio Vázquez from the Carlos III Institute of Health for providing the epidemiological data used in this work.

References

- [1] I. Podlubny, *Fractional Differential Equations: An Introduction to Fractional Derivatives, Fractional Differential Equations, to Methods of Their Solution and Some of Their Applications*, Academic Press, London, 1998.
- [2] A. Lamelas, S. R. Harris, K. Röltgen, J. P. Dangya, J. Hauser, R. A. Kingsley, T.R. Connor, A. Sied, A. Hodgson, G. Dougan, J. Parkhill, S. D. Bentley, G. Pluschke, emergence of a New Epidemic *Neisseria meningitidis* Serogroup A Clone in the African Meningitis Belt: High-Resolution Picture of Genomic Changes That Mediate Immune Evasion, *mBio* 5(5) (2014) e01974–14. doi: 10.1128/mBio.01974-14.
- [3] J. C. Cortés, F. J. Santonja, A. C. Tarazona, R. J. Villanueva, J. Villanueva-Oller, A probabilistic estimation and prediction technique for dynamic continuous social science models: The evolution of the attitude of the Basque Country population towards ETA as a case study, *Applied Mathematics and Computation* 264 (2015) 13–20. doi: 10.1016/j.amc.2015.03.128.
- [4] S. B. Yuste, L. Acedo, K. Lindenberg, Reaction front in an $A+B\rightarrow C$ reaction-subdiffusion process, *Phys. Rev. E* 69 (2004) 036126.
- [5] A. A. Kilbas, H.M. Srivastava, J. J. Trujillo, *Theory and Applications of Fractional Differential Equations*, Elsevier 633 Science, The Netherlands, 2006.
- [6] Atici, F. M., Eloe, P. W. , Initial Value Problems in Discrete Fractional Calculus, 137(3) (2009) 981989.

Some awkward issues on pairwise comparison matrices

Julio Benítez¹, Silvia Carpitella^{1,2}, Antonella Certa², Amilkar Ilaya-Ayza³, Joaquín Izquierdo¹

¹ Instituto Matemático Multidisciplinar/Universitat Politècnica de València, València, Spain, jbenitez@upv.es, jizquier@upv.es

² Dipartimento dell'Innovazione Industriale e Digitale (DIID)/Università degli Studi di Palermo, Palermo, Italy,
silvia.carpitella@unipa.it, antonella.certa@unipa.it

³ Facultad Nacional de Ingeniería, Universidad Técnica de Oruro, Ciudad universitaria s/n, Oruro, Bolivia, amilkar.cia@gmail.com

1. Introduction

Many decision-making techniques use pairwise comparisons (PCs) elicited by one or more stakeholders involved in a given corresponding decision-making process. In very complex problems, the number of criteria or options to be compared may be too large, thus limiting PC applicability to large-scale decision problems due to the so-called curse of dimensionality, that is, a large number of pairwise comparisons need to be produced from a decision maker. For example, in AHP, Saaty [1] recommends that to obtain a reasonable and consistent PC matrix, the number of comparing elements should be at most seven. In [2] and [3], arguing on limitations of the human capabilities, the maximum number of elements to be handled simultaneously is approached by a maximum of seven plus two. This limit, also called 'channel capacity', a measure of our ability to process information, is widely known in the literature (see Miller [4]), and refers to the number of elements that can be held in short term memory simultaneously.

Miller also stated that his *magic number* was for items with one aspect or attribute, and reported this to be true for various tasks. The aim was to assess how well humans can separate various levels of intensity of certain particular stimuli. Among these stimuli we have frequency, position in an interval, loudness, saltiness, size, etc. However, when more attributes are considered, then one can remember more, depending on his or her familiarity with the situation and the complexity of the subject. As a result, according to [5], Miller's magical number seven is only true for information that has one memory attribute or function – and we can work with many more. Marnell [6], using one of the examples provided by Miller, states that '*there is... no parallel between naming tonal frequencies according to a provided legend and unravelling the meaning of a map, block...*' (this last part of the comparison refers to more complex information structures). This same author also states that Miller's article discusses what he calls the span of immediate memory (also known as the capacity of our short-term memory), and makes it clear that '*the capacity of our short-term memory might well be relevant to our ability to take in and comprehend material at the atomic level ... but at the molecular level ... its relevance is doubtful*', and that '*... short-term memory is the very stuff of Miller's paper, especially its role in judgment, attention and recall*'. Marnell claimed that this theory '*needs to be radically updated to bring it into line with current knowledge in cognitive psychology*', and he cites [7] to conclude that '*a limit of 7 ± 2 is yesterday's guesstimate. Today it is 4 ± 1 for unrelated items and 15 for... [related concepts]*'.

In this contribution we argue that, in special cases, comparison matrices of more than the traditional 7 ± 2 elements may be valid. For example, when a renowned expert on a subject is confronted with a high number of elements and there is no clear possibility of clustering them following some homogeneity criteria as suggested in [2]. This is the most salient feature of the case study we address in this paper: a team of experts working on a daily basis with the management and operation of a utility infrastructure were confronted with the problem of elucidating about the ease of operation of fifteen individual parts of the infrastructure. The

PC matrix was eventually built and taking into account the team profound expertise in the problem, the matrix was considered to encompass reliable information, according to our claim. Nonetheless, aware of the problems associated with dealing with so many elements, for example when working further with alternatives or when including the PCs in an analytic network process (ANP) solution of the problem, and after observing certain structured patterns in the matrix, we thought of devising a method to consistently shrink or compress the comparison matrix, thus reducing the size of the problem. In this paper, using a linearization technique already introduced by the authors [8], we develop such a compressing or merging technique so that certain elements may be synthesized to produce a new comparison matrix that gathers some elements into clusters, while maintaining the experience and the perception of the experts, and also the consistency and, eventually, reducing the size of the problem, thus making it more manageable. Of course, the final approval of the panel of experts is deemed absolutely necessary. This size reduction is devised to be useful for a number of technical purposes. For example, to avoid PCs when assessing alternatives with respect to the criteria; reciprocally, the number of comparisons will also be lower when providing PCs among the criteria for any of the considered alternatives (in the case the ANP methodology is used). Regarding other problems, this comparison matrix clustering technique may also be useful in other interesting contexts, such as, for example, the merging of companies in stock markets, once an alliance has been produced, to avoid the whole process of PCs from scratch.

2. Main results for consistent matrices

Let us recall that if $A = [a_{ij}] \in \mathcal{M}_n$ is a consistent matrix, then there exists $v = [v_1 \dots v_n]^T \in R^n$ such that $a_{ij} = v_i v_j^{-1}$ for all $1 \leq i, j \leq n$. This vector v is the priority vector of the matrix A , and it is easily checked that v is an eigenvector of A associated to the eigenvalue n . This eigenvalue n is the Perron eigenvalue of the positive matrix A (see [9] for the complete details). Before studying how to collapse several judgments in a consistent matrix, let us see a general useful fact: let $A \in \mathcal{M}_n$ be a consistent matrix. If $z \in R^n$ is the priority vector of A , then $L(A) = \varphi_n(L(z))$, where $\varphi_n(x) = (x_i - x_j)_{i,j=1,\dots,n}$ for $x = [x_1 \dots x_n]^T \in R^n$. In fact, since $a_{ij} = z_i z_j^{-1}$ we have $\log(a_{ij}) = \log(z_i) - \log(z_j)$ for all $1 \leq i, j \leq n$, and therefore, $L(A) = \varphi_n(L(z))$.

Let $A \in \mathcal{M}_{n+m}^+$ be a consistent matrix and let us partition A as follows:

$$A = \begin{bmatrix} A_1 & A_2 \\ A_3 & A_4 \end{bmatrix}, A_1 \in \mathcal{M}_n, A_4 \in \mathcal{M}_m. \tag{1}$$

It is evident that A_1 is consistent (it is the comparison matrix of the $1, \dots, n$ judgements). Also, A_4 is the comparison matrix of the $n + 1, \dots, n + m$ judgements, which is also consistent. Let $z \in R^{n+m}$ be the priority vector of A . Let us decompose $z = \begin{bmatrix} z_1 \\ z_2 \end{bmatrix}$, where $z_1 \in R^n$. Now, one has $L(A) = \varphi_{n+m}(L(z))$.

Hence

$$\begin{aligned} L(A) &= \begin{bmatrix} L(A_1) & L(A_2) \\ L(A_3) & L(A_4) \end{bmatrix} = \varphi_{n+m}(L(z)) = L(z) \mathbf{1}_{n+m}^T - \mathbf{1}_{n+m} L(z)^T \\ &= \begin{bmatrix} L(z_1) \\ L(z_2) \end{bmatrix} \begin{bmatrix} \mathbf{1}_n^T & \mathbf{1}_m^T \end{bmatrix} - \begin{bmatrix} \mathbf{1}_n \\ \mathbf{1}_m \end{bmatrix} \begin{bmatrix} L(z_1)^T & L(z_2)^T \end{bmatrix} \\ &= \begin{bmatrix} L(z_1) \mathbf{1}_n^T - \mathbf{1}_n L(z_1)^T & L(z_1) \mathbf{1}_m^T - \mathbf{1}_n L(z_2)^T \\ L(z_2) \mathbf{1}_n^T - \mathbf{1}_m L(z_1)^T & L(z_2) \mathbf{1}_m^T - \mathbf{1}_m L(z_2)^T \end{bmatrix} \end{aligned}$$

$$= \begin{bmatrix} \varphi_n(L(\mathbf{z}_1)) & L(\mathbf{z}_1)\mathbf{1}_m^T - \mathbf{1}_n L(\mathbf{z}_2)^T \\ L(\mathbf{z}_2)\mathbf{1}_n^T - \mathbf{1}_m L(\mathbf{z}_1)^T & \varphi_m(L(\mathbf{z}_2)) \end{bmatrix}.$$

So, we have proven the following Proposition.

Proposition 1. Let $A \in \mathcal{M}_{n+m}$ be a consistent matrix decomposed as in (1) whose priority vector is $[z_1 \ z_2 \ \dots \ z_{n+m}]^T$ and let us decompose $\mathbf{z} = \begin{bmatrix} \mathbf{z}_1 \\ \mathbf{z}_2 \end{bmatrix}$, where $\mathbf{z}_1 \in R^n$. Then \mathbf{z}_1 is the priority vector of A_1 and \mathbf{z}_2 is the priority vector of A_4 .

Theorem 1. Let $A \in \mathcal{M}_{n+m}$ be a consistent matrix decomposed as in (1) whose priority vector is $[z_1 \ z_2 \ \dots \ z_{n+m}]^T$ and $M = L(A)$ be decomposed as follows:

$$M = \begin{bmatrix} M_1 & -M_2 \\ M_2^T & M_3 \end{bmatrix} \in \mathcal{M}_{n+m}, \quad M_1 \in \mathcal{M}_n, \quad M_3 \in \mathcal{M}_m.$$

Let N be produced by the collapse of the last m judgements of M , and finally, let us denote $\mathbf{w}_1 = [\log(z_1) \ \dots \ \log(z_n)]^T$ and $s_2 = \log z_{n+1} + \dots + \log z_{n+m}$. Then

- (i) $N = \begin{bmatrix} M_1 & -\mathbf{v} \\ \mathbf{v}^T & 0 \end{bmatrix}$, where $\mathbf{v} = -\mathbf{w}_1 + \frac{s_2}{m} \mathbf{1}_n$.
- (ii) $p_{n+1}(N) = N$. We obtain that $N \in \mathcal{L}_{n+1}$, or equivalently, $E(N)$ is a consistent matrix.
- (iii) The priority vector for $E(N)$ is $[z_1 \ \dots \ z_n \ \sqrt[m]{z_{n+1} \ \dots \ z_{n+m}}]^T$.

3. Case study

We study an intermittent water supply system (IWSS) (see Figure 1), one of the subsystems of the water supply system of the city of Oruro (Bolivia). It is located in the southern part of the city, consists of 15 sectors fed by a single tank, and supplies water to 37,700 inhabitants. Each sector has a specific supply schedule and specific operation tasks, such as valve maneuvering, which are manually performed.

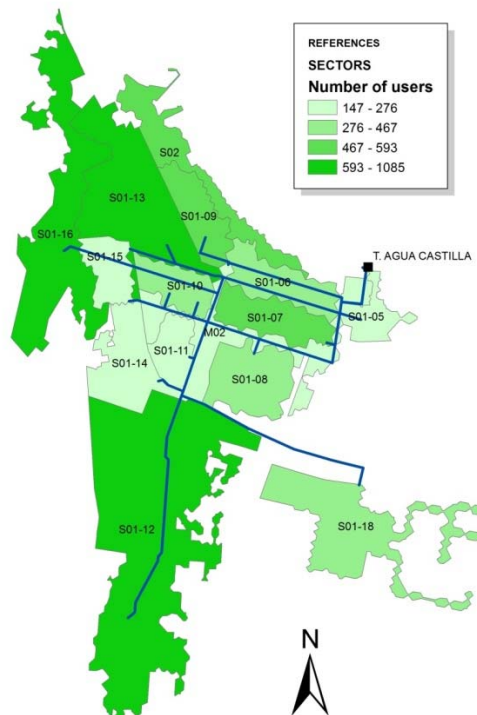


Figure 1. Studied IWSS, south area of Oruro, Bolivia

We proceeded with the pairwise comparison process, asking the experts to analyze the ease of operation of a sector with respect to another. Despite the large number of elements for comparison, the panel was eventually able to develop a coherent and reliable comparison matrix (see Table 1).

Table 1. Comparison matrix for the qualitative criterion: ease of operation for sectors. The consistency ratio for this matrix is 5.8%.

	S01-05	S01-06	S01-07	S01-08	S01-10	S01-11	S01-09	S01-13	S01-14	S01-15	S01-16	S02	M02	S01-12	S01-18	Eigen-vector
S01-05	1	5	3	1	3	1	1	1	1	1	1	3	7	1	1	0.0915
S01-06	1/5	1	1/3	1/3	1/3	1/3	1/5	1/3	1/3	1/3	1/3	5	5	1/3	1/3	0.0350
S01-07	1/3	3	1	1/3	1/3	1/3	1/3	1/3	1/3	1/3	1/3	1/3	7	1/3	1/3	0.0317
S01-08	1	3	3	1	1	1	1	1	1	1	1	3	7	1	1	0.0786
S01-10	1/3	3	3	1	1	1	1	1	1	1	1	1	7	1	1	0.0698
S01-11	1	3	3	1	1	1	1	1	1	1	1	1	7	1	1	0.0736
S01-09	1	5	3	1	1	1	1	1	1	1	1	3	7	3	1	0.0895
S01-13	1	3	3	1	1	1	1	1	1	1	3	3	7	3	1	0.0922
S01-14	1	3	3	1	1	1	1	1	1	1	3	3	7	3	1	0.0922
S01-15	1	3	3	1	1	1	1	1	1	1	3	3	7	3	1	0.0922
S01-16	1	3	3	1	1	1	1	1/3	1/3	1/3	1	1	5	1	1/3	0.0572
S02	1/3	1/5	3	1/3	1	1	1/3	1/3	1/3	1/3	1	1	5	1	1/3	0.0405
M02	1/7	1/5	1/7	1/7	1/7	1/7	1/7	1/7	1/7	1/7	1/5	1/5	1	1/5	1/7	0.0100
S01-12	1	3	3	1	1	1	1/3	1/3	1/3	1/3	1	1	5	1	1/3	0.0535
S01-18	1	3	3	1	1	1	1	1	1	1	3	3	7	3	1	0.0922

As explained before, the possibility of reducing the volume of this information may be deemed interesting, for example if posterior comparisons regarding alternatives were necessary. In addition, some patterns presented by the matrix clearly suggest the possibility of reducing the matrix size by grouping sectors, a situation that was not initially obvious. The identification of these groups will enable us to develop strategies for improvement in the technical management based on differentiated areas. Various proposals were presented to the technicians who manage the system. We describe here a successful one.

The proposal tried to use ideas provided by the technicians to guide the observation of patterns in the matrix of comparisons. Thus, sectors S01-09, S01-13, S01-14 and S01-15 were initially selected to be grouped. Theorem 1 above, by using the permutation given by (S01-05, S01-06, S01-07, S01-08, S01-10, S01-11, S01-16, S02, M02, S01-12, S01-18, S01-09, S01-13, S01-14, S01-15), gives a new comparison matrix where the last four sectors are grouped (under the identification 09-15). The matrix, which corresponds to the sector order (S01-05, S01-06, S01-07, S01-08, S01-10, S01-11, S01-16, S02, M02, S01-12, S01-18, 09-15), is given by:

1	5	3	1	3	1	1	3	7	1	1	1
0.2	1	0.333	0.333	0.333	0.333	0.333	5	5	0.333	0.333	0.383
0.333	3	1	0.333	0.333	0.333	0.333	0.333	7	0.333	0.333	0.347
1	3	3	1	1	1	1	3	7	1	1	0.858
0.333	3	3	1	1	1	1	1	7	1	1	0.763
1	3	3	1	1	1	1	1	7	1	1	0.804
1	3	3	1	1	1	1	1	5	1	0.333	0.625
0.333	0.2	3	0.333	1	1	1	1	5	1	0.333	0.442
0.143	0.2	0.143	0.143	0.143	0.143	0.143	0.2	0.2	1	0.2	0.143
1	3	3	1	1	1	1	1	5	1	0.333	0.585
1	3	3	1	1	1	3	3	7	3	1	1.008
1	2.614	2.885	1.165	1.311	1.244	1.601	2.262	9.161	1.711		1

The priority vector given by Theorem 1 is:

$$[0.126 \ 0.048 \ 0.044 \ 0.108 \ 0.096 \ 0.101 \ 0.079 \ 0.056 \ 0.014 \ 0.074 \ 0.127 \ 0.126]^T.$$

For this matrix, the Perron vector, corresponding to the Perron eigenvalue $\lambda = 13.2$, is:

$$[0.127 \ 0.053 \ 0.045 \ 0.104 \ 0.088 \ 0.095 \ 0.085 \ 0.060 \ 0.013 \ 0.084 \ 0.131 \ 0.116]^T.$$

Giving the values $CI = 0.1069$ and $CR = 7.03\%$, which is satisfactory from the consistency point of view. Continuing in the same line, a new clustering was performed, taking the latter as a starting point. In this case, sectors S01-08, S01-10 and S01-11 were the candidates for a new grouping.

Again, using Theorem 1 on the permutation of the previous matrix given by (S01-05, S01-06, S01-07, S01-16, S02, M02, S01-12, S01-18, 09-15, S01-08, S01-10, S01-11), a new comparison matrix was obtained with the last three sectors grouped (under the name 08-11), given by:

1	5	3	1	3	7	1	1	1	1.238
0.2	1	0.333	0.333	5	5	0.333	0.333	0.383	0.474
0.333	3	1	0.333	0.333	7	0.333	0.333	0.347	0.429
1	3	3	1	1	5	1	0.333	0.625	0.774
0.333	0.2	3	1	1	5	1	0.333	0.442	0.548
0.143	0.2	0.143	0.2	0.2	1	0.2	0.143	0.109	0.135
1	3	3	1	1	5	1	0.333	0.585	0.724
1	3	3	3	3	7	3	1	1.008	1.284
1	2.614	2.885	1.601	2.262	9.161	1.711	0.993	1	1.239
0.808	2.11	2.33	1.292	1.826	7.397	1.381	0.801	0.807	1

In this matrix the corresponding order is (S01-05, S01-06, S01-07, S01-16, S02, M02, S01-12, S01-18, 09-15, 8-11). The priority vector given by theorem 4 is:

$$[0.159 \ 0.061 \ 0.055 \ 0.099 \ 0.070 \ 0.017 \ 0.093 \ 0.160 \ 0.159 \ 0.128]^T.$$

For this matrix, the Perron vector, corresponding to the Perron eigenvalue $\lambda = 11.1$, is:

$$[0.149 \ 0.070 \ 0.061 \ 0.101 \ 0.070 \ 0.015 \ 0.100 \ 0.173 \ 0.144 \ 0.116]^T.$$

giving the values $CI = 0.125$ and $CR = 8.40\%$, which is still satisfactory from the consistency point of view. This proposal was positively considered by the technicians. In addition to the acceptable values of CR , the technicians appreciated that both clusters, the initial 09-15 and the subsequent 08-11, have an interesting technical interpretation, which is based on the proximity to the source of clusters 08-11 and 09-15 (which are at successive rings, consecutively further away from the source). As a result, areas or groups of sectors with similar operating characteristics are defined based on the opinion of water company technicians. This poses a new scenario (see Figure 2) that will enable a better planning in the operation and maintenance tasks of the system, such as reorganizing the manual work of the operators, who hourly open and close the valves to supply water, and the prioritization of maintenance tasks. Therefore, it becomes a very useful tool for the technical management of intermittent water supply systems, and is a fundamental criterion for a future transition to a continuous water supply.

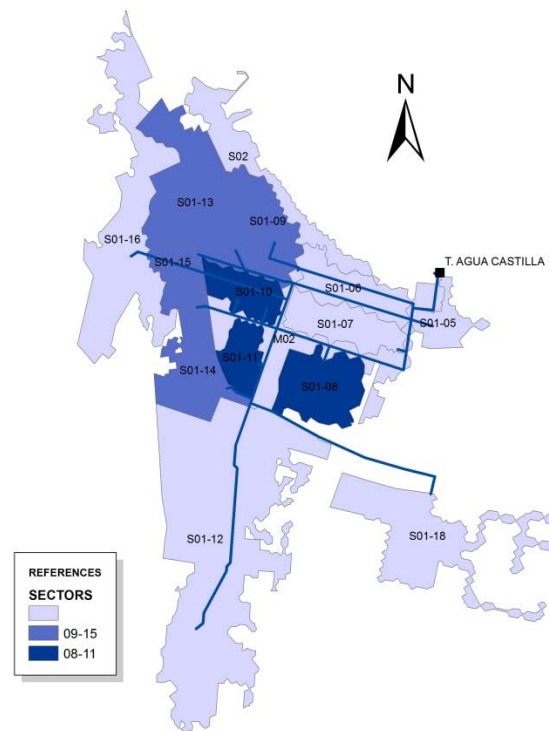


Figure 2. Studied IWSS, after cluster identification

References

- [1] Saaty, T.L. A scaling method for priorities in hierarchical structures, *Journal of Mathematical Psychology* 15, 1977, 234-281.
- [2] Saaty, T.L., Ozdemir, M.S. Why the Magic Number Seven Plus or Minus Two, *Mathematical and Computer Modelling*, 2003, vol. 38, pp. 233-244.
- [3] Ozdemir, M.S. Validity and inconsistency in the analytic hierarchy process, *Applied Mathematics and Computation*, 2005, vol. 161, pp. 707-720.
- [4] Miller, G.A. The Magic Number Seven, Plus or Minus Two: Some Limits on Our Capacity for Processing Information, *The Psychological Review*, 1956, vol. 63, pp. 81-97.
- [5] <https://rapidbi.com/millermagicalnumberseven7/> (accessed on 05/04/2015)
- [6] Marnell, G. Chunking the Information Presented to Readers. A critique of Information Mapping. *The Australian and New Zealand Journal of Technical Communication*, 33, October 2014 (<http://www.abelard.com.au/information%20mapping.pdf>).
- [7] Baddeley, A. *Working Memory, Thought, and Action*, Oxford University Press, Oxford, 2007, p. 143.
- [8] Benítez, J., Delgado-Galván, X., Izquierdo, J., Pérez-García, R. Achieving matrix consistency in AHP through linearization. *Applied Mathematical Modelling*, 35 (2011) pp. 4449-4457.
- [9] Saaty, T.L. Relative Measurement and its Generalization in Decision Making: Why Pairwise Comparisons are Central in Mathematics for the Measurement of Intangible Factors-The Analytic Hierarchy/Network Process, *Royal Spanish Academy of Sciences, Series A, Mathematics*, 102 (2) (2008) pp. 251-318.

Block iterative methods to compute the λ -modes of a nuclear power reactor

A. Carreño^{b,*}, A. Vidal-Ferrándiz^b, D. Ginestar[†], G. Verdú^b

(b) Instituto de Seguridad Industrial: Radiofísica y Medioambiental,
Universitat Politècnica de València, Camino de Vera, s/n, 46022, Valencia,

(†) Instituto Universitario de Matemática Multidisciplinar,

Universitat Politècnica de València, Camino de Vera, s/n, 46022, Valencia

November 30, 2017

1 Introduction

The neutron diffusion equation is an approximation of the neutron transport equation relying on the assumption that the neutron current is proportional to the gradient of the neutron flux by means of a diffusion coefficient.

For a given configuration of a nuclear reactor core, it is possible to force its criticality dividing the neutron production rate in the neutron diffusion equation by a positive number, λ , obtaining a neutron balance equation known as the λ -modes problem. This equation for two groups of energy and assuming that there is not up-scattering has the following form [1]:

$$\begin{bmatrix} -\vec{\nabla}(D_1\vec{\nabla}) + \Sigma_{a_1} + \Sigma_{12} & 0 \\ -\Sigma_{12} & -\vec{\nabla}(D_2\vec{\nabla}) + \Sigma_{a_2} \end{bmatrix} \begin{bmatrix} \phi_1 \\ \phi_2 \end{bmatrix} = \frac{1}{\lambda} \begin{bmatrix} \nu\Sigma_{f1} & \nu\Sigma_{f2} \\ 0 & 0 \end{bmatrix} \begin{bmatrix} \phi_1 \\ \phi_2 \end{bmatrix}, \quad (1)$$

where ϕ_1 and ϕ_2 denote the fast and thermal flux, respectively. The macroscopic cross sections D_1 , Σ_{a_1} , $\nu\Sigma_{f1}$, D_2 , Σ_{a_2} , $\nu\Sigma_{f2}$ and Σ_{12} are constants that depend on the position.

*e-mail:amcarsan@iqn.upv.es

The largest eigenvalue in magnitude characterises the criticality of the reactor core and its corresponding eigenfunction describes the steady state neutron distribution in the core. Next sub-critical eigenvalues and their corresponding eigenfunctions are useful to develop modal methods to integrate the time dependent neutron diffusion equation.

To solve the problem (1), a spatial discretization of the equations has to be selected. In this work, a high order Galerkin finite element method is used leading to an algebraic eigenvalue problem with the following structure,

$$\mathbf{L}\tilde{\phi} = \frac{1}{\lambda}\mathbf{M}\tilde{\phi}, \quad (2)$$

where $\tilde{\phi} = (\tilde{\phi}_1, \tilde{\phi}_2)^T$ is the algebraic vector of weights associated with the fast and thermal neutron fluxes (more details can be found in [1]). The finite element method has been implemented using the open source finite elements library Deal.II [2]. A set of dominant eigenvalues and their corresponding eigenvectors of problem (2) have to be computed.

2 Eigenvalue solvers

2.1 Modified Block Newton method

Given a partial generalized eigenvalue problem of the form

$$MV = LV\Lambda, \quad (3)$$

where $V \in \mathbb{R}^{n \times q}$ is a matrix of eigenvectors and $\Lambda \in \mathbb{R}^{q \times q}$ is a diagonal matrix whose elements are the desired eigenvalues. It is assumed that the eigenvectors can be factorized as $V = ZS$, where $Z^T Z = I_q$, and the biorthogonality condition $W^T Z = I$, is introduced, where W is a fixed matrix. Then, the non linear problem

$$F(Z, \Lambda) := \begin{bmatrix} MZ - LZK \\ W^T Z - I_q \end{bmatrix} = \begin{bmatrix} 0 \\ 0 \end{bmatrix}, \quad (4)$$

has to be solved. From Newton's method, a new iterated solution arises as,

$$Z^{(k+1)} = Z^{(k)} - \Delta Z^{(k)}, \quad K^{(k+1)} = K^{(k)} - \Delta K^{(k)}, \quad (5)$$

where $\Delta Z^{(k)}$ and $\Delta K^{(k)}$ are solutions of the system

$$\begin{cases} M\Delta Z^{(k)} - L\Delta Z^{(k)}K^{(k)} - LZ^{(k)}\Delta K^{(k)} = MZ^{(k)} - LZ^{(k)}K^{(k)}, \\ W^T\Delta Z^{(k)} = W^TZ^{(k)} - I_q, \end{cases} \quad (6)$$

The system (6) is coupled, since the matrix $K^{(k)}$ is not necessarily a diagonal matrix. To decouple the system, the Modified Block Newton method applies two previous steps. The first step consists of an orthogonalization to the matrix $Z^{(k)}$ using the modified Gram-Schmidt Orthogonalization. Once $Z^{(k)}$ is an orthonormal matrix, i.e., $Z^{(k)T}Z^{(k)} = I_q$, as a second step, a Rayleigh-Ritz procedure for generalized eigenvalue problems is applied, [3].

2.2 Inverse Free Krylov method

Given the problem (3) and an initial approximation (λ_0, x_0) , we aim at improving it through the Rayleigh-Ritz orthogonal projection on a certain subspace V , i.e.

$$\max_{x \in V} \lambda(x) \text{ where } \lambda(x) := \frac{x^T M x}{x^T L x}.$$

The steepest descend method, starting from (λ_0, x_0) , looks for a new iterate in the direction of

$$r_0 = \frac{(M - \lambda(x_0)L)x_0}{x_0^T L x_0}.$$

This can be considered as the Rayleigh-Ritz projection method on the subspace

$$K_1 := \text{span}\{x_0, (M - \lambda_0 L)x_0\}.$$

A natural extension can be considered that finds a new x_1 from

$$K_m = \text{span}\{x_0, (M - \lambda_0 L)x_0, \dots, (M - \lambda_0 L)^m x_0\},$$

by using the Rayleigh-Ritz projection method [4]. The projection can be carried out by constructing a basis for K_m and then forming and solving the projection problem for the pencil (M, L) . Arnoldi method is used to construct the basis K_m .

2.2.1 Acceleration technique using the Orthomin method

With the Orthomin method, a new iterated is computed

$$x^{i+1} = x^i + \alpha_i s^i,$$

where α_i is a scalar and s^i is a direction vector.

The scalar α_i is chosen to minimize

$$F(\alpha_i) = \|\lambda(x^i)L(x^i + \alpha_i s^i) - M(x^i + \alpha_i s^i)\|_2^2,$$

in the direction s^i . And the new direction vector s^{i+1} is evaluated by

$$s^{i+1} = r^{i+1} + \beta_i s^i,$$

where the parameter β_i satisfies

$$((M - \lambda_{i+1}L)s^{i+1}, (M - \lambda_{i+1}L)s^i) = 0.$$

The Inverse Free Krylov method is accelerated combining *narn* iterations of this method with *nacc* iterations of the orthomin method.

2.3 Multigrid method

A coarse mesh is used to obtain an initial guess to the solution of the problem with in a finner mesh, defining a two-mesh multigrid method. The problem associated to the coarse mesh is solved with the Krylov-Schur method. Figure 1 shows a scheme of this method.

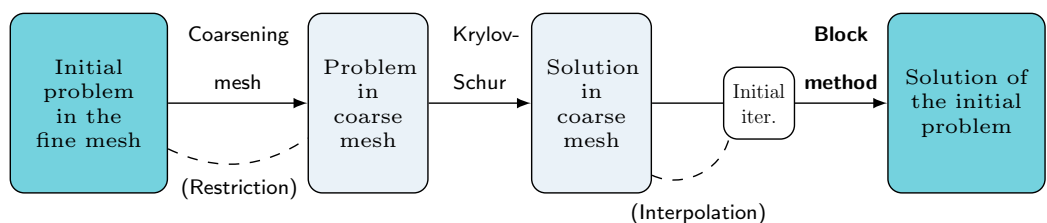


Figure 1: Two-mesh multigrid method.

3 Numerical results

To study the performance of methods the NEACRP reactor has been considered [5]. To compare the efficiency of the methods the residual errors and the computational times are represented. Figure 2(a) displays the convergence of the inverse free method using different dimensions of the Krylov subspace. It is shown, the rate of convergence increases for higher values of the dimension. However, the number of matrix-vector multiplications increases too, so a high dimension is not recommended. In Figure 2(b), the rate of convergence of the inverse free Krylov method accelerated (dim=9) with the Orthomin method are represented with different combinations. The convergence of the inverse free method without acceleration is also included. In this graph, we observe that the acceleration technique improves the convergence of the method without acceleration.

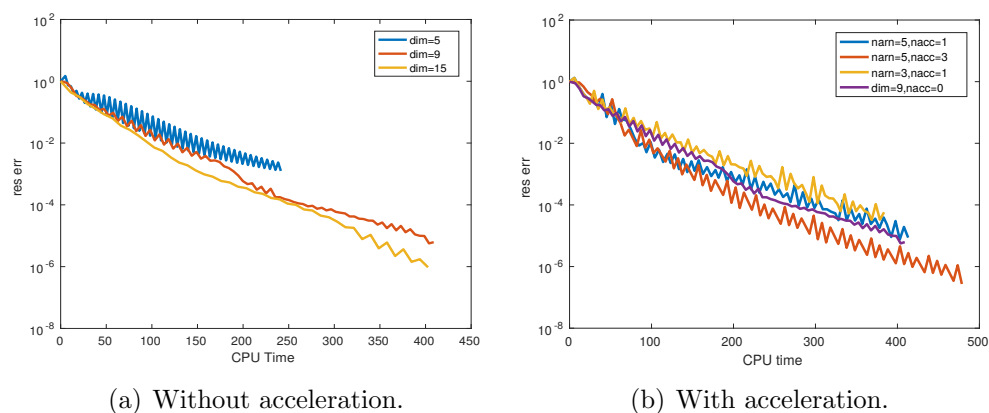


Figure 2: Residual errors against CPU time for the inverse free Krylov method.

Figure 3 shows the computational times for the benchmark problem obtained with the modified block Newton method and the inverse free Krylov method with acceleration. In this plot, we observe that the computation with the Newton method is faster than the computation with the inverse free method. The Inverse free Krylov method does not need to solve linear systems, however it needs to make a lot of matrix-vector products. In future works, we

will study other kind of accelerations to improve the convergence rates of these methods.

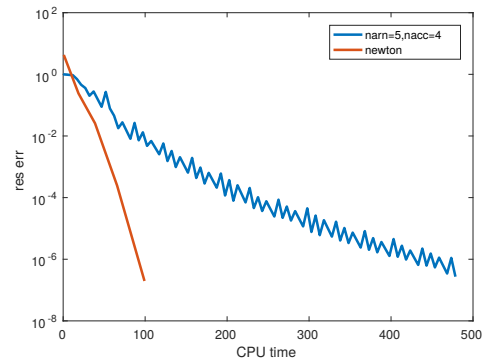


Figure 3: Residual errors against CPU time for the inverse free method accelerated and the modified Newton method.

Acknowledgments

This work has been partially supported by Spanish Ministerio de Economía y Competitividad under projects ENE2014-59442-P, MTM2014-58159-P and BES-2015-072901.

References

- [1] A. Vidal-Ferrandiz and R. Fayed and D.Ginestar and G.Verdú , “Solution of the Lambda modes problem of a nuclear power reactor using an h–p finite element method”, *Annals of Nuclear Energy* Vol. 31, pp. 338-349, 2014.
- [2] W. Bangerth and R. Hartmann and G. Kanschat. “deal.II – a General Purpose Object Oriented Finite Element Library” *ACM Trans. Math. Softw.*, Vol. 33(4), pp. 24/1-24/27, 2007.

- [3] R. Lösche and H. Schwetlick and G. Timmermann. “A modified block Newton iteration for approximating an invariant subspace of a symmetric matrix”, *Linear Algebra and its Applications*, Vol. 275, pp. 381-400, 1998.
- [4] P. Quillen, Q. Ye, “A block inverse-free preconditioned Krylov subspace method for symmetric generalized eigenvalue problems”, *Journal of computational and Applied Mathematics*, Vol 233(5), pp. 1298-1313, 2010.
- [5] Finnemann, H. and Galati, A., *NEACRP 3-D LWR core transient benchmark, final specification*, NEACRPL-335, 1991.

Constructive analytic-numerical solution of random parabolic problems in a one-dimensional random medium by a mean square Fourier integral method*

M.-C. Casabán[§], J.-C. Cortés[§] and L. Jódar[§]

(§) Instituto Universitario de Matemática Multidisciplinar,
Building 8G, access C, 2nd floor, Universitat Politècnica de València, Camino de Vera s/n,
46022 Valencia, Spain

macabar@imm.upv.es; jccortes@imm.upv.es; ljodar@imm.upv.es;

November 30, 2017

1 Introduction

This work deals with the construction of analytic-numerical solution, in the mean square sense [1], of the time-dependent random parabolic partial differential problem

$$u_t(x, t) = a_2(t) u_{xx}(x, t) + a_1(t) u_x(x, t) + a_3(t) u(x, t), \\ -\infty < x < +\infty, t > 0, \quad (1)$$

$$u(x, 0) = f(x), \quad -\infty < x < +\infty, \quad (2)$$

where $a_i(t) \equiv a_i(t, \omega) :]0, +\infty[\times \Omega \longrightarrow \mathbb{R}$, $1 \leq i \leq 3$ and $f(x) \equiv f(x, \omega) : \mathbb{R} \times \Omega \longrightarrow \mathbb{R}$ are stochastic processes (s.p.'s), defined in a complete probability

*This work has been partially supported by the Spanish Ministerio de Economía y Competitividad grant MTM2013-41765-P.

space $(\Omega, \mathcal{F}, \mathbb{P})$, that satisfy certain hypotheses.

For the random time-dependent coefficient parabolic models, the capture of the solution s.p. of the original problem involves, throughout the inverse integral transform, unbounded random integrals that makes advisable the numerical evaluation of random complicated integrals. This is a major contribution introduced here, where we extend, to the random framework, the practical Gauss-Hermite quadrature formulae for the evaluation of improper random integrals that appear in a natural way when using random integral transform methods. We also show that, a random Fourier transform method, [2], can be applied so efficiently as it has been proved to be in the solution of deterministic problems [3]. However, in the random case, not only the solution s.p. is important, but also its expectation and standard deviation. To achieve these goals, it is required the so-called L^p -random calculus [4].

2 The random Gauss-Hermite quadrature formulae

In this section, we establish some auxiliary results related to L^p -random calculus.

Lemma 1 *Let $h(\xi)$ be a complex deterministic function and let $\hat{a}(t)$ be a real s.p. such that*

$$\exists M_{\hat{a}} > 0, H_{t,\hat{a}} > 0 : \mathbb{E} [|\hat{a}(t)|^m] \leq M_{\hat{a}} (H_{t,\hat{a}})^m < +\infty, \quad \forall m \geq 0, \quad (3)$$

for every $t > 0$ fixed. Then,

$$\|\exp(h(\xi) \hat{a}(t))\|_{2,RV} \leq \sqrt{M_{\hat{a}}} \exp(\operatorname{Re}(h(\xi)) H_{t,\hat{a}}).$$

where $\operatorname{Re}(\cdot)$ denotes the real part of a complex number.

We extending to the random framework the practical Gauss-Hermite quadrature formulae for the evaluation of improper random integrals that appear in a natural way when using random integral transform methods. For $f \in L_2^{\text{SP}}(\mathbb{R} \times \Omega) = \left\{ f : \mathbb{R} \times \Omega \rightarrow \mathbb{C} / \int_{-\infty}^{+\infty} (\mathbb{E} [|f(v)|^p])^{1/p} dv < +\infty \right\}$, let us consider the following integral

$$I = I[f] = \int_{-\infty}^{+\infty} f(\xi) \exp(-\xi^2) d\xi, \quad (4)$$

which is a r.v. Since $0 < \exp(-\xi^2) \leq 1$ for all $\xi \in \mathbb{R}$ and $f \in L_2^{\text{SP}}(\mathbb{R} \times \Omega)$, one gets

$$\begin{aligned} \|I\|_{2,\text{RV}} &= \left\| \int_{-\infty}^{+\infty} f(\xi) \exp(-\xi^2) d\xi \right\|_{2,\text{RV}} \\ &\leq \int_{-\infty}^{+\infty} \|f(\xi) \exp(-\xi^2)\|_{2,\text{RV}} d\xi \leq \int_{-\infty}^{+\infty} \|f(\xi)\|_{2,\text{RV}} d\xi < +\infty. \end{aligned}$$

Then, $I[f]$ is well-defined. If we further assume that $f \in L_2^{\text{SP}}(\mathbb{R} \times \Omega)$ has continuous sample trajectories, i.e. $f(x)(\omega)$ is continuous with respect to $x \in \mathbb{R}$ for all $\omega \in \Omega$, then the r.v. (4) coincides, with probability 1, with the (deterministic) sample integrals

$$I(\omega) = I[f](\omega) = \int_{-\infty}^{+\infty} f(\xi; \omega) \exp(-\xi^2) d\xi, \quad \omega \in \Omega, \quad (5)$$

which are well-defined and thus they are convergent for all $\omega \in \Omega$ [1, Appendix I]. Then, taking advantage of the Gauss-Hermite quadrature formula of degree N , [5], we can consider the following numerical approximation

$$I_N^{\text{G-H}}[f](\omega) \approx \sum_{j=1}^N \rho_j f(\xi_{j,\text{H}}; \omega), \quad \rho_j = \frac{2^{N+1} N! \sqrt{\pi}}{(H'_N(\xi_{j,\text{H}}))^2}, \quad 1 \leq j \leq N, \quad \omega \in \Omega, \quad (6)$$

where $\xi_{j,\text{H}}$ are the roots of the deterministic Hermite polynomial, H_N , of degree N .

3 Solving random parabolic problems

We assume the following conditions under the coefficients a_i and the initial condition $f(x)$ of problem (1)–(2):

$$\begin{aligned} a_i(t), f(x) \text{ are independent r.v.'s, } \forall i: 1 \leq i \leq 3, \quad \forall(x, t), \\ -\infty < x < +\infty, \quad t > 0, \text{ both fixed, } \end{aligned} \quad (7)$$

$f(x)$ is a $\|\cdot\|_{4,\text{RV}}$ – absolutely integrable s.p.

$$\text{such that its random Fourier transform } F(\xi) \in L_4^{\text{SP}}(\mathbb{R} \times \Omega), \quad (8)$$

$$a_i(t) \text{ are } \|\cdot\|_{4,RV} - \text{continuous s.p.'s, } \forall i : 1 \leq i \leq 3, \tag{9}$$

and

$$\hat{a}_i(t) = \int_0^t a_i(s) ds, \quad 1 \leq i \leq 3, \tag{10}$$

satisfy condition (3). Let us denote by

$$a(t) := a(t, \xi) = -\xi^2 a_2(t) + i\xi a_1(t) + a_3(t), \quad \xi \in \mathbb{R} \text{ fixed,}$$

and assume that

$$\exists \delta > 0, r > 2p : \sup_{s,s^* \in [-\delta, \delta]} \mathbb{E} \left[\exp \left(r \int_{x+s}^{t+s^*} a(v) dv \right) \right] < +\infty. \tag{11}$$

Applying the random Fourier transform introduced in [2]

$$\mathfrak{F}[x(v)](\xi) = \int_{-\infty}^{+\infty} x(v) \exp(-i\xi v) dv, \quad \xi \in \mathbb{R}, \quad i = +\sqrt{-1},$$

to both sides of equation (1) and to the initial condition (2), and using its linearity, one gets for the active variable x and t fixed

$$\mathfrak{F}[u_t(\cdot, t)](\xi) = a_2(t) \mathfrak{F}[u_{xx}(\cdot, t)](\xi) + a_1(t) \mathfrak{F}[u_x(\cdot, t)](\xi) + a_3(t) \mathfrak{F}[u(\cdot, t)](\xi),$$

$$\mathfrak{F}[u(\cdot, 0)](\xi) = \mathfrak{F}[f(x)](\xi) = F(\xi).$$

By the properties of the random Fourier transform of a s.p. stated in [2], and considering the notation $\mathfrak{F}[u(\cdot, t)](\xi) = U(t)(\xi)$, one gets

$$\mathfrak{F}[u_{xx}(\cdot, t)](\xi) = -\xi^2 \mathfrak{F}[u(\cdot, t)](\xi) = -\xi^2 U(t)(\xi), \tag{12}$$

$$\mathfrak{F}[u_x(\cdot, t)](\xi) = i\xi \mathfrak{F}[u(\cdot, t)](\xi) = i\xi U(t)(\xi). \tag{13}$$

Assuming that the solution s.p. $u(x, t)$ is such that $u_t(\cdot, t)$ is Fourier transformable and that hypotheses of Lemma 2 of [2] hold, then one gets

$$\mathfrak{F}[u_t(\cdot, t)](\xi) = \frac{d}{dt} (\mathfrak{F}[u(\cdot, t)])(\xi) = \frac{d}{dt} (U(t))(\xi). \tag{14}$$

Therefore, from (12)–(14) one deduces that, for each $\xi \in \mathbb{R}$ fixed, $U(t)(\xi)$ satisfies the random IVP

$$\left. \begin{aligned} \frac{d}{dt} (U(t))(\xi) &= (-\xi^2 a_2(t) + i\xi a_1(t) + a_3(t)) U(t)(\xi), \quad t > 0, \\ U(0)(\xi) &= F(\xi). \end{aligned} \right\} \tag{15}$$

By hypotheses (7)–(11), Theorem 8 of [6] allows us to guarantee that the mean square solution s.p. of the IVP (15) is given by

$$U(t)(\xi) = \exp\left(\int_0^t a(s, \xi) ds\right) F(\xi), \quad t > 0, \quad \text{being } \xi \in \mathbb{R} \text{ fixed.} \quad (16)$$

Using formally the random inverse Fourier transform, the candidate solution s.p. of problem (1)–(2) is given by

$$u(x, t) = \mathfrak{F}^{-1}[U(t)(\xi)] = \frac{1}{2\pi} \int_{-\infty}^{+\infty} \exp\left(i\xi x + \int_0^t a(s, \xi) ds\right) F(\xi) d\xi. \quad (17)$$

Note that for every $(x, t) \in \mathbb{R} \times [0, +\infty[$ fixed, the latter random integral given in (17) is convergent in the space $L_2^{\text{SP}}(\mathbb{R} \times \Omega)$. The following result has been established

Theorem 1 *Let us consider the random IVP (1)–(2) and assume that the coefficients $a_i(t)$, $1 \leq i \leq 3$ and the initial condition $f(x)$ satisfy conditions (7)–(11). Then, the mean square solution s.p. of (1)–(2) is given by (17).*

Taking into account that $\int_0^t a(s, \xi) ds$ and $F(\xi)$, are independent r.v.’s for every $t > 0$ and $\xi \in \mathbb{R}$ due to condition (7), we can obtain the following explicit expressions for the expectation and the standard deviation of the solution s.p. (17) of the random IVP (1)–(2)

$$\mathbb{E}[u(x, t)] = \frac{1}{2\pi} \int_{-\infty}^{+\infty} \exp(i\xi x) \mathbb{E}\left[\exp\left(\int_0^t a(s, \xi) ds\right)\right] \times \mathbb{E}[F(\xi)] d\xi, \quad (18)$$

$$\begin{aligned} \mathbb{E}[(u(x, t))^2] &= \frac{1}{4\pi^2} \int_{-\infty}^{+\infty} \int_{-\infty}^{+\infty} \exp(i(\xi_1 + \xi_2)x) \\ &\quad \times \mathbb{E}\left[\exp\left(\int_0^t (a(s, \xi_1) + a(s, \xi_2)) ds\right)\right] \\ &\quad \times \mathbb{E}[F(\xi_1) F(\xi_2)] d\xi_1 d\xi_2, \\ \sqrt{\text{Var}[u(x, t)]} &= +\sqrt{\mathbb{E}[(u(x, t))^2] - (\mathbb{E}[u(x, t)])^2}. \end{aligned} \quad (19)$$

Example 1 *Let us consider the following particular case of the random IVP (1)–(2) for $-\infty < x < +\infty$ and $t > 0$,*

$$u_t(x, t) = a_2 u_{xx}(x, t) + a_1 u_x(x, t) + a_3 u(x, t), \quad (20)$$

$$u(x, 0) = \exp(-x^2). \quad (21)$$

The initial condition (21) is deterministic and admits a deterministic Fourier transform, $F(\xi) = \mathfrak{F}[f(x)](\xi) = \frac{1}{\sqrt{2}} \exp\left(\frac{-\xi^2}{4}\right)$. We will assume that coefficients a_i , $1 \leq i \leq 3$, in (20), are independent r.v.'s satisfying condition (3). We can obtain an exact s.p. of problem (20)–(21)

$$u(x, t) = \frac{1}{\sqrt{2\pi}} \frac{\exp(ta_3)}{\sqrt{4ta_2 + 1}} \exp\left(-\frac{(ta_1 + x)^2}{4ta_2 + 1}\right), \quad x \in \mathbb{R}, t > 0. \quad (22)$$

Note that for fixed (x, t) , $u(x, t)$ given by (22) can be approximated using random Gauss-Hermite quadrature formula (6) and one gets

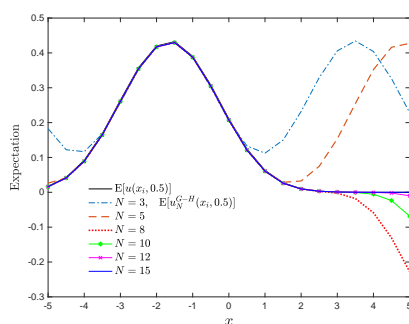
$$u_N^{G-H}(x, t) = \frac{\exp(ta_3)}{2\pi\sqrt{2}} \sum_{j=1}^N \rho_j \exp\left(-\xi_j^2 \left(ta_2 - \frac{3}{4}\right)\right) \cos(\xi_j(ta_1 + x)), \quad \left. \begin{aligned} \rho_j &= \frac{2^{N+1} N! \sqrt{\pi}}{(H'_N(\xi_j))^2}, \quad 1 \leq j \leq N. \end{aligned} \right\} (23)$$

Assume that r.v. a_1 has a gamma distribution of parameters (2; 3) truncated on the interval $[0, 6]$, $a_1 \sim \text{Gamma}_{[0,6]}(2; 3)$; a_2 has a beta distribution of parameters (2; 1), $a_2 \sim \text{Beta}(2; 1)$; and finally a_3 has an exponential distribution of parameter $\lambda = 1$ truncated on the interval $[1, 2]$, $a_3 \sim \text{Exp}_{[1,2]}(1)$.

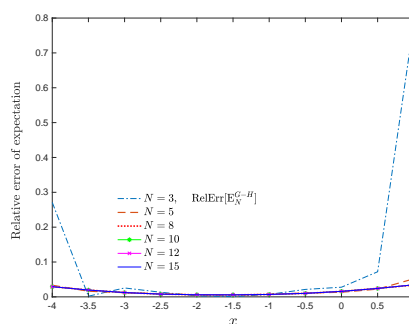
In Figures (a) and (c), we compare the exact expectation $\mathbb{E}[u(x_i, 0.5)]$, (18), and the standard deviation $\sqrt{\text{Var}[u(x, 0.5)]}$, (19), respectively, vs their numerical approximations, $\mathbb{E}[u_N^{G-H}(x, 0.5)]$ and $\sqrt{\text{Var}[u_N^{G-H}(x, 0.5)]}$ for some Hermite's polynomials of degree $N = \{3, 5, 8, 10, 12, 15\}$, at the time instant $t = 0.5$ and on the spatial domain $-5 \leq x \leq 5$. It can be seen in Figures (b) and (d) how the numerical values of the relative errors for the approximate expectation, $\text{RelErr}[\mathbb{E}_N^{G-H}]$, and the approximate standard deviation, $\text{RelErr}\left[\sqrt{\text{Var}_N^{G-H}}\right]$ decrease when the degree N increases, that is, how the approximations improving.

References

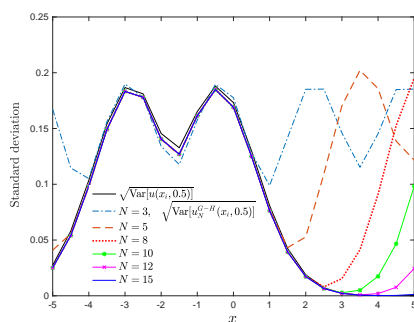
- [1] T. T. Soong, Random Differential Equations in Science and Engineering, Academic Press, New York, 1973.
- [2] M.-C. Casabán, R. Company, J.-C. Cortés, L. Jódar, Solving the random diffusion model in an infinite medium: A mean square approach, Applied Mathematical Modelling, 38 (2014) 5922–5933. doi: 10.1016/j.apm.2014.04.063



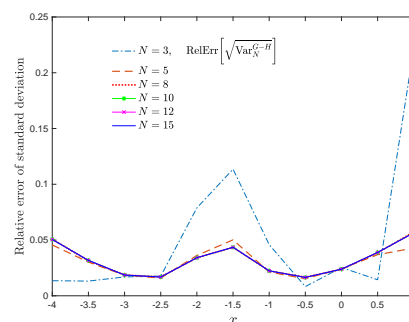
(a)



(b)



(c)



(d)

- [3] S. J. Farlow, Partial Differential Equations for Scientists and Engineers, Dover, New York, 1993.
- [4] L. Villafuerte, C.A. Braumann, J.-C. Cortés, L. Jódar, Random differential operational calculus: theory and applications, Computers and Mathematics with Applications 59 (2010) 115–125. doi: 10.1016/j.camwa.2009.08.061
- [5] L. M. Delves, J. L. Mohamed, Computational Methods for Integral Equations, Cambridge University Press, New York, 1985.
- [6] J.-C. Cortés, L. Jódar, M.-D. Roselló, L. Villafuerte, Solving initial and two-point boundary value linear random differential equations: A mean square approach, Applied Mathematics and Computation 219 (2012) 2204–2211. doi: 10.1016/j.amc.2012.08.066

A genetic algorithm to calibrate systems: a case in psychology

Antonio Caselles ^{1*}, Joan C. Micó **, Salvador Amigó ***

(*) Departament de Matemàtiques. Universitat de València.
Av. Dr Moliner, 50. 46100 Burjassot, Valencia, Spain.

(**) Instituto Universitario de Matemática Multidisciplinar,

Building 8G, 2nd floor, Universitat Politècnica de València, 46022 Valencia, Spain

(***) Departament de Personalitat, Avaluació i Tractaments Psicològics. Universitat de València
Av. Blasco Ibañez, 10. 46010, Valencia, Spain.

1. Introduction

In the application case here presented, methylphenidate is the drug being used. It is a powerful psycho-stimulant. This psycho-stimulation can be measured by the *General Factor of Personality (GFP)*, as a universal observable feature of personality. The five adjectives scale here used to measure the *GFP* is the one described by Amigó, Micó & Caselles [3]. This scale is based on the *General Factor of Personality Questionnaire* [5], which has been constructed specifically to assess *GFP* in the context of the *Unique Trait Personality Theory (UTPT)* [1][5]. The *UTPT* claims for a unique trait, as synonymous of single trait, substituted later by the equivalent concept of *GFP*, to represent the overall human personality. The *GFP* is the psychological expression of the activation level of the organism stress system. In fact, in the context of the *UTPT*, *GFP* is called also *extraversion* in a wider sense than the one used in behavioral science, i.e., in the sense of activation level of the organism stress system.

The *response model* is an integro-differential equation that has been widely assessed in the context of different experimental designs. It can reproduce the acute effect of a stimulant drug [2][6][9][10][11]. The model reproduces the dynamical pattern forecasted by Solomon & Corbit [13] and Grossberg [7], by using the hedonic scale, and by Amigó [1] for the *GFP*, i.e., a typical inverted-U.

The here performed calibration of the model is based on a genetic algorithm. Genetic algorithms (*GAs*) are Evolutionary Algorithms (*EAs*) (they adapt their parameters according to previous results) that try to imitate Natural Selection inside a population through parent selection, recombination, mutation and migration. About details on *GAs* and its use in systems calibration, see for instance: Whitley, [14], Guzmán-Cruz et al., [8] and Muraro & Dilao [12]. Nevertheless there are a lot of possible options for their definition, obviously related on how to perform *selection*, *crossover* and *mutation*. The here introduction of *immigration* could be a novelty.

2. The response model

¹ E-mail: antonio.caselles@uv.es

The kinetic part of the response model provides the evolution of the stimulus amount $s(t)$, present in plasma after intake by the individual. It is given by the time function:

$$s(t) = \begin{cases} \frac{\alpha \cdot M}{\beta - \alpha} (\exp(-\alpha \cdot t) - \exp(-\beta \cdot t)) : \alpha \neq \beta \\ \alpha \cdot M \cdot t \cdot \exp(-\alpha \cdot t) : \alpha = \beta \end{cases} \quad (1)$$

Equation (1) is the solution of two coupled differential equations [11], which assumes that no drug/stimulus is present in the organism before consumption. In (1) M is the initial amount of a drug single dose, α is the stimulus assimilation rate and β is the stimulus elimination rate. The dynamics of the *GFP* is given by the following integro-differential equation [11]:

$$\left. \begin{aligned} \frac{dy(t)}{dt} &= a(b - y(t)) + \frac{p}{b} s(t) - b \cdot q \cdot \int_0^t \mathbf{e}^{\frac{x-t}{\tau}} \cdot s(x) \cdot y(x) dx \\ y(0) &= y_0 \end{aligned} \right\} \quad (2)$$

In (2), $s(t)$ represents the stimulus; $y(t)$ represents the *GFP* dynamics; and b and y_0 are respectively its tonic level and its initial value. Its dynamics is a balance of three terms, which provide the time derivative of the *GFP*: the *homeostatic control* $a(b-y(t))$, i.e., the cause of the fast recovering of the tonic level b , the *excitation effect* $p \cdot s(t)/b$, which tends to increase the *GFP*, and the *inhibitor effect* $\int_0^t \mathbf{e}^{\frac{x-t}{\tau}} \cdot s(x) \cdot y(x) dx$, which tends to decrease the *GFP* and is the cause of a continuously delayed recovering, with the weight $\mathbf{e}^{\frac{x-t}{\tau}}$. Parameters a , p , q and τ are named respectively the *homeostatic control power*, the *excitation effect power*, the *inhibitor effect power* and the *inhibitor effect delay*. All the parameters of the model depend on the individual personality or individual biology and on the type of stimulus.

3. The genetic algorithm used for the response model calibration

The program we use for calibration has been ad hoc designed for the previously described model but it can be adapted easily for systems with the following characteristics:

- (1) Real data are deterministic. In the case of the *response model*, real *GFP* is measured by the responses of an individual to a questionnaire every some minutes. And model parameters are specific of the individual.
- (2) The system to be calibrated is deterministic.
- (3) All parameters have a continuous range of possible or plausible values from a maximum to a minimum value.
- (4) A single objective variable (function) must be considered, but it may be designed as a weighted combination of several other ones.
- (5) Parameter space (search space) is a multidimensional compact space (continuity is assumed in parameter values inside a range of possible or plausible values).
- (6) In order to assure the global character of the found optimum three strategies are considered:
 - a. A random sample may be analyzed, from the entire search space or from specific zones, in order to identify starting points.
 - b. Random migrants with reproduction capacity are introduced inside the current population in every generation.

- c. Several iterations are performed using the previous optimum as a new starting point, up to no improvement is found or the top number of iterations is reached.

3.1. The needed data

The *response mode* has seven parameters: α , β , a , b , p , q , τ and M (M may also be adjusted like the other parameters when the stimulus is not measurable, for instance: a placebo), which meaning has been previously explained. A vector of nine components containing a value for each parameter plus the corresponding *GFP* (y) may be considered as an individual of a population of possible characterizations of the system. The starting values of the parameters (given by previous knowledge), their maximum values, their minimum values, their search window width (% of their initial value), and their search step width (% of their initial value) have to be introduced at the beginning of the search process. Other needed data are the number of experimental values, their time step, and their values. The integration method (Euler or Runge-Kutta-4) and the integration step size have to be also specified. The function to be optimized may be the mean squared deviation (s^2), the determination coefficient (R^2) or the relative mean deviation.

The *GA* may be optionally used, and in the case it is used the following options must be specified: number of individuals of the population, percentage of the population corresponding to reproducers (the best individuals), number of immigrants per generation, mutant genes per thousand in a new individual, number of generations inside a given iteration, and maximum number of iterations. In the case of not using the *GA* but only analyzing a sample, it may be exhaustive or uniformly random. This sampling process also admits iterations.

3.2 The GA pseudo-code

The proposed *GA* intends to be the simplest possible one in order to be as fast as possible without restricting the possibility to find a global optimum. The following pseudo-code might be enough descriptive of the here presented *GA* that we name *PARDOSU*.

Introduce data and options

Define the initial population (vectors with random values for parameters and the objective function value)

For $i=1$ to "number of iterations", do:

 For $j=1$ to "number of generations", do:

 Arrange population from lower to higher the objective function

 Retain the best individuals and eliminate the remaining ones

 Incorporate some immigrants (randomly defined inside parameters' ranges)

 "Complete the population by reproduction (with mutation) of the present individuals, i.e.:"

 For $k="number of reproducers"+1$ to "population size", do:

 Choose randomly the "father" and the "mother" of the new individual

 For each gen (parameter) choose randomly whether it comes from "father" or "mother"

 For each gen (parameter) choose randomly whether it is newly randomly defined or not

 Next new individual

 Next generation

 If "previous optimum is not improved" Then Exit-Iterations-Loop Else Continue

 Use the optimum individual as new starting point

Next iteration

Calculate residuals by comparing the found optimum with the experimental values

Test residuals for Normality and zero-mean

If "yes" Then "calculate confidence intervals to define the optimal fitting evolution band"

Write results

4. The response model calibration

The studied application case consists in one subject that consumed 20 mg of methylphenidate. The Five Adjectives scale questionnaire (adventurous, daring, enthusiastic, merry and bored) was filled out before consumption and after consumption every 15 minutes during 4 hours. The interval of the *GFP* measures is $y \in [0, 25]$. The calibration result of the response model for the *GFP* dynamics is provided in Figure 1.

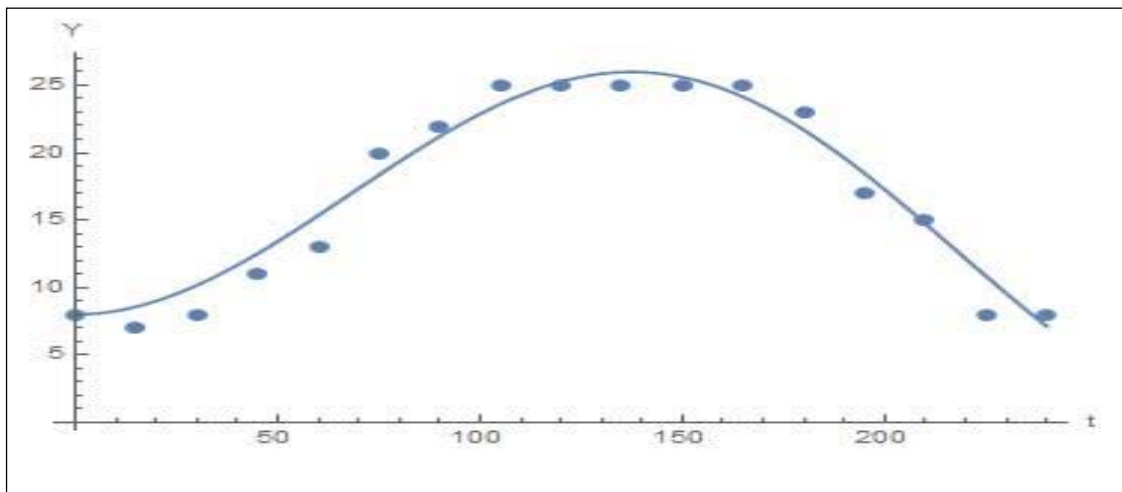


Figure 1: *GFP* (Y) versus time (t). Experimental values (dots) and the calibrated response model (line). $R^2=0.97$.

Conclusions

Figure 1 shows the calibration result of the response model for the *GFP* response as a consequence of 20 mg of methylphenidate obtained with the proposed *GA*. The obtained determination coefficient value R^2 supports model applicability as in other studies from literature (see Section 1). The algorithm shows a good performance and time efficiency.

For future work we aim to compare the efficiency of the present features of *PARDOSU* with alternative specific features, such as for instance: mutation of each parameter restricted to values close to the present one, optional equipotency of gens (at present all gens are dominant/recessive), and incest prevention. Options such as selection by competition are discarded due to they do not guarantee the permanence of the best individuals inside the population.

References

- [1] Amigó, S. (2005). *La teoría del rasgo único de personalidad. Hacia una teoría unificada del cerebro y la conducta* (The Unique Personality Trait Theory. Towards a unified theory of brain and behavior). Editorial de la Universitat Politècnica de València. Valencia, Spain.
- [2] Amigó, S., Caselles, A. & Micó, J.C. (2008). A dynamic extraversion model: the brain's response to a single dose of a stimulant drug. *British Journal of Mathematical and Statistical Psychology*, 61, 211–231.
- [3] Amigó, S., Micó, J.C. & Caselles, A. (2009a). Five adjectives to explain the whole personality: a brief scale of personality. *Revista Internacional de Sistemas*, 16, 41-43. (Available in <http://www.uv.es/caselles/>)
- [4] Amigó, S., Caselles, A., Micó, J.C. & García, J.M. (2009b). Dynamics of the unique trait of personality: blood's glutamate in response to methylphenidate and conditioning. *Revista Internacional de sistemas*, 16, 35-40.
- [5] Amigó, S., Caselles, A. & Micó, J.C. (2010). The General Factor of Personality Questionnaire (GFPQ): Only one factor to understand the personality? *The Spanish Journal of Psychology*, 13, 5-17.
- [6] Caselles, A., Micó, J.C., Amigó, S. 2011. Dynamics of the General Factor of Personality in response to a single dose of caffeine. *The Spanish Journal of Psychology*, 14, 675-692.
- [7] Grossberg, S. (2000). The imbalanced DBRAIN: from normal to schizophrenia. *Biological Psychiatry*, 48, 81-98.
- [8] Guzmán-Cruz, R., Castañeda-Miranda, R., García-Escalante, J.J., López-Cruz, J.L. (2009). Calibration of a greenhouse climate model using evolutionary algorithms. *Biosystems Engineering*, 104, 135-142.
- [9] Micó, J.C., Amigó S. & Caselles, A. (2012). Changing the General Factor of Personality and the c-fos expression with methylphenidate and Self-Regulation Therapy. *The Spanish Journal of Psychology*, 15(2): 850-867.
- [10] Micó, J.C., Caselles, A., Amigó, S., Cotolí, A. & Sanz, M.T. (2013). A mathematical approach to the body-mind problem from a System Personality theory. *Systems Research and Behavioral Science*, 30, 735–749.
- [11] Micó, J.C., Amigó, S. & Caselles, A. (2014). From the Big Five to the General Factor of Personality: a Dynamic Approach. *The Spanish Journal of Psychology*, 17, e74, 1–18.
- [12] Muraro, D., Dilao, R., (2013). A parallel multi-objective optimization algorithm for calibration of mathematical models. *Swarm and Evolutionary computation*, 8, 13-25.
- [13] Solomon, R.L. & Corbit, J.D. (1974). An opponent-process theory of motivation. I. Temporal dynamics of affect. *Psychological Review*, 81, 119-145.
- [14] Whitley, D., (2001) . An overview of evolutionary algorithms: practical issues and common pitfalls. *Information and software technology*, 43, 817-831.

Two algorithms for computing the matrix cosine based on new Hermite approximations*

Emilio Defez[★], Javier Ibáñez[‡], Jesús Peinado[‡], Jorge Sastre[†], Pedro Alonso[‡]

★ Instituto de Matemática Multidisciplinar.

‡ Departamento de Sistemas Informáticos y Computación.

† Instituto de Telecomunicaciones y Aplicaciones Multimedia.

Universitat Politècnica de València, Camino de Vera s/n, 46022, Valencia, Spain.

edefez@imm.upv.es, {jjibanez, jpeinado}@dsic.upv.es, jorsasma@iteam.upv.es, palonso@dsic.upv.es

November 30, 2017

1 Introduction

We will introduce in this work new rational-polynomial Hermite matrix expansions which permit us obtain accurate and efficient methods for computing the matrix cosine. These proposed methods are compared with the most publicized method based on Padé method for computing the matrix cosine.

The computation of matrix trigonometric functions has received remarkable attention in the last decades due to its usefulness in the solution of systems of second order linear differential equations. Several state-of-the-art algorithms have been provided for computing these matrix functions, see for example [23, 2, 20] and references therein.

The study of orthogonal matrix polynomials are becoming more and more relevant in the last decades. In particular, the matrix Hermite polynomials, introduced and studied in [17, 18] in have received considerable attention for its application in the solution of matrix differential equations, see [4]. The series of Hermite matrix polynomials have been studied for its application in the matrix exponential computation, see [21], matrix cosine approximation, [8, 9, 23] and the hyperbolic sine and cosine computation, see [7, 6], for example.

In the scalar case, Hermite polynomials $H_n(x)$ are widely used in quantum mechanics, mathematical physics, nucleon physics, and quantum optics. Recently, new formulas for series of Hermite scalar polynomials of the type $\sum_{n \geq 0} \frac{H_{2n+l}(x)}{n!} t^n, l = 1, 2, 3, \dots$ have been obtained in [16] and these formulas have been applied in quantum optics theory. The generalization of this classes of formulae for Hermite matrix polynomials $H_n(x, A)$ can be found in [10].

In this paper we will calculate the exact value of new Hermite matrix polynomial series, in particular

$$\mathcal{A}(x, t; A) := \sum_{n \geq 0} \frac{(-1)^n H_{2n+1}(x, A)}{(2n)!} t^{2n}, \mathcal{B}(x, t; A) := \sum_{n \geq 0} \frac{(-1)^n H_{2n+3}(x, A)}{(2n+1)!} t^{2n}, \quad (1)$$

which are a generalization of formulas [8, p.833]:

$$\sum_{n \geq 0} \frac{(-1)^n H_{2n}(x)}{(2n)!} t^{2n} = e^{t^2} \cos(xt\sqrt{A}), \sum_{n \geq 0} \frac{(-1)^n H_{2n+1}(x)}{(2n+1)!} t^{2n} = e^{t^2} \sin(xt\sqrt{A}), x \in \mathbb{R}, |t| < \infty \quad (2)$$

* **Acknowledgements:** This work has been supported by Spanish Ministerio de Economía y Competitividad and the European Regional Development Fund (ERDF) grant TIN2014-59294-P .

(obtained by replacing A by $\sqrt{2A}$ and taking $t = 1/\lambda$, $x = y/t$ in formulas (2.70) – (2.8) of [8]). We use formulas (1) to obtain new rational expansion in Hermite matrix polynomials of the matrix cosine.

The organization of the paper is as follows: Throughout this paper, we denote by $\mathbb{C}^{r \times r}$ the set of all the complex square matrices of size r . We denote by Θ and I , respectively, the zero and the identity matrix in $\mathbb{C}^{r \times r}$. If $A \in \mathbb{C}^{r \times r}$, we denote by $\sigma(A)$ the set of all the eigenvalues of A . We denote by $\lfloor x \rfloor$ the integer part of x and by $\lceil x \rceil$ the nearest integers to x towards infinity.

If $f(z), g(z)$ are holomorphic functions in an open set Ω of the complex plane, and if $\sigma(A) \subset \Omega$, we denote by $f(A), g(A)$, respectively, the image by the Riesz-Dunford functional calculus of the functions $f(z), g(z)$, respectively, acting on the matrix A , and $f(A)g(A) = g(A)f(A)$, see [12, p.558]. We say that matrix A is positive stable if $Re(z) > 0$ for every eigenvalue $z \in \sigma(A)$. In this case, let us denote $\sqrt{A} = A^{1/2} = \exp\left(\frac{1}{2} \log(A)\right)$ the image of the function $z^{1/2} = \exp\left(\frac{1}{2} \log(z)\right)$ by the Riesz-Dunford functional calculus, acting on the matrix A , where $\log(z)$ denotes the principal branch of the complex logarithm.

In this paper, we use consistent matrix norms. For example, in tests we use the 1–norm of a matrix $A \in \mathbb{C}^{r \times r}$ defined by $\|A\|_1 = \sup_{x \neq 0} \frac{\|Ax\|_1}{\|x\|_1}$, where $\|\cdot\|_1$ denotes the vector 1-norm defined as $\|y\|_1 = |y_1| + \dots + |y_r|$, $y \in \mathbb{C}^r$, see chapter 2 from [13]. For a positive stable matrix $A \in \mathbb{C}^{r \times r}$ the n –th Hermite matrix polynomial is defined in [17] by:

$$H_n(x, A) = n! \sum_{k=0}^{\lfloor \frac{n}{2} \rfloor} \frac{(-1)^k (\sqrt{2A})^{n-2k}}{k!(n-2k)!} x^{n-2k}, \tag{3}$$

which satisfies the three-term matrix recurrence:

$$H_{-1}(x, A) = \Theta, \quad H_0(x, A) = I, \quad H_m(x, A) = x\sqrt{2A}H_{m-1}(x, A) - 2(m-1)H_{m-2}(x, A), \quad m \geq 1. \tag{4}$$

The following result about upper bound of Hermite matrix polynomials was demonstrated in [3]:

$$\left. \begin{aligned} \|H_{2n}(x, A)\|_2 &\leq g_n(x), \quad n \geq 1 \\ \|H_{2n+1}(x, A)\|_2 &\leq |x| \left\| \left(\frac{A}{2}\right)^{-\frac{1}{2}} \right\|_2 \frac{2g_n(x)}{n+1}, \quad n \geq 0 \end{aligned} \right\}, \quad g_n(x) = \frac{(2n+1)!2^{2n}}{n!} \exp\left(\frac{5}{2} \|A\|_2 x^2\right). \tag{5}$$

2 The new formulas

We intend to calculate the exact value of the matrix series $\mathcal{A}(x, t; A)$ and $\mathcal{B}(x, t; A)$ defined by (1). First we will prove that both matrix series are convergent. Taking into account (5) one gets

$$\left\| \frac{(-1)^n H_{2n+1}(x, A)}{(2n)!} t^{2n} \right\| = |x| \left\| \left(\frac{A}{2}\right)^{-\frac{1}{2}} \right\|_2 \frac{2g_n(x)}{(n+1)(2n)!} |t|^{2n}.$$

Since $\sum_{n \geq 0} \frac{g_n(x)}{(n+1)(2n)!} |t|^{2n}$ is convergent for $|t| < \infty$, the matrix series $\mathcal{A}(x, t; A)$ is convergent in any compact real interval. Analogously, taking into account (5) again one gets

$$\left\| \frac{(-1)^n H_{2n+3}(x, A)}{(2n+1)!} t^{2n+1} \right\| = \left\| \frac{(-1)^n H_{2(n+1)+1}(x, A)}{(2n+1)!} t^{2n+1} \right\| = |x| \left\| \left(\frac{A}{2}\right)^{-\frac{1}{2}} \right\|_2 \frac{2g_{n+1}(x)}{(n+2)(2n+1)!} |t|^{2n+1}.$$

Since $\sum_{n \geq 0} \frac{g_{n+1}(x)}{(n+2)(2n+1)!} |t|^{2n+1}$ is convergent for $|t| < \infty$, the matrix series $\mathcal{B}(x, t; A)$ is convergent in any compact real interval. Using now (4) and (2) one gets

$$\begin{aligned}
\mathcal{A}(x, t; A) &= x\sqrt{2A} \sum_{n \geq 0} \frac{(-1)^n H_{2n}(x, A)}{(2n)!} t^{2n} - 4 \sum_{n \geq 1} \frac{(-1)^n H_{2n-1}(x, A)}{(2n)!} t^{2n} \\
&= H_1(x, A) e^{t^2} \cos(xt\sqrt{A}) - 2t \sum_{n \geq 1} \frac{(-1)^n H_{2n-1}(x, A)}{(2n-1)!} t^{2n-1} \\
&= H_1(x, A) e^{t^2} \cos(xt\sqrt{A}) - 2t \sum_{n \geq 0} \frac{(-1)^{n+1} H_{2n+1}(x, A)}{(2n+1)!} t^{2n+1} \\
&= H_1(x, A) e^{t^2} \cos(xt\sqrt{A}) + 2te^{t^2} \sin(xt\sqrt{A}).
\end{aligned}$$

Working in a similar form and using (4) and (2), one gets that

$$\begin{aligned}
\mathcal{B}(x, t; A) &= x\sqrt{2A} \sum_{n \geq 0} \frac{(-1)^n H_{2n+2}(x, A)}{(2n+1)!} t^{2n+1} - 2 \sum_{n \geq 0} \frac{(-1)^n (2n+2) H_{2n+1}(x, A)}{(2n+1)!} t^{2n+1} \\
&= x\sqrt{2A} \left(x\sqrt{2A} \sum_{n \geq 0} \frac{(-1)^n H_{2n+1}(x, A)}{(2n+1)!} t^{2n+1} - 2 \sum_{n \geq 0} \frac{(-1)^n (2n+1) H_{2n}(x, A)}{(2n+1)!} t^{2n+1} \right) \\
&\quad - 2 \left(\sum_{n \geq 0} \frac{(-1)^n (2n+1) H_{2n+1}(x, A)}{(2n+1)!} t^{2n+1} + \sum_{n \geq 0} \frac{(-1)^n H_{2n+1}(x, A)}{(2n+1)!} t^{2n+1} \right) \\
&= x\sqrt{2A} \left(x\sqrt{2A} e^{t^2} \sin(xt\sqrt{A}) - 2t \sum_{n \geq 0} \frac{(-1)^n H_{2n}(x, A)}{(2n)!} t^{2n} \right) \\
&\quad - 2 \left(\sum_{n \geq 0} \frac{(-1)^n H_{2n+1}(x, A)}{(2n)!} t^{2n+1} + e^{t^2} \sin(xt\sqrt{A}) \right) \\
&= e^{t^2} \sin(xt\sqrt{A}) (2x^2 A - 2I) - 2xt\sqrt{2A} e^{t^2} \cos(xt\sqrt{A}) - 2 \sum_{n \geq 0} \frac{(-1)^n H_{2n+1}(x, A)}{(2n)!} t^{2n+1}.
\end{aligned}$$

Using again (4) one gets

$$\begin{aligned}
\mathcal{B}(x, t; A) &= e^{t^2} \sin(xt\sqrt{A}) (2x^2 A - 2I) - 2xt\sqrt{2A} e^{t^2} \cos(xt\sqrt{A}) \\
&\quad - 2 \left(x\sqrt{2A} \sum_{n \geq 0} \frac{(-1)^n H_{2n}(x, A)}{(2n)!} t^{2n+1} - 2 \sum_{n \geq 1} \frac{(-1)^n (2n) H_{2n-1}(x, A)}{(2n)!} t^{2n+1} \right) \\
&= e^{t^2} \sin(xt\sqrt{A}) (2x^2 A - 2I) - 2xt\sqrt{2A} e^{t^2} \cos(xt\sqrt{A}) \\
&\quad - 2 \left(xt\sqrt{2A} e^{t^2} \cos(xt\sqrt{A}) - 2 \sum_{n \geq 1} \frac{(-1)^n H_{2n-1}(x, A)}{(2n-1)!} t^{2n+1} \right) \\
&= e^{t^2} \sin(xt\sqrt{A}) (2x^2 A - 2I) - 4xt\sqrt{2A} e^{t^2} \cos(xt\sqrt{A}) + 4t^2 \sum_{n \geq 1} \frac{(-1)^n H_{2n-1}(x, A)}{(2n-1)!} t^{2n-1}.
\end{aligned}$$

Rearranging indexes in the last series, we have

$$\begin{aligned}
\mathcal{B}(x, t; A) &= e^{t^2} \sin(xt\sqrt{A}) (2x^2 A - 2I) - 4xt\sqrt{2A} e^{t^2} \cos(xt\sqrt{A}) - 4t^2 \sum_{m \geq 0} \frac{(-1)^m H_{2m+1}(x, A)}{(2m+1)!} t^{2m+1} \\
&= e^{t^2} \sin(xt\sqrt{A}) (2x^2 A - 2I) - 4xt\sqrt{2A} e^{t^2} \cos(xt\sqrt{A}) - 4t^2 e^{t^2} \sin(xt\sqrt{A}) \\
&= e^{t^2} \sin(xt\sqrt{A}) (2x^2 A - 2I - 4t^2 I) - 4xt\sqrt{2A} e^{t^2} \cos(xt\sqrt{A}).
\end{aligned}$$

By (3), we have that $H_1(x, A) = \sqrt{2Ax}$, $H_2(x, A) = 2x^2A - 2I$, and we can write the last expression in the form

$$\mathcal{B}(x, t; A) := e^{t^2} (H_2(x, A) - 4t^2I) \sin (xt\sqrt{2A}) - 4tH_1(x, A)e^{t^2} \cos (xt\sqrt{2A}).$$

Form the previous comments, the following result has been probed:

Lemma 2.1 *Let $A \in \mathbb{C}^{r \times r}$ be a positive stable matrix. Then*

$$\begin{aligned} \mathcal{A}(x, t; A) &:= e^{t^2} \left[H_1(x, A) \cos (xt\sqrt{2A}) + 2t \sin (xt\sqrt{2A}) \right], \\ \mathcal{B}(x, t; A) &:= e^{t^2} \left[(H_2(x, A) - 4t^2I) \sin (xt\sqrt{2A}) - 4tH_1(x, A) \cos (xt\sqrt{2A}) \right]. \end{aligned} \tag{6}$$

3 On new rational-polynomial Hermite matrix expansions for the matrix cosine

Let $A \in \mathbb{C}^{r \times r}$ be a positive stable matrix, then the matrix polynomial $H_1(x, A) = \sqrt{2Ax}$ is invertible. Substituting $\sin (xt\sqrt{2A})$ given in (2) into the expression of $\mathcal{A}(x, t; A)$ given in (6) we obtain a new rational expression for the matrix cosine in terms of Hermite matrix polynomials:

$$\begin{aligned} \cos (xt\sqrt{2A}) &= e^{-t^2} \left(\sum_{n \geq 0} \frac{(-1)^n H_{2n+1}(x, A)}{(2n)!} \left(1 - \frac{2t^2}{2n+1} \right) t^{2n} \right) [H_1(x, A)]^{-1}, \\ x \in \mathbb{R}, |t| < +\infty. \end{aligned} \tag{7}$$

Substituting $\cos (xt\sqrt{2A})$ given by (2) into the expression of $\mathcal{B}(x, t; A)$ given in (6), the expression obtained is reduced to that given in (2). On the other hand, replacing the expression of $\sin (xt\sqrt{2A})$ given in (2) into $\mathcal{B}(x, t; A)$, we have another new rational expression for the matrix cosine in terms of Hermite matrix polynomials:

$$\begin{aligned} &\cos (xt\sqrt{2A}) \\ &= \frac{-e^{-t^2}}{4} \left[\sum_{n \geq 0} \frac{(-1)^n H_{2n+3}(x, A)}{(2n+1)!} t^{2n} - \underbrace{(H_2(x, A) - 4t^2I) \left(\sum_{n \geq 0} \frac{(-1)^n H_{2n+1}(x, A)}{(2n+1)!} t^{2n} \right)}_{\star} \right] [H_1(x, A)]^{-1}, \\ &x \in \mathbb{R}, |t| < +\infty. \end{aligned} \tag{8}$$

We always have one more product of matrices in formula (8), the matrix product remark by (\star) . Due to the importance of reducing the number of matrix products, see [22] for more details, we will focus on the expansion (7).

Substituting in (7) the matrix A by matrix $A^2/2$ we avoid the square roots of matrices. In addition, from (3), it follows that

$$A^{-1}H_{2n+1} \left(x, \frac{1}{2}A^2 \right) = (2n+1)! \sum_{k=0}^n \frac{(-1)^k x^{2(n-k)} A^{2(n-k)}}{k!(2(n-k)+1)!} = \tilde{H}_{2n+1} \left(x, \frac{1}{2}A^2 \right), \tag{9}$$

so the right side of (9) is still defined in the case where the matrix A is singular. In this way, we can re-write the relation (7) in terms of the matrix polynomial $\tilde{H}_{2n+1} \left(x, \frac{1}{2}A^2 \right)$, and taking $x = \lambda, \lambda \neq 0, t = 1/\lambda$, we obtain

Table 1: Values of z_m .

m	2	4	6	9	12	16
z_m	1.4440e-5	7.70884e-3	1.3286e-1	1.3292e0	5.2844	1.7679e1

$$\cos(A) = \frac{e^{-\frac{1}{\lambda^2}}}{\lambda} \sum_{n \geq 0} \frac{(-1)^n \tilde{H}_{2n+1}(\lambda, \frac{1}{2}A^2)}{(2n)! \lambda^{2n}} \left(1 - \frac{2}{(2n+1)\lambda^2}\right). \quad (10)$$

Note that expansion given in (10) is really a polynomial series in matrix A . Truncating the given series (10) until order m , we obtain the approximation $C_m(\lambda, A) \approx \cos(A)$ defined by:

$$C_m(\lambda, A) = \frac{e^{-\frac{1}{\lambda^2}}}{\lambda} \sum_{n=0}^m \frac{(-1)^n \tilde{H}_{2n+1}(\lambda, \frac{1}{2}A^2)}{(2n)! \lambda^{2n}} \left(1 - \frac{2}{(2n+1)\lambda^2}\right) \approx \cos(A), 0 < |\lambda| < +\infty. \quad (11)$$

for any matrix $A \in \mathbb{C}^{r \times r}$.

Working analogously to the proof of the formula (3.3) of [6], you have

$$\left\| \tilde{H}_{2n+1}\left(x, \frac{1}{2}A^2\right) \right\|_2 \leq (2n+1)! \frac{e \sinh\left(x \|A^2\|_2^{1/2}\right)}{\|A^2\|_2^{1/2}}. \quad (12)$$

We can perform the following approximation of the approximation error:

$$\begin{aligned} \|\cos(A) - C_m(\lambda, A)\|_2 &\leq \frac{e^{-\frac{1}{\lambda^2}}}{\lambda} \sum_{n \geq m+1} \frac{\left\| \tilde{H}_{2n+1}(\lambda, \frac{1}{2}A^2) \right\|_2}{(2n)! \lambda^{2n}} \left|1 - \frac{2}{(2n+1)\lambda^2}\right| \\ &\leq \frac{e^{1-\frac{1}{\lambda^2}} \sinh\left(\lambda \|A^2\|_2^{1/2}\right)}{\lambda \|A^2\|_2^{1/2}} \sum_{n \geq m+1} \frac{2n+1}{\lambda^{2n}} \left|1 - \frac{2}{(2n+1)\lambda^2}\right|. \end{aligned} \quad (13)$$

Taking $\lambda > \sqrt{2}$ it is follows that $\frac{2}{(2n+1)\lambda^2} < 1$, and one gets

$$\sum_{n \geq m+1} \frac{2n+1}{\lambda^{2n}} \left(1 - \frac{2}{(2n+1)\lambda^2}\right) = \frac{2 + (2m+3)\lambda^2(\lambda^2 - 1)}{\lambda^{2m+2}(\lambda^2 - 1)^2},$$

thus from (13) we finally obtain:

$$\|\cos(A) - C_m(\lambda, A)\|_2 \leq \frac{e^{1-\frac{1}{\lambda^2}} \sinh\left(\lambda \|A^2\|_2^{1/2}\right) (2 + (2m+3)\lambda^2(\lambda^2 - 1))}{\|A^2\|_2^{1/2} \lambda^{2m+3} (\lambda^2 - 1)^2}. \quad (14)$$

From this expression (14) we derived the optimal values $(\lambda_m; z_m)$ such that

$$z_m = \max \left\{ z = \|A^2\|_2; \frac{e^{1-\frac{1}{\lambda^2}} \sinh\left(\lambda z^{1/2}\right) (2 + (2m+3)\lambda^2(\lambda^2 - 1))}{z^{1/2} \lambda^{2m+3} (\lambda^2 - 1)^2} < u \right\}$$

where u is the unit roundoff in IEEE double precision arithmetic, $u = 2^{-53}$. The optimal values of m , z and λ have been obtained through a MATLAB program. The results are given in the table 1.

4 The proposed MATLAB implementations

The matrix cosine can be computed for $A \in \mathbb{C}^{n \times n}$ by the expression

$$P_m(B) = \sum_{i=0}^m p_i B^i, \quad (15)$$

where $B = A^2$, and p_i is the coefficient polynomial of Hermite expression (11), or $p_i = \frac{(-1)^i}{(2i)!}$, if the Taylor approximation is used. Since Hermite and Taylor series are accurate only near the origin, in algorithms that use these approximations the norm of matrix B must be reduced by scaling the matrix. Once the cosine of scaled matrix has been computed, the approximation of $\cos(A)$ is recovered by means of the double angle formula $\cos(2X) = 2\cos^2(X) - I$. Algorithm 1 shows a general algorithm for computing the matrix cosine based on Taylor approximation. By using the fact that $\sin(A) = \cos(A - \frac{\pi}{2}I)$, Algorithm 1 also can be easily used to compute the matrix sine.

Algorithm 1 Given a matrix $A \in \mathbb{C}^{n \times n}$, this algorithm computes $C = \cos(A)$ by Taylor/Hermite series.

```

1: Select adequate values of  $m$  and  $s$                                 ▷ Phase I
2:  $B = 4^{-s}A^2$ 
3:  $C = P_m(B)$                                                     ▷ Phase II: Compute Taylor/Hermite approximation
4: for  $i = 1 : s$  do                                              ▷ Phase III: Recovering  $\cos(A)$ 
5:    $C = 2C^2 - I$ 
6: end for

```

In Phase I of Algorithm 1, m and s can be calculated so that the Hermite or Taylor approximations of the scaled matrix is computed accurately and efficiently. In this phase some powers B^i , $i \geq 2$, are usually computed for estimating m and s and if so they are used in Phase II.

Phase II consists of computing the approximations (11) or (15). Taylor matrix polynomial approximation (15), expressed as $P_m(B) = \sum_{i=0}^m p_i B^i$, $B \in \mathbb{C}^{n \times n}$, can be computed with optimal cost by the Paterson-Stockmeyer's method [19] choosing m from the set

$$\mathbb{M} = \{1, 2, 4, 6, 9, 12, 16, 20, 25, 30, 36, 42, \dots\},$$

where the elements of \mathbb{M} are denoted as m_1, m_2, m_3, \dots . The algorithm computes first the powers B^i , $2 \leq i \leq q$ not computed in the previous phase, being $q = \lceil \sqrt{m_k} \rceil$ or $q = \lfloor \sqrt{m_k} \rfloor$ an integer divisor of m_k , $k \geq 1$, both values giving the same cost in terms of matrix products. Therefore, (15) can be computed efficiently as

$$\begin{aligned}
P_{m_k}(B) = & \quad (16) \\
& (((p_{m_k} B^q + p_{m_k-1} B^{q-1} + p_{m_k-2} B^{q-2} + \dots + p_{m_k-q+1} B + p_{m_k-q} I) B^q \\
& + p_{m_k-q-1} B^{q-1} + p_{m_k-q-2} B^{q-2} + \dots + p_{m_k-2q+1} B + p_{m_k-2q} I) B^q \\
& + p_{m_k-2q-1} B^{q-1} + p_{m_k-2q-2} B^{q-2} + \dots + p_{m_k-3q+1} B + p_{m_k-3q} I) B^q \\
& \dots \\
& + p_{q-1} B^{q-1} + p_{q-2} B^{q-2} + \dots + p_1 B + p_0 I.
\end{aligned}$$

We made two implementations based on the algorithms `cosher` [5] and `cosmtay` [20]. The MATLAB implementation `cosherm` is a modification of the MATLAB's code `cosher`, taking the values of m , z and λ of Section 3 instead of these values from [5]. The MATLAB's implementation `cosmtayher` is a modification of the MATLAB's code `cosmtay`, taking the values of z_m instead of Θ_m to obtain the approximation degree m and the scaling factor s of the matrix A , and replacing the Taylor polynomial of `cosmtay` by the "Hermite" matrix polynomial obtained from λ_m .

5 Numerical experiments

The following MATLAB implementations (version: 9.1.0.441655, R2016b) have been compared:

- `cosm`. Code based on the Padé rational approximation for the matrix cosine [1].

- `cosmtay`. Code based on the Taylor series for the matrix cosine [20].
- `cosherm`. New code for computing the matrix cosine based on the new developments of Hermites matrix polynomials (11) and the algorithm `cosmtayher` from [5].
- `cosmtayher`. New code for computing the matrix cosine based on the new developments of Hermites matrix polynomials (11) and the algorithm `cosmtayher` from [20].

In tests, fifty eight 128×128 matrices from Toolbox [14] and Eigtool [24] packages have been used. These matrices have been chosen because they have more varied and significant characteristics. For the accurate of MATLAB codes we have calculated the relative errors as

$$\frac{\|\tilde{X} - \cos(A)\|_1}{\|\cos(A)\|_1},$$

where \tilde{X} is the computed matrix cosine.

We only show the accurate and computational costs of `cosmtayher` compared to the accurate and computational costs of the other implementations, since `cosmtayher` is the implementation that presents the best performances. To compare the computational costs, the number of products of each code has been calculated, since this operation has the highest computational cost. The resolution of linear systems that appears in the code based on Padé approximation `cosm` has been calculated as $4/3$ products, because from a computational point of view, the cost of that operation compared to the product of matrices is approximately equal to $4/3$, see Table C.1 from [15, p. 336].

Table 2 shows the percentage of cases in which the relative errors of MATLAB codes `cosm`, `cosmtay` and `cosherm` are, respectively, lower and greater than the relative errors of `cosmtayher`. Table 3 show the matrix products of the four MATLAB codes.

Table 2: Error comparative between `cosmtayher` and the other MATLAB implementations.

	$E(\text{Ex}) < E(\text{cosmtayher})$	$E(\text{Ex}) > E(\text{cosmtayher})$
$\text{Ex} \equiv \text{cosm}$	21.05%	78.95%
$\text{Ex} \equiv \text{cosmtay}$	33.33%	66.67%
$\text{Ex} \equiv \text{cosherm}$	47.37%	52.63%

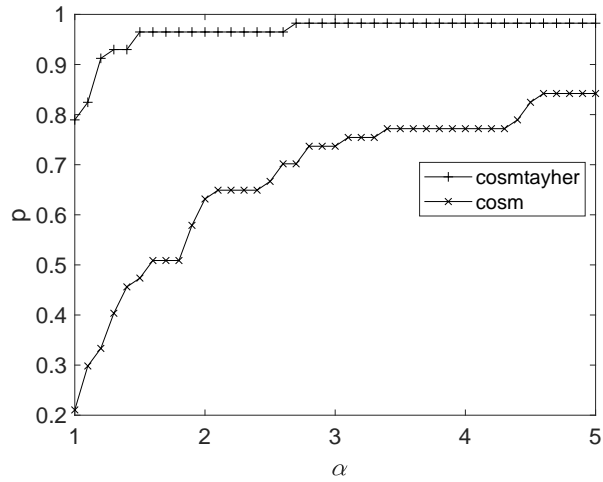
Table 3: Matrix products of the four MATLAB implementations.

<code>cosm</code>	<code>cosmtay</code>	<code>cosherm</code>	<code>cosmtayher</code>
621	508	541	355

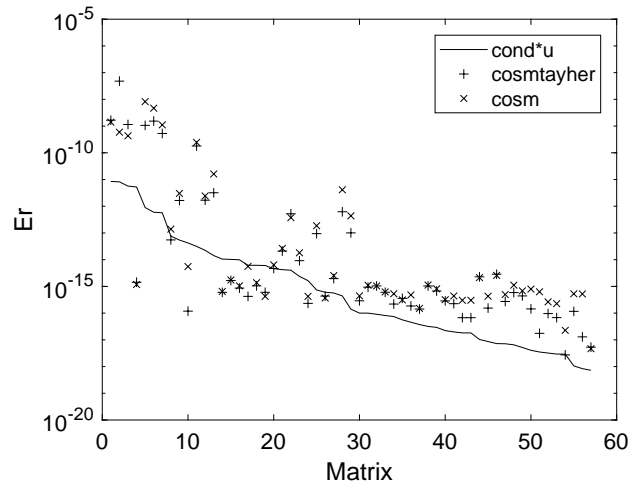
Figure 1 shows the normwise relative error and the performance profiles graphics [11]. The solid line of Subfigures 1a, 1c and 1e is the function $k_{\cos}u$, where k_{\cos} is the condition number of matrix cosine function [15, Chapter 3] and $u = 2^{-53}$ is the unit roundoff in the double precision floating-point arithmetic.

According to the results obtained, we can outline the following conclusions:

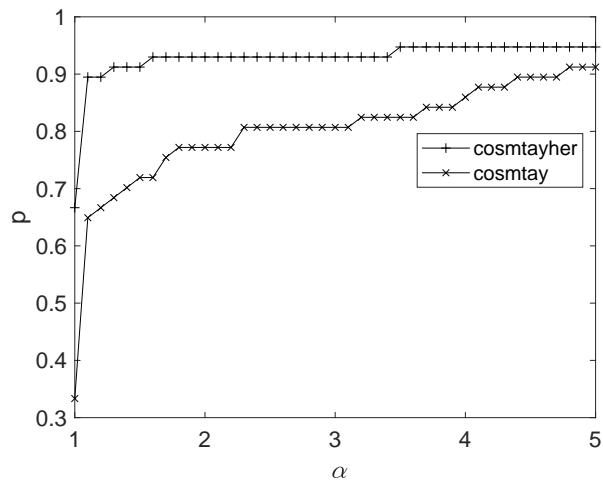
- Subfigures 1b, 1d and 1f show that the four implementations have a similar numerical stability.
- The MATLAB code `cosmtayher` has a lower computational cost than the other MATLAB codes (see Table 3).
- In general, MATLAB code `cosmtayher` is more accurate than the other MATLAB codes (see Table 2 and Subfigures 1a, 1c and 1e).



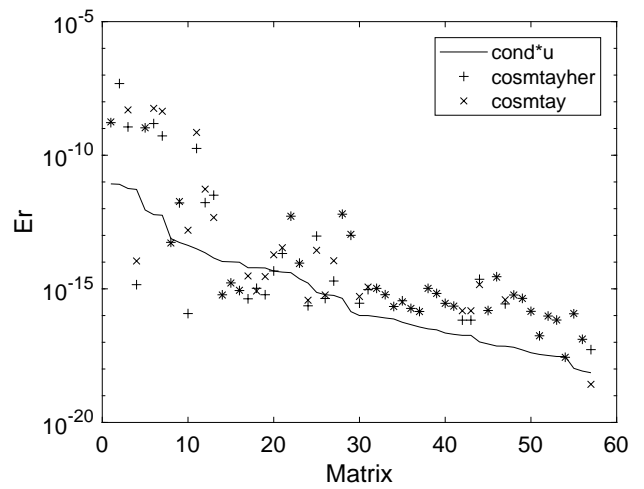
(a) Normwise relative errors of `comtayher-cosm`.



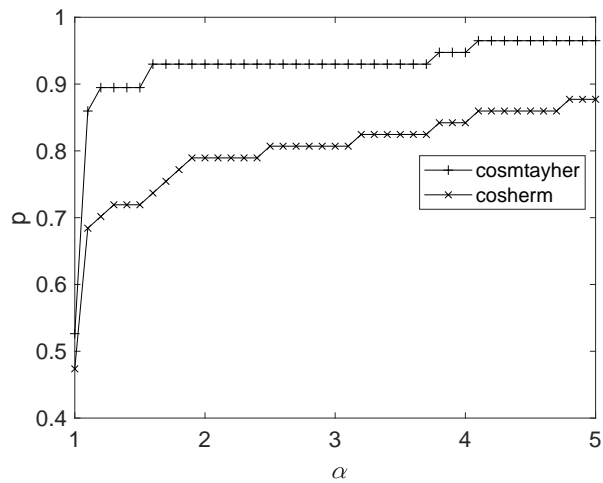
(b) Performance profile of `comtayher-cosm`.



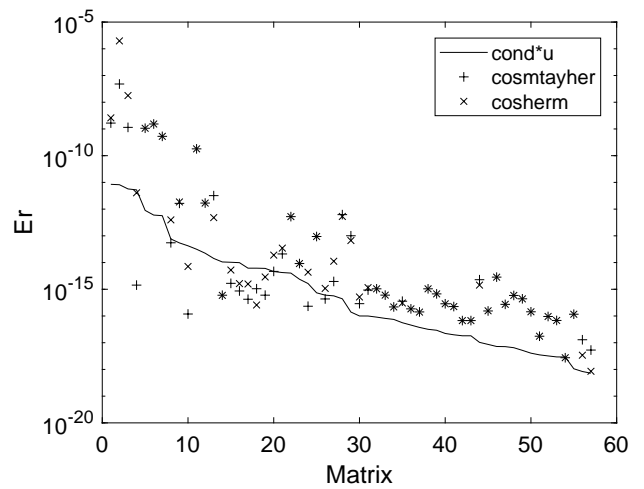
(c) Normwise relative errors of `comtayher-cosmtay`.



(d) Performance profile of `comtayher-cosmtay`.



(e) Normwise relative errors of `comtayher-cosherm`.



(f) Performance profile of `comtayher-cosherm`.

Figure 1: Normwise relative errors and the performance profiles.

6 Conclusions

In this work we have developed more accurate MATLAB implementations (`cosherm`, `cosmtayherm`) based on the new Hermite series (11) that improve others from the state of the art for the computation of the matrix cosine function (`cosm`, `cosmtay`). Among the new implementations it is worth highlighting the MATLAB implementation `cosmtayherm`, because it has a lower computational cost than the other MATLAB codes.

References

- [1] A. H. Al-Mohy, N. J. Higham, and S. D. Relton. New algorithms for computing the matrix sine and cosine separately or simultaneously. *SIAM Journal on Scientific Computing*, 37(1):A456–A487, 2015.
- [2] P. Alonso, J. Ibáñez, J. Sastre, J. Peinado, and E. Defez. Efficient and accurate algorithms for computing matrix trigonometric functions. *Journal of Computational and Applied Mathematics*, 309:325–332, 2017.
- [3] E. Defez, A. Hervás, L. Jódar, and A. Law. Bounding Hermite matrix polynomials. *Mathematical and Computer Modelling*, 40(1):117–125, 2004.
- [4] E. Defez and L. Jódar. Some applications of the Hermite matrix polynomials series expansions. *Journal of Computational and Applied Mathematics*, 99(1):105–117, 1998.
- [5] E. Defez, J. Sastre, J. Ibáñez, and P. Ruiz. Computing matrix functions arising in engineering models with orthogonal matrix polynomials. *Mathematical and Computer Modelling*, pages 1738–1743, 2011. . doi:10.1016/j.mcm.2011.11.022.
- [6] E. Defez, J. Sastre, J. Ibáñez, and J. Peinado. Solving engineering models using hyperbolic matrix functions. *Applied Mathematical Modelling*, 40(4):2837–2844, 2016.
- [7] E. Defez, J. Sastre, J. Ibáñez, J. Peinado, and M. M. Tung. A method to approximate the hyperbolic sine of a matrix. *International Journal of Complex Systems in Science*, 4(1):41–45, 2014.
- [8] E. Defez, J. Sastre, J. Ibáñez, and P. Ruiz. Computing matrix functions solving coupled differential models. *Mathematical and Computer Modelling*, 50(5):831–839, 2009.
- [9] E. Defez, J. Sastre, J. Ibáñez, and P. Ruiz. Computing matrix functions arising in engineering models with orthogonal matrix polynomials. *Mathematical and Computer Modelling*, 57(7):1738–1743, 2013.
- [10] E. Defez and M. M. Tung. A new type of hermite matrix polynomial series. *Quaestiones Mathematicae*, pages 1–8, 2017.
- [11] E. D. Dolan and J. J. Moré. Benchmarking optimization software with performance profiles. *Mathematical Programming*, 91:201–213, 2002.
- [12] N. Dunford and J. T. Schwartz. Linear operators, vol. I. *Interscience, New York*, 1958.
- [13] G. H. Golub and C. F. Van Loan. *Matrix computations*. Johns Hopkins University Press, 1996.
- [14] N. J. Higham. *The test matrix toolbox for MATLAB (Version 3.0)*. University of Manchester Manchester, 1995.
- [15] N. J. Higham. *Functions of Matrices: Theory and Computation*. SIAM, Philadelphia, PA, USA, 2008.
- [16] F. Hong-Yi and Z. De-Hui. New generating function formulae of even-and odd-Hermite polynomials obtained and applied in the context of quantum optics. *Chinese Physics B*, 23(6):060301, 2014.
- [17] J. Jódar and R. Company. Hermite matrix polynomials and second order matrix differential equations. *Approximation Theory and its Applications*, 12(2):20–30, 1996.
- [18] L. Jódar and E. Defez. On Hermite matrix polynomials and Hermite matrix functions. *Approximation Theory and its Applications*, 14(1):36–48, 1998.
- [19] M. S. Paterson and L. J. Stockmeyer. On the number of nonscalar multiplications necessary to evaluate polynomials. *SIAM Journal on Computing*, 2(1):60–66, 1973.

- [20] J. Sastre, J. Ibáñez, P. Alonso, J. Peinado, and E. Defez. Two algorithms for computing the matrix cosine function. *Applied Mathematics and Computation*, 312:66–77, 2017.
- [21] J. Sastre, J. Ibáñez, E. Defez, and P. Ruiz. Efficient orthogonal matrix polynomial based method for computing matrix exponential. *Applied Mathematics and Computation*, 217(14):6451–6463, 2011.
- [22] J. Sastre, J. Ibáñez, E. Defez, and P. Ruiz. New scaling-squaring Taylor algorithms for computing the matrix exponential. *SIAM Journal on Scientific Computing*, 37(1):A439–A455, 2015.
- [23] J. Sastre, J. Ibáñez, P. Ruiz, and E. Defez. Efficient computation of the matrix cosine. *Applied Mathematics and Computation*, 219(14):7575–7585, 2013.
- [24] TG Wright. Eigtool, version 2.1. *URL: web.comlab.ox.ac.uk/pseudospectra/eigtool*, 2009.

Wildland fire propagation modelling

V.N. Egorova^{b,*}, G. Pagnini^{b,‡}, and A. Trucchia^{b,‡}

(^b) BCAM - Basque Center for Applied Mathematics,
Alameda de Mazarredo 14, E-48009 Bilbao, Basque Country – Spain,
([‡]) Ikerbasque – Basque Foundation for Science,
Calle de María Díaz de Haro 3, E-48013 Bilbao, Basque Country – Spain,
([‡]) University of the Basque Country UPV/EHU,
Barrio Sarriena s/n, E-48940 Leioa, Basque Country – Spain.

November 30, 2017

1 Introduction

Wildfire propagation modelling is a challenging problem due to its complex multi-scale multi-physics nature. This process can be described by a reaction-diffusion equation based on the energy balance principle, see e.g. [1]. Alternative technique is the so-called level-set method (LSM) [6] and it is used in wildfire modelling [4] as well as in many other fields. In present study a methodology for fire propagation modelling that reconciles these approaches is proposed. This methodology is distinguishable and significant from both academical and industrial point of view because of the inclusion of the random effects by preserving the existing algorithms and direct implementation as a post-processing numerical routine.

The random behaviour of the fire front is caused, for example, by the turbulence and the fire-spotting phenomenon. A probability density function (PDF) is employed in order to describe the random process. In earlier studies [5] it has been shown that new independent ignitions can increase the rate of spread (ROS) of fire and therefore should be carefully studied. In this respect,

*e-mail:vegorova@bcamath.org

a physical parametrization of the fire-spotting distribution was proposed [3]. Special attention in the present study is paid to the atmospheric stability conditions. The parametrization proposed in Ref. [3] is completed by the multiple fire-spotting modelling. Afterwards special attention is paid to the study of uniqueness of the PDF and consistency with the energy balance equation. Numerical results and discussions complete the study.

2 Fire front model and non-uniqueness

Detailed explanation of the proposed method can be found in [2, 5]. Here we briefly describe the idea. Fire propagation is splitted into a drifting part and a fluctuating part. The drifting part is handled by a chosen existing method, while the fluctuating part that includes the random effects is found as a results of a comprehensive statistical description of the physical system. Thus, denoting the burning area by $\Omega(t)$, the evolution of the fire front can be defined by the following novel family of reaction-diffusion equations

$$\frac{\partial \phi_e}{\partial t} = \int_{\Omega(t)} \frac{\partial f}{\partial t} d\bar{\mathbf{x}} + \int_{\Omega(t)} \nabla_{\bar{\mathbf{x}}} [V(\bar{\mathbf{x}}, t) f(\mathbf{x}; t|\bar{\mathbf{x}})] d\bar{\mathbf{x}}, \quad (1)$$

where $\phi_e(\mathbf{x}, t) = \int_{\Omega(t)} f(\mathbf{x}; t|\bar{\mathbf{x}}) d\bar{\mathbf{x}}$ is an effective indicator function, such that for some threshold value ϕ_e^* expression $\phi_e(\mathbf{x}, t) \geq \phi_e^*$ represents the burning area. $V(\mathbf{x}, t)$ is the ROS of the fire front, $f(\mathbf{x}; t|\bar{\mathbf{x}})$ is the PDF that accounts for turbulence and fire-spotting effects.

Wildfire model can be formulated as the balance equations for energy and fuel, see [1]. However, as it is stated in [5], the reaction-diffusion equation and the LSM "can indeed be considered complementary and can be reconciled" by the proposed technique when $\Omega(t)$ is the burned area estimated by the LSM approach. The connection between these two approaches is the connection between the indicator function ϕ_e and the temperature T , that can be expressed in an amount of heat:

$$\psi(\mathbf{x}, t) = \int_0^t \phi_e(\mathbf{x}, \eta) \frac{d\eta}{\tau} = \frac{T(\mathbf{x}, t) - T_a(\mathbf{x})}{T_{ign} - T_a(\mathbf{x})}, \quad T < T_{ign}, \quad (2)$$

where τ is the ignition delay. From (2) one can see, that $\psi(\mathbf{x}, t) = 1$ entails that $T(\mathbf{x}, t) = T_{ign}$ and the spacial point \mathbf{x} at the moment t belongs to the burning area. Derivation of the energy balance equation can be found in [5], here we provide the result:

$$\frac{\partial T}{\partial t} = \epsilon T + \frac{T_{ign} - T_a}{\tau} (I_{\Omega_0}(\mathbf{x}) + W(\mathbf{x}, t)), \quad (3)$$

where T_{ign} is the ignition temperature, $T_a(\mathbf{x})$ is the ambient temperature, $I_{\Omega_0}(\mathbf{x}) = \phi_e(\mathbf{x}, 0)$ and $W(\mathbf{x}, t)$ is the rate of fuel consumed by the fire.

Equation (3) can be understood as the energy balance equation associated to the model. This preliminary result will be completed by the numerical comparison with existing models.

Denoting the wind velocity by U , the shape of the PDF is defined by the isotropic bi-variate Gaussian function (considering turbulence effects) $G(\mathbf{x} - \bar{\mathbf{x}}; t)$ and the firebrand landing distribution $q(l)$ as follows

$$f(\mathbf{x}; t|\bar{\mathbf{x}}) = \begin{cases} \int_0^\infty G(\mathbf{x} - \bar{\mathbf{x}} - l\hat{\mathbf{n}}; t)q(l)dl, & \text{downwind,} \\ G(\mathbf{x} - \bar{\mathbf{x}}; t), & \text{otherwise,} \end{cases} \quad (4)$$

where $q(t)$ is the lognormal distribution $q(l) = \frac{1}{\sqrt{2\pi}\sigma l} \exp\left(-\frac{(\ln l/\mu)^2}{2\sigma^2}\right)$. Parameter μ is the ratio between the square of the mean of landing distance l and its standard deviation, σ is the standard deviation of $\ln l/\mu$.

The physical parametrisation of the fire-spotting distribution is considered with the following parameters [3],

$$\mu = H \left(\frac{3\rho_a C_d}{2\rho_f r g} \right)^{1/2}, \quad \sigma = \frac{1}{2z_p} \ln \left(\frac{U^2}{r g} \right), \quad (5)$$

where, according to [7], the maximum loftable height is described in terms of atmospheric stability conditions, such that H_{ABL} is the height of the atmospheric boundary layer and N^2 is the Brünt-Väsälä frequency.

Taking into account the wind direction through the angle θ , σ defined in (5) becomes

$$\sigma = \frac{1}{2z_p} \ln \left(\frac{(U \cos \theta)^2}{r g} \right) \geq \sigma_0, \quad \text{with } \cos \theta \geq \frac{\sqrt{r g}}{U} \exp(z_p \sigma_0), \quad (6)$$

where σ_0 is minimum possible value of σ .

Thus, multiple fires due to the so-called fire-spotting can be modelled since secondary fires appear where (6) holds.

The uniqueness of the the effective indicator function ϕ_e requires a discussion. This analysis is based on the theorem that if an integral of a non-negative function is zero then the function is zero almost everywhere. The

result agrees also with the Radon-Nikodym Theorem, that shows that there is no one-to-one correspondence between the PDF and the effective indicator function and the following statement can be formulated: Some burning area, described by the effective indicator function can be generated by the different PDFs.

This is an important issue since it allows to model a complex topology of the burning area by a simple suitable PDF. For instance, if the fuel inside the fire zone is completely burned out the combustion ceases, that leads to the crown or ring form of the burning area since the ignitions are observed only at the leading edge of the fire perimeter. However, fire propagation in such domain can be modelled by the PDF (4) as for the entire one just with the suitable parameters.

Due to parametrization (5)-(6) the dependence of the fire front upon the atmospheric stability is found. However, there are a lot of factors that can effect the process. Such that influence of the flame geometry, mainly flame length, is going to be studied in the future.

3 Numerical results and discussions

In this section some numerical examples are provided to show the results of parametrization and multiple fire-spotting effects. The choice of fire-spotting distribution parameters is crucial for the model since it manages the fire brand travel distance. As it is shown in Figure 1 (left), the merging effect can be observed for certain parameters μ and σ .

Inclusion of condition (6) into the numerical algorithm results in multiple secondary fires in some angle θ , as it is presented in Figure 1 (right).

The proposed numerical routine can also take into account a firebreak zones. From the real data it is known that when the fire front reaches the fire-break, it stops for a while, but then it crosses the zone and continues the propagation. Moreover, spot fires can overcome the firebreak, that can cause dangerous effects. Numerical simulations for a such case are presented in Figure 2. This is a very important issue for the fire-fighters management.

The proposed method reconciles existing wildfire propagation models improving operational codes by the significant post-processing numerical algorithm. The model includes effects of turbulence and fire-spotting that results in random fire front. It allows to model the fire that overcomes a fire-break zone and increase the rate of spread. This improvement has an important

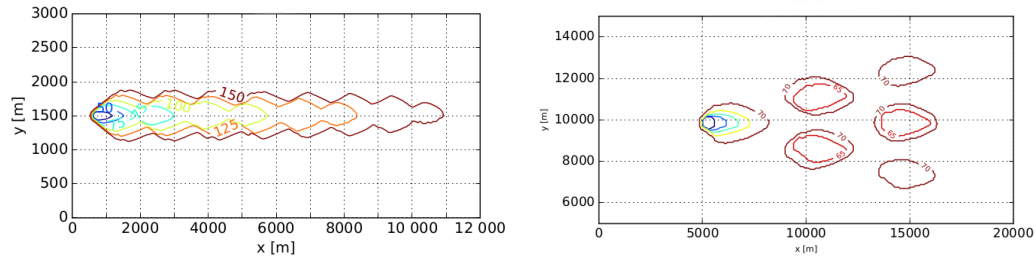


Figure 1: Fire-spotting effect: merging secondary fires with $\mu = 12$, $\sigma = 8$ (left) and multiple fire-spotting with $\mu = 9.75$ and $\sigma = 8.15$ and incorporation of (6) (right).

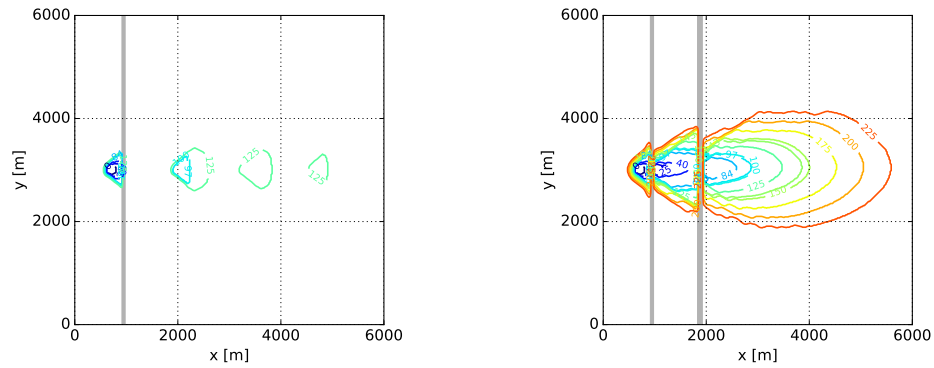


Figure 2: Wildfire propagation in the presence of the firebreak zone.

economical impact since it can be helpful for fire suppression and control. Parametrization of the fire-spotting distribution leads to the definition of the angle of the multiple fire-spotting and allows the future consideration of other factors, such as flame geometry.

The future intention is to incorporate data assimilation algorithms in order to adopt the methodology to the real topography, as well as to calibrate the model.

Acknowledgements

This research is supported by the Basque Government through the BERC 2014-2017 program and by Spanish Ministry of Economy and Competitiveness MINECO through BCAM Severo Ochoa excellence accreditation SEV-2013-0323 and through project MTM2016-76016-R "MIP" and by the PhD grant "La Caixa 2014".

References

- [1] M. I. Asensio, F. Ferragut, On a wildland fire model with radiation, *International Journal for Numerical Methods in Engineering*, vol. 54(1), pp. 137–157, 2002.
- [2] I. Kaur, A. Mentrelli, F. Bosseur, J.-B. Filippi, and G. Pagnini, Turbulence and fire-spotting effects into wild-land fire simulators, *Communications in Nonlinear Science and Numerical Simulation*, vol. 39, pp. 300 – 320, 2016.
- [3] I. Kaur and G. Pagnini, Fire-spotting modelling and parametrisation for wild-land fires, *International Congress on Environmental Modelling and Software*, Paper 55, 2016.
- [4] J. Mandel, J. D. Beezley, J. L. Coen and M. Kim, Data assimilation for wildland fires, *IEEE Control Systems*, vol. 29(3), pp. 47–65, 2009.
- [5] G. Pagnini and A. Mentrelli, Modelling wildland fire propagation by tracking random fronts, *Natural Hazards and Earth System Sciences*, vol. 14, no. 8, pp. 2249–2263, 2014.
- [6] J. A. Sethian and P. Smereka, Level set methods for fluid interfaces, *Annual Review of Fluid Mechanics*, vol. 35, pp. 341–372, 2003.
- [7] M. Sofiev, T. Ermakova, and R. Vankevich, Evaluation of the smoke-injection height from wild-land fires using remote-sensing data, *Atmospheric Chemistry and Physics*, vol. 12, no. 4, pp. 1995–2006, 2012.

Efficient three time level numerical scheme for option pricing Heston-Hull-White model

M. Fakharany^{a,b,*}, R. Company^b and L. Jódar^b

(a) *Department of Mathematics,*

Faculty of Science, Tanta University, Tanta-Egypt.

(b) *Instituto de Matemática Multidisciplinar,*

Universitat Politècnica de València, Camino de Vera s/n, 46022 Valencia, Spain.

November 30, 2017

1 Introduction

In order to construct a reliable mathematical model for commodities\options have a long time to be expired, it is convenient to consider that its interest rate is controlled by a stochastic process. In Heston model, the underlying asset and its variance are controlled by two stochastic differential equations (SDEs). By adding a third stochastic differential equation for the interest rate, the model is called the Heston-Hull-White (HHW) model. Consider a complete probability space (Ω, \mathcal{F}, P) with a time domain $[0, T]$, Ω is the set all inquiry of the stochastic economy between 0 and T . \mathcal{F} is the sigma algebra of distinguishable events at time T and P is the risk-neutral probability measure on \mathcal{F} . Here the option pricing under the probability measure P is constituted by a system of three stochastic differential equations (SDEs) given by [1, 2]

$$\begin{aligned}dS &= rSdt + \sqrt{\nu}SdW_1(t), \\d\nu &= \kappa(\eta - \nu)dt + \sigma_1\sqrt{\nu}dW_2(t), \\dr &= a(b(t) - r)dt + \sigma_2dW_3(t),\end{aligned}\tag{1}$$

*Corresponding author. Email: fakharany@aucegypt.edu

where S , ν and r are the underlying asset, its variance and interest rate. $W_1(t)$, $W_2(t)$ and $W_3(t)$ are standard Brownian motions associated with correlation factors ρ_{12} , ρ_{13} and $\rho_{23} \in (-1, 1)$ such that $dW_i dW_j = \rho_{ij} dt$, $1 \leq i, j \leq 3 \wedge j > i$. The speed of the volatility is denoted by $\kappa > 0$, η is the volatility mean, σ_1 , and σ_2 are the second order volatility and the volatility of the interest rate respectively. The parameter $a > 0$ determines the speed of mean reversion of the interest rate process and $b(t)$ represents the structure of the interest rate. Based on the non-arbitrage assumptions, the European option under HHW-model is given by [1]-[3]

$$\begin{aligned} \frac{\partial u}{\partial \tau} = & \frac{1}{2} \nu S^2 \frac{\partial^2 u}{\partial S^2} + \frac{\sigma_1^2}{2} \nu \frac{\partial^2 u}{\partial \nu^2} + \frac{\sigma_2^2}{2} \frac{\partial^2 u}{\partial r^2} + \rho_{12} \sigma_1 S \nu \frac{\partial^2 u}{\partial S \partial \nu} + \rho_{13} \sigma_2 S \sqrt{\nu} \frac{\partial^2 u}{\partial S \partial r} \\ & + \rho_{23} \sigma_1 \sigma_2 \sqrt{\nu} \frac{\partial^2 u}{\partial \nu \partial r} + r S \frac{\partial u}{\partial S} + \kappa (\eta - \nu) \frac{\partial u}{\partial \nu} + a(b(T - \tau) - r) \frac{\partial u}{\partial r} - r u, \end{aligned} \quad (2)$$

where $\tau = T - t$, $S, \nu > 0$, $r \in \mathbb{R}$, associated with the boundary conditions:

$$\begin{aligned} u(0, \nu, r, \tau) = 0, \quad \lim_{S \rightarrow \infty} \frac{\partial u}{\partial S} = 1, \quad \frac{\partial u}{\partial r}(S, \nu, r_{\min}, \tau) = 0, \\ \frac{\partial u}{\partial r}(S, \nu, r_{\max}, \tau) = 0, \quad \lim_{\nu \rightarrow \infty} u(S, \nu, r, \tau) = S, \\ \frac{\partial u}{\partial \tau} = \frac{\sigma_2^2}{2} \frac{\partial^2 u}{\partial r^2} + r S \frac{\partial u}{\partial S} + \kappa \eta \frac{\partial u}{\partial \nu} + a(b(T - \tau) - r) \frac{\partial u}{\partial r} - r u, \quad \nu = 0. \end{aligned} \quad (3)$$

Initial condition for European call option is given by the payoff

$$u(S, \nu, r, 0) = \max\{0, S - E\}, \quad (4)$$

where E is the strike price.

2 Problem Transformation

We start this section by applying a suitable mathematical transformation on (2) in order to reduce the number of the mixed derivatives. Consider the new variables (x, y, z) such that

$$x = \sigma_1 \ln S, \quad y = \nu - \rho_{12} \sigma_1 \ln S, \quad z = r - \frac{2\sigma_2(\rho_{23} - \rho_{12}\rho_{13})}{\sigma_1 \tilde{\rho}_{12}^2} \sqrt{\nu}. \quad (5)$$

The new PDE based on the transformation (5) becomes

$$\begin{aligned} \frac{\partial u}{\partial \tau} = & \alpha(x, y) \left(\frac{\partial^2 u}{\partial x^2} + \tilde{\rho}_{12}^2 \frac{\partial^2 u}{\partial y^2} \right) + \hat{\rho} \frac{\partial^2 u}{\partial z^2} + \beta(x, y) \frac{\partial^2 u}{\partial x \partial z} + \gamma(x, y, z) \frac{\partial u}{\partial x} \\ & - \tilde{\gamma}(x, y, z) \frac{\partial u}{\partial y} + \hat{\gamma}(x, y, z, \tau) \frac{\partial u}{\partial z} - \check{\gamma}(x, y, z) u, \end{aligned} \quad (6)$$

where

$$\begin{aligned}
 \alpha(x, y) &= \frac{\sigma_1^2}{2}(y + \rho_{12}x), \\
 \hat{\rho} &= \frac{1}{2} \left(\frac{\sigma_2}{\hat{\rho}_{12}^2} \right)^2 \left((\rho_{12}^2 - \tilde{\rho}_{12}^2)\rho_{23}^2 - 2\rho_{13}\rho_{12}^3\rho_{23} + (\rho_{12}\rho_{13})^2 + \tilde{\rho}_{12}^4 \right), \\
 \beta(x, y) &= \frac{\sigma_1\sigma_2(\rho_{13}-\rho_{12}\rho_{23})}{\hat{\rho}_{12}^2} \sqrt{y + \rho_{12}x}, \\
 \gamma(x, y, z) &= \sigma_1 \left(z + \frac{2\sigma_2(\rho_{23}-\rho_{12}\rho_{13})}{\sigma_1\hat{\rho}_{12}^2} \sqrt{y + \rho_{12}x} - \frac{1}{2}(y + \rho_{12}x) \right), \\
 \tilde{\gamma}(x, y, z) &= \rho_{12}\gamma(x, y, z) + \kappa((y + \rho_{12}x) - \eta), \\
 \hat{\gamma}(x, y, z, \tau) &= a(b(T - \tau) - z + \frac{2\sigma_2(\rho_{23}-\rho_{12}\rho_{13})}{\sigma_1\hat{\rho}_{12}^2} \sqrt{y + \rho_{12}x}) + \frac{\hat{\rho}_1}{\sqrt{y+\rho_{12}x}} - \hat{\rho}_2\sqrt{y + \rho_{12}x}, \\
 \hat{\rho}_1 &= \frac{\sigma_2(\rho_{13}\rho_{12}-\rho_{23})(4\kappa\eta-\sigma_1^2)}{4\sigma_1\hat{\rho}_{12}^2}, \\
 \hat{\rho}_2 &= \frac{\kappa\sigma_2}{\hat{\rho}_{12}^2\sigma_1}(\rho_{12}\rho_{13} - \rho_{23}), \\
 \check{\gamma}(x, y, z) &= z + \frac{2\sigma_2(\rho_{23}-\rho_{12}\rho_{13})}{\sigma_1\hat{\rho}_{12}^2} \sqrt{y + \rho_{12}x}.
 \end{aligned} \tag{7}$$

The boundary conditions and payoff under the transformation are given by

$$\begin{aligned}
 \lim_{x \rightarrow -\infty} u(x, y, z, \tau) &= 0, \quad \sigma_1 \lim_{x \rightarrow \infty} \left(\frac{\partial u}{\partial x} - \rho_{12} \frac{\partial u}{\partial y} \right) = e^{\frac{x}{\sigma_1}}, \\
 \frac{\partial u}{\partial z} \Big|_{z_{\min}} &= 0, \quad \frac{\partial u}{\partial z} \Big|_{z_{\max}} = 0, \quad \lim_{y+\rho_{12}x \rightarrow \infty} u(x, y, z, \tau) = e^{\frac{x}{\sigma_1}}, \\
 \frac{\partial u}{\partial \tau} &= \left(2\sigma_1 z - \frac{\kappa\eta}{\rho_{12}} \right) \frac{\partial u}{\partial x}, \quad y = -\rho_{12}x, \\
 u(x, y, z, 0) &= \max\{0, e^{\frac{x}{\sigma_1}} - E\}.
 \end{aligned} \tag{8}$$

Note that under the transformation (5), two mixed derivative are eliminated, consequently, removing eight points stencil from the corresponding finite scheme.

3 The finite difference scheme Construction

The time domain is discretized by the mesh points $\tau_n = n\Delta\tau$, $0 \leq n \leq N_\tau$, and the spatial variables x , y and z are divided by the nodes $x_i = x_0 + i\Delta x$, $y_j = y_0 + j\Delta y$, $z_k = z_0 + k\Delta z$, $0 \leq i \leq N_x$, $0 \leq j \leq N_y$ and $0 \leq k \leq N_z$. The first partial derivative of the option with respect to time is discretized using the three time-level approximation [4], while first and second order spacial derivatives are discretized using implicit central approximations. Let $u(x_i, y_j, z_k, \tau_n) \approx U_{i,j,k}^n$ consequently, the corresponding

finite difference scheme is discretized by

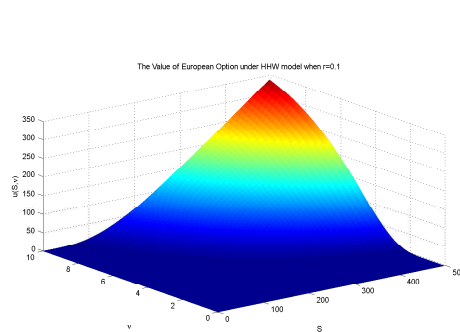
$$\begin{aligned} & \hat{a}_{ijk}(1)U_{i,j,k}^{n+1} + \hat{a}_{ijk}(2)U_{i+1,j,k}^{n+1} + \hat{a}_{ijk}(3)U_{i-1,j,k}^{n+1} + \hat{a}_{ijk}(4)U_{i,j+1,k}^{n+1} + \hat{a}_{ijk}(5)U_{i,j-1,k}^{n+1} \\ & + \hat{a}_{ij}(6) \left(U_{i+1,j,k+1}^{n+1} - U_{i+1,j,k-1}^{n+1} - U_{i-1,j,k+1}^{n+1} + U_{i-1,j,k-1}^{n+1} \right) + \hat{a}_{ijk}^n(7)U_{i,j,k+1}^{n+1} \\ & + \hat{a}_{ijk}^n(8)U_{i,j+1,k-1}^{n+1} = U_{i,j,k}^n - \frac{1}{4}U_{i,j,k}^{n-1}, \end{aligned} \tag{9}$$

where $\hat{a}_{ijk}(l)$, $l = 1, 2, \dots, 5$, $\hat{a}_{ij}(6)$, $\hat{a}_{ijk}^n(7)$ and $\hat{a}_{ijk}^n(8)$ are the discretization coefficients. The derivatives at the boundaries are discretized using the central approximations and the points outside the computational domain are eliminated by solving their equations with the scheme (9) at the same points, in order to obtain a finite difference scheme with a truncation error of the second order of the spatial variables and time stepsizes.

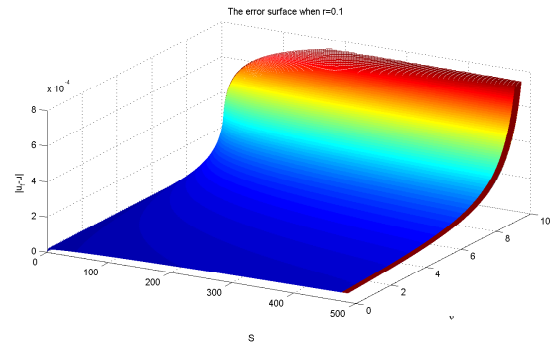
4 Numerical Example

In this section, we provide an example for the associated error of the proposed finite difference scheme (9) using MatLab.

Example 1. Consider an European call option problem (2)-(4) under HHW-model with parameters $T = 1$, $E = 100$, $S_{\max} = 14E$, $\nu_{\max} = 10$, $r_{\min} = -1$, $r_{\max} = 1$, $\sigma_1 = 0.04$, $\sigma_2 = 0.03$, $\kappa = 3$, $\eta = 0.12$, $a = 0.2$, $b(t) = 0.05 - 0.01e^{-t}$, $\rho_{12} = 0.6$, $\rho_{13} = 0.2$, $\rho_{23} = 0.4$. Consequently, $x \in [-3, 3]$, $y \in [-2, 12]$ and $z \in [-1.2, 1]$, the number of mesh points are chosen such that $N_x = 20$, $N_y = 50$, $N_z = 10$ and $N_\tau = 40$. The value of the option is calculated at a finer grid (100, 200, 100, 100) and (20, 50, 10, 40), after that we obtain the absolute difference as a function in (S, ν, r) at the expiration time. Figure (1.a) shows the option value as a function of (S, ν) and Figure (1.b) reveals the associated absolute error.



(1.a) The option price u as a function of S and v .



(1.b) The Error surface when $r = 0.1$

References

- [1] T. Haentjens and K. J. in't Hout, *ADI finite difference schemes for the Heston-Hull-White PDE*, Cornell University Library arXiv:1111.4087 [q-fin.CP] 17 Nov 2011.
- [2] L. A. Grzelak and C. W. Oosterlee, *On the Heston Model with Stochastic Interest Rates*, SIAM Journal on Financial Mathematics, 2(1) (2011), pp. 255–286.
- [3] S. Guo, L. A. Grzelak and C. W. Oosterlee, *Analysis of an affine version of the Heston-Hull-White option pricing partial differential equation*, Applied Numerical Mathematics, 72 (2013), pp. 143–159.
- [4] G. D. Smith, *Numerical solution of partial differential equations: Finite difference methods (3rd ed.)*, Clarendon Press, Oxford, UK, 1985.

Modeling eutrophication using the hybrid ABC–SVM–based approach, multilayer perceptron neural network and M5 model tree in the Pozón de la Dolores lake (Northern Spain)

P.J. García Nieto^b *; E. García-Gonzalo^b,
J.R. Alonso Fernández[†], C. Díaz Muñoz[†]

(^b) Department of Mathematics, University of Oviedo,
Faculty of Sciences, C/ Calvo Sotelo s/n, 33007 Oviedo, Spain.

([†]) Cantabrian Basin Authority, Spanish Ministry of Agriculture, Food and Environment,
Plaza de España 2, 33007 Oviedo, Spain.

November 30, 2017

1 Introduction

The aim of this study was to obtain a predictive model able to perform an early detection of the eutrophication in water bodies such as lakes. This study presents a novel hybrid algorithm, based on support vector machines (SVM) approach in combination with the artificial bees colony (ABC) technique, for predicting the eutrophication from biological and physical-chemical input parameters determined experimentally through samplings in the Pozón de la Dolores lake and subsequent analysis in a certificate laboratory. This optimization technique involves hyperparameter setting in the SVM training

*e-mail: lato@orion.ciencias.uniovi.es

procedure, which significantly influences the regression accuracy. Additionally, a multilayer perceptron network (MLP) and M5 model tree were fitted to the experimental data with comparison purposes. Indeed, regression with optimal hyperparameters was performed and coefficients of determination equal to 0.90 for the Total phosphorus estimation and 0.92 for the Chlorophyll concentration were obtained when this hybrid ABC–SVM–based model was applied to the experimental dataset, respectively. Furthermore, the results obtained with the MLP approach and M5 model tree are clearly worse. The agreement between experimental data and the model confirmed the good performance of the latter.

Eutrophication is a water enrichment in nutrients (mainly phosphorus) that generally leads to symptomatic changes and deterioration of water quality and all its uses in general, when the production of algae and other aquatic vegetations are increased in water bodies [1]. Additionally, Chlorophyll a (*Chl-a*) is also an important responsive variable closely related to water eutrophication. *Chl-a* is the major photosynthetic pigment of algae and macrophytes and it is usually used as an estimator for algae growth. Therefore, total phosphorus, total nitrogen and *Chl-a*, namely eutrophication indicators, are routinely monitored to identify the trophic status of natural water bodies [2,3]. At the same time, eutrophication is an important environmental problem in lakes (e.g. the Pozón de la Dolores lake (see Fig. 1)).

To fix ideas, the objective of this innovative study is to evaluate the application of support vector machines (SVMs) approach in combination with the evolutionary optimization technique known as Artificial Bee Colony (ABC) as well as the Multilayer Perceptron (MLP) and M5 model tree to identify eutrophication in water bodies (lakes, reservoirs, etc.), comparing the results obtained among the three techniques through its performances [4].

On the other hand, in order to carry out the optimization mechanism corresponding to the kernel optimal hyperparameters setting in the SVM training, the artificial bee colony (ABC) technique was used here with success. The artificial bee colony technique is an optimization algorithm based on the intelligent foraging behavior of honey bee swarms [5].

In summary, hybrid ABC optimized SVM (ABC–SVM) models as well as the MLP model and M5 model tree were used as automated learning tools, training them in order to predict the eutrophication from the biological and physical-chemical input parameters in the Pozón de la Dolores lake. Specifically, the Pozón de la Dolores is a lake located just 5.5 km from the center of the Bay of Santander (see Fig. 1).



Figure 1: Aerial photograph of the Pozón de la Dolores lake and the Bay of Santander (Northern Spain).

2 Materials and methods

2.1 Experimental dataset

The data used for the ABC-SVM, MLP and M5 tree analyses were collected over 9 years (2006–2014) from several samples in Pozón de la Dolores lake. The total number of samples processed was 244. The information is quantitative on the abundance of phytoplankton species. Specifically, this reservoir was sampled several times a month from January 16, 2006 to December 25, 2014, following the sampling protocols for lakes and reservoirs of the *Spanish Ministry of Agriculture, Food and Environment*, which are consistent with the guidelines established by the European Union and international agencies dealing with these issues [2, 6].

The input variables are the quantity of phytoplankton species (*Cyanobacteria*, Diatoms, Euglenophytes, *Dinophlagellata*, Chrysophytes, Chlorophytes and Cryptophytes) and physical-chemical parameters (water temperature, turbidity, nitrate concentration, ammonium ion concentration, dissolved oxygen concentration, conductivity and pH). The output variables are two ecological indicators linked to the algae growth used to evaluate the eutrophication in lakes and reservoirs: Total phosphorus (mg P/L) and Chlorophyll concentration (*Chl-a*) ($\mu\text{g/L}$).

2.2 Computational procedure

2.2.1 Support vector machine (SVM) method

The Support Vector Regression (SVR) uses the same principles as the SVM for classification, with only a few minor differences. In the case of regression, a margin of tolerance, ε , is set in approximation to the SVM. The main idea is always the same: to minimize error, individualizing the hyperplane which maximizes the margin, keeping in mind that part of the error is tolerated. As a consequence, new predictions y' can be formulated as in linear SVR [4, 7]:

$$y' = \sum_{i=1}^L (\alpha_i^+ - \alpha_i^-) \mathbf{x}_i \cdot \mathbf{x}' + b$$

In case of a nonlinear SVR, the kernel functions $k(\mathbf{x}_i, \mathbf{x}_j) = \Phi(\mathbf{x}_i) \cdot \Phi(\mathbf{x}_j)$ transform the data into a higher dimensional feature space to make it possible to perform the linear separation [4, 7]:

$$y' = \sum_{i=1}^L (\alpha_i^+ - \alpha_i^-) k(\mathbf{x}_i, \mathbf{x}') + b$$

2.2.2 The artificial bee colony (ABC) algorithm

In the ABC optimization technique, the colony consists of three groups of bees [5] employed bees, onlookers and scouts. It is assumed that there is only one artificial employed bee for each food source. Employed bees go to their food source and come back to hive and dance on this area. The employed bee whose food source has been abandoned becomes a scout and starts to search for finding a new food source. Onlookers watch the dances of employed bees and choose food sources depending on dances.

2.3 Multilayer perceptron (MLP) neural network

The multilayer perceptron (MLP) is a kind of artificial neural networks (ANNs) that consists of an input layer and an output layer and one or more hidden layers of nonlinearly-activating nodes [8]. An MLP is a feedforward artificial neural network model that maps input data onto a set of appropriate output. It is a modification of the standard linear perceptron in that it uses three or more layers of neurons (nodes) with nonlinear activation functions.

2.4 M5 model tree

M5 Model Tree (M5Tree), first introduced by Quinlan [9], is based on a binary decision tree. It has linear regression functions at the terminal (leaf) nodes, which develops a relationship between input and output variables. Unlike decision tree, it can also be used for quantitative data [10].

3 Analysis of results and discussion

The biological and physical-chemical input variables considered in this research work were indicated above in subsection 2.1 [2,3]. The total number of predicting variables used to build the hybrid ABC–SVM–based model, MLP approach and M5 model tree was 14. The output predicted variables (Total phosphorus and *Chl-a*) are measured in mg P/L and $\mu\text{g/L}$ [2, 3], respectively.

In this study, we have built three different models (specifically, the ABC–SVM–based model, the MLP approach and M5 model tree) taking as dependent variables Total phosphorus and *Chl-a*, respectively. Indeed, in order to estimate the Total phosphorus and *Chl-a* from other biological and physical-chemical parameters, it is important to select the model that best fits the experimental data. In this sense, we have chosen ABC optimization technique as a suitable, efficient and simple method [5] for tuning the SVR. Fig. 2 shows the flowchart of this new hybrid ABC–SVM–based model developed in this study.

Finally, this research work was able to predict the Total phosphorus in agreement to the actual experimental values observed using the ABC–RBF–SVM–based model with great accurateness and success. Indeed, Fig. 3 shows the comparison between the Total phosphorus values observed and predicted by using the M5 tree model (see Fig. 3(a)), MLP model (see Fig. 3(b)), and ABC–SVM–based model with RBF kernel (see Fig. 3(c)). It is necessary the use of a SVM model with an ABC–based optimization technique in order to achieve the best effective approach to nonlinearities present in this regression problem. Obviously, these results coincide again with the outcome criterion of goodness-of-fit (R^2) so that the ABC–RBF–SVM–based model has been the best fitting. [2,3]

Similarly, Fig. 4 shows the comparison between the Chlorophyll concentration values observed and predicted by using the M5 tree model, MLP

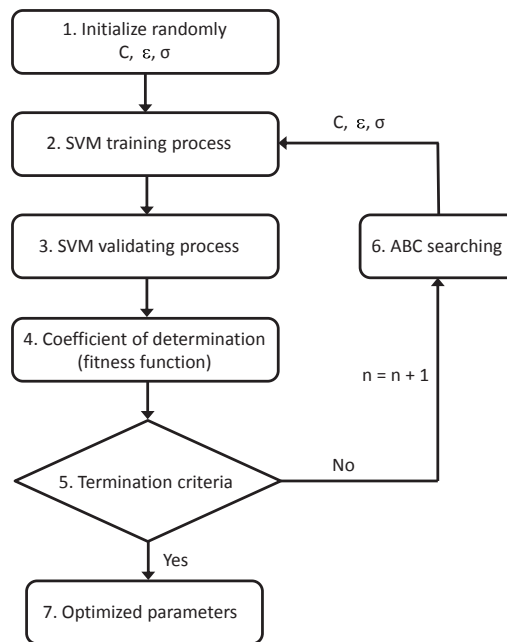


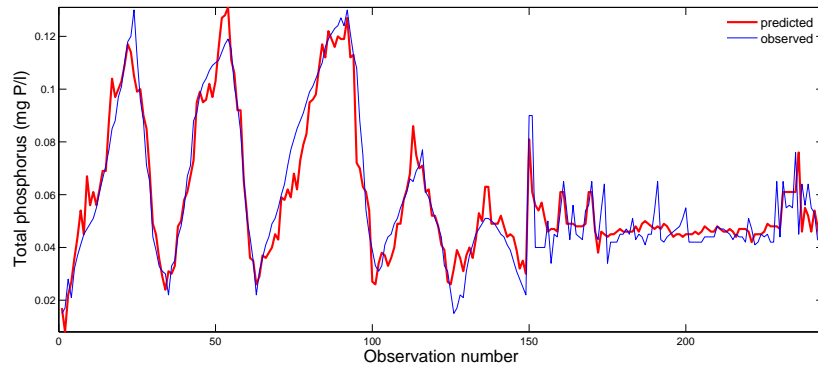
Figure 2: Flowchart of the new hybrid ABC-SVM-based model.

approach and ABC-RBF-SVM-based model. Again, it has been necessary the use of a SVM model with a ABC-based optimization technique in order to achieve the best effective approach to the eutrophication in water bodies such as the Pozón de la Dolores lake.

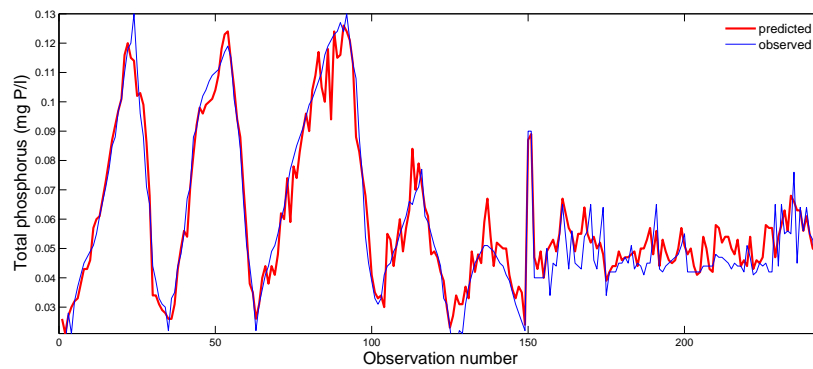
4 Conclusions

Based on the experimental and numerical results, the main findings of this research work can be summarized as follows:

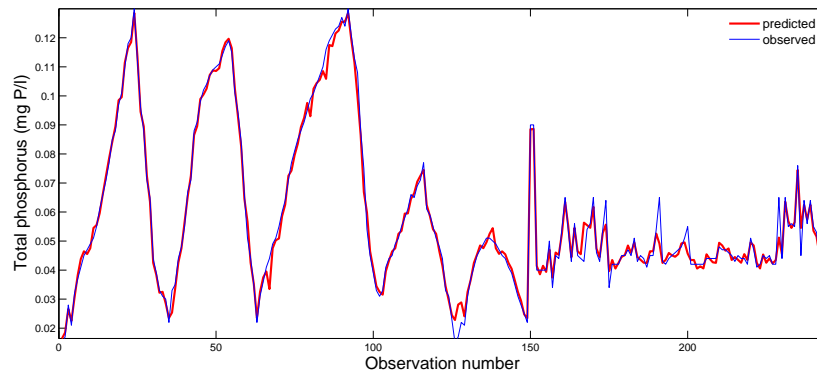
- Firstly, eutrophication is a very common and serious problem in water bodies such as lakes, reservoirs and so on. The diagnostic techniques commonly used based on the traditional methods (such as the assessment of eutrophication in lakes and reservoirs through the periodic sampling and subsequent analysis in an accredited laboratory) are expensive from both the material and human points of view. Consequently, the development of alternative diagnostic techniques is necessary. In this sense, the new hybrid ABC-RBF-SVM-based method



(a)

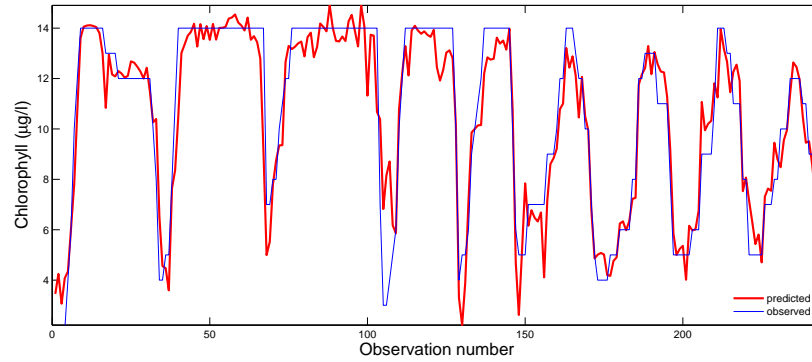


(b)

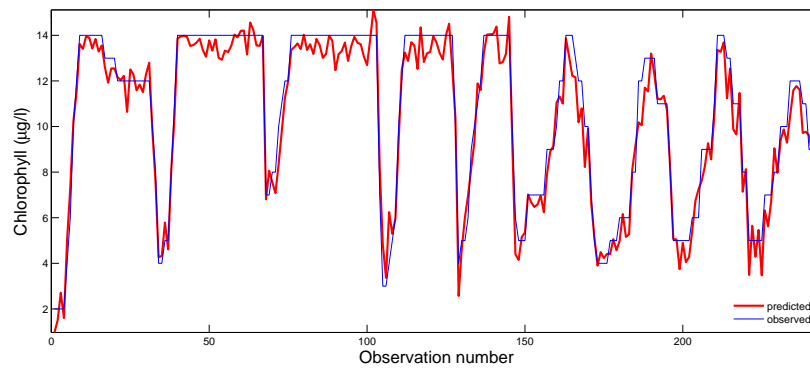


(c)

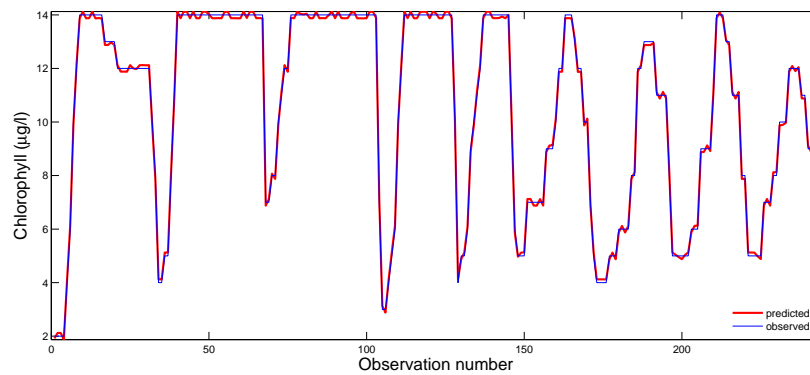
Figure 3: Comparison between the Total phosphorus values observed and predicted by using the M5 tree model, MLP approach and ABC-RBF-SVM-based model: (a) M5 tree model ($R^2 = 0.84$); MLP network ($R^2 = 0.84$); and RBF-SVM model ($R^2 = 0.90$).



(a)



(b)



(c)

Figure 4: Comparison between the Chlorophyll concentration values observed and predicted by using the M5 tree model, MLP approach and ABC-RBF-SVM-based model: (a) M5 tree model ($R^2 = 0.83$); (b) MLP network ($R^2 = 0.83$); and (c) RBF-SVM model ($R^2 = 0.92$).

used in this work is a good choice to evaluate the eutrophication in the Pozón de la Dolores lake.

- Secondly, a high coefficient of determination equal to 0.90 was obtained when this hybrid ABC–RBF–SVM–based model was applied to the experimental dataset corresponding to the Total phosphorus (see Fig. 3). Similarly, a high coefficient of determination equal to 0.92 was obtained when this new hybrid ABC–RBF–SVM–based model was applied to the experimental dataset corresponding to Chlorophyll concentration (see Fig. 4).
- Thirdly, the significance order of the input variables involved in the prediction of the eutrophication was set. Specifically, the physical-chemical input variable Water temperature could be considered the most influential parameter in the prediction of the Total phosphorus, while the *Euglenophytes* concentration is for the Chlorophyll concentration. In this regard, it is also important to highlight the influential role of the Turbidity and *Dinophlagellata* concentration in the dependent variables Total phosphorus and Chlorophyll concentration, respectively.
- Finally, this innovative methodology could be applied to other eutrophication processes with similar or different sources of pollutants for water with success, but it is always necessary to take into account the specificities of each location.

Acknowledgements

Authors wish to acknowledge the pollutant data in the Pozón de la Dolores lake of Santander (Northern Spain) supplied by the Cantabrian Basin Authority (Spanish Ministry of Agriculture, Food and Environment).

References

- [1] R.D. Grundy, Strategies for control of man-made eutrophication, *Environ. Sci. Tech.* 5 (1971) 1184–1190.
- [2] C.S. Reynolds, *Ecology of Phytoplankton*, Cambridge University Press, New York, 2006.

- [3] C. Brönmark, L.-A. Hansson, *The Biology of Lakes and Ponds*, Oxford University Press, New York, 2005.
- [4] T. Hastie, R. Tibshirani, J. Friedman, *The Elements of Statistical Learning*, Springer-Verlag, New York, 2003.
- [5] D. Karaboga, B. Basturk, A powerful and efficient algorithm for numerical function optimization: artificial bee colony (ABC) algorithm, *J. Global Optim.* 39 (3) (2007) 459–171.
- [6] Directive 2000/60/EC of the European Parliament and of the Council of 23 October 2000, Establishing a framework for community action in the field of water policy, L-327, Luxembourg, 2000.
- [7] I. Steinwart, A. Christmann, *Support Vector Machines*, Springer, New York, 2008.
- [8] S. Haykin, *Neural Networks. A comprehensive foundation*, Prentice Hall, New York, 1999.
- [9] J.R. Quinlan, Learning with continuous classes, in: *Proceedings of Australian Joint Conference on Artificial Intelligence*, World Scientific Press, Singapore, 1992, pp. 343–348.
- [10] M. Pal, S. Deswal, M5 model tree based modelling of reference evapotranspiration, *Hydrol. Process.* 23 (10) (2009) 1437–1443.

Efficient class of iterative schemes with memory for solving nonlinear problems*

Alicia Cordero,[†] Neus Garrido,[‡] Esther Gómez,[§]
and Juan R. Torregrosa,[¶]

Instituto de Matemáticas Multidisciplinar,
Universitat Politècnica de València, Camino de Vera, s/n, 46022-Valencia, Spain
Facultat de Ciències Matemàtiques, Universitat de València

November 30, 2017

1 Introduction

Finding the solution α of a nonlinear equation $f(x) = 0$, where $f : I \subset \mathbb{R} \rightarrow \mathbb{R}$ is a scalar function in an open interval I , has been for many decades an important task in different fields of science and technology. This nonlinear problem is widely solved using iterative methods. The best-known iterative scheme is Newton's method,

$$x_{k+1} = x_k - \frac{f(x_k)}{f'(x_k)}, \quad k \geq 0,$$

which has quadratic convergence and is characterized by its simplicity and economy of operations and functional evaluations.

*This research was partially supported by Ministerio de Economía y Competitividad MTM2014-52016-C2-2-P and Generalitat Valenciana PROMETEO/2016/089

[†]e-mail: acordero@mat.upv.es

[‡]e-mail: neusgasa@alumni.uv.es

[§]e-mail: estgo@alumni.uv.es

[¶]e-mail: jrtorre@mat.upv.es

In the last years, many multi-step methods have been proposed to improve the order of convergence of Newton's scheme and its computational efficiency; see for example [2–5] and the references therein. As an example, we consider third-order Traub's scheme [1] which is the starting point of the present work. Its iterative expression is

$$\begin{aligned} y_k &= x_k - \frac{f(x_k)}{f'(x_k)}, \\ x_{k+1} &= y_k - \frac{f(y_k)}{f'(x_k)}, \quad k \geq 0. \end{aligned} \tag{1}$$

Recently, several multi-step iterative methods with memory have been developed. This kind of iterative methods uses information from the current and previous iterations and can increase the convergence order and the computational efficiency of methods without memory with the same number of functional evaluations. For a background study regarding the acceleration of convergence order via with memorization, one should see e.g. [6, 7].

Our aim in this work is to introduce some accelerating parameters in (1) (and in its derivative-free version) such that the new scheme allows us to accelerate the order of convergence without new functional evaluations per iteration. Finally, numerical tests are shown to confirm the theoretical results and to compare the convergence orders.

2 Traub type methods with or without derivatives

First of all, we add two accelerator parameters in Traub's method and we obtain the following family of iterative schemes:

$$\begin{aligned} y_k &= x_k - \frac{f(x_k)}{f'(x_k) + \delta_1 f(x_k)}, \\ x_{k+1} &= y_k - \frac{f(y_k)}{f'(x_k) + \delta_2 f(x_k)}, \quad k \geq 0. \end{aligned} \tag{2}$$

The order of convergence of this family is analyzed below.

Theorem 2.1 *Let $f : I \subset \mathbb{R} \rightarrow \mathbb{R}$ be a real function sufficiently differentiable in an open interval I . If $\alpha \in I$ is a simple root of $f(x) = 0$ and x_0 is*

close enough to α , then the iterative method (2) has convergence order 3, for any values of parameters δ_1 and δ_2 , being its error equation

$$e_{k+1} = (\delta_1 + c_2)(\delta_2 + 2c_2)e_k^3 + \mathcal{O}(e_k^4), \quad (3)$$

where $e_k = x_k - \alpha$ and $c_j = \frac{f^{(j)}(\alpha)}{j!f'(\alpha)}$, $j \geq 2$.

Now, we analyze how to improve the convergence order of the family by analyzing its error equation. Of course, if $\delta_1 = -c_2 = \frac{f''(\alpha)}{2f'(\alpha)}$ or $\delta_2 = -2c_2$ the order of convergence increase, at least, in one unit, but α is not known. So, we need to approximate $f'(\alpha)$ and $f''(\alpha)$ transforming the iterative schemes in other ones with memory. For this purpose, we use the Newton's polynomial interpolation of second degree in points x_k, x_{k-1} and y_{k-1} , $N_2(t; x_k, x_{k-1}, y_{k-1}) = N_2(t)$, which is defined by:

$$N_2(t) = f(x_k) + f[x_k, x_{k-1}](t - x_k) + f[x_k, x_{k-1}, y_{k-1}](t - x_k)(t - x_{k-1}).$$

If we set the approximations

$$f'(\alpha) \approx N_2'(x_k), \quad f''(\alpha) \approx N_2''(x_k),$$

we will have the following accelerator parameters:

$$\delta_{1,k} \approx -\frac{1}{2} \frac{N_2''(x_k)}{N_2'(x_k)}, \quad \delta_{2,k} \approx -\frac{N_2''(x_k)}{N_2'(x_k)}. \quad (4)$$

Then, we can observe that the using of the previous parameters originates a method with memory. In addition, the next result shows how much the order of convergence has increased with respect to the method without memory.

Theorem 2.2 *Let $f : I \subset \mathbb{R} \rightarrow \mathbb{R}$ be a real function sufficiently differentiable in an open interval I . If $\alpha \in I$ is a simple root of $f(x) = 0$ and x_0 is close enough to α , then the iterative method (2) with the values $\delta_{1,k}$ and $\delta_{2,k}$ defined by (4) converges to α with order of convergence $p \approx 4.65$.*

Now, we carry out a study similar to the previous one but using the derivative-free version of Traub's method. First, we transform the iterative

scheme (2) in a derivative-free one by replacing $f'(x_k)$ with a divided difference of first order. So, let us consider the family of iterative methods

$$\begin{aligned} w_k^1 &= x_k + \rho_1 f(x_k), \\ y_k &= x_k - \frac{f(x_k)}{f[x_k, w_k^1]}, \\ w_k^2 &= x_k + \rho_2 f(x_k), \\ x_{k+1} &= y_k - \frac{f(y_k)}{f[x_k, w_k^2]}, \quad k \geq 0. \end{aligned} \tag{5}$$

In the following result we describe that the methods of this family have the same convergence order. Furthermore, their error equation has an interesting structure.

Theorem 2.3 *Let $f : I \subset \mathbb{R} \rightarrow \mathbb{R}$ be a real function sufficiently differentiable in an open interval I . If $\alpha \in I$ is a simple root of $f(x) = 0$ and x_0 is close enough to α , then the iterative methods (5) converge to α with order of convergence 3, for any value of parameters ρ_1 and ρ_2 , being its error equation*

$$e_{k+1} = (1 + f'(\alpha)\rho_1)(2 + f'(\alpha)\rho_2)c_2^2 e_k^3 + \mathcal{O}(e_k^4), \tag{6}$$

where $e_k = x_k - \alpha$ and $c_j = \frac{f^{(j)}(\alpha)}{j!f'(\alpha)}$, $j \geq 2$.

In a similar way as before, for improving the convergence order of (5) we use the Newton's polynomial interpolation of second degree, $N_2(t)$, in the same points as before but using the following approximations:

$$\rho_{1,k} \approx -\frac{1}{N_2'(x_k)}, \quad \rho_{2,k} \approx -\frac{2}{N_2'(x_k)}. \tag{7}$$

Therefore, with the incorporation of the parameters (7) in the iterative scheme (5), we have again a method with memory whose order of convergence is analyzed below.

Theorem 2.4 *Let $f : I \subset \mathbb{R} \rightarrow \mathbb{R}$ be a real function sufficiently differentiable in an open interval I . If $\alpha \in I$ is a simple root of $f(x) = 0$ and x_0 is close enough to α , then the iterative method (5) with the accelerator parameters (7) converges to α with order of convergence $p \approx 4.64$.*

It can be observed that the use of methods with memory is decisive for increasing the order of convergence in both cases. Moreover, the "memorizing" process that has been made in this work allows us to rise the convergence order more than a unit with no additional functional evaluations, which is really interesting from the point of view of the computational efficiency.

In the following section we carry out a comparison between the iterative schemes (2) and (5) and the different approximations for their accelerator parameters by using some numerical examples.

3 Numerical results

In this section, we have tested Method 1, (2), and Method 2, (5), by using the approximations for the accelerator parameters given by (4) and (7), respectively. Our main goal is to compare the computational efficiency between the methods studied during this work. In order to get this aim, let us consider the following test functions:

- $f_1(x) = \sin(x) - \frac{x}{2}$.
- $f_2(x) = \ln(x^2 + x + 2) - x + 1$.
- $f_3(x) = x^2 + \sin(\frac{x}{5}) - \frac{1}{4}$.
- $f_4(x) = e^{-x^2+x+2} - x$.

Numerical computations have been carried out using variable precision arithmetic with Matlab R2016b with 2000 significant digits.

Table 1 shows, for each test function and some initial estimations, the number of iterations required to obtain $|x_{k+1} - x_k| < 10^{-200}$ or $|f(x_{k+1})| < 10^{-200}$, and the approximated computational order of convergence, ACOC, introduced in [4]:

$$p \approx ACOC = \frac{\ln |(x_{k+1} - x_k)/(x_k - x_{k-1})|}{\ln |(x_k - x_{k-1})/(x_{k-1} - x_{k-2})|}.$$

As we can observe, numerical results only agree with the theoretic convergence order for the Method 2. On the other hand, the values of the ACOC obtained for Method 1 is due to the divided differences used for the approximations in the accelerator parameters, which are quite unstable. However, in the first iterations of Method 1 these values are in concordance with the theory developed before.

	iterations	ACOC	$ x_{k+1} - x_k $	$ f(x_{k+1}) $
$f_1, x_0 = 2$				
Method 1	5	3.58	5.419e-178	2.386e-633
Method 2	4	4.64	9.576e-81	2.501e-374
$f_2, x_0 = 4$				
Method 1	4	3.496	2.153e-70	7.305e-252
Method 2	4	4.503	4.625e-129	3.247e-602
$f_3, x_0 = 0.5$				
Method 1	4	3.502	3.845e-56	1.003e-201
Method 2	4	4.961	9.009e-74	5.98e-343
$f_4, x_0 = 2$				
Method 1	5	3.61	9.903e-112	3.057e-396
Method 2	4	4.743	4.858e-45	3.911e-207

Table 1: Comparison between Method 1 and Method 2

References

- [1] J.F. Traub, Iterative Methods for the Solution of Equations. New York, Chelsea Publishing Company, 1982.
- [2] A. Cordero, J.G. Maimó, J.R. Torregrosa, M.P. Vassileva, Solving non-linear problems by Ostrowski-Chun type parametric families, *Math. Chemistry*, 53: 430–449, 2015.
- [3] S. Amat, S. Busquier, C. Bermúdez, S. Plaza, On two families of high order Newton type methods, *Appl. Math. Lett.*, 25: 2209–2217, 2012.
- [4] A. Cordero, J.R. Torregrosa, Variants of Newton’s method using fifth-order quadrature formulas, *Appl. Math. Comput.*, 190: 686–698, 2007.
- [5] S. Weerakoon, T.G.I. Fernando, A variant of Newton’s method with accelerated third-order convergence, *Appl. Math. Lett.*, 13 (8): 87–93, 2000.

- [6] M.S. Petković, B. Neta, L.D. Petković, J. Džunić, *Multipoint Methods for Solving Nonlinear Equations*, Amsterdam, Academic Press, 2013.
- [7] M.S. Petković, B. Neta, L.D. Petković, J. Džunić, Multipoint methods for solving nonlinear equations: a survey, *Appl. Math. Comput.*, 226: 635–660, 2014.

A methodology for the detection of rail irregularities and defects based on the vehicle dynamic response

Beatriz Baydal Giner^{1}, Miriam Labrado Palomo², Claudio Masanet Sendra³, Clara Zamorano Martín⁴*

*^{1, 2, 3} Institute of Multidisciplinary Mathematics, Polytechnic University of Valencia, Camino de Vera,
46022 Valencia, Spain*

⁴ Universidad Politécnica de Madrid. Calle Ramiro de Maeztu, 7, 28040 Madrid

**Corresponding author. E-mail: beabaygi@cam.upv.es. Telephone: +34 96 387 70 00*

1. Introduction

The intense development of high speed railways in the recent years, together with a constant increase of passenger comfort standards have led to a considerable rise in quality requirements for the railway infrastructure. In this regard, if the rails are not perfectly aligned and smooth, such irregularities will induce extra vehicle oscillations and an increase of dynamic loads. In consequence, passenger comfort might be threatened and maintenance costs of both track structure and rolling stock may significantly rise [1, 2].

The measurement of rail irregularities has been traditionally done manually by maintenance workers; and more recently with the help of special machinery (*e.g.*, inspection cars and multiple tampering machines), which implies high maintenance costs [3]. Therefore, an intense research has been carried out over the past decade in order to develop different techniques for an indirect detection of rail defects, where the dynamic response of the running vehicle is used instead of a direct measurement on the rail [4]. In this sense, this paper presents a methodology for the assessment of rail defects and irregularities based on acceleration registers measured on the vehicle.

2. Description of the method

This section presents in detail, the methodology followed for the indirect assessment of rail defects and irregularities, which can be divided in two phases: i) data acquisition; and ii) data processing. In this regard, the time history of accelerations is registered on the vehicle body by means of tri-axial accelerometers; while its position on the track is constantly recorded with a GPS. Then, the measurements are processed and transformed into 3D rail geometry data along the railway line, according to the algorithm described below and presented in Fig. 1.

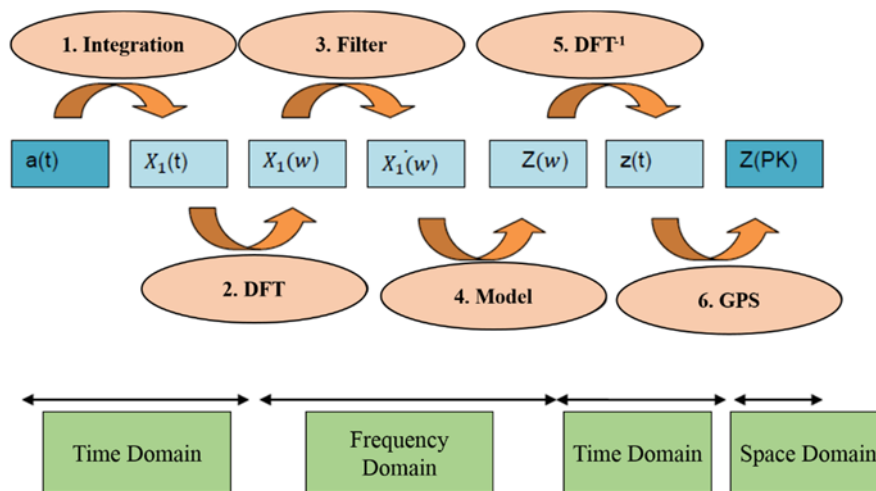


Fig. 1. Scheme of the data processing algorithm

First, the recorded time history of accelerations is double-integrated over time through eq.(1) in order to obtain the time history of vehicle displacements.

$$x(t) = x_0 + v_0 \cdot t + \int \int_0^t a(t) \cdot dt \cdot dt \quad (1)$$

Where $x(t)$ and $v(t)$ are the displacement and acceleration time histories, respectively; and x_0 , v_0 are the initial values of vehicle displacements and velocities. Once the vehicle displacements have been calculated in the time domain, they shall be transformed into the

frequency domain in order to allow a subsequent filtering of the data. This process is carried out by means of the Fourier transform in a discrete form (DFT, eq.(2)).

$$x(\omega) = \sum_{r=1}^n x(t) \cdot e^{\frac{2\pi i(r-1)(s-1)}{n}} \quad (2)$$

Where coefficients r and s vary from 1 to n ; and n is the total number of points in the data series. A high-pass filtering of the signal is then performed with the aim of removing low frequencies (*i.e.*, long wavelength components), since they do not correspond to rail irregularities or alignment defects, but to track geometry regular variations, such as cant and slope changes.

The fourth step of the algorithm deals with the vehicle-track interaction. In this phase, the displacements on the wheel-rail interface are calculated by solving the system of differential equations provided by the two-masses model of the vehicle - eq. (3) -. The model explicitly accounts for the effect of the unsprung mass (*i.e.*, wheelset) and a combination of sprung (*i.e.*, car body) and semi-sprung (*i.e.*, bogie) masses.

$$\begin{aligned} m_2 \ddot{x}_2 + c_2 (\dot{x}_2 - \dot{x}_1) + k_2 (x_2 - x_1) &= 0 \\ m_1 \ddot{x}_1 - c_2 \dot{x}_2 + c_2 \dot{x}_1 - k_2 x_2 + (k_1 + k_2) x_1 - k_1 z &= 0 \end{aligned} \quad (3)$$

Where m_1 is the unsprung mass; m_2 is the combination of sprung and semi-sprung masses; k_1 is the track stiffness; and k_2, c_2 are the stiffness and damping coefficients of the primary suspension, respectively. The recorded data have been transformed in the previous step into the frequency domain for filtering; and thus, eq.(3) is transformed into eq.(4) by means of the Fourier transform properties [5] and solved in such domain.

$$\begin{aligned} -m_2 \omega^2 X_2 + ic_2 \omega (X_2 - X_1) + k_2 (X_2 - X_1) &= 0 \\ -m_1 \omega^2 X_1 - ic_2 \omega X_2 + ic_2 \omega X_1 - k_2 X_2 + (k_1 + k_2) X_1 - k_1 Z &= 0 \end{aligned} \quad (4)$$

Once the rail geometry is known in the frequency domain, the results shall be transformed back to the time domain, which is performed by means of the inverse discrete Fourier transform shown in eq. (5).

$$z(t) = \frac{1}{n} \sum_{r=1}^n Z(\omega) \cdot e^{-2\pi i \frac{(r-1)(s-1)}{n}} \quad (5)$$

Finally, the rail geometry dataset in the time domain is transformed into the space domain by correlating its values with the locations provided by the GPS.

3. Model validation

In order to determine the validity of the described algorithm, a field data gathering campaign was carried out along a 1500 m, straight track stretch in Lonquén, Chile. The results provided by such method were visually and statistically compared with those obtained by means of a commercial tool of proven reliability (*i.e.*, a mobile rail scanner). Figure 2 presents the registered rail geometry data series, which shows a good agreement between the new model and the commercial solution, although the signal noise presents a higher amplitude in the first one. For the sake of concision, only results from one rail are shown. On the other hand, position and magnitude of major rail defects is properly detected with both methods. In this regard, two significant defects are located near positions 755 and 1460 m, with a similar magnitude (4 - 5 mm).

Concerning the statistical comparison, a goodness-of-fit indicator (C) has been defined according to eq.(6), and represents the average error with respect to a reference maximum value (M_{ref}).

$$C = \frac{\sum_{i=1}^n c_i}{n} \rightarrow c_i = \frac{|M_{nm,i} - M_{cm,i}|}{M_{ref}} \cdot 100 \quad (6)$$

Where $M_{nm,i}$ and $M_{cm,i}$ are the values obtained on each point i with the new method and the commercial method, respectively; n is the total amount of points measured; and M_{ref} is a reference value of the maximum admissible deviation, set to 5 mm according to the manufacturer of the mobile rail scanner. It should be taken into account that allowing measurement errors higher than 5 mm (or within this magnitude) would “hide” the real defects under signal noise, thus reducing the effectiveness of the method.

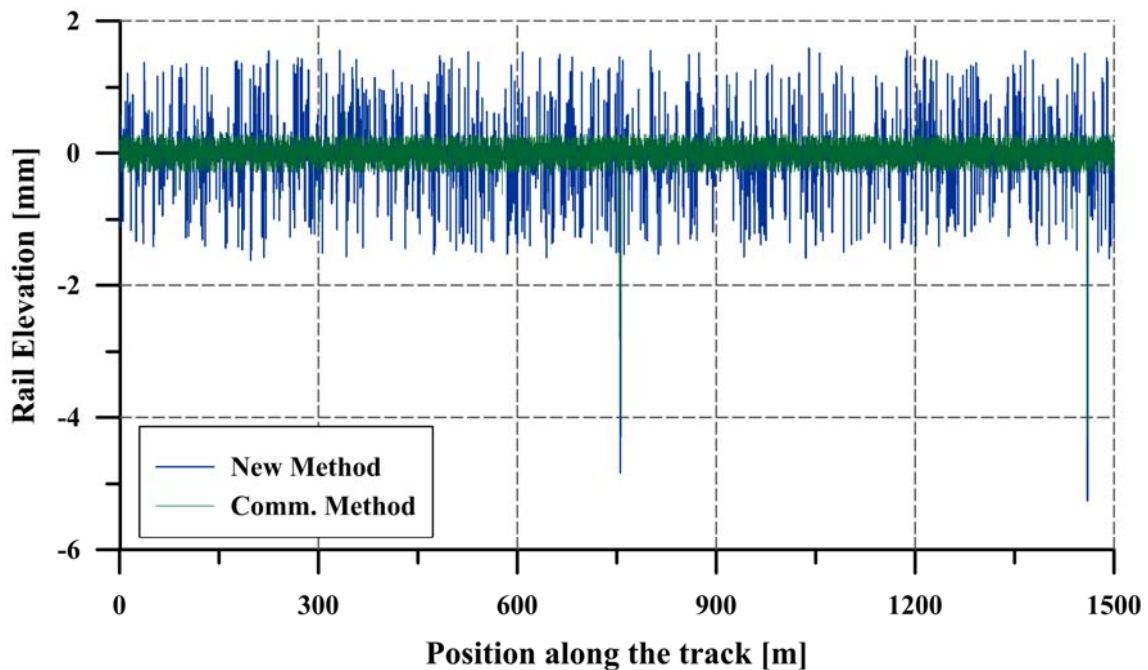


Fig. 2. Rail geometry data registered and processed according to the proposed methodology (blue); and those provided by a mobile rail scanner (green)

An average error value $C = 4.72\%$ has been obtained, and hence, the validity of the proposed methodology for the detection of rail defects and imperfections can be confirmed.

4. Conclusions

Along this paper, a new methodology for the detection of rail defects has been presented and described in detail. The algorithm is based on the register of the vehicle accelerations along a track stretch and its later processing in order to obtain the rail geometry. It has been successfully validated over a 1500 m long real track stretch and constitutes a useful and more affordable tool for rail inspection. Further developments of this technique should be oriented to the refinement of data filtering (and therefore the reduction the signal noise), as well as to validation over longer and more complex track stretches (*e.g.*, canted curves, slopes, stiffness transitions).

References

- [1] Fesharaki, M. and Wang, T.L. The Effect of Rail Defects on Track Impact Factors. *Civil Engineering Journal*, 2016. 2(9): p. 458 - 473.
- [2] Real, J.I., Zamorano, C., Real, T., and Morales, S. New Transition Wedge Design Composed by Prefabricated Reinforced Concrete Slabs. *Latin American Journal of Solids and Structures*, 2016. 13: p. 1431 - 1449.
- [3] Kawasaki, J. and Youcef-Toumi, K. Estimation of Rail Irregularities. in *American Control Conference*. 2002. Anchorage, U.S.A.
- [4] Cantero, D. and Basu, B. Railway infrastructure damage detection using wavelet transformed acceleration response of traversing vehicle. *Structural Control and Health Monitoring*, 2014. 2015(22): p. 62 - 70.
- [5] Melis, M. *Apuntes de Introducción a la Dinámica Vertical de la Vía y a las Señales Digitales en Ferrocarriles*. 1st ed, 2008, Madrid, Spain. 795.

Application of a modified concrete for vibration attenuation in railway infrastructures

Antonio José Pérez^{1}, Teresa Real Herráiz², Fran Ribes Llarío³, Julia Real Herráiz⁴*

¹ *CHM, Avd. Jean Claude Combaldieu, s/n, 03008 Alicante, Spain*

^{2, 3, 4} *Institute of Multidisciplinary Mathematics, Polytechnic University of Valencia, Camino de Vera, 46022 Valencia, Spain*

**Corresponding author. E-mail: ajperez@chm.es. Telephone: +34 965 145 205*

1. Introduction

Propagation of railway-induced vibrations through the soil and its transmission to surrounding structures is a matter of major concern, since it may affect the operation of sensitive equipment or even human comfort. Therefore, a significant amount of research has been carried out regarding mitigation of train-induced vibrations at some point of the emission-transmission path: i) at the source, by preventing its generation; ii) along the ground, by avoiding its transmission; and iii) in the vicinity of the receiver.

In this regard, measures adopted to interrupt the transmission path have the advantage that no intervention on the track is needed and multiple buildings can be benefited, if this measure is performed close enough to the track. Among the existing alternatives, wave barriers may be highlighted, since they can be implemented in any moment of the railway lifespan without interfering on its operation. Nevertheless, restrictions imposed by the environment (*e.g.*, roads, buildings) usually exist and may considerably affect the barrier design. Hence, when the barrier geometry and position is restricted, the election of an appropriate in-fill material is of utmost importance to ensure a satisfactory performance of the mitigation measure.

On the other hand, the recycling of scrap tyres has become a viable option for sustainable construction in the past years by means of using recycled waste tyre rubber as an aggregate substitute in concrete [1]. In this sense, the addition of such particles to the concrete leads to a considerable reduction of its compressive and tensile strength, as well as an increase of its elasticity, deformability and damping. Hence, due to its excellent properties for vibration attenuation, such modified concretes arise as an excellent option for wave barrier in-fill material. Moreover, the decrease in resistance (both compressive and tensile) can be compensated if a certain amount polypropylene fibres is added to the mixture, thus reducing the main drawbacks of the new material.

The purpose of this research project is therefore to analyse the vibration attenuation efficiency of a modified concrete (i.e., with added polypropylene fibres and scrap tyres aggregate) acting as a wave barrier in-fill material.

2. Description of the FEM numerical model

With the aim of analysing the efficiency of the new concrete, four scenarios have been proposed: a case zero with no mitigation measure; and three different configurations made out of the modified concrete. In this regard, a 3D FEM numerical model has been developed within ANSYS LS-DYNA V.14 commercial software, which has been later calibrated and validated with real measurements from a field experiment. The vibrational problem can be solved by means of the equation of motion expressed by eq.(1).

$$[M]\{\ddot{\mathbf{u}}\} + [C]\{\dot{\mathbf{u}}\} + [K]\{\mathbf{u}\} = \{\mathbf{F}^{\alpha}(\mathbf{t})\} \quad (1)$$

Where $[M]$, $[C]$ and $[K]$ are the global mass, damping and stiffness matrices, respectively; $\ddot{\mathbf{u}}$, $\dot{\mathbf{u}}$ and \mathbf{u} are the acceleration, velocity and displacement vectors; and $\mathbf{F}^{\alpha}(\mathbf{t})$ contains

the time-dependent forces, which are introduced as harmonic forces. The global damping matrix C is generally defined by eq.(2).

$$[C] = \alpha[M] + \beta[K] + \sum_{i=1}^{nm} \beta_i [K_i] + \sum_{j=1}^{ne} [C_j] \quad (2)$$

Where α and β are the Rayleigh coefficients; and nm , ne are the total number of materials and elements of the system, respectively. However, for the sake of simplicity, it can be considered without a significant reduction of accuracy [2, 3] that the damping matrix only contains the stiffness term, as shown in eq.(3).

$$[C] = \beta[K] \quad (3)$$

Where the global damping coefficient (β) is *a priori* unknown and should be estimated through the calibration process. The model global dimensions have been set according to [4] in order to avoid undesired wave reflection effects, and the modelling of the rail and the railpad has been simplified following the recommendations of [5]. It consists of a 48 m long ballasted track stretch, with 80 wooden sleepers and UIC-54 rails. Different soil characteristics have been applied on the stratum located under the track and that located behind the barrier (see Fig. 1) to better reproduce the real field conditions.

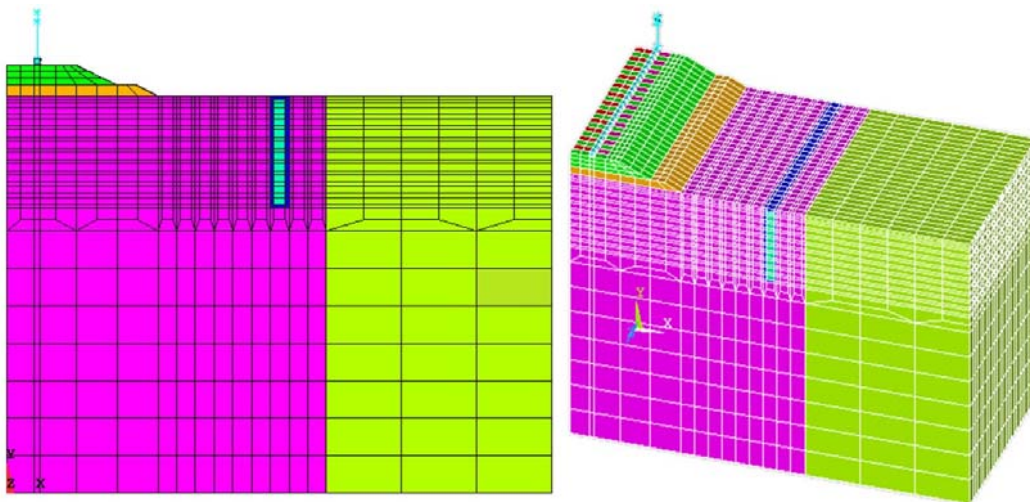


Fig. 1. Numerical mesh example (longitudinally reduced) for the hollow-block solution

The considered vehicle is an ALCO S321 locomotive with two bogies and 6 wheelsets (see Fig. 2) running at a speed of 150 km/h over the track stretch. Given the maximum frequency of interest (100 Hz) and the material properties (Rayleigh wave velocity) a minimum element size of 0.17 m has been established.



Fig. 2. Sketch and dimensions (mm) of the ALCO S321 locomotive used for this study

3. Considered scenarios

Four different scenarios have been modelled in order to determine the attenuation effectivity of the new material: i) a zero case with no mitigation measure (C0); ii) a case with a solid-block wave barrier (C1); iii) a case with a hollow-block wave barrier (C2); and iv) a case with a 0.3 m thick wave impeding block (WIB) located beneath the embankment (C3). In both cases C1 and C2, the barrier is 3 m deep and is located at a distance of 3 m, parallel to the track. Figure 3 presents below a simplified sketch of the four aforementioned cases.

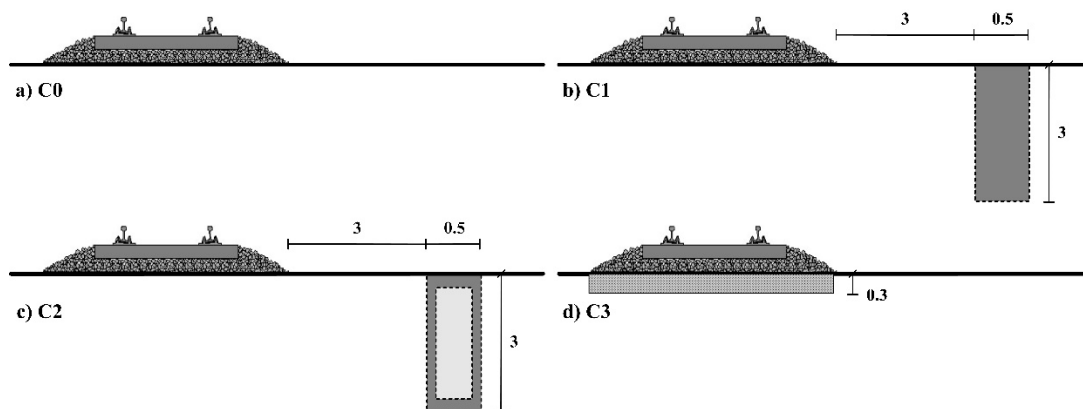


Fig. 3. Front-view sketch of the considered scenarios: a) C0, b) C1; c) C2 and d) C3

4. Results

The vertical particle velocity and acceleration time histories were obtained in 7 points along a line perpendicular to the track, from the rail web to the soil surface behind the trench. Then, the decibel scale adopted by the U.S. Department of Transportation - V_{dB} and A_{dB} - and defined by eq.(4), was applied to the data on each point.

$$V_{dB} = 20 \cdot \log_{10} \frac{v_{y,rms}}{5 \cdot 10^{-8}}, \quad A_{dB} = 20 \cdot \log_{10} \frac{a_{y,rms}}{5 \cdot 10^{-8}} \quad (4)$$

A comparison of the results obtained for each case is presented in Fig. 4 in terms of particle velocities and accelerations. It shows a reduction in both parameters as the distance from the track increases for all the considered cases, as expected. Furthermore, all the proposed mitigation measures induce a reduction of vibrations in the area located furthest away from the track, while such reduction is generally negligible on the track structure ($x < 3$ m) except for C3. The latter is due to the mitigation mechanism of each solution, which is different for the vertical barriers (cases C1 and C2) and the horizontal WIB (case C3).

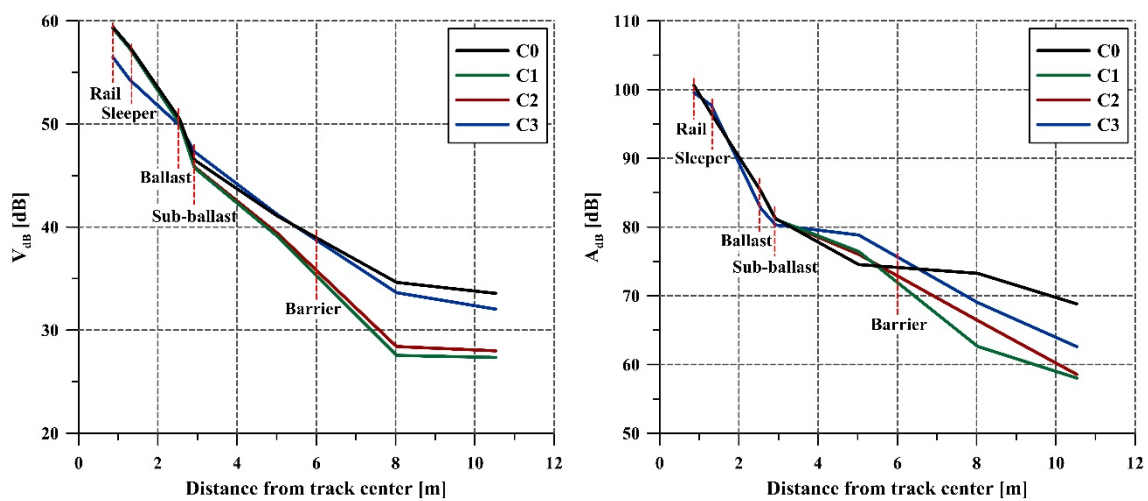


Fig. 4. Velocity (left) and acceleration (right) results for all the modelled alternatives

Regarding the mitigation capacity of the different alternatives, both barrier cases present a similar behaviour, with up to 40% reduction of vertical particle velocities and up to 15% of vertical accelerations with respect to the case without any mitigation measure. It should be also noted that a minor increment in vertical accelerations is induced by all three alternatives (between 3% - 5%) in the zone near the track ($3 \text{ m} < x < 6 \text{ m}$), which is probably due to partial wave reflection on the barrier surface. Thus, it can be concluded that the modified concrete proposed in this paper is effective for the reduction of train induced vibrations, although its absolute efficiency will highly depend on the final constructive disposition.

References

- [1] Su, H., Yang, J., Ling, T.C., Ghataora, G.S., and Dirar, S. Properties of concrete prepared with waste tyre rubber particles of uniform and varying sizes. *Journal of Cleaner Production*, 2015. 91: p. 288 - 296.
- [2] Real, J.I., Galisteo, A., Real, T., and Zamorano, C. Study of wave barriers design for the mitigation of railway ground vibrations. *Journal of Vibroengineering*, 2012. 14(1): p. 408-422.
- [3] Real, J.I., Zamorano, C., and Ribes, F. Wave barriers for the reduction of railway induced vibrations. Analysis in tracks with geometric restrictions. *Journal of Vibroengineering*, 2014. 16(6): p. 2821-2833.
- [4] Shahraki, M. and Witt, K.J. 3D Modeling of Transition Zone between Ballasted and Ballastless High-Speed Railway Track. *Journal of Traffic and Transportation Engineering*, 2015. 3: p. 234 - 240.
- [5] Montalbán, L., Villaronte, J.A., Masanet, C., and Real, J. An artificial neural network model as a preliminary track design tool. *Journal of Rail and Rapid Transit*, 2015. 230(4): p. 1105 - 1117.

Attenuation performance of track stiffness transitions under different vehicle speeds

Fernando Roca Barceló^{1}, Jorge del Pozo², Teresa Real Herráiz³, Julia Real Herráiz⁴*

^{1, 3, 4} Institute of Multidisciplinary Mathematics, Polytechnic University of Valencia, Camino de Vera, 46022 Valencia, Spain

² Universidad Europea de Madrid. Calle Tajo, s/n, 28670 Villaviciosa de Odón, Madrid

**Corresponding author. E-mail: fernanroca@gmail.com. Telephone: +349638770000*

1. Introduction

Abrupt discontinuities in the vertical stiffness of a railway track (*e.g.*, due to the presence of a rigid structure, or a connection between ballasted and non-ballasted track), generally induce an amplification of vibrations on both the vehicle and the track. Hence, such critical segments – which are commonly referred as transition zones –, are highly exposed to material degradation, geometry distortion and loss of passenger comfort [1].

In this regard, an extensive research has been performed in the last years in order to better understand the dynamics of track transitions as well as all the processes involved. Hence, diverse solutions – usually known as track stiffness transitions – have been proposed to provide a smoother stiffness change between track sections. However, to the best of the authors knowledge, no research has fully studied the effect of vehicle speed and only one value is generally used instead of considering a wider range [2].

The aim of this research is thus to explicitly analyse the effect of train speed on the vibration attenuation capacity of two different track stiffness transitions: a concrete slab wedge and a hot mixed asphalt (HMA) transition. For this purpose, a 3D FEM numerical model has been developed within commercial software ANSYS. It has been calibrated

and validated with data of a real track stretch of the high speed line Madrid-Barcelona; and has been later used to reproduce three different scenarios (two transition typologies plus a zero case without transition) and vehicle speeds (50, 160 and 300 km/h).

2. Numerical model

The numerical model consists of two different sub-models, namely the track-soil model and the vehicle model. Both the track and the soil have been reproduced using 8-node hexahedral elements; and the material behaviour has been assumed to be isotropic linear elastic, since the effect of the train does not induce large strains in the soil. Due to the symmetry of the problem, only half of the track has been modelled in the longitudinal direction z and a total model length of 54 m (90 sleepers) has been considered. The cross sectional (x,y) dimension is 10 m, which is enough to avoid wave reflection boundary problems and still involves an acceptable computational cost [3]. The boundary conditions have been defined as a constraint of the perpendicular displacement on each edging plane, according to [4]. Additionally, in order to accurately reproduce tensional discontinuities on the sleeper-ballast contact, it has been modelled with bounded perpendicular D.O.F.s.

With the aim of simplifying, the vehicle has been reduced to a three-mass model (wheelset, bogie, and car-body). In this sense, point elements have been selected for modelling the masses, which are linked by springs and dampers reproducing the primary and secondary suspensions. The wheel/rail interaction is modelled as a Hertzian spring and a node-to-beam contact, allowing for sliding and loss of contact by means of the Penalty algorithm. On the other hand, a full Newton-Raphson method has been employed for solving the nonlinear equations, while the transient dynamic equilibrium has been addressed by means of a Newmark implicit time integration.

A real 8-car AVE S-103 train running at 300 km/h on a real track stretch has been considered for the calibration of the model. The numerical results were superposed in order to reproduce the effect of the 32 wheelsets of the train, and four unknown parameters were determined through the calibration process: three Young moduli (soil, ballast and sub-ballast); and the stiffness matrix multiplier for damping (β).

The model has been later validated by comparing its results with registers of another two AVE S-103 trains running at 300 km/h and 216 km/h. The comparison between the registered and calculated accelerations on the ballast layer below the sleepers is shown in Fig. 1, where slight differences can be seen between measured and calculated data for both train speeds, although maximum peaks and time-scaling are well reproduced.

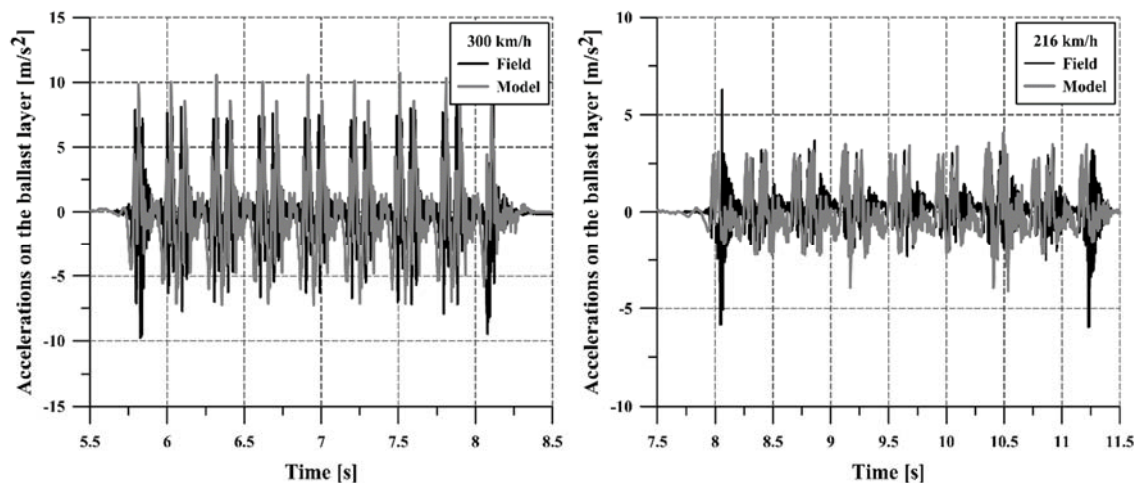


Fig. 1. Real (black) and modelled (grey) vertical accelerations on the ballast layer for a train running at 300 km/h (left) and 216 km/h (right).

3. Considered scenarios

In order to study the influence of vehicle speed on the performance of a track transition between an embankment and a culvert, three scenarios have been defined: i) an abrupt stiffness transition (*i.e.*, a case 0 without any mitigation measure); ii) a concrete slab wedge located under the sub-ballast layer, similar to that developed in [1]; and iii) an

HMA wedge placed within the sub-ballast layer, designed according to [5]. In this regard, Fig. 2 presents a scheme of the cases with smooth transition.

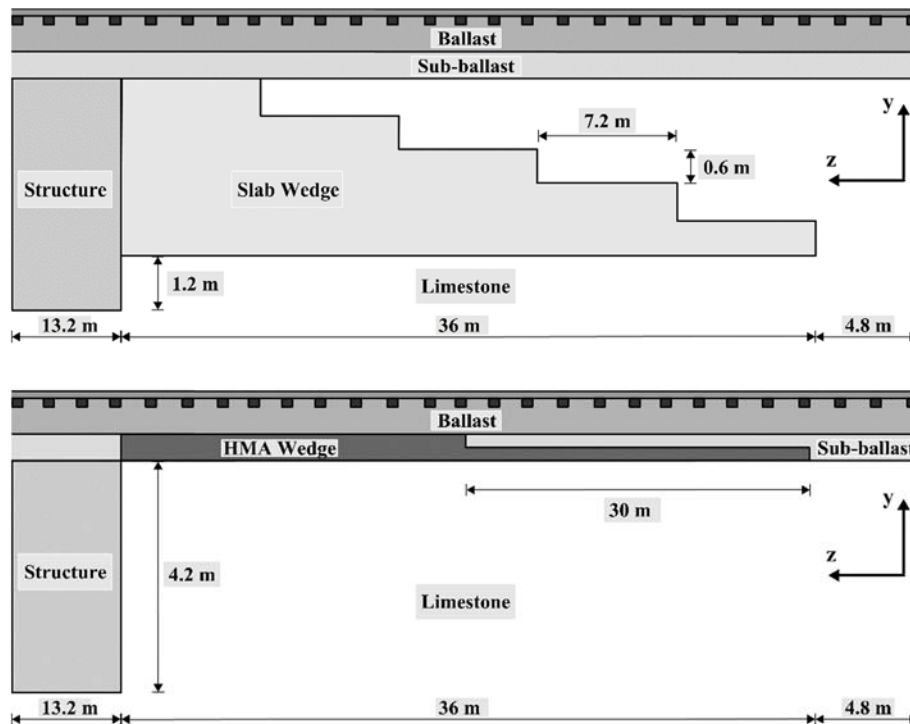


Fig. 2. Profile scheme of the modelled alternatives: up, concrete slab wedge; down, hot mix asphalt wedge

For both scenarios, the vehicle running direction is set from the embankment to the structure (i.e., soft to stiff direction) since it has been found in previous studies [6] to be the most critical one.

4. Results and conclusions

A total of nine cases have been modelled, resulting from the combination of the three scenarios and vehicle speeds considered. The vertical particle velocity time-history has been extracted on the surface of 24 sleepers located close to the transition zone. Given the high amount of data available, the use of an indicator is employed in order to simplify the analysis and clarify the contribution of train speed on the performance of each

transition typology. Therefore, the decibel scale adopted by the U.S. Department of Transportation - or VdB -, which is defined by eq.(1), has been calculated on each point of the track. Such metric is closely related with the analysis of human comfort under vibrations, since it describes the smoothed vibration amplitude of the entire time history.

$$V_{dB} = 20 \cdot \log_{10} \frac{v_{y,rms}}{5 \cdot 10^{-8}} \quad (1)$$

Where $v_{y,rms}$ is the root mean square amplitude of the particle velocity time history. Results are presented in Fig. 3, where the vertical black line indicates the embankment-culvert transition section.

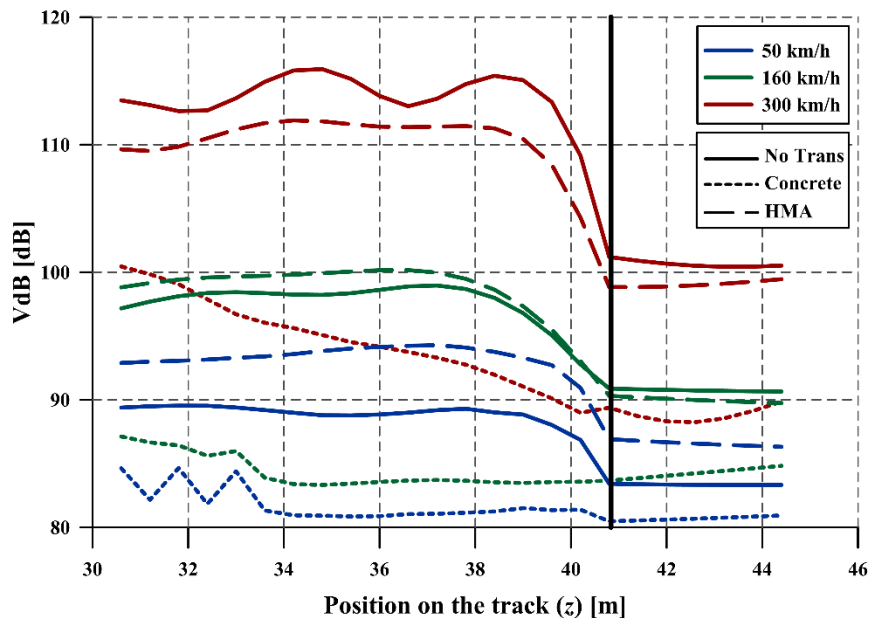


Fig. 3. Effect of vehicle speed on soil vibrations for different transition typologies.

It can be determined from Fig. 3 that train speed has a significant influence on the variation of vertical particle velocities between soft and stiff sections, which considerably increases for higher values of vehicle speed, and particularly for very high speeds (*i.e.*, 300 km/h). Such effect occurs for all the considered scenarios and is more pronounced in the soft section (*i.e.*, track over the embankment). Hence, it can be concluded that placing a track stiffness smooth transition may only be worthwhile in high speed lines.

On the other hand, regarding the comparison between the analysed transition typologies, it can be confirmed that the concrete slab wedge induces significantly higher reductions of the particle velocities on the soil (more than 50% reduction in all cases, when compared to case zero) than the HMA wedge. Furthermore, V_{dB} values are slightly higher for the HMA wedge when compared to the case without smooth transition for low and medium train speeds (*i.e.*, 50 km/h and 160 km/h). Such effect may be due to the partial substitution of the sub-ballast layer with a layer of hot mix asphalt (significantly stiffer), which may cause a match between the vehicle speed and the critical speed of the system and hence increase the vibrational response.

References

- [1] Real, J., Zamorano, C., Real, T., and Morales-Ivorra, S. New Transition Wedge Design Composed by Prefabricated Reinforced Concrete Slabs. *Latin American Journal of Solids and Structures*, 2016. 13: p. 1431 - 1449.
- [2] Sañudo, R., dell'Olio, L., Carrascal, I.A., and Diego, S. Track transitions in railways: A review. *Construction and Building Materials*, 2016. 112: p. 140 - 157.
- [3] Shahraki, M. and Witt, K.J. 3D Modeling of Transition Zone between Ballasted and Ballastless High-Speed Railway Track. *Journal of Traffic and Transportation Engineering*, 2015. 3: p. 234 - 240.
- [4] Montalbán, L., Real, J., and Real, T. Mechanical characterization of railway structures based on vertical stiffness analysis and railway substructure stress state. *Journal of Rail and Rapid Transit*, 2012. 227(1): p. 74 - 85.
- [5] Rose, J.G. and Anderson, J.S. Long-term Performance of Asphalt Underlayment Trackbeds for Special Trackbed Applications, in *Annual Conference and Exposition of the American Railway Engineering and Maintenance-of-Way Association 2006*: Louisville, U.S.A.
- [6] Dahlberg, T. Railway Track Stiffness Variations – Consequences and Countermeasures. *International Journal of Civil Engineering*, 2010. 8(1).

Detection of earthquake-induced soil liquefaction in harbours based on changes of the structure vibration modes

Piter Moscoso Godoy^{1*}, Fran Ribes Llario², Víctor Ramos Vicedo³, Julia Real Herráiz⁴

¹ Dirección General de Obras Públicas, Ministerio de Obras Públicas, MOP, Santiago de Chile

^{2, 3, 4} Institute of Multidisciplinary Mathematics, Polytechnic University of Valencia, Camino de Vera,
46022 Valencia, Spain

*Corresponding author. E-mail: piter.moscoso@mop.gov.cl

1. Introduction

Soil liquefaction usually takes place under conditions of rapid and intense stresses (*e.g.*, earthquakes) in low cohesion soils (*e.g.*, granular) with a high humidity content. Such stresses induce a severe particle relocation and thus a reduction of the effective stress (σ'), which according to Terzaghi's principle (eq.(1)) results in an abrupt increase of pore pressures (u). Moreover, if the decrease of effective stresses is high enough, the soil will behave as a viscous liquid, thus losing its shear resistance.

$$\sigma = \sigma' + u \quad (1)$$

In this regard, harbour and coastal structures such as quays or breakwaters located within areas of high seismicity, present an elevated risk of failure due to liquefaction, since coastal grounds are generally formed by granular, low cohesive materials and the water table is situated close to or above the surface.

However, it should also be taken into account that soil liquefaction is not an automatic and instantaneous process but a continuous one, which requires a certain duration and intensity to completely develop. Therefore, different phases (*i.e.*, no liquefaction, partial

liquefaction and total liquefaction) can be distinguished [1] in the process, which would affect the structure in diverse manners. In this sense, modal analysis of structures arises as a very useful and versatile tool for the assessment of failure risk in structures subjected to soil liquefaction. Such technique aims to determine the degree of affection of a structure (and thus the risk of failure) by analysing variations in its vibrational response due to soil liquefaction. In this respect, laboratory scaled tests [1] have demonstrated that natural frequencies of the structure may suffer a strong decrease (up to 50% for total liquefaction), while the damping coefficient might be increased up to 20%.

This research project takes advantage of the aforementioned knowledge in order to develop a methodology for the detection of soil liquefaction in harbours, based on a continuous monitoring of the vibrational response of the structure to be analysed.

2. Proposed methodology

First of all, the real-time variations in pore pressure and the vibrational response of the structure should be registered by placing pressure transducers and tri-axial accelerometers in different points of the ground and the quay. Then, if a sudden increase in pore pressure is detected (*e.g.*, due to an earthquake) the degree of liquefaction will be evaluated by analysing the variations in natural frequencies and damping coefficient of the structure.

To this aim, the registered values will be compared with a catalogue of different liquefaction scenarios elaborated prior to the operational phase by means of a numerical model. In this regard, a modal analysis will be carried out considering the soil-structure system as a simplified Winkler beam model (see Fig. 1).

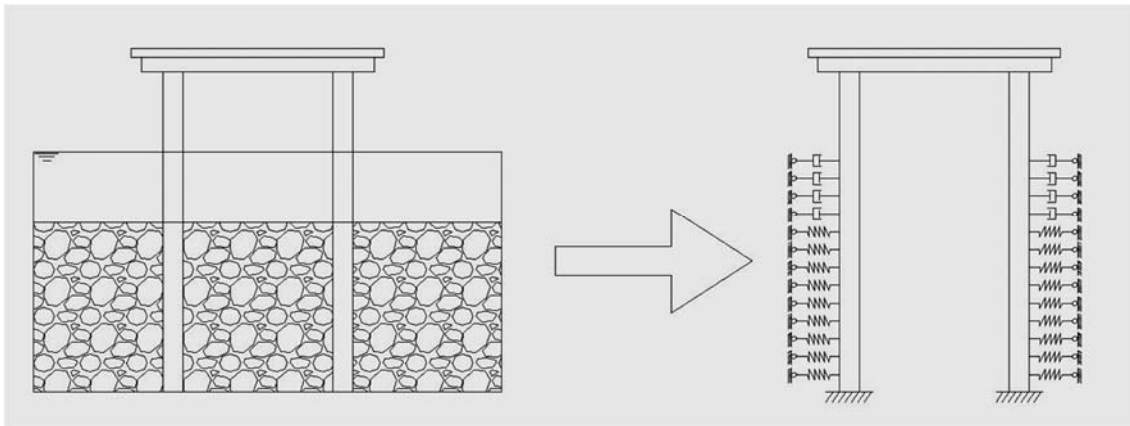


Fig. 1. Simplified Winkler beam model of the soil-structure system

The model reproduces the effect of the soil surrounding the structure as a group of non-linear elastic-plastic springs with variable stiffness (*i.e.*, depending on the liquefaction depth and intensity given by the pressure transducers), while the dissipation effect of the water table is modelled by means of dampers with a certain viscosity [1, 2]. The election of a non-linear model for the springs allows to consider plasticising of the soil, while the structure materials can be considered elastic linear without substantially diminishing the accuracy of the model.

2. Model validation

Because of the inherent uncertainty in terrain mechanical properties, model calibration and validation became an important phase of the research. In order to ensure about the adequate behaviour of the model, two different extreme scenarios were processed: infinite and zero support stiffness. This provided the range of maximum and minimum first natural frequencies of the structure independently of the liquefaction. Both were 2.31 Hz and 3.85 Hz, which are inside the typical range in this sort of structures.

After validation, the initial ground stiffness was estimated using real field measurements of accelerations – determine spring constants [49,14 MN/m] -.

3. Cases of study

Eight different cases of study were studied, corresponding to eight different levels of liquefaction [0,2,3,4,....,7 m].

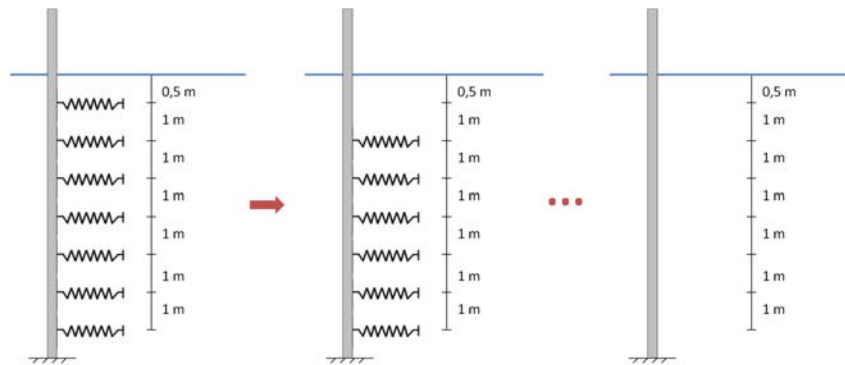


Fig. 2 Different liquefaction levels scheme.

Variation in three first vibration modes (long. translation, transversal translation, torsion) was studied for each liquefaction level.

3. Numerical model results

Obtained results for non-liquefaction case are:

Mode	Freq (Hz)
1	2,4675
2	2,7203
3	3,0921

Chart 1: Modal freq. for three first vibration modes in non-liquefied foundation.

And estimated variation for each mode and level of liquefaction:

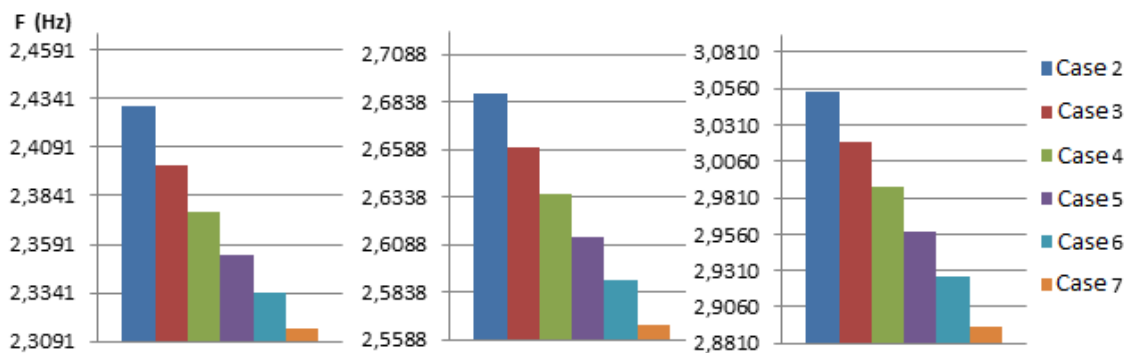


Fig. 3 : Evolution of modal freq. for 1st mode (left), 2nd mode (centre) and 3rd mode (right) vs liquefaction level.

3. Field test results

Regarding non-liquefied case, results obtained from frequency domain analysis of vibrations showed following frequencies for three first modes:

Mode	Freq. Numerical model (Hz)	Field measured freq. (Hz)	Relative deviation (%)
1	2,4675	1,909	9,87
2	2,7203	2,090	12,71
3	3,0921	3,590	19,12

Chart 2: Numerical model vs. field test frequencies.

4. Conclusions

Proposed methodology for liquefaction monitoring based on variation of first natural frequencies of the structure allowed to identify and quantify this phenomena.

Comparison between numerical modelling of a quay structure and its foundation with modal analysis carried out and field test vibration analysis in frequency domain showed that is possible to estimate with live data the liquefaction level on an offshore structure with an acceptable accuracy – less than 20% error in higher modal frequencies [3]-.

In addition, it is possible to delimit maximum deviation assumed by applying this methodology. Extreme values of infinite and zero soil stiffness allow to obtain maximum and minimum possible frequencies range. Thus, it eases results interpretation when estimated stiffness value is fixed and cooperates to perform more accurate models.

It is also showed how natural frequencies decrease with soil stiffness leakage due to liquefaction phenomena and how is it possible to apply accelerometers distributed in the structure to identify modal parameters which depend on soil mechanical properties.

5. References

- [1] Lombardi, D. and Bhattacharya, S. Modal analysis of pile-supported structures during seismic liquefaction. *Earthquake Engineering Structural Dynamics*, 2013. 43(1): p. 119 - 138.
- [2] Brandenberg, S.J. Behavior of Pile Foundations in Liquefied and Laterally Spreading Ground, in *Civil and Environmental Engineering*, 2005, University of California Davis. p. 340.
- [3] Serrano, J. (2015) Análisis dinámico experimental y numérico de una presa bóveda. ETSICCP, Universidad Politécnica de Madrid.

Development of a high precision algorithm for predictive maintenance of industrial belt conveyors

Miriam Labrado Palomo^{1}, Claudio Masanet Sendra², Fernando Roca Barceló³, Jose Luis Velarte González⁴*

^{1, 2, 3, 4} Institute of Multidisciplinary Mathematics, Polytechnic University of Valencia, Camino de Vera, 46022 Valencia, Spain

**Corresponding author. E-mail: milabpa@cam.upv.es. Telephone: +349638770000*

1. Introduction

Belt conveyors are commonly used as continuous transport equipment in industries, since they present a high efficiency, large capacity, simple construction, and do not require intense maintenance works. Moreover, they constitute a key element of the entire industrial process; and a severe failure of one conveyor may result into a stop of production. On the other hand, one of the most frequent reasons for rotating machinery breakdown is deterioration of the rolling element bearings (REB) [1].

Traditional maintenance techniques (*e.g.*, corrective maintenance, preventive maintenance) generally involve substantially higher costs and may even reduce the production capacity in case that a critical failure occurs. In this context, predictive maintenance techniques based on a continuous monitoring of each component, arise as a more efficient and cost-effective solution (*i.e.*, maintenance tasks are performed only when necessary).

Among such techniques, those based on a vibrational analysis of the conveyor components (*e.g.*, FFT and envelope demodulation) permit a real-time, simple and

accurate detection of a wide variety of failure typologies [2]. However, REB vibratory signals are non-stationary, non-linear and relatively weak, which makes them susceptible of being masked by stronger signals, such as the noise generated by other components. Consequently, the aim of this research project is to develop a high precision system for early prediction of failures and deterioration of industrial conveyor bearings. Moreover, the methodology is applied to a field case study to analyse the state of an industrial conveyor.

2. Proposed methodology

In order to evaluate the real-time state of conveyor bearings, the acceleration time-histories of the key components of the conveyor are first registered during operation, by means of tri-axial accelerometers. Such registers should be then analysed, and an algorithm has been developed for this purpose consisting of two different phases: a pre-processing module and a processing module (see Fig. 1).

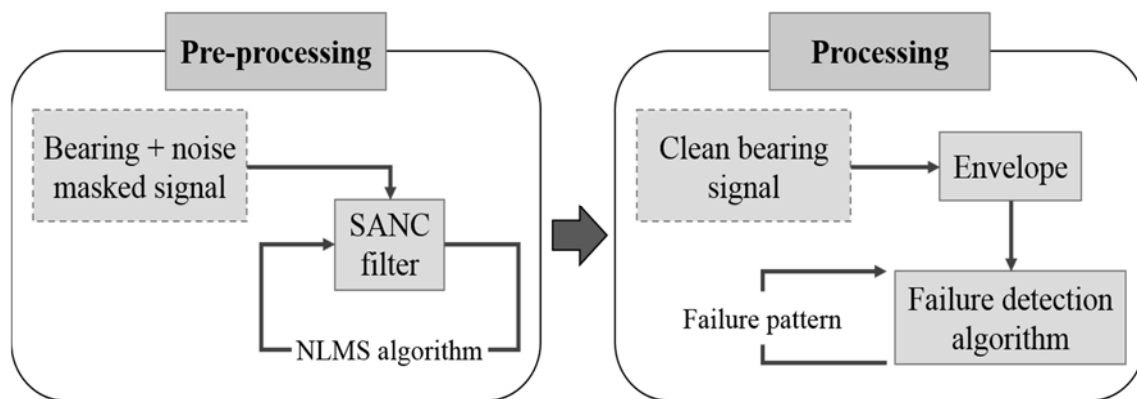


Fig. 1. Scheme of the proposed algorithm

First, the pre-processing module separates and eliminates the noise from the bearing vibratory signal by means of a self-adaptive noise cancellation (SANC) filter with a normalised least mean square (NLMS) learning algorithm. The SANC filter permits the

separation of a signal in two components; one of them deterministic (in this case, the bearings vibrational response) and the other, non-deterministic (the noise) [3]. To this aim, a delayed version of the input signal is processed with a transversal filter and subtracted from the input signal to estimate a prediction error [4]. Then, the transversal filter weights are adaptively adjusted (by the NLMS algorithm) so as to minimise the output error.

In a second phase, the processing module (which is based on the envelope method) analyses the signal and determines the bearing deterioration. First, the clean vibratory signal of the conveyor bearing is introduced and the envelope is calculated by means of the Hilbert transform. The envelope is later transformed into the frequency domain by means of the Fast Fourier Transform (FFT). This process intensifies the main components of the dynamic signal, which permits a simpler and more precise analysis of the machine vibratory pattern.

Finally, the algorithm compares the registered pattern with that of a bearing with a certain failure and determines the state of the monitored element. A failure pattern catalogue should be thus introduced in the system prior to the operation phase for an adequate identification of bearing pathologies.

3. Case study

The proposed methodology has been implemented in Matlab[®] computing environment and has been later applied to the analysis of a field case study. In this regard, different elements of an A-800 L-1076-EH industrial conveyor were monitored on a mineral aggregate production plant in Murcia, Spain. To this aim, vibrations were registered on the head and tail drums as well as on an intermediate roller (see Fig. 2) by means of three ADXL345 digital accelerometers connected to Arduino controllers.

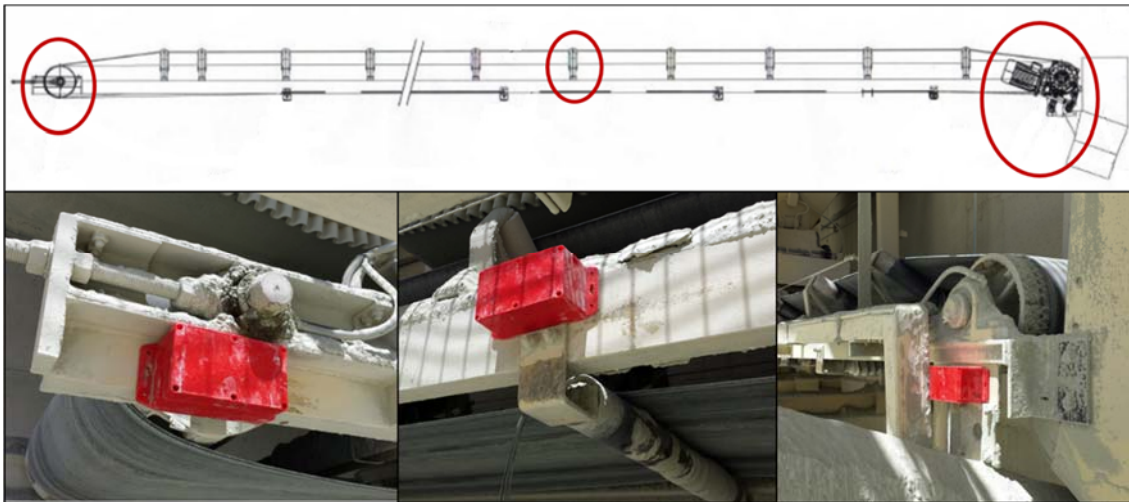


Fig. 2. Disposition of accelerometer groups along the industrial conveyor for the model validation: on the tail drum, left; on a roller, centre; on the head drum, right.

The acceleration registers showed that the principal vibrations occur in the vertical direction and therefore, only the measurements related to such directions will be analysed in the following. In this sense, Fig. 3 presents the row data (in both time and frequency domains) obtained from the head drum during a time lapse of 10 s, together with the processed results (*i.e.*, filtered data and envelope).

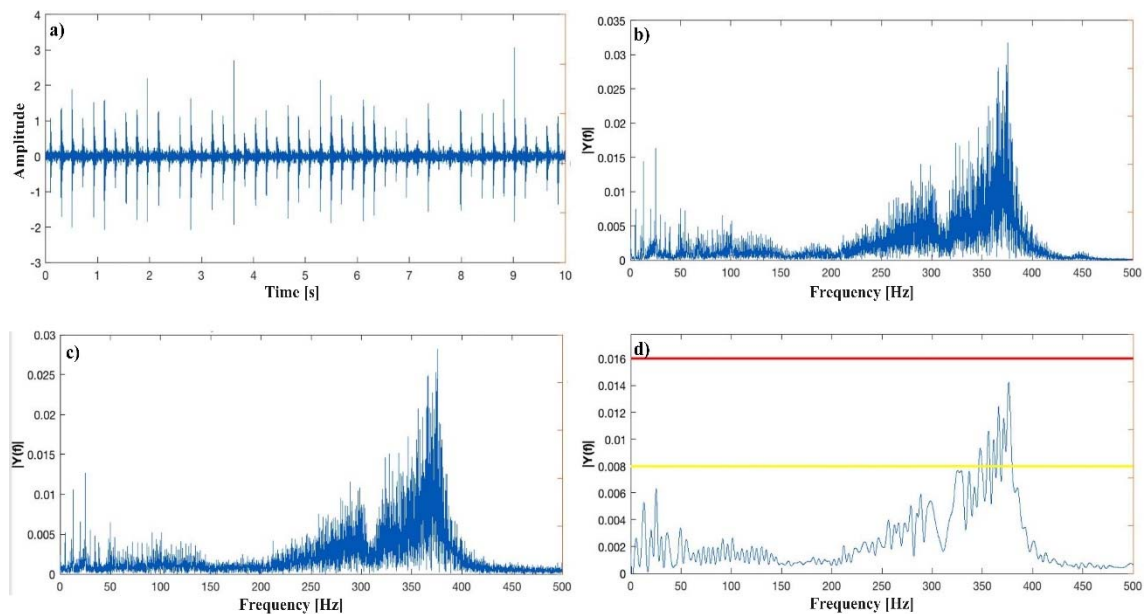


Fig. 3. Acceleration registers from the head drum: a) row data in the time domain; b) row data in the frequency domain; c) filtered data; d) envelope

Furthermore, it should be noted that the results of the roller and the tail drum are omitted in this paper for the sake of concision, since they show a similar behaviour to those of the head drum. Regarding the later, the filtering process eliminates the signal noise contained in Fig. 3b, which leads to a clean vibrational signal describing the state of the component (Fig. 3c). Then, the processing module obtains the envelope (Fig. 3d) by means of the Hilbert transform. The yellow line on Fig. 3d is a user-input threshold value related to each conveyor component failure mode. For its determination it is necessary to carry out a preliminary analysis on the conveyor in order to determine the magnitude of the frequency peaks associated to each type failure (*i.e.*, elaborate a failure catalogue).

Once the envelope has been calculated and the threshold value has been established, the algorithm evaluates the number of times that each frequency overcomes the threshold. The later permits to determine if it is due to a random event (no repetition) or if it is related to a failure of the component (periodically repeated). In this case, the algorithm detects several frequency values surpassing the threshold, although all them are associated to random events, since they do not present repetition (see Fig. 4).

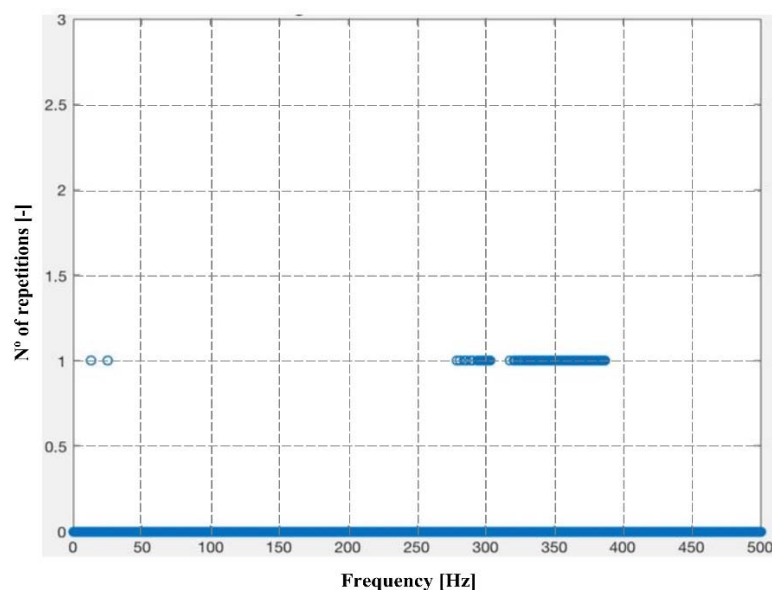


Fig. 4. Repetition of the frequencies surpassing the threshold

4. Conclusions

Along this paper, a highly precise new methodology has been developed for the predictive maintenance of industrial belt conveyors. The system consists of registering the real-time accelerations of the different components of the conveyor. Then, the raw data are transformed into the frequency domain for filtering and the envelope of the signal is obtained. The last step is the comparison of the envelope with a user-introduced failure threshold (to be obtained in advance), which determines the actual state of the conveyor component. A field case study on a real industrial belt conveyor has been presented in order to illustrate an application of the proposed methodology.

References

- [1] Ben Ali, J., Fnaiech, N., Saidi, L., Chebel-Morello, B., and Fnaiech, F. Application of empirical mode decomposition and artificial neural network for automatic bearing fault diagnosis based on vibration signals. *Applied Acoustics*, 2014. 89: p. 16 - 27.
- [2] Dybala, J. and Zimroz, R. Rolling bearing diagnosing method based on Empirical Mode Decomposition of machine vibration signal. *Applied Acoustics*, 2014. 77: p. 195 - 203.
- [3] Starr, A. and Rao, B.K.N. Condition Monitoring and Diagnostic Engineering Management. in *COMADEM*. 2001. Manchester, UK.
- [4] Antoni, J. and Randall, R.B. Unsupervised noise cancellation for vibration signals: part I - evaluation of adaptive algorithms. *Mechanical Systems and Signal Processing*, 2004. 18(1): p. 89 - 101.

Effect of mixture gradation and thickness on the cooling process of hot mix asphalts

Julia Real Herráiz^{1*}, Beatriz Baydal Giner², Miriam Labrado Palomo³, Adrián Zornoza Arnao⁴

^{1, 2, 3, 4} *Institute of Multidisciplinary Mathematics, Polytechnic University of Valencia, Camino de Vera, 46022 Valencia, Spain*

**Corresponding author. E-mail: jureahe@tra.upv.es. Telephone: +349638770000*

1. Introduction

One of the most important factors affecting the design and performance of hot mix asphalt (HMA) pavements is to ensure an adequate compaction of the mixture, since it controls the resulting quality (*e.g.*, high durability, absence of irregularities). In this sense, several parameters influence the compaction process, such as pouring temperature, base typology and bitumen content. Among them, pouring temperature is of major concern, since it governs the compaction process and therefore determines the final quality of the product.

Nevertheless, given that mixture temperature is generally much higher than the ambient one, it tends to rapidly decrease (especially for the case of thin asphalt layers), thus shortening the available compaction time [1]. Moreover, the cooling process does not take place homogeneously along the entire thickness, being more accelerated on the lower layers (*i.e.*, those located right over the base) than close to the free surface [2]. In this regard, the thermal properties of the mixture, which strongly depend on its gradation [3], can be modified in order to increase the cooling time and ease the compaction process.

Hence, the purpose of this research work is to analyse the effect of varying the layer thickness and mixture grading on the cooling process of an HMA pavement.

2. Description of the model

In order to reproduce the cooling process of an HMA pavement, a 3D FEM model has been developed within ANSYS commercial software, and 10 different combinations (two mixture gradings and five pavement thicknesses) have been modelled. Concerning the HMA mixtures, two typologies with very different grading have been studied:

- Stone mastic asphalt (SMA). A gap-graded HMA designed to maximize durability and deformation resistance by using a structural basis of stone-on-stone contact.
- Asphalt concrete (AC) with a 90% of 16 mm passing aggregate (AC16)

On the other hand, the selected thicknesses for the pavement layer (h) are 2, 4, 5, 8 and 10 cm, placed over a 22 cm deep soil-cement base, a 40 cm deep sub-base, and a 60 cm deep embankment (Fig. 1). Additionally, the model is 2 m wide (*i.e.*, in the transversal direction of the road) and 5 m long (*i.e.*, in the longitudinal direction).

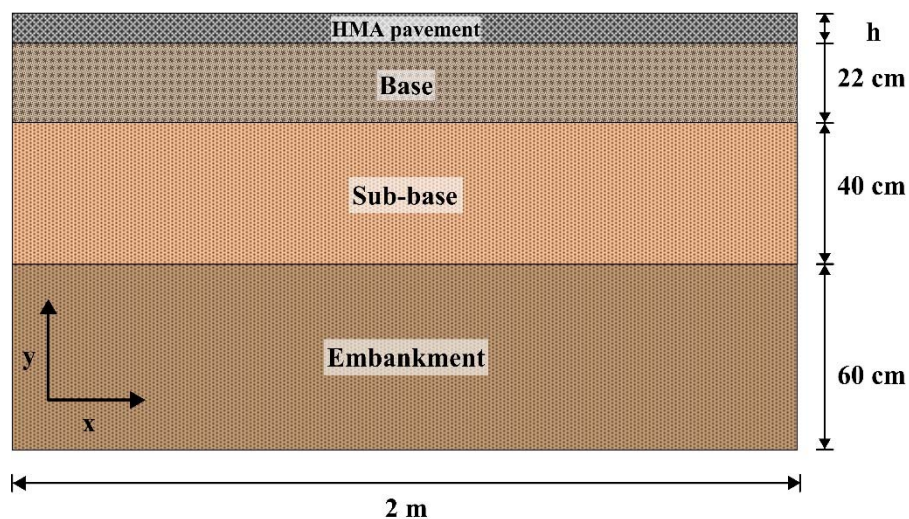


Fig. 1. Road section modelled in ANSYS

Tri-dimensional 8-node elements SOLID70 with thermal conduction capability have been used for modelling the solid materials; while the HMA-air interface is reproduced by means of bi-dimensional SURF152 elements.

3. Analysis of results

A transient analysis has been carried out with a total cooling time of 5 h; and the initial temperatures for the mixture and the soil-air environment have been set to 140 °C and 25 °C, respectively. Moreover, the variation of density, thermal conductivity and specific heat of both mixtures due to temperature fluctuation has been accounted (see Table 1).

Table 1. Thermal properties considered for the study

Layer		Density [kg/m ³]	K (W/mK)	C _p [J/kgK]
AC16	25 °C	2372	2.5	659
	50 °C	2370	2.1	779.5
	75 °C	2368	1.9	900
SMA	25 °C	2297	1.81	1116
	50 °C	2295	1.63	1240
	75 °C	2293	1.45	1364
Base		2000	1.4	1050
Embankment		2000	0.77	920
Air		-	0.0257	1005

As an example of the results obtained, Fig. 2 presents the temperature evolution over the first 3 h of a 4 cm thick AC16 mixture (left) and a 4 cm thick SMA mixture (right). The temperature has been calculated in three different points: i) on the open surface of the mixture (green line); ii) on the mixture-base interface (blue line); and iii) on the base (red line). The figure shows a similar tendency for both mixtures, which rapidly cool during the first 30 – 60 minutes, although the process is considerably longer (3980 s vs. 7200 s) and the equilibrium temperature, higher (64.5 °C vs. 67.1 °C) for the SMA.

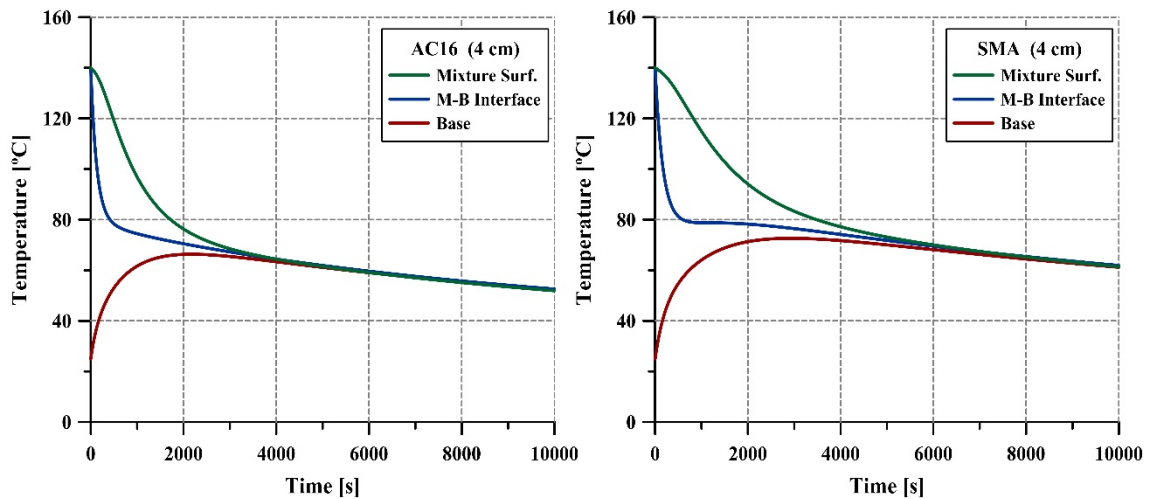


Fig. 2. Temperature evolution during the cooling process of a 4 cm thick AC16 (left) and SMA (right) mixtures

In order to simplify the comparison process between different mixture gradations and thicknesses, the aforementioned indicators (*i.e.*, equilibrium temperature and the time to reach it) have been calculated for all the considered combinations and are presented in Fig. 3. Moreover, the maximum thermal amplitude in the mixture layer (*i.e.*, maximum temperature difference between a point on the mixture surface and one in the base-mixture interface) and its time of occurrence have also been obtained and are shown in the figure.

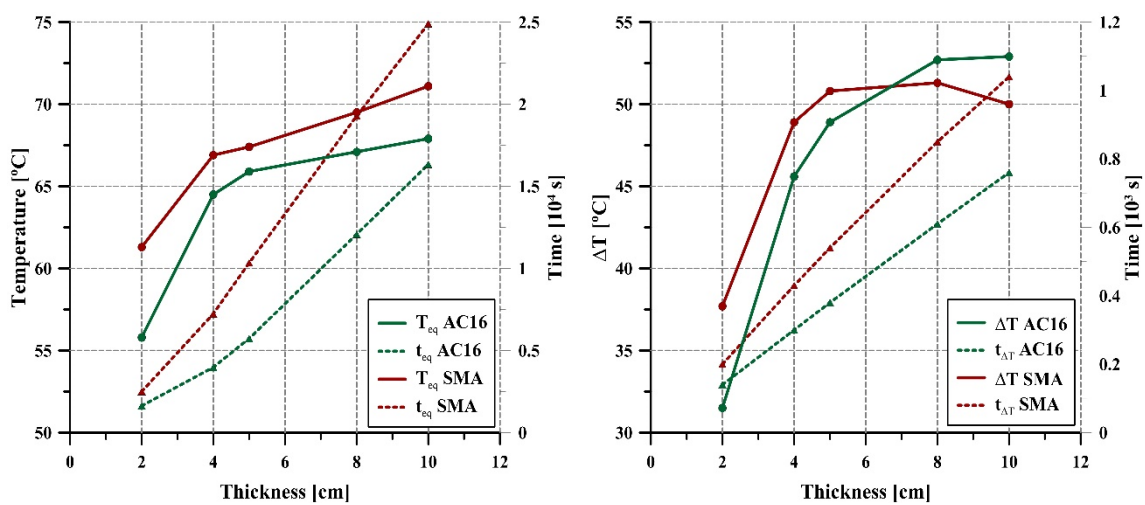


Fig. 3. Evolution of the equilibrium temperature (left) and maximum thermal amplitude in the asphalt layer (right) for different mixture gradations and thicknesses

As can be seen in Fig. 3, both the equilibrium temperature and the time necessary to reach equilibrium in the asphalt layer invariably increase with layer thickness. However, while such increment is roughly linear regarding time, the equilibrium temperature presents a more abrupt growth from 2 cm to 4 cm and becomes approximately linear for larger thickness values. Furthermore, the gap-graded asphalt mixture (SMA) presents higher equilibrium temperatures and longer times for all the considered thicknesses. Therefore, it can be concluded that increasing the layer thickness or using gap-graded mixtures may lead to a considerably higher quality of the compaction process.

On the other hand, the maximum thermal amplitude within the asphalt layer also increases with thickness, which may contribute to a poor compaction. Nevertheless, it tends to stabilize for higher thickness values (8 cm onwards for AC16 and 5 cm onwards for SMA). In this regard it should be pointed out that the gap-graded mixture presents a better behaviour (*i.e.*, lower thermal amplitude values) than the AC16 for thick layers (8 cm and 10 cm).

4. Conclusions

In this paper, the effect of layer thickness and mixture grading on the cooling process of a hot mix asphalt has been explicitly evaluated. For this purpose, a 3D FEM numerical model of a standard road section has been developed within ANSYS commercial software. Five different layer thicknesses (2 – 10 cm) and two mixture gradings (AC16 and SMA) have been modelled, from which the following conclusions may be drawn:

- An augment in layer thickness invariably increases both the equilibrium temperature and time.

- A gap-graded asphalt mixture (such as the SMA) presents higher equilibrium temperatures and longer times for all the considered layer thicknesses thus enhancing the quality of the compaction process.
- The maximum thermal amplitude within the asphalt layer increases with layer thickness up to a value that depends on the mixture type (5 cm for SMA and 8 cm for AC16) from which it stabilizes.
- The gap-graded mixture presents lower thermal amplitude values than the asphalt concrete for large values of layer thickness.

References

- [1] Chang, C.M., Chang, Y.J., and Chen, J.S. Effect of Mixture Characteristics on Cooling Rate of Asphalt Pavements. *Journal of Transportation Engineering*, 2009. 135(5): p. 297 - 304.
- [2] Corlew, J.S. and Dickson, P.F. Methods for calculating temperature profiles of hot-mix asphalt concrete as related to the construction of asphalt pavements, in *Assoc Asphalt Paving Technol Proc* 1994.
- [3] Mrawira, D.M. and Luca, J. Effect of aggregate type, gradation, and compaction level on thermal properties of hot-mix asphalts. *Canadian Journal of Civil Engineering*, 2006. 33(11): p. 1410 - 1417.

Numerical modelling of flying ballast phenomenon on high speed lines. Part A: Analysis of the train-track aerodynamic interaction by means of field data and a CFD model

Claudio Masanet Sendra^{1}, Fernando Roca Barceló², Jorge del Pozo³, Julia Real Herráiz⁴*

^{1, 2, 4} Institute of Multidisciplinary Mathematics, Polytechnic University of Valencia, Camino de Vera, 46022 Valencia, Spain

³ Universidad Europea de Madrid. Calle Tajo, s/n, 28670 Villaviciosa de Odón, Madrid

**Corresponding author. E-mail: clmasen@upv.es. Telephone: +349638770000*

1. Introduction

Ballasted high speed railway lines might eventually experience a phenomenon known as flying ballast (or ballast projection). It consists of ballast particles becoming airborne under the effect of a running train, and may lead to safety and management problems on both the rails and the vehicle [1]. In this regard, the aerodynamic field generated between the track and the rolling stock plays a key role, being able to set in motion the ballast particles under certain circumstances [2]. Such displacements may be either superficial or aerial and derive into new particle projections (*i.e.*, by colliding with nearby particles), thus amplifying the phenomenon.

A considerable amount of scientific research has been carried out in the recent years in order to study the processes involved as well as to propose mitigation measures, concluding that the problem can be addressed either by acting on the vehicle or the track aerodynamics (or on both). In this sense, the present research project aims to develop a new heavy ballast, made out of concrete and other high-density recycled materials, to be less prone to suffer the flying ballast phenomenon. Within this project, the new material

has been numerically and physically modelled in order to better know its behaviour, test its efficiency and determine the most convenient design parameters.

The numerical modelling of the new ballast behaviour under the passage of a high speed train has been divided in two clearly differentiated segments: i) the aerodynamic interaction between the track (i.e., ballast, rails and sleepers) and the vehicle, which determines the initiation of motion of the ballast particles; and ii) the mechanical behaviour of the ballast (accounting for its nature as a discrete medium) under the vibrational and aerodynamic excitation induced by the train.

This paper describes a simplified aerodynamic model of the vehicle-track system, which is able to reproduce the air flux generated in the vicinity of the upper ballast layer due to the relative train-track displacement. It is later used to obtain the averaged aerodynamic loading (velocity profile and turbulence) induced on the ballast particles after several train passages, by means of a CFD (computational fluid dynamics) numerical model and field measurements from [3]. Such loads shall be later introduced in a DEM model of the track for the entire flying ballast phenomenon to be modelled [4].

2. Description of the model

The model is based on the hypothesis that the air flux between the train and the ballast can be assimilated to a developed turbulent Couette flux [1] with certain added particularities such as: i) periodical variability of the planar distance due to the presence of sleepers and irregular vehicle geometry (*e.g.*, train equipment, car-car connections); and ii) development of a boundary layer starting from the train nose and extending along the nearby region, which moderates the air flux along the first meters (typically 25 m).

Prior to the development of the model, the reference system (x,y,z) and main planes (top of rail -TOR-, top of sleeper -TOS- and top of ballast -TOB-) shall be identified. In this regard, Fig. 1 presents a schematic description of the aforementioned elements.

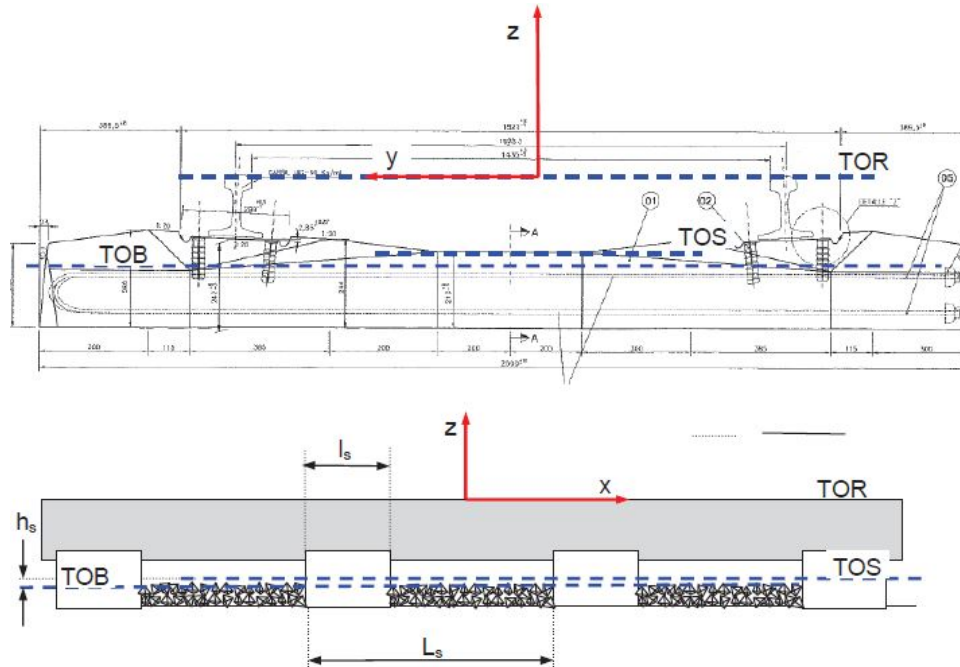


Fig. 1 Scheme of the reference system and main planes

Measurements from previous field data gathering campaigns showed that the maximum train-induced pulling velocities (and thus the maximum aerodynamic loading on the ballast particles) occur in the central area of the track ($y = 0$). Hence, the simplified model has been developed to predict the air flux in such zone and initially, on a point between two sleepers ($x = 0$). The selection of a position in z of for the model definition should take into account that the area of interest is that where the ballast particles are more susceptible of suffering the flying ballast phenomenon (*i.e.*, those directly exposed to the air flux). Given the standard dimensions of a high speed railway line, the minimum reference z value (z_{BS}) can be defined between two sleepers ($-1.5 < x < 1.5$) by eq.(1).

$$z_{BS}(x) = \begin{cases} -1.050 & |x| < 1 \\ -0.875 & 1 < |x| < 1.5 \end{cases} \quad (1)$$

The simplified flux model will be therefore calculated only in the area of occurrence of the phenomenon ($z_{TOR} < z < z_{BS}$). In this regard, for any magnitude φ , the averaged phase value at $x = 0$ can be expressed as:

$$\langle \varphi \rangle(0, z, t) = \langle \varphi \rangle_0(z, t) \quad (2)$$

For a given value of x , the temporal modulation of averaged magnitudes is strongly correlated and hence, the spatial (z) and temporal (t) dependences of eq.(2) can be separated in two components, as in eq.(3).

$$\langle \varphi \rangle_0(z, t) \approx f_{0\varphi}(z) \cdot g_{0\varphi}(t) \quad (3)$$

Averaging eq. (3) along a certain period such as the entire passage of a train (denoted), it is possible to reduce it to eq.(4).

$$f_{0\varphi}(z) = \overline{\langle \varphi \rangle_0(z, t)} \quad (4)$$

Where the averaged function is denoted by an overbar and given that the time-averaging of $\overline{g_{0\varphi}(t)} = 1$. Considering eqs. (3) and (4), the simplified flux description in a point different to $x = 0$ (e.g., over the sleeper in $x = \pm 1.5$) can be done by means of a correction function $f_{1\varphi}(x, z)$, which leads to eq.(5).

$$\overline{\langle \varphi \rangle(x, z, t)} = f_{1\varphi}(x, z) \cdot \overline{\langle \varphi \rangle_0(z, t)} = f_{1\varphi}(x, z) \cdot f_{0\varphi}(z) \quad (5)$$

And therefore,

$$f_{1\varphi}(x, z) = \frac{\overline{\langle \varphi \rangle(x, z, t)}}{f_{0\varphi}(z)} \quad (6)$$

Where $f_{1\varphi}(0, z) = 1$ for any magnitude φ . Moreover, $f_{1\varphi}(x, z)$ can be obtained either through field measurements in different points of the track (i.e., varying x) or by CFD

modelling of the entire flux field along a simplified train-track geometry. Once the correction function is known, the calculation of the phase-averaged field of any fluid variable can be done by means of eq.(7).

$$\langle \varphi \rangle(x, z, t) \approx f_{1\varphi}(x, z) \cdot f_{0\varphi}(z) \cdot g_{\varphi}(x, t) \quad (7)$$

3. Model calibration and validation

The model calibration and validations has been performed by means of a combination of CFD modelling and real field data from a gathering campaign. In this regard, the fluid variables considered have been the phase-averaged axial fluid velocity its fluctuations (u and u' , respectively). The functions $f_{0u}(z)$ and $f_{0u'}(z)$, which refer to the field on a central point between two sleepers ($x = 0$) have been calculated and compared with both, experimental measurements and results from CFD modelling (see Fig. 2) in order to determine the accuracy of the simplified analytical model. The comparison shows a good agreement between both real data and CFD model results with the analytical functions and therefore, the proposed model can be considered valid for estimating the fluid field in a point located in the centre between two sleepers.

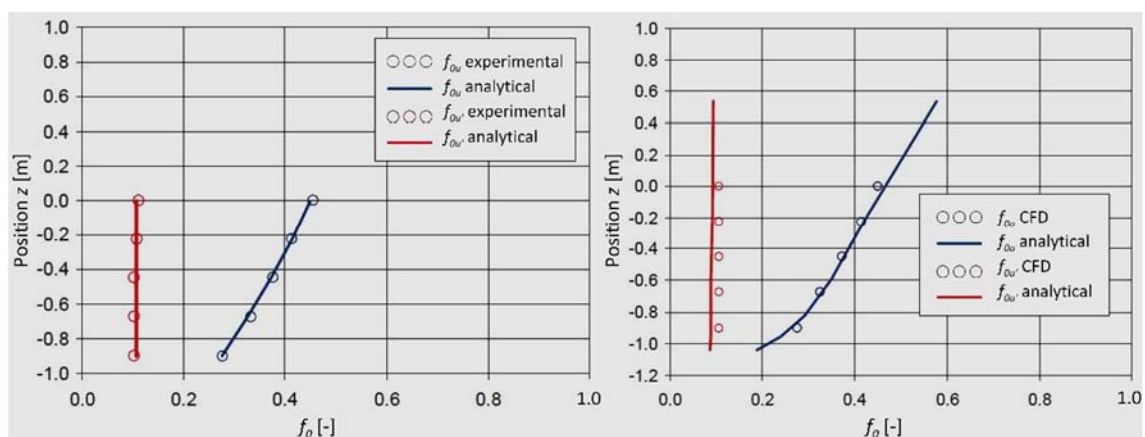


Fig. 2. Comparison of the analytical functions $f_{0u}(x, z)$ -blue- and $f_{0u'}(x, z)$ -red- with real track measurements (left) and CFD modelling results (right).

On the other hand, the correction functions $f_{1u}(x, z)$ and $f_{1u'}(x, z)$ cannot be directly obtained from the analytical model without data provided by numerical simulations or real measurements. In this sense, a comparison between both methods is shown in Fig. 3 for a point located on a sleeper, with the aim of verifying the accuracy of numerical results, which can be obtained in a considerably simpler, faster and less expensive manner. In general terms the comparison proves that although the CFD model does not perfectly reproduce the real measurements, it presents a maximum deviation of 10% and therefore can be considered a valid tool for the estimation of the correction functions.

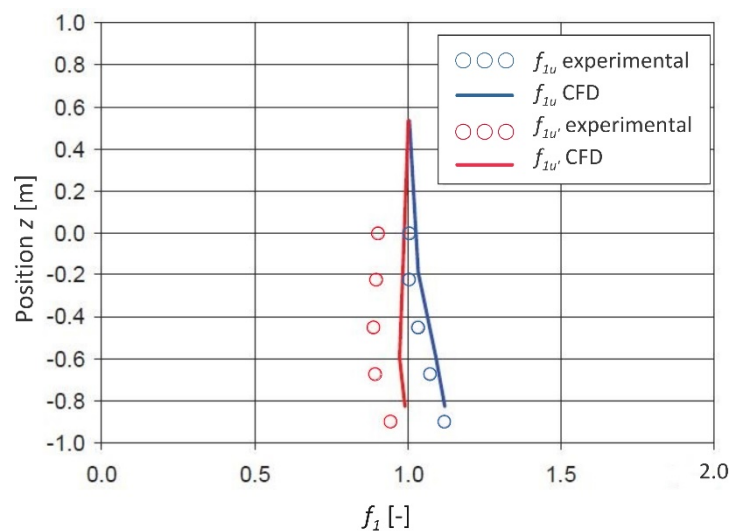


Fig. 3. Correction functions obtained through CFD modelling and experimentally

References

- [1] Quinn, A.D., Hayward, M., Baker, C.J., Schmid, F., Priest, J.A., and Powrie, W. A full-scale experimental and modelling study of ballast flight under high-speed trains. *Journal of Rail and Rapid Transit*, 2009. 224(2): p. 61 - 74.
- [2] Lazaro, B.J., Gonzalez, E., Rodriguez, M., Rodriguez, M., Osma, S., and Iglesias, J. Characterization and Modelling of Flying Ballast Phenomena in High-speed Train Lines, in 9th World Congress on Railway Research 2011: Lille, France. p. 12.

- [3] ADIF Aurigidas: estudio del comportamiento aerodinámico tren-vía a velocidades superiores a 300 km/h. El fenómeno del levante de balasto, 2012, ADIF: Madrid, Spain.
- [4] Real, T., Peset, J., Colomer, E., and Real, J.I. Numerical modelling of flying ballast phenomena on high speed lines. Part B: Analysis of the stability of the ballast layer by means of a DEM model, in *Mathematical Modelling in Engineering & Human Behaviour 2017*: Valencia, Spain.

Numerical modelling of flying ballast phenomenon on high speed lines. Part B: Analysis of the stability of the ballast layer by means of a DEM model

Teresa Real Herráiz^{1}, Joan Peset², Ernesto Colomer Rosell³, Julia Real Herráiz⁴*

*^{1, 3, 4} Institute of Multidisciplinary Mathematics, Polytechnic University of Valencia, Camino de Vera,
46022 Valencia, Spain*

**Corresponding author. E-mail: teresa.real@ua.es. Telephone: +349638770000*

1. Introduction

The projection of ballast particles due to the aerodynamic field generated by the circulation of a train is an issue of major concern for high speed line managers, since it may lead to severe safety and maintenance problems [1]. Hence, a significant research effort has been done in the recent years to better understand the processes involved as well as to propose solutions to reduce the incidence of such phenomenon.

In this sense, the present research project is aimed to develop a new type of ballast made out of modified concrete and high-density recycled materials. Therefore, numerical and physical modelling has been performed in order to test the behaviour of the new material under flying ballast conditions, as well as to determine the most convenient design parameters. Regarding the numerical modelling, it has been divided in two different segments: i) the aerodynamic interaction between the track and the vehicle, which determines the initiation of motion of the ballast particles and is described in detail in [2]; and ii) the mechanical behaviour of the ballast (accounting for its nature as a discrete medium) under the vibrational and aerodynamic excitation induced by the train.

2. Numerical model

This paper delves into the second segment and thus describes in detail the modelling of the ballast particles under certain aerodynamic loading conditions by means of a DEM (discrete element method) model developed within YADE-DEM commercial software. Such technique is based on the discretization of the material in a group of independent elements, which allows to accurately reproduce the discontinuous and heterogeneous nature of ballast. Once the model is defined, a sensitivity analysis has been performed regarding several key parameters.

- *Geometry of the modelled particles*

It has been found that the most adequate solution (taking into account both computing resources and accuracy of results) is to combine several assemblages of 5 to 7 spherical elements with different radius, so that the grading of the final aggregate fulfils the official regulations for high speed railway lines.

- *Settlement of the particles after placement*

In this regard, two cases have been modelled: i) considering only the action of gravity on the ballast particles; and ii) considering the application of an additional compaction force. Results show that the later induces an unrealistic settlement of the modelled particles, creating a flat surface that does not correspond to that of real ballast. Hence, only the action of gravity is considered hereafter.

- *Size and length of the model*

Three different thickness of the ballast layer (15, 40 and 60 cm) and two model lengths (0.6 m and 10 m) have been tested in order to determine the effect on the accuracy of the results. In this sense, a 40 cm thickness of the ballast layer, which fulfils the official requirements for high speed lines, produces accurate results within an acceptable

computational effort. On the other hand, although a 10 m model length yields to very precise results, it also requires unaffordable computation times and thus several random shorter segments (0.6 m long each) have been considered instead. The width of the model has been set to 1.435 m for all the cases.

The conclusions drawn from the sensitivity analysis are of utmost importance for the optimization of the numerical modelling of the entire phenomenon, which has been later performed to determine the optimal shape of the new ballast material. In this concern, the projection of a spherical particle over a 0.6 m ballasted track segment has been reproduced (see Fig. 1). Nine different configurations have been modelled by combining three flying particle weights (100 g, 150 g and 200 g) and three ballast particle shapes (conventional, cubic and spherical). It should be noted that the term “ballast particle shape” refers to the form of the entire assemblage representing each ballast particle, not to the individual elements conforming such assemblages (which are spheres in all cases, as concluded from the sensitivity analysis). Moreover, the conventional shape refers to that characteristic of crushed ballast. The coding of the cases is as follows: a letter A, B or C is related to the projected particle weight, while the number 1, 2 or 3 refers to the ballast shape in the aforementioned orders (*e.g.*, B2 means 150 g and cubic shape).

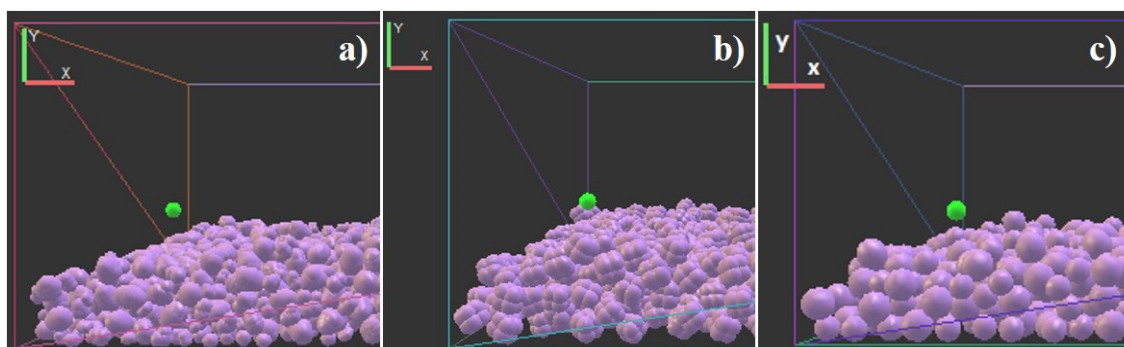


Fig. 1. Modelling of a spherical particle projection over a track segment with different ballast particle shapes: a) conventional; b) cubic; c) spherical.

3. Results

With the purpose of analysing the effect of ballast shape in the flying ballast process (and thus determine the most appropriate shape for the new ballast material), the velocity and position on the longitudinal (x) direction of the projected particle has been calculated for each case for both the aerial and superficial transport phases.

In this regard, Fig. 2 presents the results for a 150 g spherical particle projected over a track segment with conventional-shaped and cubic-shaped ballast particles (*i.e.*, cases B1 and B2, respectively). The initial velocity of the projected particle has been considered to be 1 m/s and its starting position is the centre of the first sleeper ($x = 0.108$ m) in all the scenarios. The abrupt decrease in particle velocity occurring after 0.15 s in case 4 (left) and 0.10 s in case 5 (right) marks the moment when the particle impacts the ballast and the superficial transport phase starts.

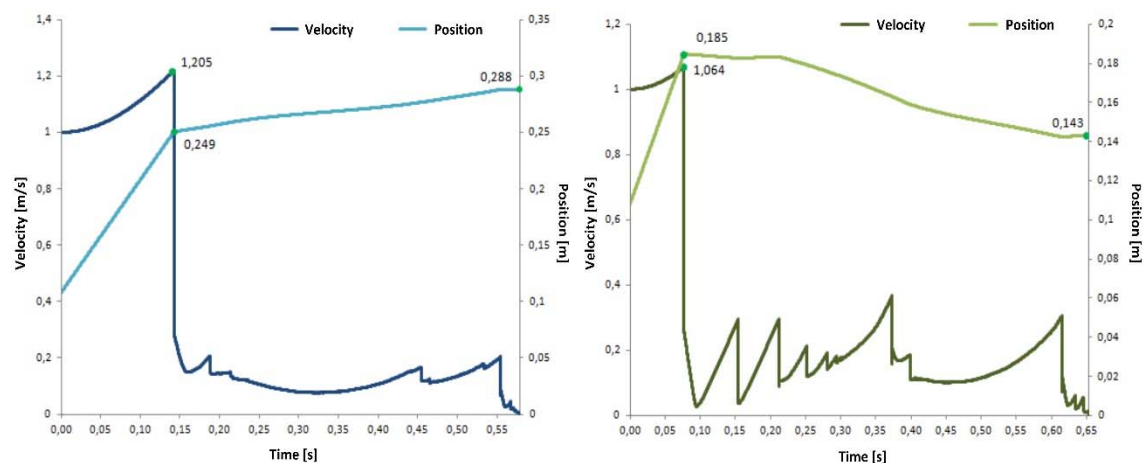


Fig. 2. Particle velocity and position for cases B1 (left) and B2 (right)

On the other hand, Fig. 3 presents the results obtained in cases A3 and C3, which respectively correspond to a 100 g and 200 g particle projected over a track segment with spherical-shaped ballast particles.

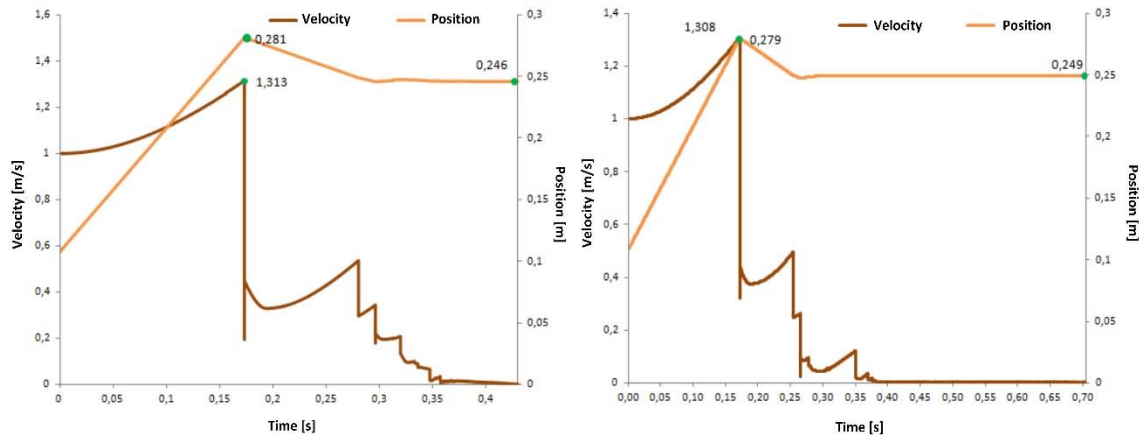


Fig. 3. Particle velocity and position for cases A3 (left) and C3 (right)

Regarding the results shown in Fig. 2 and Fig. 3, it can be concluded that cubic-shaped ballast reduces the particle displacement in both the aerial and superficial transport phases, when compared to the conventional-shaped ballast. Moreover, an increment of the projected particle weight does not necessarily reduce its displacement along the ballast layer. Although for the sake of succinctness, only the results from cases A3, B1, B2 and C3 have been graphically presented in the paper, an accurate analysis of the process should also account for the other 5 modelled combinations. Therefore, a complete overview of the 9 cases is presented in Table 1, where several relevant parameters (*e.g.*, aerial and superficial displacements, impact time) are indicated.

Table 1. Summary of the numerical modelling results

Case	Aerial transport phase		Impact	Superficial transport phase	
	Pos. [m]	Displacement. [m]	Time [s]	Pos. [m]	Displacement [m]
A1	0.250	0.142	0.143	0.254	0.004
A2	0.183	0.075	0.078	0.144	0.039
A3	0.281	0.173	0.175	0.246	0.035
B1	0.249	0.141	0.142	0.288	0.039
B2	0.185	0.077	0.079	0.143	0.042
B3	0.279	0.171	0.169	0.248	0.031
C1	0.246	0.138	0.145	0.262	0.016
C2	0.183	0.075	0.076	0.153	0.030
C3	0.279	0.171	0.162	0.249	0.030

As shown in Table 1, the track segment modelled with cubic-shaped ballast particles presents the lowest displacement values (up to 35% lower) during the aerial phase and the highest ones during the superficial phase for all the considered particle weights. On the other hand, the spherical ballast induces the largest aerial displacements, while the conventional one presents the lower superficial values for all the modelled weights. Nevertheless, the lowest total displacement (*i.e.*, accounting for both phases) is achieved with cubic-shaped ballast, with an average 30% reduction respect to the conventional-shaped particles and 45% respect to the spherical ones.

4. Conclusions

With the aim of studying the flying ballast phenomenon, a 3D DEM numerical model has been presented in this paper and a sensitivity analysis has been carried out to determine the most appropriate model parameters to provide accurate results within an acceptable computation time. Furthermore, the model has been used for analysing three particle shapes for a new ballast under diverse conditions. The major conclusion of such analysis is that the cubic-shaped particles arise as the most convenient ones for the new material, since they provide 30% to 45% lower displacement values than the other two alternatives.

References

- [1] Quinn, A.D., Hayward, M., Baker, C.J., Schmid, F., Priest, J.A., and Powrie, W. A full-scale experimental and modelling study of ballast flight under high-speed trains. *Journal of Rail and Rapid Transit*, 2009. 224(2): p. 61 - 74.
- [2] Masanet, C., Roca, F., del Pozo, J., and Real, J.I. Numerical modelling of flying ballast phenomenon on high speed lines. Part A: Analysis of the train-track aerodynamic interaction by means of field data and a CFD model, in *Mathematical Modelling in Engineering & Human Behaviour 2017*: Valencia, Spain.

Predictive maintenance of tunnels based on real-time acceleration registers on the concrete revetment

Fran Ribes Llarío^{1}, Clara Zamorano Martín², Beatriz Baydal Giner³, José Luis Velarte González⁴*

^{1, 3, 4} Institute of Multidisciplinary Mathematics, Polytechnic University of Valencia, Camino de Vera, 46022 Valencia, Spain

² Universidad Politécnica de Madrid. Calle Ramiro de Maeztu, 7, 28040 Madrid

**Corresponding author. E-mail: frarilla@cam.upv.es. Telephone: +349638770000*

1. Introduction

Properly scheduling maintenance and conservation tasks of a tunnel is a matter of utmost importance in order to ensure its adequate functioning, safety and reliability. In this regard, the most usual maintenance strategy is preventive maintenance, where cyclic conservation tasks are scheduled based on the analysis of historical repair data [1]. However, such approach cannot prevent unexpected system failures and generally implies unnecessary maintenance, since it does not take into account the current health state of the structure, which considerably increases maintenance costs. On the other hand, corrective maintenance is another widely used strategy, where the scheduling of repair and conservation tasks is done after a failure has been detected. Such technique usually involves significant costs and reduces the capacity of the infrastructure, since major repair tasks may be expensive and even require the closure of the tunnel.

Therefore, with the aim of overcoming the drawbacks of the aforementioned methodologies, predictive maintenance arises as a more efficient technique accounting for the real-time health state of the structure. It consists of a continuous monitoring of the tunnel, which allows to evaluate its health state and thus the need of maintenance before

the occurrence of a failure. Furthermore, it should be taken into account that the conservation of the concrete revetment is one of the most important tasks among those composing tunnel maintenance, since this region of the structure is more vulnerable to critical failures [2].

In this regard, a methodology has been developed within this research project for the predictive maintenance of tunnels based on acceleration registers measured on the concrete revetment of the structure.

2. Proposed methodology

For this purpose, tri-axial accelerometers should be placed on the most vulnerable locations (to be determined depending on the typology of the tunnel section) of each instrumented section. Then, the time history of accelerations is transformed into the frequency domain by means of a discrete form of the Fast Fourier Transform (FFT, see eq.(1)) and the *peak picking method* can be applied.

$$x(\omega) = \sum_{r=1}^n x(t) \cdot e^{\frac{2\pi i(r-1)(s-1)}{n}} \quad (1)$$

Where coefficients r and s vary from 1 to n ; and n is the total number of points in the data series. Once in the frequency domain, a low-pass filtering of the signal is performed with the aim of removing high frequencies out of the range of interest (0 – 100 Hz).

The next step is the application of the *peak picking method*, a technique based on the hypothesis that the dynamic response of the resonance peaks is determined by a single mode, which is valid for low damping structures (*e.g.*, concrete) and sufficiently separated modes [3]. Hence, the Power Spectrum Density (PSD) is obtained from the data series in the frequency domain and the average normalized PSD value (ANPSD) is calculated for

every instrumented section of the tunnel. According to the method, if a variation is detected on the first frequency peak of a certain tunnel section, it can be concluded that such section presents damage.

Once the damaged sections have been identified, the PSD ratio (RPSD) is calculated, which permits the classification of the damage into four different categories depending of its variation: i) no defect if the variation is close to zero; ii) presence of cavities or lack of thickness if it is constantly negative; iii) perimeter crack if it is constantly positive; and iv) radial crack if the variation does not present a clear trend and oscillates around zero.

Finally, the location and magnitude of the damage can be determined by comparing the acceleration measurements on the studied section with the results provided by a 2D Distinct Element Method (DEM) numerical model. To this aim, a variety of cases comprising different damage typologies, magnitudes and positions should be executed and analysed prior to the implementation of the method, thus creating a wide damage catalogue valid for any section of the tunnel.

Such numerical technique considers materials as a group of individual particles, thus permitting independent displacements and rotations of each one, as well as the occurrence of new contacts/loss of contact between them. Therefore, it constitutes an excellent tool for the numerical modelling of cases where discontinuities appear on the material as a consequence of the deformation process. The Mohr-Coulomb criteria and the Coulomb sliding criteria have been adopted for the modelling of the mechanical behaviour of the rock and the rock-revetment interface, respectively. Moreover, a Rayleigh damping coefficient of 1-2% and viscous boundary conditions have been considered in order to accurately reproduce real materials and avoid boundary reflections.

3. Cases of study

Approached casuistry is based on different three different type of defects performance: longitudinal cracks, circumferential cracks and cavity. Thus, variables of study are, for each defect, location, depth (only in cracks), amplitude angle (cavity and circumferential cracks) and growing direction (back-through-inside / inside-through-back in longitudinal cracks and cavities). This results in 26 different scenarios (25 damaged plus 1 undamaged as reference).

3. Results and discussion

Logarithmic normalization of RPSD (NRPSD) was established in order to enable an adequate comparison between different direction RPSD – which often differ in more than one order of magnitude -.

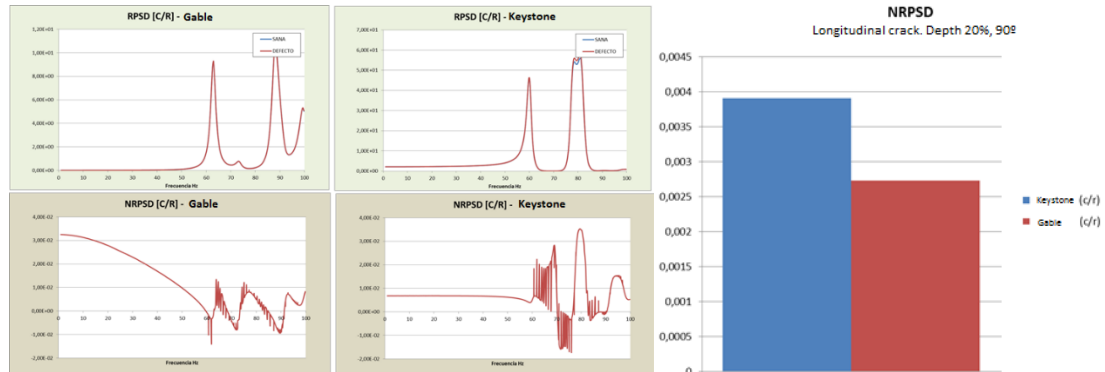


Fig. 1: Example of RPSD circumferential/radial (top left), NRPSD (c/r) vs freq. (bottom left) and averaged NRPSD (right).

NRPSD histograms were compared in order to characterize the influence of each defect properties and establish a behaviour pattern for its identification.

For longitudinal cracks, depth increase is proportional to $RPSD^{C/R}$ increase (i), invert growing direction also inverts the sign of $RPSD^{C/R}$ (ii), inside-to-back direction originates greater absolute $RPSD^{C/R}$ values than backwards (iii).

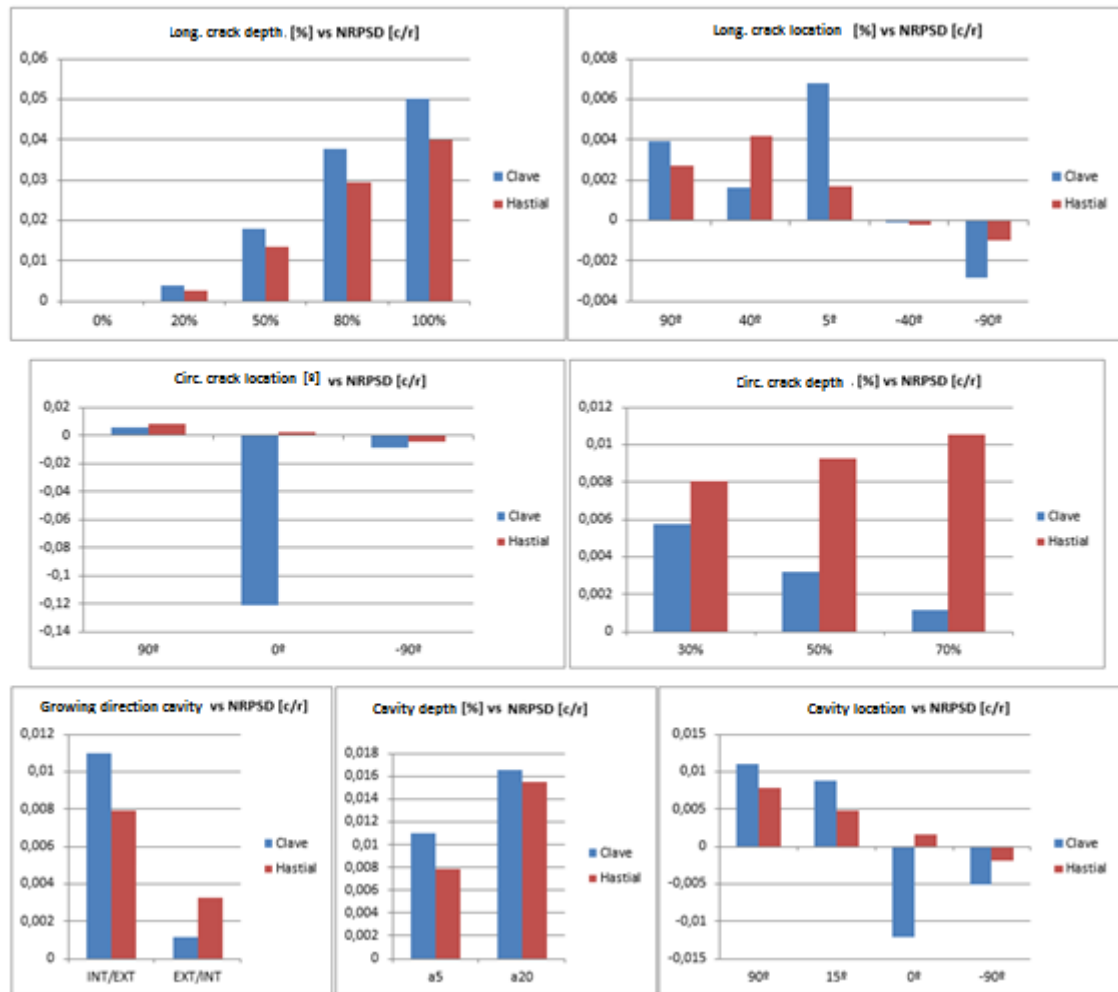


Fig. 2: Defect parameters influence on $NRPSD^{C/R}$ comparison.

For circumferential cracks: major amplitude increases $RPSD^{C/R}$ values (iv); usually, glade accelerometers will detect more intensity signal ($RPSD$) than keystone ones (v); as crack location depth increases, as higher difference values between glade and keystone $RPSD$ are obtained (vi); circumferential cracks cause major absolute values of $RPSD^{C/R}$ than longitudinal ones (vii).

For cavities: which are located on the inside surface of lining, keystone sensor will register more intense signal than gable one (viii); $RPSD^{C/R}$ increases with cavity amplitude angle as also occurs in circumferential cracks (ix);

4. Conclusions

In this paper, 26 different scenarios have been approached to analyse the influence of different parameters which define the defect location and magnitude. One of this scenarios correspond to undamaged section and was used to calibrate a 2D DEM model which was used after to replicate 25 alternatives of damage based on three most common defect types: longitudinal cracks, circumferential cracks and cavities.

A damage indicator based on the relationship between different directions (Circumferential [C], Radial [R] and Longitudinal [L]) stiffness (RPSD) was used.

Exposed methodology enables to detect, identify, quantify and gives an approximated location of three different types of defects in tunnel lining using only a couple of accelerometers per section.

5. References

- [1] Lee, D. and Pan, R. Predictive maintenance of complex system with multi-level reliability structure. *International Journal of Production Research*, 2017: p. 1-17.
- [2] Yuan, Y., Jiang, X., and Liu, X. Predictive maintenance of shield tunnels. *Tunnelling and Underground Space Technology*, 2013. 38: p. 69 - 86.
- [3] Freire, C. Implementación y validación del método mejorado de descomposición en el dominio de la frecuencia (EFDD) para la identificación de los parámetros modales de estructuras genéricas utilizando ruido ambiente. Estudio del rango de aplicabilidad en función del modelo estructural y las condiciones de uso, 2011, Universidad de Las Palmas de Gran Canaria: Spain.

Stability of parametric family of iterative methods for root-finding *

Alicia Cordero[†], Lucía Guasp[‡] and Juan R. Torregrosa[§]

Instituto de Matemáticas Multidisciplinar,

Universitat Politècnica de València, Camino de Vera, s/n, 46022-Valencia, Spain

November 30, 2017

1 Introduction

Nonlinear systems $F(x) = 0$, where $F : D \subseteq \mathbb{R}^n \rightarrow \mathbb{R}^n$, $n \geq 1$, is a nonlinear function defined in a convex set D , are often used for modeling real problems arising in science and engineering as, for example, in the analysis of dynamical models of chemical reactors, preliminary orbit determination of satellites, in radioactive transfer, in economics modeling problems, transport theory, etc. These problems lead to a rich blend of mathematics, numerical analysis and computing science.

In general, for solving these equations iterative methods must be used. The proliferation of iterative schemes for solving nonlinear equations ($n = 1$) has been spectacular in the last years (we can see an overview in [1]). The most of them are variants of Newton's method obtained by means of different procedures. The direct composition of known methods with a later treatment to reduce the number of functional evaluations, the weight function procedure, etc. are some of the most used techniques for designing new schemes.

*This research was partially supported by Ministerio de Economía y Competitividad MTM2014-52016-C2-2-P and Generalitat Valenciana PROMETEO/2016/089

[†]e-mail: acordero@mat.upv.es

[‡]e-mail: luguaal@ade.upv.es

[§]e-mail: jr Torre@mat.upv.es

In the literature, iterative methods are analyzed under different points of view. A research area that is getting strength nowadays consists of applying discrete dynamics techniques to the associated fixed point operator of iterative methods. The dynamical behavior of such operators when applied on the simplest nonlinear function (a low degree polynomial) gives us relevant information about its stability and performance. This study is focused on the asymptotic behavior of fixed points, as well as in its associated basins of attraction. Indeed, in case of families of iterative schemes, the analysis of critical points (where the derivative of the rational function is null), different from the roots of the polynomial, not only allows to select those members of the class with better properties of stability, but also to classify iterative methods of the same order in terms of their dynamics.

In the last years, the use of tools from complex dynamics has allowed the researchers in this area of numerical analysis to deep in the understanding of the stability of iterative schemes (see, for example, [2–6]). The analysis, in these terms, of the rational function R associated to the iterative procedure applied on quadratic polynomials, gives us valuable information about its role on the convergence's dependence on initial estimations, the size and shape of convergence regions and even on a possible convergence to fixed points that are not solution of the problems to be solved or to attracting cycles. Moreover, if a family of parametric schemes is studied, the most stable elements of the class can be chosen, by means of an appropriate use of the parameter plane.

In this paper, we analyze the dynamical behavior of a parametric family of two steps iterative methods, for solving nonlinear equations $f(x) = 0$, whose iterative expression is

$$\begin{aligned} y_k &= x_k - \frac{f(x_k)}{f'(x_k)}, \\ x_{k+1} &= y_k - \left(\alpha_1 + \alpha_2 \frac{f'(y_k)}{f'(x_k)} + \alpha_3 \left(\frac{f'(y_k)}{f'(x_k)} \right)^2 \right) \frac{f(y_k)}{f'(x_k)}, \end{aligned} \quad (1)$$

for $k = 0, 1, 2, \dots$, where α_1 , α_2 and α_3 are parameters.

The following result establishes the order of convergence of family (1).

Theorem 1 *Let $f : D \subseteq \mathbb{R} \rightarrow \mathbb{R}$ be sufficiently differentiable at each point of an open interval D such that $\bar{x} \in D$ is a simple solution of equation $f(x) = 0$ and the initial estimation x_0 is close enough to \bar{x} . Then, sequence $\{x_k\}_{k \geq 0}$*

obtained from expression (1) converges to \bar{x} with order 4 when $\alpha_2 = 3 - 2\alpha_1$ and $\alpha_3 = -2 + \alpha_1$, being in this case the error equation

$$e_{k+1} = (13 - 4\alpha_1)C_2^3 e_k^4 + O(e_k^5)$$

where $C_j = \frac{1}{j!} \frac{f^{(j)}(\bar{x})}{f'(\bar{x})}$, $j = 2, 3, \dots$ and $e_k = x_k - \bar{x}$.

There exists an element of the family, corresponding to $\alpha_1 = 13/4$, with fifth-order of convergence.

2 Dynamical behavior

In order to analyze the dynamical behavior of family (1) on quadratic polynomials we choose a generic one $p(z) = (z - a)(z - b)$, with $a \neq b$. If we apply (1) on $p(z)$, a rational operator depending to parameters a, b and α_1 , $T_{p,\alpha_1,a,b}(z)$, is obtained.

By means of the conjugacy map $h(z) = \frac{z - a}{z - b}$, (a Möbius transformation), with the following properties:

$$\text{i) } h(\infty) = 1, \quad \text{ii) } h(a) = 0, \quad \text{iii) } h(b) = \infty,$$

operator $T_{p,\alpha_1,a,b}(z)$ on quadratic polynomials is conjugated to operator $O_{\alpha_1}(z)$,

$$\begin{aligned} O_{\alpha_1}(z) &= (h \circ T_{p,\alpha_1,a,b} \circ h^{-1})(z) \\ &= -z^4 \frac{13 - 4\alpha_1 + 14z + 14z^2 + 6z^3 + z^4}{-1 - 6z - 14z^2 - 14z^3 - 13z^4 + 4\alpha_1 z^4}. \end{aligned} \tag{2}$$

We analyze the fixed and critical points of operator $O_{\alpha_1}(z)$. Some results about the stability of the fixed points are obtained and the behavior of the independent free critical points, used as initial guesses, give us interesting parameter planes. From them (see Figure 1) we can extract valuable information about the stability of the different members of the family.

This parameter plane has been obtained by associating each point of the plane with a complex value of α_1 , i.e., with an element of family (1). Every value of α_1 belonging to the same connected component of the parameter plane give rise to subsets of schemes of family (1) with similar dynamical behavior.

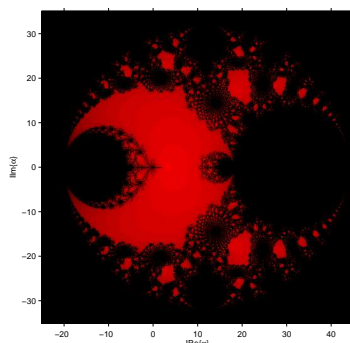


Figure 1: Parameter plane of family (1)

When we consider the free critical points (critical points different to the roots) as a starting point of the iterative scheme of the family associated to each complex value of α_1 , we paint this point of the complex plane in red if the method converges to any of the roots (zero and infinity) and they are black in other cases. A mesh of 1000×1000 points has been used, 500 has been the maximum number of iterations involved and 10^{-3} the tolerance used as a stopping criterium.

The dynamical plane associated to a value of the parameter, that is, obtained by iterating an element of family, is generated by using each point of the complex plane as initial estimation. We paint in blue the points whose orbit converges to infinity, in orange the points converging to zero, in other colors those points whose orbit converges to one of the strange fixed points and in black if it reaches the maximum number of iterations without converging to any of the fixed points.

There are some regions in the parameter spaces whose corresponding iterative methods have good numerical behavior, in terms of stability and efficiency. We have chosen some values in these regions $\alpha_1 = 13/4, 2, 12, 8$ and we have shown in Figure 2 the corresponding dynamical planes.

On the other hand, unstable behavior is found when we choose values of α_1 in the black region of parameter planes. In Figure 3 we show the dynamical planes of the iterative schemes corresponding to the values of parameter $\alpha_1 = -30, 69, 16$.

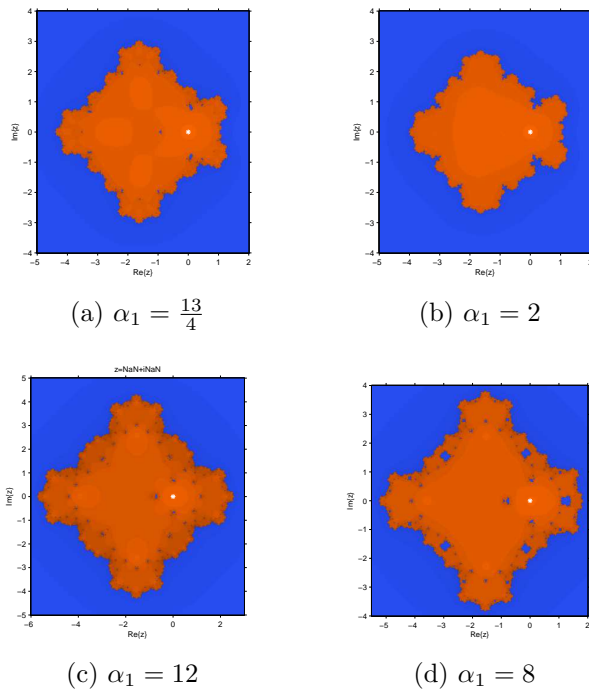


Figure 2: Some dynamical planes with stable behavior

References

- [1] Cordero, A. and Torregrosa, J.R. On the design of optimal iterative methods for solving nonlinear equations, Chapter of the book: *Advances in iterative methods for nonlinear equations*, Springer 2016.
- [2] Amat S., Busquier S., Bermúdez C. and Plaza S. On two families of high order Newton type methods, *Appl. Math. Lett.* 25: 2209–2217, 2012.
- [3] Cordero A., Ferrero A. and Torregrosa J.R. Study of the dynamics of third-order iterative methods on quadratic polynomials, *Math. Comput. Simulations*, 119: 57–68, 2016.
- [4] Cordero A., García-Maimó J., Torregrosa J.R., Vassileva M.P. and Vindel P. Chaos in King’s iterative family, *Appl. Math. Lett.* 26: 842–848, 2013.

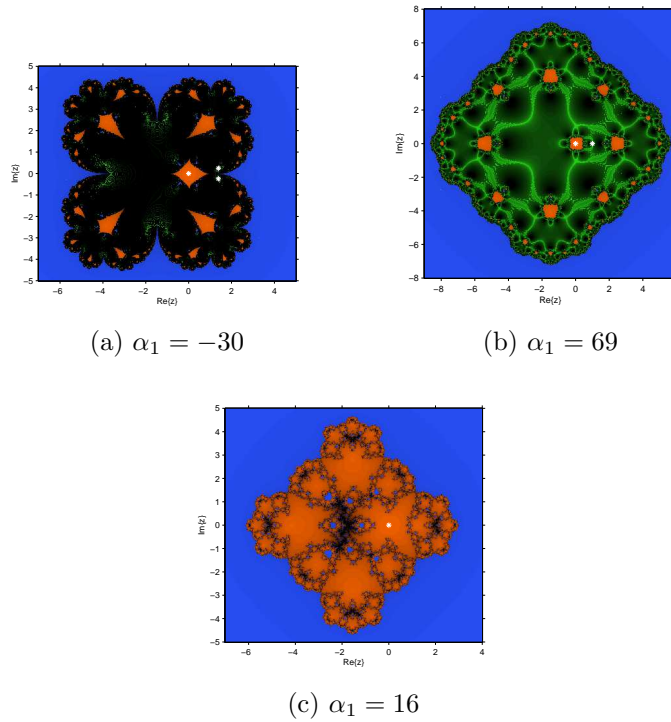


Figure 3: Dynamical planes with unstable behavior

- [5] Cordero A., Torregrosa J.R. and Vindel P. Dynamics of a family of Chebyshev-Halley type method, *Appl. Math. Comput.* 219: 8568–8583, 2013.
- [6] Neta B., Chun C. and Scott M. Basins of attraction for optimal eighth order methods to find simple roots of nonlinear equation, *App. Math. Comput.* 227: 567–592, 2014.
- [7] Sharma J.R. and Arora H. Improved Newton like methods for solving systems of nonlinear equations, *Sema Journal*, 74: 147–163, 2017.

Network analysis for inferring spatio-temporal predictive models in water demand consumption

C. Navarrete-López^b, M. Herrera^o*, B. M. Brentan[†], E. Luvizotto Jr[†]
and J. Izquierdo[‡]

(^b) Faculty of Environmental Engineering, Universidad Santo Tomás, Bogotá, Colombia

(^o) EDEn - Dept. of Architecture and Civil Eng., University of Bath, UK

([†]) Computational Hydraulic Laboratory, University of Campinas, Brazil

([‡]) Fluing - IMM, Universitat Politècnica de València, Spain

November 30, 2017

1 Introduction

This work proposes to approach multiple time series analysis of water consumption data. The information is arranged in a network composed by water sources and consumption nodes. The abstraction of a water distribution system (WDS) to a network analysis is approached by understanding water pipes (or set of pipes) as network links. Reservoirs, tanks, and water consumption points (or set of points forming district metered areas) are represented as network nodes. These nodes have different properties depending on the role they have on the water supply. Basic network analyses provide information regarding the most important link in the network or the nodes most strongly or weakly connected to water sources such as reservoirs and tanks. This prior information is based on graph-theoretical measures such as edge and node betweenness, k-shortest paths, and minimal spanning trees [1]. After

*amhf20@bath.ac.uk:

approaching this graph-theoretical framework it is possible to have valuable network characteristics. This opens the possibility to know which network areas are strongly correlated among themselves or which links are the most important for meeting water demand requirements at every node.

The process continues by proposing a WDS division into district metered areas (DMA). Historical records of water demand are collected at each of these DMA and a multiple time series analysis is approached at several levels of resolution of the water demand time series. The proposal is that the predictive model computed at any DMA can support the predictive model approached for another DMA depending on the relationship among these network areas. This work introduces a neural network framework to handle this interconnectivity of spatially distributed predictive models. To speed up the whole process while maintaining a high accuracy it is proposed an Extreme Learning Machine process [2]. This is conditioned by predictive models coming from another DMAs. We find out that this combined model beats single approaches accuracy when testing its performance.

2 Conditioning Extreme Learning Machines

An artificial neural network (ANN) is an interconnected group of artificial neurons. Each neuron executes a non-linear computation based on the input values and the resulting value is fed to other neurons. Neurons are usually arranged as series of interconnected layers. Based on the data presented to the network, an algorithm (usually back-propagation) is used to iteratively adjust the neuron connection weights so as to improve the predictive performance of the network [3].

An Extreme Learning Machine (ELM) is a 2-layer ANN in which the hidden nodes are randomly initialized and then fixed without iteratively tuning. The only free parameters need to be learned are the connections (or weights) between the hidden layer and the output layer [4]. This guarantees a superior regularization performance and consequently a better generalization for the model. There exists the possibility of ill conditioning the ELM output model approach if there is not a priori notion of scaling the first layer. This is the main aim of this work, where instead of using random seeds it is proposed to use as ELM input ANN features computed for each DMA in which the original water network is divided. This is done as the database is spatially distributed in several related time series corresponding to the above men-

tioned DMAs. The ANN for the i -th DMA will impact the ELM for the j -th DMA following the relationship given by the correlation between the i -th and j -th DMA demands, and geo-social and topological characteristics. This represents the basis for a conditioning ELM approach, which overall process is shown in Figure 1

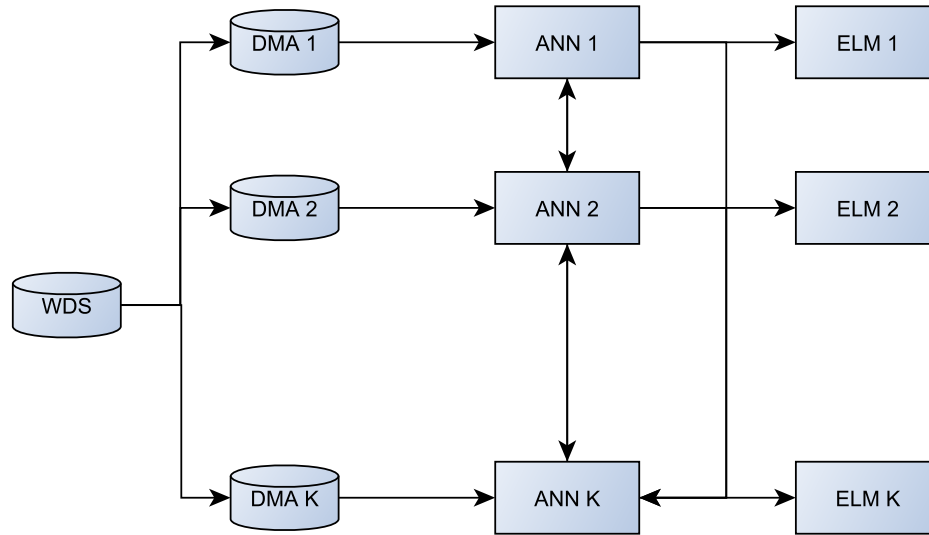


Figure 1: Proposed scheme for a spatio-temporal conditioning ELM process

3 Experimental study

This study uses water demand data collected from operational DMAs in Franca, Brazil, as an extension of the previous case-study already analysed by the authors [5]. Water consumption data corresponds to metered data at each DMA inlet every 20 minutes from May 2012 until December 2013. The results enhance previous approaches providing higher accuracy. As the model takes into account spatio-temporal characteristics it supports a better understanding on how water demand has DMA relationships varying throughout the whole WDS.

4 Conclusions

This work takes advantage of a previous DMA partition of a water network to improve the efficiency and accuracy of predictive models. So, time series forecasting are shown to be enhanced by ensemble of spatially related predictive models. This is investigated by proposing a novel conditioning approach for the ELM algorithm in which the initial values are inherited by combining individual, previously computed, predictive models per DMA.

ELM learning speed can be thousands of times faster than traditional feed-forward network learning algorithms such as back-propagation. Further work on near real-time water management control and operation can be focused on having major advances w.r.t. these good ELM properties.

References

- [1] Manuel Herrera, Edo Abraham, and Ivan Stoianov. A graph-theoretic framework for assessing the resilience of sectorised water distribution networks. *Water Resources Management*, 30(5):1685–1699, 2016.
- [2] Guang-Bin Huang, Qin-Yu Zhu, and Chee-Kheong Siew. Extreme learning machine: theory and applications. *Neurocomputing*, 70(1):489–501, 2006.
- [3] Christopher M Bishop. *Neural networks for pattern recognition*. Oxford university press, 1995.
- [4] Gao Huang, Guang-Bin Huang, Shiji Song, and Keyou You. Trends in extreme learning machines: A review. *Neural Networks*, 61:32–48, 2015.
- [5] Bruno M Brentan, Edevar Luvizotto Jr, Manuel Herrera, Joaquín Izquierdo, and Rafael Pérez-García. Hybrid regression model for near real-time urban water demand forecasting. *Journal of Computational and Applied Mathematics*, 309:532–541, 2017.

A Procedure of Generation of Directed Graphs for the Comparative Study of Algorithms for the Detection of Communities.

J.M. Montañana^b *, A. Hervás[†], and P.P. Soriano[‡]

(b) High Performance Computing Center Stuttgart (HLRS)

University of Stuttgart, Stuttgart, Germany. <http://orcid.org/0000-0002-7522-3423>

(†) Instituto Universitario de Matemática Multidisciplinar,

Universitat Politècnica de València, València, Spain, <http://orcid.org/0000-0002-6880-502X>

(‡) SEPyC,

Universitat Politècnica de València, València, Spain, <http://orcid.org/0000-0002-9147-2681>.

1 Introduction

Many complex systems in the real world in which there is interaction between the elements can be modeled as graphs or networks. The elements are represented by nodes and the relationships between them as edges. We can talk about directed graphs and symmetric or non-directed graphs. In some cases, the relations, edges, have associated attributes that may be numeric, which we call weights, or categorical, called labels.

We can find graphs where the elements are highly related among them, there are many more edges than nodes: dense graphs, or what is more usual, graphs where the number of edges is much smaller than they could have at most: dispersed graphs.

A common characteristic element on these graphs is the existence of certain sets of nodes referred as communities. The nodes in a community are highly connected between them and poorly connected with nodes at other communities. Nodes grouped in the same community have common characteristics that make them play a certain role within the graph.

*e-mail: ahervas@mat.upv.es

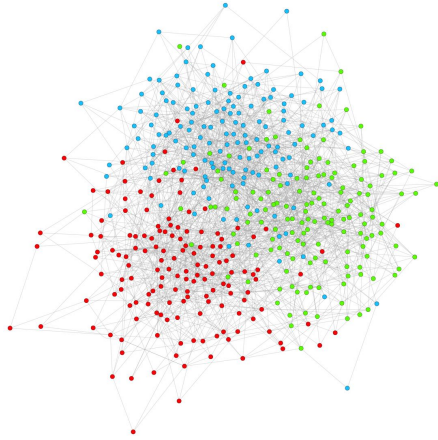


Figure 1: Dense graph

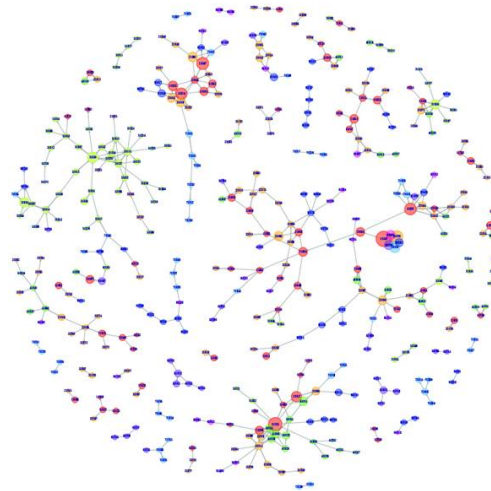


Figure 2: Disperse Graph

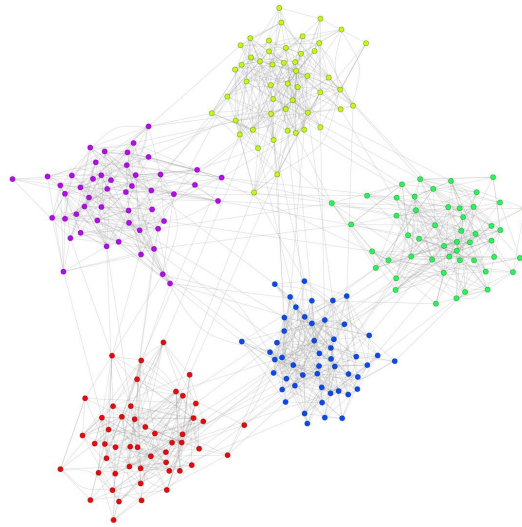


Figure 3: Communities in a graph

Several techniques and algorithms have been developed for the detection and study of communities, which is a constantly evolving area of work. Each

algorithm may detect different communities in the same graph, which goodness has to be analyzed depending on the properties of the graph.

In order to be able to compare the capacity of these algorithms it can be used synthetic community graph generators on which these algorithms of community detection can be applied, and in this way obtain benchmarking of their detection capacities.

The benchmarking process consists of generating graphs with those algorithms, and apply the detection algorithm under study after the addition of new edges between nodes of different communities.

The NMI index allows to compare the different detection of communities: If communities are the same, then, the value of NMI is 1; while in the opposite case, if the communities are completely different, then, the value is 0. These graphs show the added percentage of links between communities on the x-axis, and the degree of similarity in the detected communities on the y-axis.

The high number of edges within communities allows continuing to detect the same communities even after adding some links between communities. Previous works show that the original set of communities at some different types of graphs is no longer detected after increasing a 50% the number of edges.

Notice that the most common practice in designing these generators is to use random graphs, assigning probabilities to the existence of each edge. This allows obtaining different types of graphs, more or less homogeneous, according to the established criteria [1, 2, 3, 4]. However, even there are synthetic graph generators for a wide variety of graphs, there is some kind of graphs not being generated. In particular, there are not any generator which produces graphs like in Figure 2.

In our work, we are interested in finding the communities in graphs like the one in Figure 2, which is a disperse graph with directed and weighted edges. That graph is not homogeneous, the weights of the edges are very different, not all nodes are connected to the rest within the same community. In particular, the Girvan-Newman algorithm is not able to detect these communities after adding a few edges between communities [1, 6].

2 Algorithm

In the best of our knowledge, the main existing Graph generator was published in [4]. The next command line produces the most similar graph to the

graph in the Figure 2 that can be generated with it. The parameters in the command line corresponding to the statistical values of the Figure 2.

`./benchmark -N 200 -k 2.48 -maxk 9 -mut 0 -muw 0 -minc 3 -maxc 36`

Unfortunately, the distribution in our graph shows a large number communities of small size than those of other sizes, (see Figure 2). However, the synthetic has a linear proportion between the number of communities of each size and the community sizes. In particular, our analysis shows that our distribution of community sizes is adjusted with a Weibull function, such distribution appears in Figure 4.(a).

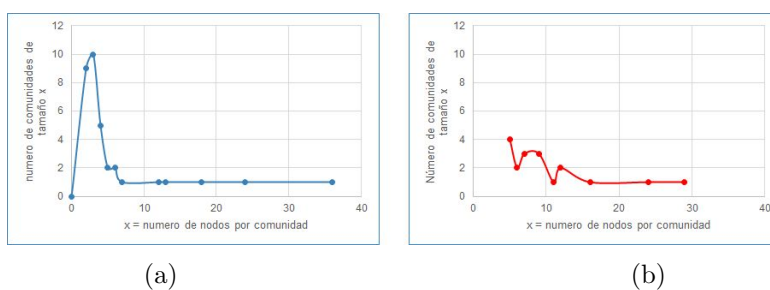


Figure 4: Amount of communities by their number of nodes, (a) for the graph in the figure 2, and (b) for the graph generated with [4].

The existing random graph generators require as input statistics the bounding limits on the number of nodes per community, number of communities, and the amount of edges per node. However, it is not enough for generating graphs like in Figure 2. Therefore, we consider that it is needed additional parameters like the number of nodes per community and number of communities. In this paper, we propose the algorithm 1, which generates communities with the distribution of sizes defined by the Weibull function, and the edges and their weights are defined random paths inside each community.

3 Conclusions

We proposed a generator of directed weighted graphs which accepts the same input parameters as the “Fortunato et al” generator: the number of vertices, the average degree of edges, the maximum degree of edges, the minimum for the community sizes and the maximum for the community sizes.

Algorithm 1: Directed Graphs Generator

```

1 Function Generator (total_communities)
   // Definition of the size of each community
2   for  $c = 0 \rightarrow total\_communities - 1$  do
3      $num\_vertices\_community[c] = rand\_scaled\_weibull(total\_communities)$ 
   // Definition of the number of output links of each vertex
4   for  $v = 0 \rightarrow num\_vertices\_community[c] - 1$  do
5      $N = num\_vertices\_community[c]$ 
6      $total\_output\_edges[c, v] = round(rand\%(1.2/\sqrt{N} + 1))$ 
   // Edges in the community are defined using random paths
7   for  $path = 1 \rightarrow 100 + num\_vertices\_community[c] * 20$  do
8     if  $path == 1$  then
9        $v = rand\_weibull\_vertex(c)$ 
10       $inc\_weight = 1.21$ 
11      for  $step = 1 \rightarrow 5$  do // length of the path
12         $output\_edge = rand\%total\_output\_edges[c, v]$ 
13         $edge\_weight(v, output\_edge) * = inc\_weight$ 
14        if  $undefined\_output\_edge(v, output\_edge)$  then
15           $next\_v = rand\_weibull\_vertex(c)$ 
16           $define\_output\_edge(v, output\_edge, next\_v)$ 
17        else
18           $next\_v = next\_vertex(v, output\_edge)$ 
19         $v = output\_edge$ 

```

In addition, it provides the desired distribution of community sizes and the distribution of weights of links as in the graph of the Figure 2.

References

- [1] Girvan M. and Newman M. E. (2002). Community structure in social and biological networks. *Procs of the National Academy of Sciences*, vol. 99, no. 12, pp. 7821-7826.
- [2] Lancichinetti A. and Fortunato S. (2009) Community detection algorithms: A comparative analysis. *Physical review E* 80(5):056117.
- [3] Lancichinetti A. and Fortunato S. (2009). Benchmarks for testing community detection algorithms on directed and weighted graphs with overlapping communities. *Physical review E* 80(1):016118.

- [4] Lancichinetti A., Fortunato S., and Radicchi F. (2008). Benchmark graphs for testing community detection algorithms. *Physical review E* 78(4):046110.
- [5] Newman, M. E. (2003). The structure and function of complex networks. *SIAM review*, 45(2), 167-256.
- [6] Newman M. E. and Girvan M. (2004). Finding and evaluating community structure in networks *Physical review E*, vol. 69, no. 2, p. 026-113.

A discontinuous Galerkin framework for option pricing problems with stochastic volatilities

J. Hozman^{b*} and T. Tichý[†]

(b) Faculty of Science, Humanities and Education, Technical University of Liberec,
Studentská 2, 461 17 Liberec, Czech Republic,

(†) Faculty of Economics, VŠB-Technical University of Ostrava,
Sokolská třída 33, 702 00 Ostrava, Czech Republic.

November 30, 2017

1 Introduction to one-factor stochastic volatility models

The modern theory of option pricing was based on the ideas of Black-Scholes (BS) framework firstly published in [1]. Nowadays it is widely accepted that these models are not sufficiently accurate in capturing the real world features of the stock markets, because its idealized assumptions do rarely hold in practice. One of them is the limitation of constant volatility, which can be relaxed by models with assumptions of stochastic volatility. There are a number of models, e.g., models by Hull-White [6], Scott [8], Stein-Stein [10] or Heston [4]. A standard mathematical approach to these models leads to partial differential equations (PDEs) completed by the system of boundary and terminal (initial) conditions, where the (semi) closed-form solution is not always attainable and one has to construct numerical approximations.

The performance demands on the numerical valuation process is very high and several techniques have been developed to obtain efficient pricing

*e-mail: jiri.hozman@tul.cz

algorithms over last years, from lattice/trees methods [2], over finite difference schemes [9] to finite element approaches [11]. These methods have also its limitations in the treatment of numerical option pricing under more complex market conditions such as an assumption of a stochastic volatility. Therefore, it should be convenient to follow novel alternative option pricing schemes which are also robust with respect to different market conditions that need to be taken into account. In this work we propose a numerical technique based on the discontinuous Galerkin method (see [7]) to unify the option pricing under a wide spectrum of volatility models with one stochastic process.

Let us consider a financial asset whose price is given by the stochastic differential equation

$$dS_t = \mu S_t dt + \sigma_t S_t dW_t, \tag{1}$$

where $\mu S_t dt$ is a drift term with a constant rate μ , W_t is a Brownian motion and σ_t is the volatility. Further, we assume that $\sigma_t = f(Y_t)$ for some non-negative function f with the domain of definition D_f and Y_t is the general driving process

$$dY_t = A(Y_t)dt + B(Y_t)dZ_t, \tag{2}$$

where nothing will be assumed about the functions $A(\cdot)$ and $B(\cdot)$, and the second Brownian motion Z_t is correlated to W_t with factor $\rho \in (-1; 1)$.

Note that a suitable choice of A and B can include different processes such as lognormal, mean-reverting OU process or CIR process. Secondly, the setting of f together with the value of the correlation coefficient leads to particular stochastic volatility models. The frequently used models are listed in the following table (α, β and m are nonnegative constants).

Model	$A(Y)$	$B(Y)$	function f	correlation
Heston	$\alpha(m - Y)$	$\beta\sqrt{Y}$	$f(Y) = \sqrt{Y}$	$\rho \neq 0$
Hull-White	αY	βY	$f(Y) = \sqrt{Y}$	$\rho = 0$
Scott	$\alpha(m - Y)$	β	$f(Y) = \exp(Y)$	$\rho = 0$
Stein-Stein	$\alpha(m - Y)$	β	$f(Y) = Y $	$\rho = 0$

Next, we consider a European option on the financial asset S (for the sake of clarity we omit the subscript t) with maturity T and assume instantaneous risk-free interest rate r . The option price $V(S, Y, t)$ depends on the underlying asset S , the driving process Y and the actual time t . A common approach based on no arbitrage principle, Itô stochastic calculus and a construction of

a sophisticated portfolio lead to the pricing PDE, which can be decomposed in the following way

$$\frac{\partial V}{\partial t} + \mathcal{L}_{BS}^f(V) + \mathcal{L}_{corr}^f(V) + \mathcal{L}_{proc}(V) - \mathcal{L}_{prem}(V) = 0, \quad (3)$$

for $S > 0, Y \in D_f, t \in [0, T)$. The differential operators in (3) represent Black-Scholes part, correlation, driving process and premium defined as

$$\begin{aligned} \mathcal{L}_{BS}^f(V) &= \frac{1}{2}f^2(Y)S^2\frac{\partial^2 V}{\partial S^2} + rS\frac{\partial V}{\partial S} - rV, & \mathcal{L}_{corr}^f(V) &= \rho B(Y)Sf(Y)\frac{\partial^2 V}{\partial S\partial Y}, \\ \mathcal{L}_{proc}(V) &= \frac{1}{2}B^2(Y)\frac{\partial^2 V}{\partial y^2} + A(Y)\frac{\partial V}{\partial Y}, & \mathcal{L}_{prem}(V) &= B(Y)\Lambda(S, Y, t)\frac{\partial V}{\partial Y}, \end{aligned}$$

where the premium term $\mathcal{L}_{prem}(V)$ represents the market price of the volatility risk defined by the specific function Λ for particular stochastic volatility model.

In order to obtain the initial boundary value problem, the pricing equation has to be restricted to a bounded domain $\Omega \subset \mathbb{R}^+ \times D_f$ and closed with the set of initial and boundary conditions. Since (3) is backward in time, the terminal (initial) condition at maturity date T is given by the payoff function $V^0(S)$ depending on the type of an option (call or put). Due to the localization of (3) on Ω , one has to prescribe mixed boundary conditions on appropriate parts of $\partial\Omega$, which are chosen compatible with the payoff and using knowledge on the asymptotic behavior of options.

2 Numerical approach to pricing PDEs

Since the pricing equation is closely related to the convection-diffusion equation, which exhibits parabolic and hyperbolic behavior in dependency on a proportion of the convection and diffusion parts, the numerical schemes for solving of such equation should be constructed with respect to these properties. Here, we extend the DG framework from [5] with some modifications with respect to the unified approach to studied volatility models.

We construct solution $V_h = V_h(t)$ from the finite dimensional space S_h^p consisting from piecewise polynomial, generally discontinuous, functions of the p -th order defined on the domain Ω . Using a method of lines leads to a system of the ordinary differential equations

$$\frac{d}{dt}(V_h, \varphi_h) + \mathcal{A}_h(V_h, \varphi_h) = 0 \quad \forall \varphi_h \in S_h^p, \forall t \in (0, T), \quad (4)$$

where the initial condition is given by V^0 , (\cdot, \cdot) denotes the inner product in $L^2(\Omega)$ and the form $\mathcal{A}_h(\cdot, \cdot)$ stands for the DG semi-discrete formulation of the operator $\mathcal{L}_{BS}^f + \mathcal{L}_{corr}^f + \mathcal{L}_{proc} - \mathcal{L}_{prem}$. Consequently, we realize the discretization in time by Crank-Nicolson scheme and obtain at each time level $t_m \in [0, T]$ the sparse matrix equation

$$\left(\mathbf{M} + \frac{\tau}{2}\mathbf{A}\right)V_{m+1} = \left(\mathbf{M} - \frac{\tau}{2}\mathbf{A}\right)V_m + \frac{\tau}{2}(F_{m+1} + F_m), \quad (5)$$

where τ is the time step, the vector V_m is related to the DG solution $V_h(t_m)$, the matrix \mathbf{M} to the mass matrix, the matrix \mathbf{A} to the bilinear form \mathcal{A}_h and the vector F_m to the boundary conditions, respectively.

The rest part is devoted to the numerical results, which are presented on reference market data in order to illustrate the usage of DG method to pricing of options under two different stochastic volatility models. All computations are carried out with an algorithm implemented in the solver Freefem++, the detailed description can be found in [3]. We use piecewise linear, quadratic and cubic approximations on structured triangular grids. To specify the implementation settings the time step is set proportional to one calendar day and GMRES is used as a sparse solver for (5).

In the first benchmark we want to price European call option under the Hull-White model. To be consistent with the reference experiment from [6] we consider a unit strike, half-year maturity, zero risk-free interest rate and the following stochastic volatility parameters: $\alpha = 0$, $\beta = 1$. We compute discrete solutions on one fixed grid having mesh size $h = 0.01$. The comparative results are evaluated at reference level $Y_{ref} = 0.01$ and depicted in Figure 1, which shows general relationship between the option price under stochastic volatility model and the BS price. One can easily observe that the numerical results are of higher accuracy and better match reference values as the polynomial order increases. More precisely, the corresponding price differences are significantly apparent at or near at the strike price.

As the second problem, the valuation of European call option under the Stein-Stein model is performed on reference market data from [10]. Our aim is to investigate the behaviour of option values with respect to varying strikes under fixed parameters: $T = 0.5$, $r = 0.0953$, $\alpha = 16$, $m = 0.25$, $\beta = 0.4$. For different strikes, we compute solutions on one fixed grid with spacing 480×10 . The numerical solutions are evaluated at given reference node $[S_{ref}, Y_{ref}] = [100, 0.25]$ and recorded in Table 1 along with the reference values. The obtained results give fairly the same values as in [10] for higher polynomial

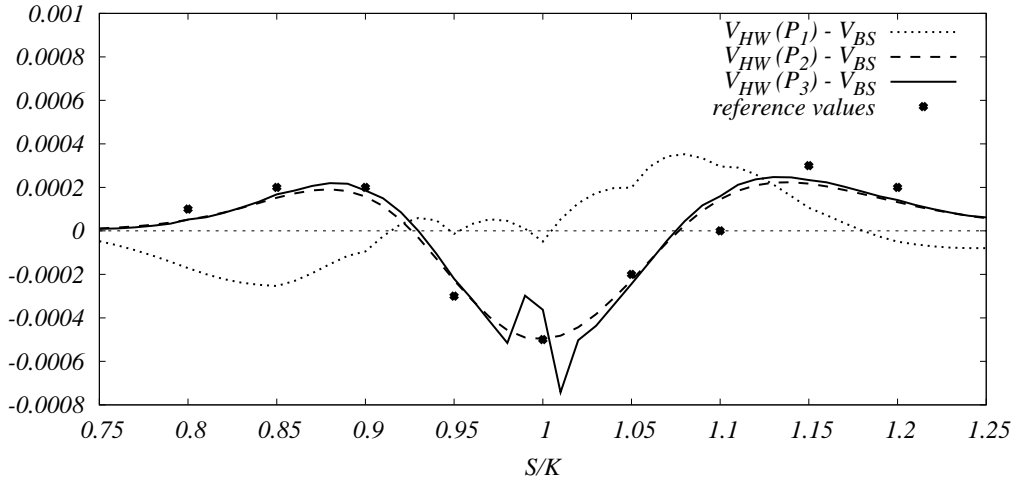


Figure 1: Option price differences between Hull-White model and BS model with volatility 10%.

orders. Finally, note that our observations illustrate typical findings common for the European options priced under stochastic volatility models.

\mathcal{K}	ref. value [10]	$V_h(P_1)$	$V_h(P_2)$	$V_h(P_3)$
90	16.09	16.1580	16.0924	16.0914
95	12.62	12.7092	12.6250	12.6235
100	9.65	9.7455	9.6518	9.6504
105	7.20	7.2875	7.1978	7.1956
110	5.24	5.3164	5.2431	5.2407
115	3.74	3.7870	3.7384	3.7360
120	2.61	2.6366	2.6154	2.6132

Table 1: Comparison of approximate option values of Stein-Stein model at reference node $[S_{ref}, Y_{ref}]$ for different scenarios and polynomial orders.

Acknowledgements

Both authors were supported through the Czech Science Foundation (GAČR) under project 16-09541S. The support is greatly acknowledged. Furthermore,

the second author also acknowledges the support provided within SP2017/32, an SGS research project of VŠB-TU Ostrava.

References

- [1] F. Black, and M. Scholes, The pricing of options and corporate liabilities. *Journal of Political Economy*, 81:637-659, 1973.
- [2] J.C. Cox, S. Ross, and M. Rubinstein, Option pricing: A simplified approach. *Journal of Financial Economics*, 7:229-264, 1979.
- [3] F. Hecht, New development in FreeFem++. *Journal of Numerical Mathematics*, 20(3-4):251-265, 2012.
- [4] S. Heston, A closed-form solution for options with stochastic volatility with applications to bond and currency options. *Review of Financial Studies*, 6:327-343, 1993.
- [5] J. Hozman, and T. Tichý, A discontinuous Galerkin method for numerical pricing of European options under Heston stochastic volatility. AIP Conference Proceedings, 1789, article no. 030003, 2016.
- [6] J. Hull, and A. White, The Pricing of Options on Assets with Stochastic Volatilities. *Journal of Finance*, 42:281-300, 1987.
- [7] B. Rivière, *Discontinuous Galerkin Methods for Solving Elliptic and Parabolic Equations: Theory and Implementation*. SIAM, 2008.
- [8] L.O. Scott, Option Pricing When the Variance Changes Randomly: Theory, Estimation, and an Application. *Journal of Financial and Quantitative Analysis*, 22:419-438, 1987.
- [9] R.U. Seydel, *Tools for Computational Finance*. Berlin, Springer, 2008.
- [10] E.M. Stein, and J.C. Stein, Stock Price Distributions with Stochastic Volatility: An Analytic Approach. *Review of Financial Studies*, 4:727-752, 1991.
- [11] J. Topper, *Financial Engineering with Finite Elements*. Wiley, 2005.

Exponential methods for solving non-autonomous linear wave equations

Philipp Bader^{b, *}, Sergio Blanes[†],
Fernando Casas[‡], Nikita Kopylov^{*}

(b) UJI, bader@uji.es

(†) IMM, UPV, serblaza@imm.upv.es

(‡) UJI, casas@uji.es

(b) IMM, UPV, nikop1@upvnen.upv.es

November 30, 2017

1 Introduction

The general theme of the present article is the numerical integration of the 2nd-order time-dependent linear partial differential equation

$$u_{tt}(x, t) = f(t, x, \partial_x, \dots) u(x, t), \quad x \in R^d, \quad t \geq 0, \quad (1)$$

equipped with the initial conditions $u(x, 0) = u_0(x)$ and $u_t(x, 0) = u'_0(x)$. We consider the case when f is a linear operator and traps the solution into a bounded region such that $u(x, t)$ and its derivatives attenuate far away from the region of interest. Thanks to this property accurate solutions can be obtained using high-order numerical methods as the schemes will not suffer from order reduction.

After spatial discretization, the operator f is represented by a matrix $N(t)$ and eq. (1) can be expressed as a 2nd-order ODE system:

$$y''(t) = N(t)y(t), \quad y(t_0) = y_0, \quad y'(t_0) = y'_0, \quad y \in R^r, \quad t \geq 0. \quad (2)$$

*e-mail:

An equivalent 1st-order linear non-autonomous system is given by

$$z'(t) = A(t)z(t), \quad A(t) = \begin{pmatrix} 0 & I \\ N(t) & 0 \end{pmatrix}, \quad z = \begin{pmatrix} y \\ y' \end{pmatrix} = \begin{pmatrix} q \\ p \end{pmatrix}, \quad z \in R^{2r}. \quad (3)$$

Matrix $N(t)$ has two important properties. Firstly, usage of a fine spatial grid results in a matrix of large dimension. Secondly, when $N(t)$ is a symmetric negative definite matrix, the solution is highly oscillatory.

To build high-order methods with a reduced computational cost we employ and expand the results obtained in [2, 3, 5]. Exponential integrators have been shown to produce accurate results for similar problems since they can provide highly oscillatory numerical solutions. We base our exponential methods on the Magnus expansion, taking into account the particular algebraic structure of $A(t)$ in eq. (3). Since the problem considered in this work require the computation of matrix exponentials action on the state vector. For this reason, we employ Krylov-type methods .

In the present work, using the particular structure of the problem, we show that exponential Magnus-decomposition integrators with Krylov-type exponentials show good efficiency compared to other types of exponential methods. We construct 4th- and 6th-order methods of the form

$$\Upsilon^{[p]} = \prod e^{\sum x_i A_i},$$

where the action of each exponential on the vector state can be evaluated efficiently. We analyse different classes of schemes and their performance for solving the non-autonomous wave equation; we describe the results in terms of accuracy versus computational cost, expressed in the number of matrix–vector multiplications.

2 Methods based on the Magnus expansion

The Magnus expansion [7] expresses the solution of eq. (3) on $[t_n; t_n + h]$ as a single exponential

$$\Phi(t_n, h) = \exp \Omega(t_n, h), \quad \Omega(t_n, h) = \sum_{k=1}^{\infty} \Omega_k(t_n, h). \quad (4)$$

The terms Ω_k of the Magnus series are given by

$$\Omega_1(t_n, h) = \int_{t_n}^{t_n+h} A(\tau_1) d\tau_1, \quad \Omega_2(t_n, h) = \frac{1}{2} \int_{t_n}^{t_n+h} \int_{t_n}^{\tau_1} [A(\tau_1), A(\tau_2)] d\tau_2 d\tau_1, \dots \tag{5}$$

where $[A, B] = AB - BA$ is the matrix commutator of A and B . When $N(t)$ in eq. (3) is real and symmetric, Ω and any truncation $\widehat{\Omega}^{[p]} = \sum_{k=1}^p \Omega_k$ of order p , belong to the symplectic Lie algebra, and symplecticity is preserved.

The Magnus expansion eq. (4) can be approximated up to order $p = 2s$ in terms of $A(t)$ in an easy way. If one considers a polynomial $\tilde{A}(t)$ of degree $s - 1$ in t that interpolates $A(t)$ on the interval $[t_n, t_n + h]$ at the points $t_n + c_i h$, $i = 1, \dots, s$; c_i are the nodes of the Gauss–Legendre quadrature rule of order $2s$ on the interval $[0, 1]$. Here we consider $s = 3$ and $c_1 = \frac{5-\sqrt{15}}{10}$, $c_2 = \frac{1}{2}$, $c_3 = \frac{5+\sqrt{15}}{10}$ Given

$$\alpha_1 = \begin{pmatrix} 0 & hI \\ \mu_1 & 0 \end{pmatrix}, \quad \alpha_j = \begin{pmatrix} 0 & 0 \\ \mu_j & 0 \end{pmatrix}, \quad j > 1$$

with

$$\mu_1 = hN_2, \quad \mu_2 = \frac{\sqrt{15}h}{3}(N_3 - N_1), \quad \mu_3 = \frac{10h}{3}(N_3 - 2N_2 + N_1), \tag{6}$$

where $N_i = N(t_n + c_i h)$, it is immediate to check that $\alpha_1 = \mathcal{O}(h)$, $\alpha_2 = \mathcal{O}(h^2)$, $\alpha_3 = \mathcal{O}(h^3)$. A 6th-order approximation $\Omega^{[6]} = \Omega + \mathcal{O}(h^7)$, is given by (see [3, 4] and references therein)

$$\Omega^{[6]} = \alpha_1 + \frac{1}{12}\alpha_3 - \frac{1}{12}[12] + \frac{1}{360}[113] - \frac{1}{240}[212] + \frac{1}{720}[1112], \tag{7}$$

where $[ij \dots kl]$ represents the nested commutator $[\alpha_i, [\alpha_j, [\dots, [\alpha_k, \alpha_l] \dots]]]$.

In this case $[2, 3] = 0$ and $[2, 1, 2]$ is a nilpotent matrix so, the resulting algebra allows a simple representation and has some structural properties that enable one to build new methods with a particular structure.

3 Krylov-type matrix exponentiaton

Due to the structure of $A(t)$ it is possible to build exponential methods in which some of the exponentials are obtained analytically. However, some

of the exponentials need to be computed. There exist a lot of methods for matrix exponentiation. However, large-dimensional matrices render these exponentials computationally unreasonable. Hence the need for a method that does not require straightforward matrix multiplications, e.g., Krylov-type methods.

In general, given a vector $v \in R^{2r}$ and a matrix $A \in R^{2r \times 2r}$, Krylov methods produce an orthonormal basis $\{v, Av, \dots, A^{m-1}v\}$, which spans an m -dimensional subspace, and a Hessenberg matrix of coefficients H_m . Let V_m be a matrix constructed of the basis vectors columnwise. Then, e^{Av} is approximated by the first column of the following product:

$$\beta V_m e^{H_m}, \quad \beta := \|v\|_2. \tag{8}$$

4 Results

The new 6th-order exponential methods, obtained via Magnus expansion, are summarized in the following relations: $K = N_3 - N_1, \quad L = N_1 - 2N_2 + N_3$

$$\begin{aligned} C_1^{[6]} &= -\frac{\sqrt{15}}{3}x_0K, \quad C_2^{[6]} = +\frac{\sqrt{15}}{3}x_0K; \\ D_1^{[6]} &= N_2 - \frac{\sqrt{15}}{3}\frac{x_2}{x_1}K + \frac{10}{3}\frac{x_3}{x_1}L, \quad D_2^{[6]} = N_2 + \frac{10}{3}\frac{x_5}{x_4}L, \\ D_3^{[6]} &= N_2 + \frac{\sqrt{15}}{3}\frac{x_2}{x_1}K + \frac{10}{3}\frac{x_3}{x_1}L, \end{aligned}$$

with x_i having the values:

$$\begin{aligned} x_0 &= 0.01544620325088392, \quad x_1 = 0.5670407188654774, \quad x_2 = 0.1567979554672175, \\ x_3 &= 0.08574816028245607, \quad x_4 = -0.1340814377309548, \quad x_5 = -0.08816298723157881. \end{aligned}$$

$$\begin{aligned} \Upsilon_3^{[6]} &= \begin{pmatrix} I & 0 \\ hC_2^{[6]} & I \end{pmatrix} \exp \left(x_1 h \begin{pmatrix} 0 & I \\ D_3^{[6]} & 0 \end{pmatrix} \right) \exp \left(x_4 h \begin{pmatrix} 0 & I \\ D_2^{[6]} & 0 \end{pmatrix} \right) \times \\ &\quad \times \exp \left(x_1 h \begin{pmatrix} 0 & I \\ D_1^{[6]} & 0 \end{pmatrix} \right) \begin{pmatrix} I & 0 \\ hC_1^{[6]} & I \end{pmatrix}. \end{aligned}$$

$$\begin{aligned} C_1^{[6]} &= +\frac{\sqrt{15}}{3}x_0K + \frac{10}{3}x_1L, \quad C_2^{[6]} = -\frac{\sqrt{15}}{3}x_0K + \frac{10}{3}x_1L, \quad D_1^{[6]} = N_2 + \frac{\sqrt{15}}{3}\frac{x_3}{x_2}K + \\ &\frac{10}{3}\frac{x_4}{x_2}L, \quad D_3^{[6]} = N_2 - \frac{\sqrt{15}}{3}\frac{x_3}{x_2}K + \frac{10}{3}\frac{x_4}{x_2}L,; \\ E_1^{[6]} &= \frac{\sqrt{15}}{3}x_5K, \end{aligned}$$

where the coefficients are the following:

$$x_0 = \frac{1}{20}(1 + \frac{1}{11}(-6 + \sqrt{3})), \quad x_1 = \frac{1}{104}(3 + \frac{1}{5}(-6 + \sqrt{3})), \quad x_2 = \frac{1}{2},$$

$$x_3 = \frac{1}{55}(6 - \sqrt{3}), \quad x_4 = \frac{1}{520}(-6 + 3(6 - \sqrt{3})), \quad x_5 = \frac{1}{60}(-2 + \frac{3}{11}(6 - \sqrt{3})),$$

$$\tilde{\Upsilon}_3^{[6]} = \begin{pmatrix} I & 0 \\ hC_2^{[6]} & I \end{pmatrix} \exp \left(x_2 h \begin{pmatrix} 0 & I \\ D_3^{[6]} & 0 \end{pmatrix} \right) \exp \left(h \begin{pmatrix} hE_1^{[6]} & 0 \\ 0 & -hE_1^{[6]} \end{pmatrix} \right) \times$$

$$\times \exp \left(x_2 h \begin{pmatrix} 0 & I \\ D_1^{[6]} & 0 \end{pmatrix} \right) \begin{pmatrix} I & 0 \\ hC_1^{[6]} & I \end{pmatrix}.$$

Furthermore, the exponentials in these methods are computed using Krylov approximation in order to deal with the large dimension of the system.

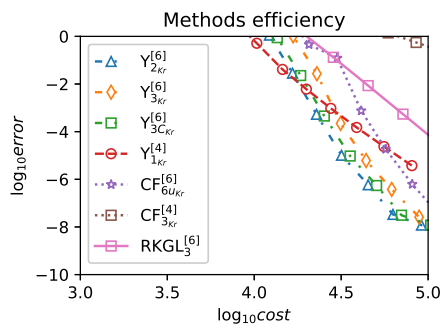
The methods are compared with classical Runge–Kutta methods and commutator-free (CF) methods from [1], which have a similar structure on the following benchmark equation:

$$\partial_t^2 u = \partial_x^2 u - (1 + \varepsilon \cos \delta t) x^2 u, \quad t \in [0, 20\pi], \quad x \in [-10, 10];$$

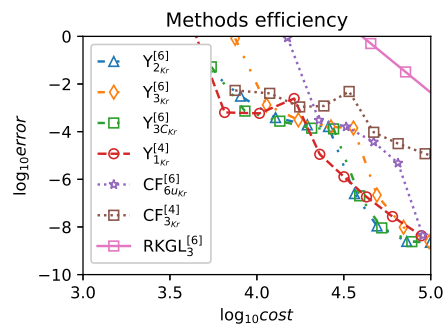
$$u(x, 0) = e^{-\frac{1}{2}(x-9.5)^2} + 0.79e^{-\frac{1}{2}(x+5)^2}, \quad u'(x, 0) = 0;$$

$$u(-10, t) = u(10, t).$$

As expected, Magnus–decomposition methods show better performance in case of highly oscillating systems, i.e. when δ is small and ε is relatively large.



(a) $\delta = 1, \varepsilon = 1$



(b) $\delta = 1/1000, \varepsilon = 10$

References

- [1] A. Alvermann and H. Fehske, High-order commutator-free exponential time-propagation of driven quantum systems, *J. Comp. Phys.*, **230** (2011), 5930-5956.
- [2] P. Bader, S. Blanes, F. Casas, N. Kopylov, and E. Ponsoda, Symplectic integrators for second-order linear non-autonomous equations, *J. Comp. Appl. Math.*, **330** (2018), 909-919.
- [3] P. Bader, S. Blanes, E. Ponsoda and M. Seydaoğlu, Symplectic integrators for the matrix Hill equation, *J. Comp. Appl. Math.*, **316** (2017), 47-59.
- [4] S. Blanes, Time-average on the numerical integration of non-autonomous differential equations. Submitted.
- [5] M. Hochbruck and A. Ostermann, Exponential integrators, *Acta Numerica*, **19** (2010), 209-286.
- [6] A. Iserles, *A First Course in the Numerical Analysis of Differential Equations*, 2nd edn, Cambridge University Press, Cambridge (2008).
- [7] W. Magnus. On the exponential solution of differential equations for a linear operator, *Comm. Pure and Appl. Math.*, **VII**, (1954) 649-673.

Glucose model optimization for specific patients

C. Burgos^(a), J.C. Cortés^(a),
J.I. Hidalgo ^(b) , D. Martínez-Rodríguez^(a) * R.-J. Villanueva^(a).

(a) Instituto Universitario de Matemática Multidisciplinar,
Universitat Politècnica de València

(b) Departamento de Arquitectura de Computadores y Automática,
Universidad Complutense de Madrid

November 30, 2017

1 Introduction

Since the last few years, glucose modeling has become a very prolific field of study. Different models have been proposed [1], [2], being the aim of all of them the explanation and eventually prediction of plasma glucose concentrations. The correct modeling of glucose would allow to predict risk situations in people who suffers diabetes or insulin resistance. It also may be used as a powerful tool in diet composition for people suffering this disease, having greater control of body reactions in known activities, as for example sport events.

This study is based on a previous model developed by Dalla Man, Rizza and Cobelli [1]. This model is formed by several subsystems connected in a close loop feedback, depending all of them on each other along the time. This fact transforms the combination of equations in a really complex system, where any small change in its parameter may produce destabilization in the response of the system.

*e-mail: damarro3@etsii.upv.es

Dalla Man et al. [1] obtained parameter values describing what is known as *in silico* patients. This means that the authors of the model obtained a range of values where the model has the same magnitude order in behaviour than normal people. However, they do not obtain the values for a single person, but a confidence interval for many of them. The aim of this paper is to obtain customized values for those parameters, in such a way that it may be used in clinic patients.

2 Methodology

In order to accomplish the objective of the study, the first thing that has been done is the computer modeling of the paper written by Dalla Man et al. MATLAB software has been used as programming language. The model is split in seven subsystems: Glucose Kinetics, Insulin Kinetics, Rate of Appearance, Endogeneous Production, Utilization, Secretion and Renal Excretion, as it can be seen in Figure 1. Each subsystem has its own parameters, and all of them depend on each other.

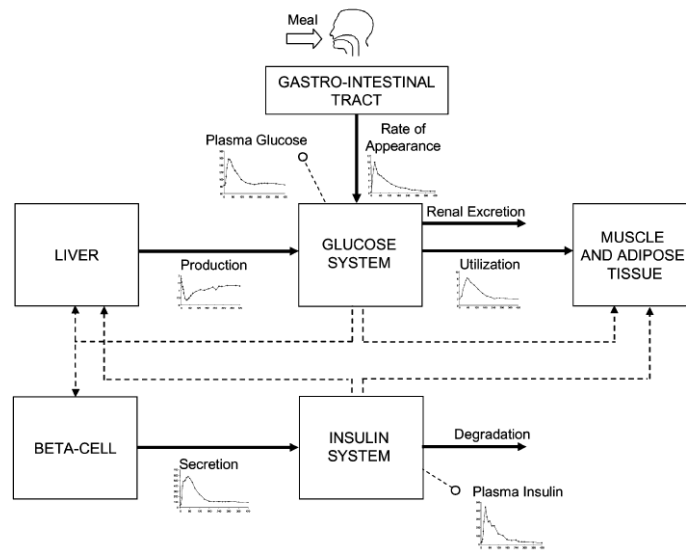


Figure 1: Subsystems from Dalla Man et al. model [1].

The mathematical model has been transformed from differential equations

into difference equations in order to be discretized and being able to simulate with mathematical methods.

In order to obtain data to fit the model with a single patient, an author of the study has measured his plasma glucose level during twenty hours and written down all his glucose ingest during that time. The weigh of the patient is 95 kg and the activity performed during the study may be considered as medium, with sport periods and resting periods.

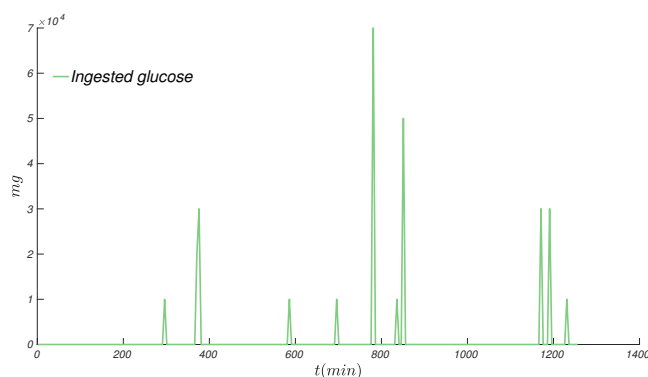


Figure 2: Ingested glucose during measurement.

The model has been fitted with a modified *Particle Swing Optimization* (PSO) algorithm [3]. The modification made is related with mutations of the 30% on particles, avoiding the stuck of the optimal solution after a few iterations. Parameters are let to change 500% of the initial values found by Dalla Man et al. Unstable solutions are discarded during the fitting, which tries to find the best values of the set of parameters that minimizes the error committed.

The error has been calculated as:

$$\sum_{i=0}^{minutes} \|Measured\ Glucose_i - Modeled\ Glucose_i\| \tag{1}$$

where $\|\cdot\|$ denotes the euclidean norm, so mean square error has been considered.

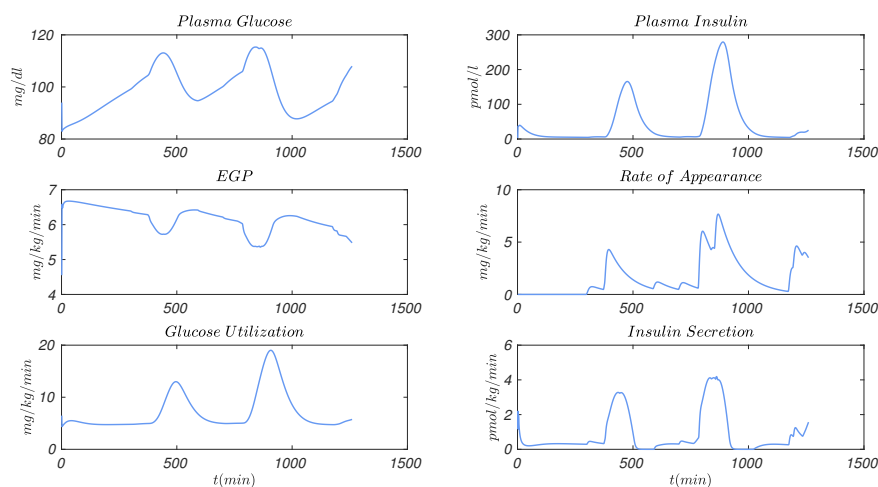


Figure 3: Real patient model output values.

3 Results

The first step to consider the parameters obtained from the PSO algorithm as valid is the comparison between the output of the model and the output from [1]. The results of the output are shown in Figure 3. All the outputs are in the same order of magnitude as the ones obtained in [1]. The model is stable, cyclical and has enclosed values. The comparison between predicted glucose and measured glucose can be seen at Figure 4. Ingested glucose has been plotted in Figure 2. Comparing glucose ingest, the rate of appearance in plasma and plasma glucose levels, it can be seen that there is a clear correlation, existing a slight delay between both values of the model.

However, only with data plotted in previous figures, the validation of the parameters obtained cannot be ensured. In order to have an objective measurement method, [4] and [5] methods have been used. Both methods were developed at the end of the XX Century, in 1987 and 2000 respectively, with the aim of quantifying the error made by the glucose gauge during the glucose measurement compared with the real value.

Graphics of these methods compare the measured values by the device and the real values obtained with more accurate procedures. Real glucose is plotted in the horizontal axis, and measured glucose is plotted in the vertical

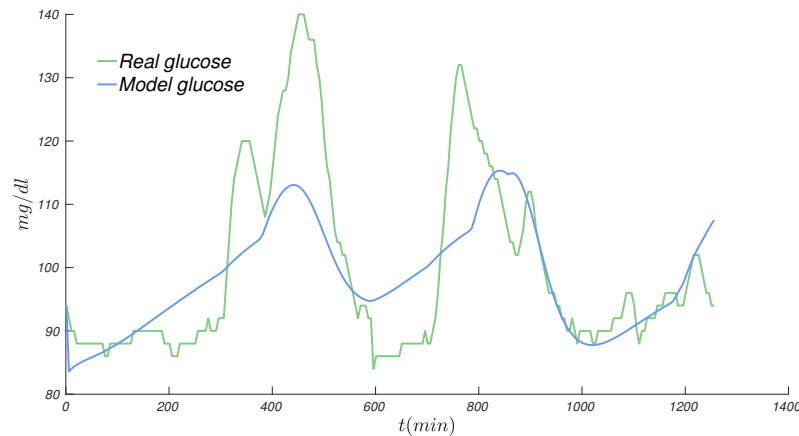


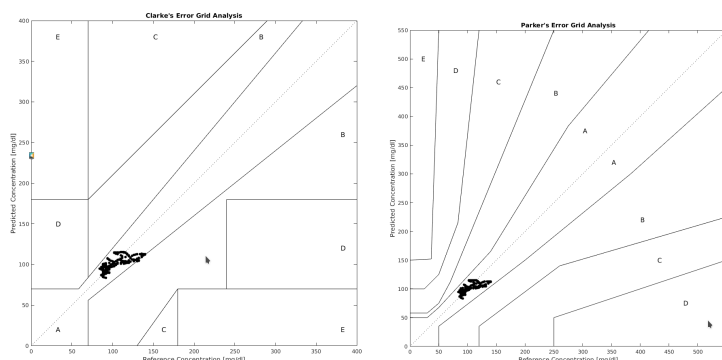
Figure 4: Comparison between experimental and modelled data.

axis. If there is no difference between both values, the point of the plot is set in the line that cross the graphic. The rest of the graphic is divided into different areas, each one with a specific meaning.

- A area is considered under the 20% of error made by the reference of the gauge.
- B area is considered as an error of the gauge, but with no harmful treatment.
- C area is considered as an error of the gauge that leads into an unnecessary treatment.
- D area is considered as a failure of the gauge, that is unable to detect hypoglycemia or hyperglycemia.
- E area is considered as a failure of the gauge that leads to treat hypoglycemia as hyperglycemia and vice versa.

As it is seen in Figure 5, fitting of the model obtained from the PSO algorithm is inside acceptable values, being all of them in the A area. This means that the error made is less than the reference of the gauge.

Once the computer model has been validated, the simulation is performed during four more hours after the experimental data with the aim of prove



(a) Clarke's graphic. (b) Parker's graphic.

Figure 5: Validation graphics.

that the model is still stable after the validation time. The ingested glucose for the prediction has been considered as null. Both data, the experimental and the modelled are plotted in Figure 6. After the red line, the plot shows the values of the simulation that lasts 240 minutes.

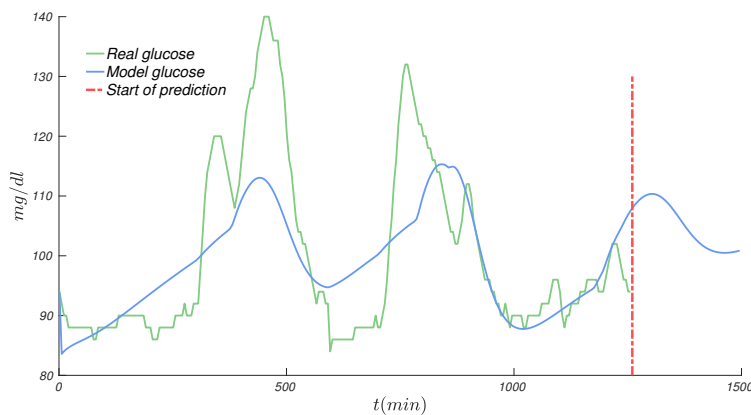


Figure 6: Glucose prediction during four hours.

The prediction has the same tendency as the previous data, and after appearing all the glucose that was being processed in the gastro-intestinal track, plasma glucose levels decrease slowly. There is not any irregular behavior as it was supposed.

4 Conclusions

As it has been explained throughout the study, it has been proved that glucose prediction can be applied not only to *in silico* patients, but also in specific patients. Parameters fitting of Dalla Man et al. model has been calculated, and a prediction for four hours time lapse has been considered with satisfactory results. For future studies, a computer application might be done in order to approach this technical technique to health workers. Summing up, the results may be considered acceptable, opening a new study line with the objective of applying these findings to clinical practice.

References

- [1] Chiara Dalla Man, Robert A. Rizza, Claudio Cobelli, "Meal Simulation Model of the Glucose-Insulin System", IEEE Transactions on Biomedical Engineering, Volume: 54, Issue: 10, Oct. 2007 <http://dx.doi.org/10.1109/TBME.2007.893506>.
- [2] Alain Bock, Gregory François, Denis Gillet, "A therapy parameter-based model for predicting blood glucose concentrations in patients with type 1 diabetes", Computer methods and programs in biomedicine. 118:107-123, 2015. <http://dx.doi.org/10.1016/j.cmpb.2014.12.002>
- [3] C. Jacob, N. Khemka, "Particle Swarm Optimization in Mathematica. An Exploration Kit for Evolutionary Optimization", IMS'04, Proc. Sixth International Mathematica Symposium, Banff, Canada, (2004).
- [4] Clarke WL, Cox D, Gonder-Frederick LA, Carter W, Pohl SL. Evaluating clinical accuracy of systems for self-monitoring of blood glucose. Diabetes Care 10:622-628, 1987. PMID:3677983.
- [5] Parkes JL, Slatin SL, Pardo S, Ginsberg BH. A new consensus error grid to evaluate the clinical significance of inaccuracies in the measurement of blood glucose. Diabetes Care. 2000; 23(8):1143-1148. <https://doi.org/10.2337/diacare.23.8.1143>.

Semilocal convergence study under omega continuity condition

Sukhjit Singh ^b, Eulalia Martinez [†]*, D.K. Gupta [‡], and A. Kumar [‡]

(^b) Department of Mathematical Sciences,
I.K.G. Punjab Technical University Jalandhar,

([†]) Instituto de Matematica Multidisciplinar,
Universitat Politècnica de València,

([‡]) Department of Mathematics,

I.I.T. Kharagpur.

November 30, 2017

Abstract

The semilocal convergence of an efficient fifth order iterative method is established under weaker conditions for solving nonlinear equations. It is done by assuming omega continuity condition on second order Fréchet derivative. The novelty of our work lies in the fact that several examples are available where Lipschitz and Hölder condition fails but omega condition holds. Existence and uniqueness theorem is established along with R-order and error bounds. The R-order is found to be $4+q$, $q \in (0, 1]$. Numerical experiments involving nonlinear integral equations are performed to show the applicability of the method. Finally the existence and uniqueness balls are obtained along with error bounds for all the examples.

*e-mail: eumarti@mat.upv.es

1 Introduction

Let X and Y are Banach spaces and consider solving

$$G(x) = 0$$

where $G : \Omega \subseteq X \rightarrow Y$ be a nonlinear operator in an open convex domain $\Omega_0 \subseteq \Omega$. Solution of various real life problems such as dynamical systems, boundary value problems etc. are obtained by solving these equations (see, [1, 2]). The most well known quadratically convergent Newton's method to solve (1) is defined for $k \geq 0$, by

$$x_{k+1} = x_k - \Gamma_k G(x_k) \quad (1)$$

where, $\Gamma_k = G'(x_k)^{-1}$ and x_0 is the initial point. Various modification of Newton's method are proposed to increase the order of convergence and efficiency. In literature [3, 4, 5, 6, 7, 8], authors have established the semilocal convergence of higher order iterative methods under various continuity conditions.

Recently, the semilocal convergence of an efficient fifth order method is established in [9] under Lipschitz condition on F'' . It is given for $k = 0, 1, 2 \dots$ by

$$\begin{aligned} y_k &= x_k - \Gamma_k G(x_k), \\ z_k &= y_k - \Gamma_k G(y_k), \\ x_{k+1} &= z_k - G'(y_k)^{-1} G(z_k), \end{aligned} \quad (2)$$

In real life applications, various numerical examples are available which neither satisfies Lipschitz nor Hölder condition. This motivate us to establish the semilocal convergence of an efficient fifth order method under weaker conditions.

2 Semilocal convergence analysis

Let $\Gamma_0 = G'(x_0)^{-1} \in BL(Y, X)$ exists at $x_0 \in \Omega$, where $BL(Y, X)$ denotes the set of bounded linear operators from Y to X and the following conditions hold.

$$(1) \quad \|\Gamma_0\| \leq \beta_0$$

- (2) $\|\Gamma_0 G(x_0)\| \leq \eta_0$
- (3) $\|G''(x)\| \leq M$
- (4) $\|G''(x) - G''(y)\| \leq \omega(\|x - y\|)$, $x, y \in \Omega$, for a continuous non-decreasing real function $\omega(x)$, $x > 0$, $\omega(0) \geq 0$ such that, $\omega(tx) \leq t^q \omega(x)$ for $t \in [0, 1]$, $x \in (0, \infty)$ and $q \in [0, 1]$.

Let $r_0 = M\beta_0\eta_0$, $s_0 = \beta_0\eta_0\omega(\eta_0)$ and define sequences $\{r_k\}$, $\{s_k\}$ and $\{\eta_k\}$ for $k = 0, 1, 2 \dots$, by

$$r_{k+1} = r_k \phi(r_k)^2 \psi(r_k, s_k), \tag{3}$$

$$s_{k+1} = s_k \phi(r_k)^{2+q} \psi(r_k, s_k)^{1+q}, \tag{4}$$

$$\eta_{k+1} = \eta_k \phi(r_k) \psi(r_k, s_k), \tag{5}$$

where,

$$\phi(u) = \frac{1}{1 - ug(u)}, \tag{6}$$

$$g(u) = \left(1 + \frac{u}{2} + \frac{u^2}{2(1-u)} \left(1 + \frac{u}{4} \right) \right), \tag{7}$$

and

$$\begin{aligned} \psi(u, v) &= \frac{u^2}{2(1-u)} \left(1 + \frac{u}{4} \right) \left[\frac{v}{1+q} \left(\frac{u^{1+q}}{2^{1+q}} + \frac{1}{2+q} \left(\frac{u^2}{2(1-u)} \left(1 + \frac{u}{4} \right) \right)^{1+q} \right) \right. \\ &\quad \left. + \frac{u}{2} \left(u + \frac{u^2}{2(1-u)} \left(1 + \frac{u}{4} \right) \right) \right]. \end{aligned} \tag{8}$$

Let $h(u) = g(u)u - 1$. Since, $h(0) = -1$ and $g(u)$ is increasing function, therefore, $h(u)$ has a real root ν . If $u \in (0, \nu)$, we get $g(u)u < 1$.

Lemma 2.1. *Let $\phi(u)$, $g(u)$ and $\psi(u, v)$ are given by (6), (7) and (8) respectively. If $0 < r_0 < \nu$ and $\phi(r_0)^2 \psi(r_0, s_0) < 1$, then*

(i) $\phi(u)$ and $\psi(u)$ are increasing functions and $\phi(u) > 1$, $g(u) > 1$ for $u \in (0, \nu)$.

(ii) $\psi(u, v)$ is an increasing function of u , for $u \in (0, \nu)$.

(iii) $\{r_k\}$, $\{s_k\}$ and $\{\eta_k\}$ are decreasing sequences and $r_k g(r_k) < 1$ as well as $\phi(r_k)^2 \psi(r_k, s_k) < 1$ for $k \geq 0$.

Lemma 2.2. *Let $\phi(u)$ and $\psi(u, v)$ are given by (6) and (8), respectively. If $\gamma \in (0, 1)$ then $\phi(\gamma t) < \gamma \phi(t)$ and $\psi(\gamma u, \gamma^{1+q} v) < \gamma^{3+q} \psi(u, v)$.*

Lemma 2.3. Let $\gamma = \phi(r_0)^2\psi(r_0, s_0)$, $0 < r_0 < \nu$ and $\delta = \frac{1}{\phi(r_0)}$. Then,

(i) $r_k \leq \gamma^{(4+q)^{k-1}} r_{k-1} \leq \gamma^{\frac{(4+q)^{k-1}}{3+q}} r_0$ and $s_k \leq \left(\gamma^{(4+q)^{k-1}}\right)^{1+q} s_{k-1} \leq \left(\gamma^{\frac{(4+q)^{k-1}}{3+q}}\right)^{1+q} s_0$.

(ii) $\phi(r_k)\psi(r_k, s_k) \leq \frac{\gamma^{(4+q)^k}}{\phi(r_0)} \forall k \in N$.

(iii) $\eta_k \leq \gamma^{\frac{(4+q)^k-1}{3+q}} \delta^k \eta_0$.

Using the above results, we will establish the following recurrence relations and convergence theorem.

- (I) $\|\Gamma_k\| \leq \phi(r_{k-1})\|\Gamma_{k-1}\|,$
- (II) $\|\Gamma_k G(x_k)\| \leq \phi(r_{k-1})\psi(r_{k-1}, s_{k-1})\eta_{k-1},$
- (III) $M\|\Gamma_k\| \|\Gamma_k G(x_k)\| \leq r_k,$
- (IV) $\|\Gamma_k\| \|\Gamma_k G(x_k)\| \omega(\|\Gamma_k G(x_k)\|) \leq s_k,$
- (V) $\|x_k - x_{k-1}\| \leq g(r_{k-1})\eta_{k-1}.$

Theorem 2.1. Let $r_0 = M\beta_0\eta_0 < \nu$, $s_0 = \beta_0\eta_0\omega(\eta_0)$ and assumptions (1)-(4) hold. Then for $\bar{B}(x_0, R\eta_0) \subseteq \Omega$, where $R = \frac{g(r_0)}{1 - \delta\gamma}$, the sequence $\{x_k\}$ generated by (2) converges to the solution of (1). Moreover, $y_k, z_k, x_{k+1}, x^* \in \bar{B}(x_0, R\eta_0)$ and x^* is the unique solution in $B\left(x_0, \frac{2}{L_1\beta_0} - R\eta_0\right) \cap \Omega$. The error bound for iterates is given as follows.

$$\|x_k - x^*\| \leq g(r_0)\delta^k \frac{\gamma^{\frac{(4+q)^k-1}{3+q}}}{1 - \delta\gamma^{(4+q)^k}} \eta_0.$$

3 Numerical examples

In this section, we consider nonlinear Hammerstein type integral equation which arises in dynamical model of a chemical reactor (see, [10]) given by

$$x(r) + \sum_{i=1}^m \int_a^b K_i(r, s)S_i(x(s))ds = f(r), \quad r \in [a, b], \tag{9}$$

where functions f , K_i and S_i for $i = 1, 2, \dots, m$ are known, the solution x is to be determined and $-\infty < a < b < +\infty$. In order to solve (9), we have to solve

$$G(x)(u) = x(u) + \sum_{i=1}^m \int_a^b K_i(u, v)S_i(x(v))dv - f(u) \tag{10}$$

If $S'_i(x(u))$ is (M_i, α_i) - Hölder continuous in Ω , then, under max-norm, we have

$$\|G''(x) - G''(y)\| \leq \sum_{i=1}^m M_i \|x - y\|^{\alpha_i}, \quad M_i \geq 0, \quad \alpha_i \in [0, 1], \quad \forall x, y \in \Omega. \quad (11)$$

For different α_i , G'' neither satisfies Lipschitz nor Hölder condition but satisfies the weaker ω -condition. Using the proposed study, we obtain the existence and uniqueness balls for the solution along with error bounds.

4 Conclusions

Using recurrence relations, semilocal convergence of an efficient fifth order iterative method is presented under weaker conditions for solving nonlinear equations. The convergence theorem is established along with error bounds. Different examples involving nonlinear integral equations are solved to show the applicability of the approach. Existence and uniqueness balls are obtained along with error bounds for the considered examples.

Acknowledgments

This work was supported supported in part by the project of Generalitat Valenciana, Prometeo/2016/089, and the project MTM2014-52016-C2-2-P of the Spanish Ministry of Science and Innovation.

References

- [1] Argyros, I.K., Hilout, S., Tabatabai, M.A., Mathematical Modelling with Applications in Biosciences and Engineering. New York, Nova Publishers, 2011.
- [2] Argyros, I.K., Hilout, S., Numerical methods in Nonlinear Analysis. New Jersey, World Scientific Publ. Comp., 2013.
- [3] Kantorovich, L.V., Akilov, G.P., Functional Analysis. Oxford, Pergamon Press, 1982.

- [4] Amat, S., Hernández, M.A., Romero, N. A modified Chebyshev's iterative method with at least sixth order of convergence *Applied Mathematics and Computation*, 206(1): 164-174, 2008.
- [5] Hernández, M.A. Chebyshev's approximation algorithms and applications *Computers and Mathematics with Applications*, 41(3-4): 433-445, 2001.
- [6] Hueso, J.L., Martínez, E. Semilocal convergence of a family of iterative methods in Banach spaces *Numerical Algorithms*, 67(2): 365-384, 2014.
- [7] Wang, X., Kou, J., Gu, C. Semilocal convergence of a class of Modified Super-Halley Methods in Banach Spaces *Journal of Optimization Theory and Applications*, 153(3): 779-793, 2012.
- [8] Wu, Q., Zhao, Y. Newton-Kantorovich type convergence theorem for a family of new deformed Chebyshev method *Applied Mathematics and Computation*, 192(2): 405-412, 2008.
- [9] Singh, S., Gupta, D.K., Martínez, E., Hueso, J.L. Semilocal convergence analysis of an iteration of order five using recurrence relations in Banach spaces *Mediterranean Journal of Mathematics*, 13(6): 4219-4235, 2016.
- [10] Bruns, D., Bailey, J. Nonlinear feedback control for operating a non-isothermal cstr near an unstable steady state *Chemical Engineering Science*, 32(3): 257-264, 1977.

Mathematical model based on the diffusion of electronic commerce in Spain

I.-C. Lombana^(a) * ; C. Burgos^(b) † ;
J.C. Cortés^(b) ‡ ; D. Martínez Rodríguez^(b) § ; R.-J. Villanueva^(b) ¶

(a) Facultad de Ingeniería Civil - Campus Ibagué, Universidad Cooperativa de Colombia.

(b) Instituto Universitario de Matemática Multidisciplinar, Universitat Politècnica de València

November 30, 2017

1 Model Building

Electronic commerce has numerous advantages because offers saving time when we purchase a good, offers the possibility of reviewing without depending on schedules of traditional stores, access to a wider variety and quantity of articles, in many cases, with lower prices, etc.

Taking into account official data from INE [4], the total population is divided into 2 subgroups, 16-44 years old and 45-74 years old where every age group is divided into two subgroups, the first one consisting of people adopting this technology and the second one who do not. We propose a type-epidemiological mathematical model to study the dynamics of e-commerce in Spain based on a nonlinear system of difference equations whose parameters are the innovation coefficients, associated with each age group and related to advertising and the imitation coefficients, related to the influence of an adopting technology group on non-adopting group.

*e-mail: ivan.lombana@campusucc.edu.co

†e-mail: clabursi@posgrado.upv.es

‡e-mail: jccortes@imm.upv.es

§email: damarro3@etsii.upv.es

¶e-mail: rjvillan@imm.upv.es

2 Model Building

This section deals with the construction and the scaling of the model. We will work with a demographical model of two age groups of ages together with ones that describe the diffusion of the electronic commerce.

The difference between our model and different models described in the literature [1], [2], [3] is the variation of the population during the time.

2.1 Demographical model

A consistent age-structured demographic model is required in order to integrate demographic information from INE [4] with the aim of constructing a reliable diffusion model for e-commerce. This age-structured model considers two different age groups due to significant changes in both age groups respect to e-commerce data.

- Group 1 (G_1): Population aged between 15 and 44 years old.
- Group 2 (G_2): Population aged between 45 and 74 years old.

The demographic model is given by the following system of difference equations [5]:

$$\begin{aligned} G_1(t+1) &= \mu - c_1 G_1(t) - d_1 G_1(t). \\ G_2(t+1) &= c_1 G_1(t) - d_2 G_2(t). \end{aligned} \tag{1}$$

where:

- μ is the yearly birth rate (assuming that almost nobody dies between 0 and 14 years).
- d_1 is the yearly death rate in the first group.
- d_2 is the rate of people outgoing from the model.
- c_1 is the yearly growth rate from G_1 to G_2 .

We calculate the parameters of the demographic model taking into account the available data from [4], these results are given by table 1.

2.2 Electronic commerce model

In this section, we propose a discrete model which describes the dynamics of these data over the time. In order to formulate the mathematical diffusion model to study the e-commerce in Spain, first of all we introduce the following variables:

- $N_i(t)$ ($i = 1, 2$), denotes the amount of population of group G_i that does not adopt the technology (e-commerce), at time instant t (months).
- $Y_i(t)$ ($i = 1, 2$), denotes the amount of population of group G_i that adopt the technology (e-commerce), at time instant t (months).

	μ^j	d_1^j	Death Rate in G_2 + People leaving the model
$j = 2007$	0.010857	7.16805×10^{-04}	0.041911
$j = 2008$	0.011275	6.70342×10^{-04}	0.041609
$j = 2009$	0.010647	6.10648×10^{-04}	0.041415
$j = 2010$	0.010421	5.62175×10^{-04}	0.041152
$j = 2011$	0.010068	5.40130×10^{-04}	0.041042
$j = 2012$	0.009638	5.13720×10^{-04}	0.040945
$j = 2013$	0.007109	4.67524×10^{-04}	0.040734
$j = 2014$	0.009171	4.57443×10^{-04}	0.040619
$j = 2015$	0.009015	4.48471×10^{-04}	0.040668

Table 1: Demographic data calculated from INE [4]. Parts per unit.

For the people who adopt the technology ($Y_i(t)$, $i = 1, 2$), we distinguish: the ones that adopt the e-commerce influenced by the society (imitators) and the others that adopt the technology by themselves (innovators). On the other hand, for the population who have not adopt the technology ($N_i(t)$, $i = 1, 2$), we can distinguish the people who never have bought by the Internet or those who have not bought by Internet in the last six months.

The diffusion of the technology will be represented by the transmission of an individual from the population $N_i(t)$ to $Y_i(t)$ ($i = 1, 2$) through the coefficients of innovation or imitation described by:

- p_1, p_2 are the coefficients of innovation for the i -th group.
- $\alpha_1, \alpha_2, \alpha_3, \alpha_4$ are the e-commerce influence coefficients $i = 1, 2$ of the Y_i on N_j ($i, j = 1, 2$) age group, that is when someone who has bought yet by the Internet influences another person who has not yet done.
- γ_i , ($i = 1, 2$) are the coefficients that describe the behavior when an individual who has already bought by the Internet does not buy anymore in six months, so he/she gets susceptible.

Furthermore, we will consider the following assumptions:

- Let us assume homogeneous population mixing, i.e., each individual can contact with any other individual [5].
- Let us assume that nobody dies between 0 and 14 years, thus people with 15 years old enter into the system in $N_1(t)$ with a rate given by μ .
- Let us assume that the total population ($P_T(t)$) is not constant, i.e. it changes over the time and the total population is defined by $P_T(t) = N_1(t) + Y_1(t) + N_2(t) + Y_2(t)$.

Under the above assumptions, and considering that the time step is defined by months, our age-structured mathematical diffusion model for e-commerce in Spain is based on the nonlinear system of ordinary difference equations given by eqs. (2) to (5). fig. 1 shows a compartmental representation of this system.

$$N_1(t + 1) = N_1(t) - \frac{d_1}{12}N_1(t) + \gamma_1 Y_1(t) - \frac{c_1}{12}N_1(t) - N_1(t) \frac{\alpha_1 Y_1(t) + \alpha_2 Y_2(t)}{P_T(t)} - p_1 N_1(t) + \frac{\mu}{12} P_T(t), \tag{2}$$

$$Y_1(t + 1) = Y_1(t) + \frac{d_1}{12}Y_1(t) - \gamma_1 Y_1(t) - \frac{c_1}{12}Y_1(t) + N_1(t) \frac{\alpha_1 Y_1(t) + \alpha_2 Y_2(t)}{P_T(t)} + p_1 N_1(t), \tag{3}$$

$$N_2(t + 1) = N_2(t) - \frac{d_2}{12}N_2(t) + \gamma_2 Y_2(t) + \frac{c_1}{12}N_1(t) - N_2(t) \frac{\alpha_3 Y_1(t) + \alpha_4 Y_2(t)}{P_T(t)} - p_2 N_2(t), \tag{4}$$

$$Y_2(t + 1) = Y_2(t) - \frac{d_2}{12}N_2(t) - \gamma_2 Y_2(t) + \frac{c_1}{12}N_1(t) + N_2(t) \frac{\alpha_3 Y_1(t) + \alpha_4 Y_2(t)}{P_T(t)} + p_2 N_2(t). \tag{5}$$

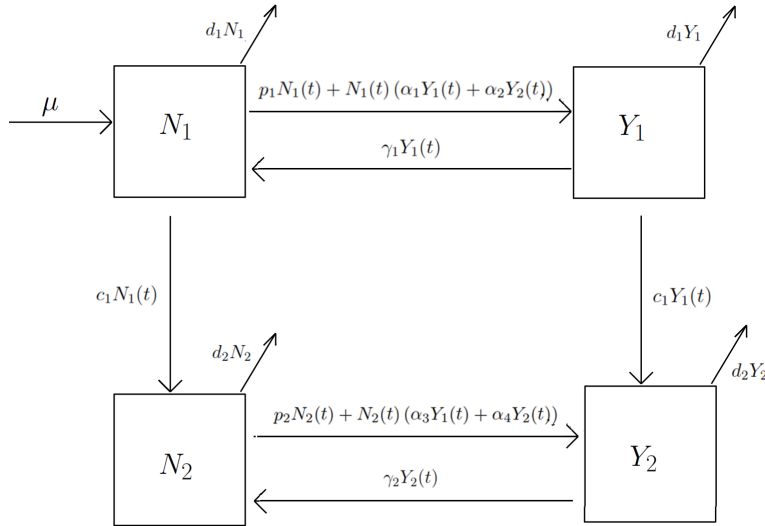


Figure 1: Compartmental model. The boxes represent the populations and the arrows transitions between populations.

Now, we are going to scale the model. Scaling the model is interesting because data population use to be given in percentage. To this aim first of all, we add all the expressions eqs. (2) to (5) in order to establish a relation between $P_T(t + 1)$ and $P_T(t)$.

$$P_T(t + 1) = P_T(t) + \frac{\mu}{12} P_T(t) - \frac{d_1}{12}(N_1(t) + Y_1(t)) - \frac{d_2}{12}(N_2(t) + Y_2(t)). \tag{6}$$

If we define:

$$n1(t) := \frac{N_1(t)}{P_T(t)}, \quad y1(t) := \frac{Y_1(t)}{P_T(t)}, \quad n2(t) := \frac{N_2(t)}{P_T(t)}, \quad y2(t) := \frac{Y_2(t)}{P_T(t)}, \quad (7)$$

and we divide eq. (2) by $P_T(t + 1)$ we obtain

$$\frac{N_1(t + 1)}{P_T(t + 1)} = \frac{\frac{\mu}{12}P_T(t) + N_1(t) - \frac{d_1}{12}N_1(t) + \gamma_1Y_1(t) - \frac{c_1}{12}N_1(t) - N_1(t)\frac{\alpha_1Y_1(t) + \alpha_2Y_2(t)}{P_T(t)} - p_1N_1(t)}{P_T(t) + \frac{\mu}{12}P_T(t) - \frac{d_1}{12}(N_1(t) + Y_1(t)) - \frac{d_2}{12}(N_2(t) + Y_2(t))}. \quad (8)$$

Then we divide numerator and denominator eq. (8) by $P_T(t)$ obtaining:

$$n_1(t+1) = \frac{n_1(t) + \frac{\mu}{12} - \frac{d_1}{12}n_1(t) + \gamma_1y_1(t) - n_1(t)(\alpha_1y_1(t) + \alpha_2y_2(t)) - c_1n_1(t) - p_1n_1(t)}{1 + \frac{\mu}{12} - \frac{d_1}{12}(n_1(t) + y_1(t)) - \frac{d_2}{12}(n_2(t) + y_2(t))}. \quad (9)$$

Using the same procedure in eqs. (3) to (5), we obtain the following scaled system of difference equations:

$$n_1(t + 1) = \frac{n_1(t) + \frac{\mu}{12} - \frac{d_1}{12}n_1(t) + \gamma_1y_1(t) - n_1(t)(\alpha_1y_1(t) + \alpha_2y_2(t)) - c_1n_1(t) - p_1n_1(t)}{1 + \frac{\mu}{12} - \frac{d_1}{12}(n_1(t) + y_1(t)) - \frac{d_2}{12}(n_2(t) + y_2(t))}, \quad (10)$$

$$y_1(t + 1) = \frac{y_1(t) - \frac{d_1}{12}y_1(t) - \gamma_1y_1(t) + n_1(t)(\alpha_1y_1(t) + \alpha_2y_2(t)) - c_1y_1(t) + p_1n_1(t)}{1 + \frac{\mu}{12} - \frac{d_1}{12}(n_1(t) + y_1(t)) - \frac{d_2}{12}(n_2(t) + y_2(t))}, \quad (11)$$

$$n_2(t + 1) = \frac{n_2(t) - \frac{d_2}{12}n_2(t) + \gamma_2y_2(t) - n_2(t)(\alpha_3y_1(t) + \alpha_4y_2(t)) + c_1n_1(t) - p_2n_2(t)}{1 + \frac{\mu}{12} - \frac{d_1}{12}(n_1(t) + y_1(t)) - \frac{d_2}{12}(n_2(t) + y_2(t))}, \quad (12)$$

$$y_2(t + 1) = \frac{y_2(t) - \frac{d_2}{12}y_2(t) - \gamma_2y_2(t) + n_2(t)(\alpha_3y_1(t) + \alpha_4y_2(t)) + c_1y_1(t) - p_2n_2(t)}{1 + \frac{\mu}{12} - \frac{d_1}{12}(n_1(t) + y_1(t)) - \frac{d_2}{12}(n_2(t) + y_2(t))}. \quad (13)$$

3 Conclusion

In this paper, we propose a type-epidemiological mathematical model to study the dynamics of e-commerce in Spain using real data from INE (Spanish Statistical Institute). This model allows us to describe the diffusion of e-commerce with varying the population size.

The conclusions obtained from this study are:

- E-commerce development might be approximated to a type-epidemiological mathematical model.

- Population might be divided in two groups with different behavior.
- The model must be scaled in order to establish a relation between the model and the data collected from the INE.

In future studies, the aim of the authors is to fit the model parameters described in this paper with e-commerce available data. This future work would be useful trying to make predictions on the development of e-commerce over the next years.

Acknowledgements

This work has been partially supported by the Ministerio de Economía y Competitividad grant MTM2013-41765-P.

References

- [1] R.T. Frambach, An integrated model of organizational adoption and diffusion of innovations. *European Journal of Marketing*, 27:22–41, 1993.
- [2] V. Mahajan, E. Mullerm F.M. Bass, New product diffusion models in marketing: A review and directions for research. *The journal of Marketing*, 54:1–26, 1990.
- [3] D. Zhang, A. Ntoko, Mathematical model of technology diffusion in developing countries. *Computational methods in decision-making, economics and finance*, 526–539, 2002.
- [4] <http://www.ine.es>.
- [5] H.W. Hethcote, The Mathematics Of Infectious Diseases. *Society For Industrial and Applied Mathematics*, 42:599–653, 2000.

A New Content Location and Data Retrieval Algorithm for Peer to Peer in Smart Microgrids

S. Marzal[†]*, R. Salas-Puente[†], R. Gonzalez-Medina[†],
G. Garcera[†], and E. Figueres[†]

([†]) Universidad Politecnica de Valencia, Camino de Vera s/n, 46022 Valencia, Spain,
silmarro@upv.es, rosapue1@posgrado.upv.es, raugonme@upv.es,
ggarcera@eln.upv.es, efiguere@eln.upv.es.

November 30, 2017

1 Extend Abstract

Microgrid is a low voltage distributed network formed by various distributed energy resources (DERs) consisting of a variety of loads, microsources (MS), energy storages systems (SS), and plugin hybrid electric vehicles (PHEVs), (See Figure 1) [1]. Microgrids have emerged as a powerful, resilient and sustainable power grid by incorporating advanced renewable energy systems for power generation that can integrate and manage large amount of distributed energy resources in real time. Microgrids can operate in grid-connected mode and islanded mode disconnected from the main grid at the point of common coupling (PCC) in case of faults and be reconnected once the fault has disappeared. In addition, a microgrid must have its own control to ensure the correct operation and coordination of the different DERs.

The communication network plays a critical role in microgrids due to the increase number of renewable resources and microgeneration units (Distributed energy resources, DERs) that are being deployed in them [2]. Now,

*e-mail:silmarro@upv.es

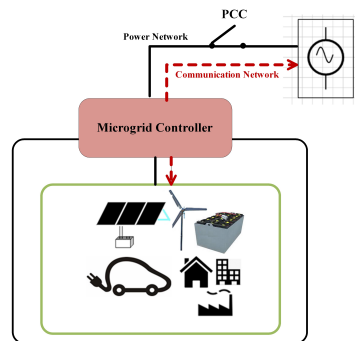


Figure 1: Simplified scheme of a microgrid.

the communication infrastructure must have the ability to easily handle an increasing amount of data traffic or services requests and must to provide a real-time monitoring and control operation of all these nodes leading to move from a centralized communication infrastructure to a decentralized one [3].

The evolution towards the future smart microgrid requires the development of distributed communication architectures and protocols. Recently a new paradigm of Peer-to-Peer (P2P) communications has become the focus of intense research in the field of control and communication structures in microgrids due to they allow robustness, efficiency, scalability and flexibility characteristics [4]. To add smart control which achieves efficient energy management of distributed energy resources, Peer-to-Peer (P2P) has been considered as promising technology that can provide interesting opportunities on control and optimization microgrid operation [5].

Peer-to-peer (P2P) overlay networks are distributed systems without any hierarchical organization or centralized control. These systems avoid a single point of failure and are scalable because the available resources grow with the number of nodes joining the network. Nodes are capable to cooperate to achieve a common goal and they have self-organization capabilities. In these networks the connectivity between nodes is carried out through a physical IP network while network topology is created in a virtual network, called overlay, which are built on top of the physical networks. Overlays allow increased flexibility, extensibility and adaptive reconfiguration. This implies that each node communicates with each other to create self-organizing overlay structures on top of the subjacent physical networks [5].

There are two classes of overlay networks: Unstructured and Structured.

Traditionally Peer-to-Peer networks are mainly developed for file sharing and both structured and unstructured overlay P2P systems are designed for quick search and efficient file storage mechanisms for a huge number of files [6].

On one side, unstructured P2P network has a random and unstructured mesh network topology. There is not an algorithm for organization. The information and data resources are distributed among peers. Flooding lookup technique is used to locate resources and data retrieval in unstructured P2P. Each peer that uses this technique propagates a request to directly connected peers through a successively deeper search in the system. The propagation remains until the message time to live (TTL) threshold (typically four) has been exceeded [7]. This flooding creates a large amount of signal traffic and makes use of a lot of network bandwidth and very high CPU/memory usage. These characteristics do not result in a scalable and efficient system.

On the other hand, structured P2P networks have a dedicated network and a well-defined topology where peers are responsible to the information and data resource. In structured overlays, Distributed Hash Tables (DHT) is used to routing in order to locate resources in the network. In this strategy each peer has a local table (DHT-Distributed Hash Tables) which is used as a lookup algorithm to route the request data according to node tables. DHT tables allows peers find data addressed using flat identifiers (IDs) where IDs and IP addresses node are registered for each neighbouring node. This kind of P2P system improves the network communication usage.

DHT is the most efficient lookup technique, since the resources discovery can be satisfied in a bounded number of steps even in a large scale distributed systems. The proposed algorithm is based on Chord protocol. For DHT lookup algorithms, Chord is the most popular structured routing protocol [8]. Chord DHT-overlay organizes peers on a virtual ring topology. In this protocol each node is responsible of a collection of keys in the space of keys. Each node in the ring upholds a routing table, called the finger table, which is used by the lookup algorithm. The lookup algorithm is started by one node in the ring in order to find a particular key in the space-keys or by an external request and follows these steps [8]: i) Firstly checks if the node which started the search is in charge of that key. If this is true the search is over and the algorithm ends, ii) Otherwise the node will employ its finger table to localize the successor of the target nodes key and request the search of the key to the target node.

As described, Chord specifies which node is responsible of each group of keys and it regulates communication between nodes. However, Chord does

not specify any retrieval data mechanism [9], i.e. each node stores keys to locate information of the key which is responsible, although each node should establish its own methods to find this information. In addition, traditional DHT-Chord does not consider locality [10]. Locality allows creating a group of peers for a particular task. Peers with close interests create shortcuts and use them to locate content. The underlying physical network path could be significantly different from the path on the overlay network if locality in DHT-Chord is not considered. Therefore, the lookup latency in the overlay network could be quite higher and decrease the performance of the applications running over the DHTData Layer [10](See Figure 3). In the specific case of microgrids, these logical groups are often categorized by their nodes functionality (loads, generators, storage system, etc.).

As a result, for achieve these capabilities and create an operational peer, several software layers need to be built as shown in Figure 3.

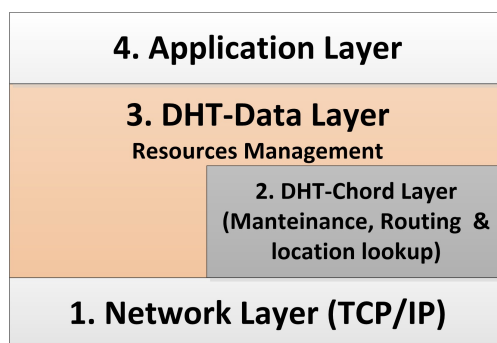


Figure 2: Main Functional Layers of a Peer-to-Peer Application

On the basis of Chord lookup algorithm, the target to achieve in this work is to embed DHT-Data layer functions (layer 3) into DHT-Chord Layer (layer 2) trying minimizing impact of the lookup Chord algorithm to the network performance. This is very important indeed for microgrids since peer-to-peer networks are principally developed for file and processor cycle sharing and network usage resource are less critical than microgrid operation where high efficiency in terms of quality network requirements (high bandwidth and low-latency) is required [11, 12].

In this way, a new clustering algorithm based in Chord approach has been developed. DERs functionality has been embedded into finger table and routing management has been modified in order to: i) Add locality

capabilities for creating node clusters with close interests, ii) Provide location of information and data retrieval, iii) Reduce communications overhead.

An experimental setup has been build up to evaluate the performance of the proposed algorithm.

Figure 4 shows the comparison of proposed and Chord algorithm.

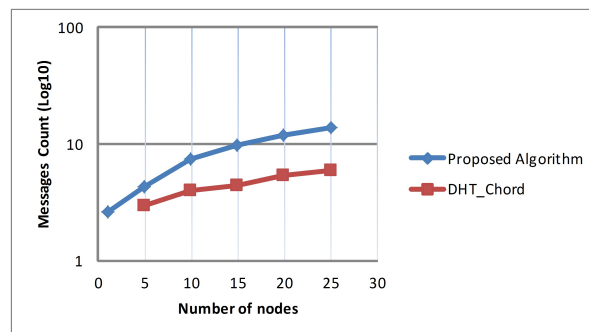


Figure 3: Average Messages count comparison between proposed lookup and retrieval data algorithm and chord lookup algorithm with different network size.

It can be seen, the differences are not significant, as might be expected. Chord algorithm average messages are referred only to the lookup process while proposed algorithm the messages count are referred to total average messages sent into the network for lookup and retrieval processes, thus enabling the reduction of the overall data traffic on the network and end-to-end latencies.

In the case this work will be accepted, in the extended version of the paper, it will be provided a detailed description of the proposed algorithm, its mathematical framework and other experimental results that not appear.

References

- [1] H. Reduan and J. Khyan. A comprehensive review of the application characteristics and traffic requirements of a smart grid communications network. *Computer Networks*, 57(3):825–845, 2013.
- [2] X. Yi and P.Wang. Security framework for wireless communications in smart distribution grid. *IEEE Trans. on Smart Grid*, 2(1):809–818, 2011.

- [3] A. K. M. Baki. Continuous monitoring of smart grid devices through multi protocol label switching. *IEEE Trans. on Smart Grid*, 5(3):1210–1215, 2014.
- [4] J. Engels H. Almasalma and G. Deconinck. Peer-to-peer control of microgrids. In *Proc. IEEE YRS 2016. IEEE Benelux PELS/PES/IAS Young Researchers Symposium. Eindhoven,, 2016.*
- [5] N. Nandagopal M. Cameron, M. Stumptner and et al. Rule-based peer-to-peer framework for decentralised real-time service oriented architectures. *Science of Computer Programming*, 97:202–234, 2015.
- [6] et al A. Maiti, A. Maxwell. Node allocation in peer-to-peer overlay networks based remote instrumentation with smart devices. In *In Telecommunication Networks and Applications Conference (ITNAC), 2016 26th International*, pages 191–198, 2016.
- [7] Van Moorsel De Mello, E. R. and et al. Evaluation of p2p search algorithms for discovering trust paths. In *In European Performance Engineering Workshop. Springer Berlin Heidelberg.,* pages 112–124, 2007.
- [8] A. Malatras. State-of-the-art survey on p2p overlay networks in pervasive computing environments. *Journal of Network and Computer Applications*, 55:1–23, 2015.
- [9] M.F. Kaashoek F. Dabek, E. Brunskill and et al. Building peer-to-peer systems with chord, a distributed lookup service. In *n Hot Topics in Operating Systems, 2001. Proceedings of the Eighth Workshop on,* pages 81–86, 2001.
- [10] X. Zhang W. Wu, Y. Chen and et al. Ldht: Locality-aware distributed hash tables. In *In Information Networking, 2008. ICOIN 2008. International Conference, 2008.*
- [11] P. Kansal and A. Bose. Bandwidth and latency requirements for smart transmission grid applications. *IEEE Trans. on Smart Grid*, 3(3):1344–1352, 2012.
- [12] D. Kicak et al V.C. Gungor, D. Sahin. A survey on smart grid potential applications and communication requirements. *IEEE Transactions on Industrial Informatics*, 9(1):28–42, 2013.

A mathematical invariance principle to study the body-mind problem

Joan C. Micó^{1}, Salvador Amigó^{**}, Antonio Caselles^{***}*

(*) Institut Universitari de Matemàtica Multidisciplinar.
Universitat Politècnica de València.

Camí de Vera s/n., 46022, ciutat de València, Spain.

(**) Departament de Personalitat, Avaluació i Tractaments Psicològics.
Universitat de València,

Av. Blasco Ibáñez 21, 46010, ciutat de València, Spain.

(***) Departament de Matemàtica Aplicada.
Universitat de València.

Dr. Moliner 50, 46100 Burjassot, Spain.

1. Introduction

The first rational approach to the body-mind problem is given to Plato as a dualism between sensitive (body) and intelligible (mind) worlds. Aristotle substitutes Plato's dualism for a matter-shape dualism, considering in his approach psychology, in early ages of philosophy, as a part of physiology. In the Middle Ages the Christian dualism between body and soul (mind) is the dominant thought. Descartes defends a substantial dualism of body and mind but connected through the pineal glandule, although Spinoza and Leibnitz reduce the dualism to two aspects of an all, rather than two total separated aspects. In the twentieth century the positivism proposes the associationism as a way to study the relationship between body and mind through the scientific method. Basically, ending the twentieth century and starting the twenty-first century, two philosophers of science have studied deeply the body-mind problem: Karl R. Popper [1] and Mario Bunge [2].

No researcher denies in the present that body and mind work intimately integrated. A way to observe their relationship is to study the psychological and biological responses to drug consumption. In fact, in the application case presented to study the body-mind problem, methylphenidate is the drug used. It is a powerful psycho-stimulant. The psycho-stimulation can be measured by the General Factor of Personality (GFP), as a universal observable amount of personality (mind). In fact, to measure the GFP, the five adjectives scale has been used in the application case [3]. This scale is based on the General Factor of Personality Questionnaire [4], which has been constructed specifically to assess GFP in the context of the Unique Trait Personality Theory (UTPT) [3, 5]. The UTPT claims for a unique trait, as synonymous of single trait, substituted later by the equivalent concept of GFP, to describe the overall human personality. The GFP is the psychological expression of the activation level of the organism stress system. In fact, in the context of the UTPT, GFP is also called as extraversion in a wider sense than the used in behavioural science, i.e., in the sense of activation level of the organism stress system.

Glutamate (body) is connected with the GFP (mind) because it plays a system roll in the overall biological processes related to the activation of the organism stress system, and thus to GFP. See the work [5] for this question. The aim to use methylphenidate as the stimulus in the application case is because, in addition to its psycho-stimulant effect, its acute administration activates the production of glutamate [6]. Thus, it is a universal observable amount of the biological bases of personality (body), and it can be measured by its molar concentration in blood [7]. Therefore, the double response produced by methylphenidate, psychological (mind) and biological (body), emphasizes its importance in the application case presented.

The response model is an integro-differential equation that has been widely assessed in the context of different experimental designs. It can reproduce the acute effect of a stimulant drug at the both levels of description considered in this work [8, 9, 10, 11, 12]. The model reproduces the dynamical pattern forecasted by Solomon & Corbit [13] and Grossberg [14], by using the hedonic scale, and Amigó [5] for the GFP, i.e., a typical inverted-U dynamical pattern.

The assumption of a mathematical invariance principle, which claims that the psychological (mind) and biological (body) responses hold the response model, provides the bridge model, a second order partial differential equation. It has been assessed, in a more primitive mathematical structure (a first order partial differential equation), where the drug provided is caffeine [12], to study the co-evolution of the GFP and the Big Five traits. Although published before, it has been assessed subsequently in a more evolved mathematical structure: a coupled system of two first order partial differential equations [11]. There, the co-evolution of the GFP, the regulator gen c-fos and glutamate are studied as a

¹ E-mail: jmico@mat.upv.es

consequence of methylphenidate consumption. However, it is still more primitive than the bridge model here presented.

In this paper the response model is presented, and by using the invariance principle, the bridge model is deduced. By using the outcomes of the application case both models are validated. The response model is validated by calibration for both responses: the GFP, measured by the five adjectives list, and the glutamate, measured by the molar concentration in blood. Subsequently the bridge model is validated by using the calibrated values of the response model parameters.

2. The response model

The kinetic part of the response model provides the evolution of the drug stimulus amount, $s(t)$, in organism, after being consumed by the individual. It is given by the time function:

$$s(t) = \begin{cases} \frac{\alpha \cdot M}{\beta - \alpha} (\exp(-\alpha \cdot t) - \exp(-\beta \cdot t)) : \alpha \neq \beta \\ \alpha \cdot M \cdot t \cdot \exp(-\alpha \cdot t) : \alpha = \beta \end{cases} \quad (1)$$

Eq. 1 is the solution of two coupled differential equations [12], which assumes that no drug is present in the organism before consumption. In Eq. 1 M is the initial amount of a drug single dose, α is the drug assimilation rate and β is the drug distribution rate. The dynamics of the GFP is given by the following integro-differential equation [12]:

$$\left. \begin{aligned} \frac{dy(t)}{dt} &= a(b - y(t)) + \frac{p}{b} s(t) - b \cdot q \cdot \int_0^t e^{-\frac{x-t}{\tau}} \cdot s(x) \cdot y(x) dx \\ y(0) &= y_0 \end{aligned} \right\} \quad (2)$$

In Eq. 2, $s(t)$ represents the stimulus given by Eq. 1; $y(t)$ represents the GFP dynamics; and b and y_0 are respectively its tonic level and its initial value. Its dynamics is a balance of three terms, which provide the time derivative of the GFP: the *homeostatic control* ($a(b - y(t))$), i.e., the cause of the fast recovering of the tonic level b , the *excitation effect* ($p \cdot s(t)/b$), which tends to increase the GFP, and the *inhibitor effect* ($b \cdot q \cdot \int_0^t e^{-\frac{x-t}{\tau}} \cdot s(x) \cdot y(x) dx$), which tends to decrease the GFP and is the cause of a continuously delayed recovering, with the weight $e^{-\frac{x-t}{\tau}}$. Parameters a , p , q and τ are named respectively the *homeostatic control power*, the *excitation effect power*, the *inhibitor effect power* and the *inhibitor effect delay*. All the parameters of the model depend on the individual personality or individual biology and on the type of stimulus.

3. The bridge model

To deduce the bridge model, the starting point is assuming the invariance principle, i.e., the glutamate dynamical response can be also described by the response model given by Eq. 2, but with different parameter values. If $g(t)$ is the glutamate variable, g_0 its initial value, and A , B , P , Q and T are the parameters, the response model corresponding to the glutamate response can be written as:

$$\left. \begin{aligned} \frac{dg(t)}{dt} &= A(B - g(t)) + \frac{P}{B} s(t) - B \cdot Q \cdot \int_0^t e^{-\frac{x-t}{T}} \cdot s(x) \cdot g(x) dx \\ g(0) &= g_0 \end{aligned} \right\} \quad (3)$$

Note in Eq. 3 that $s(t)$ is the stimulus function of Eq. 1. Thus, the invariance principle assumes that the influence of the stimulus on the GFP and on glutamate is the same. To find the mathematical relationship between glutamate and the GFP and the time t , the hypothesis stated is:

$$g = g(t, y) \quad (4)$$

Taking the time derivative in Eq. 4:

$$\frac{dg(t, y)}{dt} = \frac{\partial g(t, y)}{\partial t} + \frac{\partial g(t, y)}{\partial y} \frac{dy}{dt} \quad (5)$$

Substituting Eqs. 2 and 3 in Eq. 5, and considering now that the time function $g(t)$ is, from Eq. 4, a two-variables function:

$$\begin{aligned} A(B - g(t, y)) + \frac{P}{B} s(t) - B \cdot Q \cdot f(t, y) &= \\ = \frac{\partial g(t, y)}{\partial t} + \frac{\partial g(t, y)}{\partial y} \left(a(b - y) + \frac{p}{b} s(t) - b \cdot q \cdot z(t) \right) \end{aligned} \quad (6)$$

Take into account in Eq. 6 that, in order to simplify, and for subsequent computations that:

$$z(t) = \int_0^t e^{-\frac{x-t}{\tau}} \cdot s(x) \cdot y(x) dx = e^{-\frac{t}{\tau}} \int_0^t e^{\frac{x}{\tau}} \cdot s(x) \cdot y(x) dx \quad (7)$$

$$f(t, y) = \int_0^t e^{\frac{x-t}{T}} \cdot s(x) \cdot g(x, y) dx = e^{-\frac{t}{T}} \int_0^t e^{\frac{x}{T}} \cdot s(x) \cdot g(x, y) dx \quad (8)$$

The way to avoid the delayed term $f(t, y)$ in Eq. 6, specified by Eq. 8, is to convert it in a second order partial differential equation. To do this, the partial time derivative is taken in both sides of Eq. 6:

$$-A \frac{\partial g(t, y)}{\partial t} + \frac{P}{B} s'(t) - B \cdot Q \frac{\partial f(t, y)}{\partial t} = \frac{\partial^2 g(t, y)}{\partial t^2} + \frac{\partial^2 g(t, y)}{\partial t \partial y} \left(a(b - y) + \frac{p}{b} s(t) - b \cdot q \cdot z(t) \right) + \frac{\partial g(t, y)}{\partial y} \left(\frac{p}{b} s'(t) - b \cdot q \cdot z'(t) \right) \quad (9)$$

Note from Eqs. 7 and 8 that:

$$z'(t) = -\frac{1}{\tau} z(t) + s(t) \cdot y \quad (10)$$

$$\begin{aligned} \frac{\partial f(t, y)}{\partial t} &= -\frac{1}{T} e^{-\frac{t}{T}} \int_0^t e^{\frac{x}{T}} \cdot s(x) \cdot g(x, y) dx + e^{-\frac{t}{T}} \cdot e^{\frac{t}{T}} \cdot s(t) \cdot g(t, y) = \\ &= -\frac{1}{T} f(t, y) + s(t) \cdot g(t, y) \end{aligned} \quad (11)$$

The substitution of Eqs. 10 and 11 in Eq. 9 provides:

$$-A \frac{\partial g(t, y)}{\partial t} + \frac{P}{B} s'(t) + \frac{B \cdot Q}{T} f(t, y) - B \cdot Q \cdot s(t) \cdot g(t, y) = \frac{\partial^2 g(t, y)}{\partial t^2} + \frac{\partial^2 g(t, y)}{\partial t \partial y} \left(a(b - y) + \frac{p}{b} s(t) - b \cdot q \cdot z(t) \right) + \frac{\partial g(t, y)}{\partial y} \left(\frac{p}{b} s'(t) + \frac{b \cdot q}{\tau} \cdot z(t) - b \cdot q \cdot s(t) \cdot y \right) \quad (12)$$

The next step is the elimination of the integral term $\frac{B \cdot Q}{T} f(t, y)$ in Eq. 12. First, the term $B \cdot Q \cdot f(t, y)$ is isolated from Eq. 6:

$$B \cdot Q \cdot f(t, y) = A(B - g(t, y)) + \frac{P}{B} s(t) - \frac{\partial g(t, y)}{\partial t} - \frac{\partial g(t, y)}{\partial y} \left(a(b - y) + \frac{p}{b} s(t) - b \cdot q \cdot z(t) \right) \quad (13)$$

Subsequently Eq. 13 is substituted in Eq. 12, and after reorganization:

$$\begin{aligned} \frac{\partial^2 g(t, y)}{\partial t^2} + \left(a(b - y) + \frac{p}{b} s(t) - b \cdot q \cdot z(t) \right) \frac{\partial^2 g(t, y)}{\partial t \partial y} + \left(\frac{p}{b} s'(t) + \frac{b \cdot q}{\tau} \cdot z(t) - b \cdot q \cdot s(t) \cdot y + \right. \\ \left. \frac{1}{T} \left(a(b - y) + \frac{p}{b} s(t) - b \cdot q \cdot z(t) \right) \right) \frac{\partial g(t, y)}{\partial y} + \left(A + \frac{1}{T} \right) \frac{\partial g(t, y)}{\partial t} = \frac{A}{T} (B - g(t, y)) - B \cdot Q \cdot s(t) \cdot \\ g(t, y) + \frac{P}{T \cdot B} s(t) + \frac{P}{B} s'(t) \end{aligned} \quad (14)$$

Eq. 14 must be completed with the boundary conditions:

$$g(0, y) = g_0 \quad (15)$$

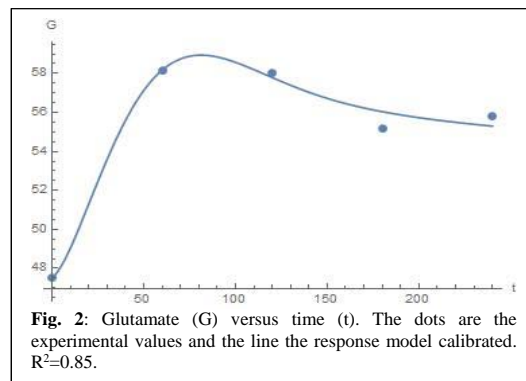
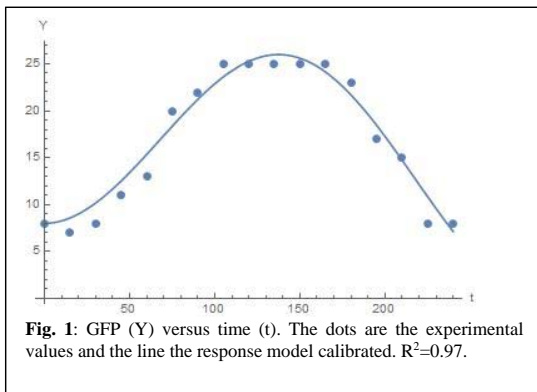
$$\frac{\partial g}{\partial t}(0, y) = A(B - g_0) \quad (16)$$

Eqs. 14, 15 and 16 provide the bridge model sought. Note that $z(t)$ is considered a time function obtained from the numerical solution of Eqs. 2 and 10.

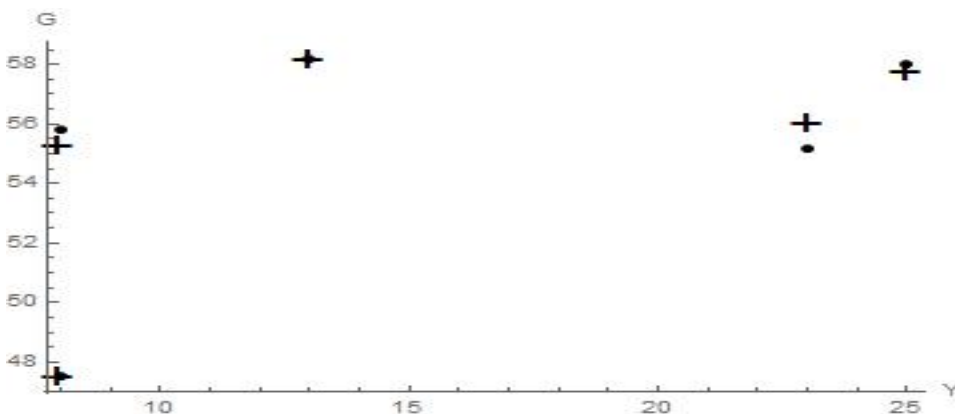
4. The response and bridge models validation

The application case consists in one subject that consumed 20 mg of methylphenidate. The five adjectives scale (adventurous, daring, enthusiastic, merry and bored) was filled out before consumption and after consumption every 15 minutes for 4 hours, and the interval of the *GFP* measures is $y \in [0, 25]$. In addition, a sample of blood was extracted to the subject, before consumption and after consumption every 1 hour. A mass spectrometer is used to obtain the glutamate level in blood. The analysis of the sample provides concentrations of glutamate measured by the direct molar concentration (mc) in blood, and it is used with a scale multiplied by 10^{18} mc. With this scale, the glutamate concentration varies in the interval $g \in [0, 60]$.

The calibration of the response model for the *GFP* dynamics is provided in Fig. 1 and for the glutamate dynamics in Fig. 2.



The theoretical values of the bridge model, $g(t, y)$, are given by the numerical solutions of Eqs. 14, 15 and 16, by considering the optimal parameter values arisen in the calibration of the response model. These numerical solutions have been obtained with the NDSolve function of the MATHEMATICA 10.4 program. The validation is provided in Fig. 3.



Conclusions

Figs. 1 and 2 provide the calibration of the response model, respectively for the GFP response (mind) and for the glutamate response (body), as a consequence of 20 mg of methylphenidate. The visual inspection of these figures as well as the high determination coefficients (R^2) supports the response model validation. In addition, the visual inspection of Fig. 3 and the corresponding high determination coefficient (R^2) provide also the bridge model validation.

Particularly, the response model can be considered validated in the context of the application case presented, supporting its universality, due to it has been already validated in the context of different application cases provided in the literature of Section 1.

However, the bridge model has been validated for first time in the present mathematical structure. The two past application cases cited in Section 1 where it has been validated presented a lesser complexity. The growth in complexity is necessary to overcome two difficulties. In [12] the invariance principle is applied to a differential equation with a non-delayed inhibitor effect. As a consequence, by assuming the invariance principle, the bridge model becomes a first order partial differential equation. In fact, the simplified response model fits the caffeine response. But generally, other stimuli, such as methylphenidate, need to have a delayed inhibitor effect to fit the response. The way to find a more general bridge model is to convert first the delayed integro-differential equation in a system of two coupled differential equations. Subsequently, by assuming the invariance principle, the bridge model is deduced with a third artificial independent variable in two coupled first order partial differential equations. However, this bridge model provides often unstable numerical solutions, due to the arbitrariness of the boundary conditions [11]. Therefore, the present bridge model is an attempt to overcome these difficulties. Then, it needs to be validated in the context of more future application cases.

Let us stress the importance of the bridge model: it represents the co-evolution of the GFP (mind) and glutamate (body) as a consequence of methylphenidate consumption. On a hand, the importance of the GFP as representative of mind must not be neglected. The GFP represents the apex of a hierarchical model of personality that involves the Big Five traits [4, 5]. In addition glutamate as representative of body has neither to be neglected. It takes part of an overall set of biochemical processes related with the stress system in organism [5].

Therefore, the co-evolution that provides the bridge model is a fruitful mathematical approach to study the integrated relationship of body and mind. In fact, its structure shows that this relationship has a dynamical nature, which can be considered a scientific discovering about the subject in

question. It is, finally, a step to better understand the ancient body-mind problem from a mathematical and successful approach.

References

- [1] K. R. Popper. Knowledge and the Body-Mind Problem. In defense of interaction. Routledge, London, New-York 1994.
- [2] M. Bunge. The body-mind problem. A psychobiological approach. Pergamon Press L.td, Oxford 2002.
- [3] S. Amigó, J. C. Micó & A. Caselles. Five adjectives to explain the whole personality: a brief scale of personality. *Revista Internacional de Sistemas*, Vol. 16 (2009), pp. 41-43 (Available in <http://www.uv.es/caselles/>).
- [4] S. Amigó, A. Caselles & J. C. Micó. The General Factor of Personality Questionnaire (GFPQ): Only one factor to understand the personality? *The Spanish Journal of Psychology*, Vol. 13 (2010), pp. 5-17.
- [5] S. Amigó. La teoría del rasgo único de personalidad. Hacia una teoría unificada del cerebro y la conducta (The Unique Personality Trait Theory. Towards a unified theory of brain and behavior). Editorial de la Universitat Politècnica de València. Valencia 2005.
- [6] A. A. Boldyrev, D. O. Carpenter & P. Johnson. Emerging evidence for similar role of glutamate receptors in the nervous and immune systems. *Journal of Neurochemistry*, Vol. 95 (2005), pp. 913-918.
- [7] S. Amigó, A. Caselles, J. C. Micó & J. M. García. Dynamics of the unique trait of personality: blood's glutamate in response to methylphenidate and conditioning. *Revista Internacional de sistemas*, Vol. 16 (2009), pp. 35-40 (Available in <http://www.uv.es/caselles/>).
- [8] S. Amigó, A. Caselles, & J. C. Micó. A dynamic extraversion model: the brain's response to a single dose of a stimulant drug. *British Journal of Mathematical and Statistical Psychology*, Vol. 61 (2008), pp. 211-231.
- [9] A. Caselles, J. C. Micó & S. Amigó. Dynamics of the General Factor of Personality in response to a single dose of caffeine. *The Spanish Journal of Psychology*, Vol. 14 (2011), pp. 675-692.
- [10] J. C. Micó, S. Amigó & A. Caselles. Changing the General Factor of Personality and the c-fos expression with methylphenidate and Self-Regulation Therapy. *The Spanish Journal of Psychology*, Vol. 15 (2) (2012), pp. 850-867.
- [11] J. C. Micó, A. Caselles, S. Amigó, A. Cotolí & M. T. Sanz. A mathematical approach to the body-mind problem from a System Personality theory. *Systems Research and Behavioral Science*, Vol. 30 (2013), pp. 735-749.
- [12] J. C. Micó, S. Amigó, & A. Caselles. From the Big Five to the General Factor of Personality: a Dynamic Approach. *The Spanish Journal of Psychology*, Vol. 17, e74 (2014), pp. 1-18.
- [13] R. L. Solomon & J. D. Corbit. An opponent-process theory of motivation. I. Temporal dynamics of affect. *Psychological Review*, Vol. 81 (1974), pp. 119-145.
- [14] S. Grossberg. The imbalanced DBRAIN: from normal to schizophrenia. *Biological Psychiatry*, Vol. 48 (2000), pp. 81-98.

An approach to assess the competitiveness in Logistics Centers through the analysis of its effectiveness

Victoria Muerza¹, Emilio Larrodé², Carolina García-Planté²

¹ARAGON INSTITUTE OF ENGINEERING RESEARCH (i3A). Edificio de I+D+i, C/ Mariano Esquillor s/n – 50018, Zaragoza (Spain). Tel: +34 976 761888. vmuerza@unizar.es

²UNIVERSITY OF ZARAGOZA. Dpto. de Ingeniería Mecánica. C/ María de Luna, 3 – 50018. Zaragoza (Spain). Tel: +34 976 762319. elarrode@unizar.es, cgplante@gmail.com

1. INTRODUCTION

From a business point of view, the decision to locate the distribution center of a firm in a given logistics center can condition its performance, since the movement and storage of products is increasingly important in the current industrial landscape, as a part of the firm's supply chain, being a key element of its competitiveness (Porter, 2000).

There have been proposed some methodologies for the location selection's problem (e.g. Chen, 2001; Kayikci, 2010; Kampf et al., 2011) by using different approaches (e.g. Analytic Hierarchy Process, Topsis, Artificial Neural Network). The location selection's problem usually considers some common criteria (e.g. accessibility, security, costs, environmental impact, proximity to customers, proximity to suppliers, possibility of expansion, quality of service, infrastructure conditions and human resource). However, the effectiveness has not usually been considered in the decision making process. Understanding the effectiveness of a logistics center allows its sustainable development, from the point of view of a company analyzing possible locations for its distribution center, the study of this aspect should be considered in order to identify the most competitive alternative.

The main objective of this paper is to identify the determining factors that affect the effectiveness of a logistics center, and propose a model based on the analytic hierarchy process (AHP), for the assessment of its competitiveness.

2. ANTECEDENTS

2.1. Concept of Logistics Center

There is no consensus in the literature when defining the concept of logistics center. Several authors gather a compilation of the different terms used (Meiduté, 2005; Rimiene and Grunday, 2007). The most common terms are Logistics Park, Logistics Platform, Freight Village, Logistics Center, although there are other terms (e.g. dry port, distribution terminal).

This paper adopts the definition given by The European Logistics Platforms Association (Europlatforms, 2017) which considers:

“A Logistics Center is a center in a defined area within which all activities relating to transport, logistics and the distribution of goods – both for national and international transit, are carried out by various operators on a commercial basis. The operators can either be owners or tenants of buildings and facilities (warehouses, distribution centres, storage areas, offices, truck services, etc.), which have been built here”.

According to Europlatforms, a Logistics Center should preferably be served by a multiplicity of transport modes and be managed in a single and neutral legal body.

2.2. Effectiveness and competitiveness in logistics centers

Moreno-Jiménez (2006) considers the effectiveness implies "doing the right thing", that is, identifying the relevant aspects and using them appropriately to solve the problem, which implies long-term strategic planning. Therefore, the effectiveness will mean the sustainable development of the logistics center as a whole, giving a level of service according to the demand of the users and the general requirements of the logistics activity.

On the other hand, as regards the concept of competitiveness, Porter (2000) considers it is

determined by the productivity, defined as the value of the product generated by a unit of labor or capital. A logistics infrastructure is considered competitive when its positioning is superior compared to other alternatives. To achieve sustainable growth and a competitive market position, a number of factors should be analyzed, which encompass a global and strategic vision of the logistics center.

2.3. The analytic hierarchy process (AHP)

AHP is a multicriteria methodology used in decision-making processes. It is included in the group of so-called 'discrete', since it considers the number of alternatives is discrete and each of them can be explicitly treated. This tool allows the consideration of multiple scenarios, actors, factors and criteria (tangible and intangible). It builds an absolute scale, associated with the priorities of the elements being compared, based on a four-step process: (i) modeling, (ii) valuation, (iii) prioritization and (iv) synthesis (Saaty, 1980; 1994). The AHP approach requires the translation of perceptions into numerical scales. One of the most used mechanisms is the Saaty's scale through pairwise comparisons (Saaty, 1980).

The priorities of the model ($w_i=1, \dots, n$) can be obtained by means of different methods. In this paper it is applied the eigenvector problem

$$Aw = \lambda_{max} w \quad \sum_{i=1}^n w_i = 1 \tag{1}$$

where $A=(a_{ij})$ is the reciprocal pairwise comparison matrix, λ_{max} is the principal eigenvalue of A and w is the vector of priorities. The measure of inconsistency in judgements have been obtained by means of the *Consistency Index- CI* (Saaty, 1980), expressed as

$$CI = \frac{\lambda_{max} - n}{n - 1} \tag{2}$$

where λ_{max} is the principal eigenvalue of the judgements matrix, and n its order. When the reciprocal comparison matrix is consistent $\lambda_{max} = n$, and $CI=0$. Saaty proposed the *Consistency Ratio- CR* as a way of normalize the measurement, that is given by

$$CR = \frac{CI}{RI(n)} \tag{3}$$

where $RI(n)$ is the Random Consistency Index for matrices of order n , obtained by means of the simulation of 100,000 reciprocal matrices randomly generated (Aguarón and Moreno-Jiménez, 2003).

3. MODEL DEVELOPMENT

The proposed model consists of four levels: goal (G- to measure the effectiveness and competitiveness of a logistics center), 2 criteria (C), 8 subcriteria (SC), and 18 attributes (A). The assessment of the hierarchy has been carried out by a group of five experts (Administration representative, park manager, logistics operative, user company, logistics researcher) working in a context of group decision making (single decision based on consensus).

The elements of the model and the priorities obtained (with exception of the goal) are defined in Table 1 and Table 2. The group elicited 1 judgment for the pairwise comparison matrix that compared the relative importance of the actors versus the factors with respect to the goal; 12 judgments (6+6) when comparing the eight sub-criteria with respect to the criteria (two pairwise comparison matrices), 12 judgments (1+3+1+3+1+1+1+1) when comparing the attributes with respect to the sub-criteria (eight pairwise comparison matrices). All pairwise comparison matrices have acceptable inconsistencies ($CR < 0.10$). The overall inconsistency of the model is acceptable (0.08).

Table 1. Model prioritization

C1. Actors										C2. Factors							
SC1		SC2			SC3		SC4			SC5		SC6		SC7		SC8	
w(A1)	w(A2)	w(A3)	w(A4)	w(A5)	w(A6)	w(A7)	w(A8)	w(A9)	w(A10)	w(A11)	w(A12)	w(A13)	w(A14)	w(A15)	w(A16)	w(A17)	w(A18)
0,068	0,068	0,018	0,003	0,003	0,058	0,019	0,009	0,001	0,002	0,033	0,298	0,246	0,049	0,019	0,058	0,024	0,024

Table 2. Elements of the proposed model

Elements	Description
C1. Actors	Entities and groups of people involved in the activity of the logistics center.
SC1. Property	Entity that owns the park.
<i>A1. Public Property</i>	The Logistics Center belongs to the Administration.
<i>A2. Private Property</i>	Company or group of companies.
SC2. Management	Independent, it guarantees a centralized control of operations and ensures the strategy of the initiative.
<i>A3. Top management</i>	Maintains the strategic mission of the logistics center, ensures the accomplishment of the requirements considered objectives of the park.
<i>A4. Commercial management</i>	It positions the logistics center in the market and analyzes its approach through the appropriate selection of located companies' typology.
<i>A5. Technical –operational management</i>	Management of the infrastructure technical aspects, which affect its daily operation. It cannot be neglected for giving a service of quality.
SC3. Direct users	The companies located in the logistics center which have chosen this location to carry out its activity.
<i>A6. CEO</i>	Organization working with the strategic alignment and acts according to this view.
<i>A7. Economical-Technological commercial management</i>	Departments analyzing the operational aspects of the supply chain management. They evaluate the tangible parameters and give advice on the adequacy of the operative to the mission of the company.
SC4. Indirect users	Logistic operators and transport infrastructure managers. Essential for the operation of the logistics center.
<i>A8. Direct services</i>	Logistic operators and transport infrastructure managers.
<i>A9. Complementary services</i>	Commercial, social, environmental support activities and technology and communication facilitation activities (shopping centers, financial institutions, restaurants, etc).
<i>A10. Workers</i>	Includes all types of activities in the logistics center.
C2. Factors	Aspects related to the effectiveness and competitiveness of the logistics center.
SC5. Technical-operational	The operational and structural aspects of the logistics center.
<i>A11. Characteristics of the center</i>	Surface for logistics activities, level of occupation, brand image, existence of synergies, etc.
<i>A12. Technological-operational characteristics</i>	Geostrategic position, infrastructures and capacity, extension of the influence area.
SC6. Economic	Establishment and maintenance costs in a logistics center, and expected profitability.
<i>A13. Cost</i>	Expected cost for the company for its location in a logistics center. This factor depends mainly on the property, and secondly on the management entity.
<i>A14. Induced profitability</i>	Expected profitability for the companies of the logistics center.
SC7. Social	Availability and quality of employment, with its effect in the logistics center and the region.
<i>A15. Employment</i>	The property factor, particularly the public property, ensures that the workforce is not a problem for the initiative, and even promotes regulations for that purpose.
<i>A16. Innovation and knowledge</i>	The advanced and innovative provision in new technologies is fundamental in the automation of the logistic processes, with a consequence in a dynamization of the workforce, maximizing the use of resources.
SC8. Environmental	Beneficial effect of the supply chain management improvement to minimize the negative impact of logistics operations.
<i>A17. Regulatory compliance</i>	The environmental aspect must be considered from the design stage. The most modern environmental treatment solutions available with less unwanted effects are valued.
<i>A18. Environmental improvements</i>	Wastewater treatment for reuse, optimization of electrical use, existence of renewable energy for the maintenance of the logistics center and supply to users, use of efficient transport.

4. CASE STUDY

The application of the model has been carried out through the comparison of three logistics centers in Spain (S): S1. Zaragoza Logistics Platform (PLAZA), S2. Coslada Transport Center, Madrid (CTC) and S3. Vitoria-Gasteiz Intermodal Transport and Logistics Center (CTV). The selected logistics centers are comparable in the decision-making process for a given company, since they offer a similar activity that satisfies its needs. The valuation of the three alternatives has been made by the group of experts based on their knowledge and expertise and the available information on these logistics centers.

From a global point of view, it can be seen that the final or total priorities of the alternatives are: $w(S1) = 0.564$; $w(S2) = 0.143$; $w(S3) = 0.293$. The ranking of alternatives shows that PLAZA (S1 > S3 > S2) is the preferred alternative in terms of effectiveness and competitiveness (Figure 1).

Plaza	.564
CTC	.143
CT Vitoria	.293

Figure 1. Final priorities of the analyzed alternatives

If analyzed the ranking of alternatives from the point of view of the Actors it can be seen (Figure 2a) PLAZA is the preferred alternative followed by CTC (S1> S2> S3). However, the same analysis from the point of view of the Factors (Figure 2b) shows there is a rank reversal of the alternatives, although PLAZA remains preferred over the other two alternatives (S1> S3> S2).

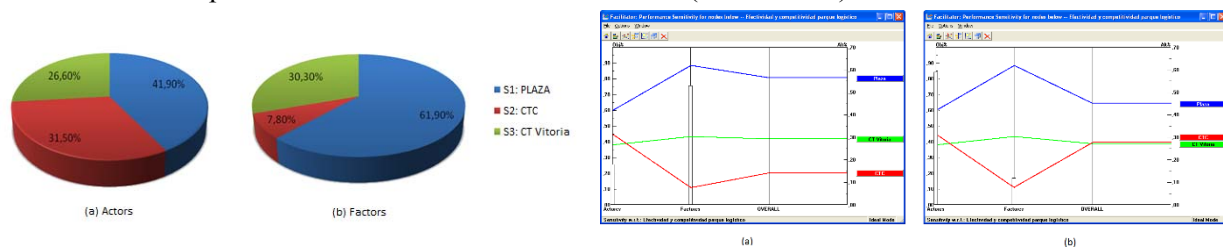
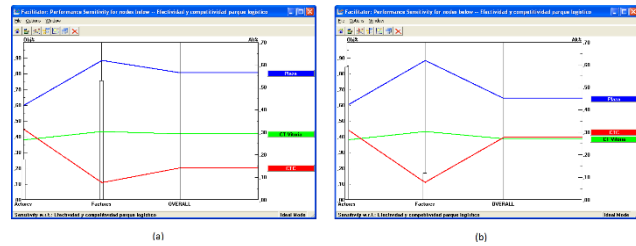


Figure 2. Preference of the alternatives with respect to the actors and factors of the model



The sensitivity analysis of the model has been carried out by using the Expert ChoiceTM software. The Performance graph (Figure 3) provides information on the total priorities of the alternatives and their global behavior with respect to the criteria. It can be seen that the best alternative, S1, dominates the other two alternatives both in the actors and factors criteria (Figure 3a). By introducing changes in the weights of the criteria it can be produced a rank reversal of the best alternative at a global level. Carrying out a simulation (Figure 3b) it is necessary to increase the weight of the Actors criterion by 59% for CTC to be the preferred alternative over CT Vitoria, although the preferred alternative remains being PLAZA. In any case, this change is quite improbable due to the radical changes needed with regards to the initial values.

In short, the sensitivity analysis confirms that the ranking S1>S3> S2 is strongly robust and that PLAZA is the most effective and competitive alternative.

5. CONCLUSIONS

This paper proposes a model for the assessment of the effectiveness and competitiveness of a logistics center. A hierarchy of the factors involved has been obtained through the application of the AHP methodology with relative measures. The economic factor, particularly the company location costs in the logistics center (A13), together with the technological-operational characteristics of the logistics center (A12) are the main influential factors. The environmental factor has average relevance, consolidating the general trend of commitment to the environment and the use of efficient and sustainable resources.

The validation of the model has been carried out by means of the analysis of three logistics centers in Spain, under similar conditions of supply for a company, determining that PLAZA is the most competitive option. In the case of three comparable alternatives, the application of AHP with relative measurements is advisable. However, when the number is greater than 7 ± 2 it is recommended to use AHP with absolute measurements, allowing to establish a recommendable level of competitiveness.

REFERENCES

- Aguarón, J., and J. M. Moreno-Jiménez. 2003. The Geometric Consistency Index: Approximated Thresholds. *European Journal of Operational Research*, 147 (1), pp. 137–145.
- Chen, C-T. (2001). A fuzzy approach to select the location of the distribution center. *Fuzzy Sets and Systems*, 118(1), pp. 65-73.
- Europlatforms (2017). The European Logistics Platforms Association. Definition, Available at: <http://www.europlatforms.eu/definition/>. Accessed 20 March 2017.
- Kampf, R., Průša, P. and Savage, C. (2011). Systematic location of the public logistic centres in Czech Republic. *Transport*, 26(4), pp. 425-432.
- Kayikci, Y. (2010). A conceptual model for intermodal freight logistics centre location decisions. *Procedia - Social and Behavioral Sciences*, 2(3), pp. 6297-6311.
- Meidutė, I. (2005). Comparative Analysis of the Definition of Logistics Centres. *Transport*, 20(3), pp. 106-110.
- Moreno-Jiménez, J.M. (2006). E-Cognocracia: Nueva Sociedad, Nueva Democracia. *Estudios de Economía Aplicada*, 24(1-2), 559–581.
- Porter, M. (2000). Location, competition, and economic development: local clusters in a global economy. *Economic Development Quarterly*, 14(1), pp. 15-34.
- Rimieni K and Grundey, D. (2007), Logistics Centre Concept through Evolution and Definition. *Engineering Economics*, 4(54), pp. 87-95.
- Saaty, T.L. (1980). *The Analytic Hierarchy Process*. McGraw-Hill, New York.
- Saaty, T.L. (1994). *Fundamentals of Decision Making and Priority Theory with the Analytic Hierarchy Process*. RWS Publications, Pittsburgh, PA.

Mathematical Modelling of Shafts in Drives

T. Náhlík^b *; P. Hrubý[†], and D. Smetanová[‡]

(b) Department of Informatics and Natural Sciences, The Institute of Technology and Business
Okružní 517/10, 370 01 České Budějovice, Czech Republic

(†) Department of Mechanical Engineering, The Institute of Technology and Business,
Okružní 517/10, 370 01 České Budějovice, Czech Republic,

(‡) Department of Informatics and Natural Sciences, The Institute of Technology and Business
Okružní 517/10, 370 01 České Budějovice, Czech Republic.

November 30, 2017

1 Introduction

Propeller shafts of drive vehicles transmit a torque at relatively large distances. The shafts are based on long and slender, and must be dimensioned not only in terms of torsional stress, but it is also necessary to monitor its resistance to lateral vibration. Due to the continuous operational area, the shafts are needed to operate in sub-critical speed. It is necessary to find the critical speed. Due to results of previous works and experiments, it is not possible to model the shafts using procedures that are commonly reported in the literature [1, 2], but it is necessary to formulate a model that allows to respect that with increasing the angular velocity of rotation significantly reduce the spectrum of natural frequency relative lateral vibrations.

*e-mail:nahlik@mail.vstecb.cz

2 Formulation of the problem

Propeller shafts are in a steady state stressed by excitation bending moments harmonic, and their vectors are orthogonal to the rotating plane of a relevant fork Hooks joints (Figure 1).

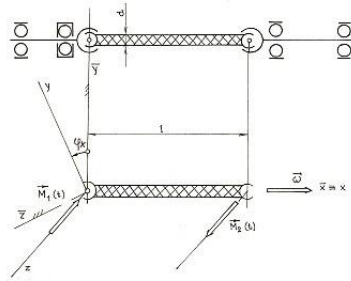


Figure 1: Model of propeller shafts

We build a model on assumption of formation relative spatial bending vibration in the shaft system $O(x, y, z)$

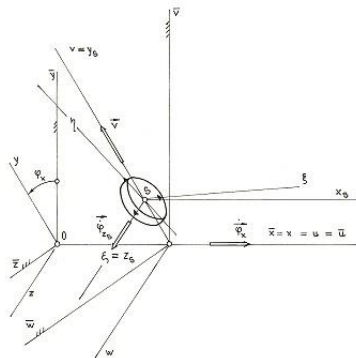


Figure 2: Coordinates system of the shaft

(Figure 2), which rotates at an angular speed $\vec{\varphi}_x$. We can reduce the dimensionality of the problem from 3D to 2D by neglecting the Coriolis force and gyroscopic moments acting on the element of the shaft. Then we can solve the problem in the rotating plane $O(x, y)$. The instantaneous state of the element is determined by the angular velocity $\vec{\varphi}_x$, the velocity \vec{v}_x and the angular velocity $\vec{\varphi}_{z_s}$. We would like to build a mathematical model of a coupling shaft to calculate spectral and modal properties of the connecting shaft including the natural frequency of bending oscillations.

3 Physical Discretization

We will replace the drive shaft shown in the Figure 1 (consider solid bearings) by discrete mechanical system with only one degree of freedom. This will system will be divided into two equal halves which will represent an intangible spring (Figure 3) having rigidity $\frac{k}{2}$.

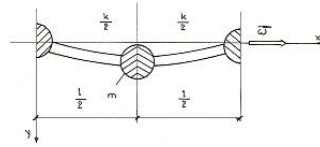


Figure 3: Replacing of the drive shaft by divided system of one degree of freedom.

The mass is concentrated to the endpoints of the springs. This means that two fixed points belongs to the support and two others fixed points will merge in to one in the middle of the shaft. This middle point will have the mass of $m = \frac{Sl\rho}{2}$, where S is the cross-section area, l is length of the shaft and ρ is density. This model can be simply transform to model of the spring (Figure 4).

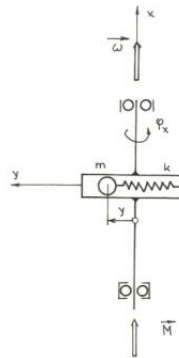


Figure 4: Modelling of the shaft by the spring

In this case we can determine the stiffness of this spring as $k = \frac{48EJ}{l^3}$, where E is modulus of elasticity in tension, J is defined as $J = \frac{\pi}{4}r^4$ and l is length of the shaft. Assuming the constant angular velocity ω it is necessary to introduce the moment \bar{M} . Now we can write equations for kinetic and

potential energy of the spring.

$$E_k = \frac{1}{2}m\dot{y}^2 + \frac{1}{2}m(y\dot{\varphi}_x)^2 \quad (1)$$

$$E_p = \frac{1}{2}ky^2 \quad (2)$$

And also equations of motion.

$$m\ddot{y} + (k - m\omega^2)y = 0, M - 2my\dot{y}\omega = 0 \quad (3)$$

We can rewrite the equation of relative oscillating movement in rotating plane in the form:

$$\ddot{y} + \Omega^2 y = 0 \quad (4)$$

Where $\Omega = \sqrt{\frac{k}{m} - \omega^2}$ is the natural frequency of relative undamped oscillations. By modification of this equation we obtain:

$$\Omega^2 + \omega^2 = \frac{k}{m} \quad (5)$$

which is equation of the circle with origin in $O(\omega, \Omega)$ and radius $\frac{k}{m}$.

4 Test model

Parameter of the test model (propeller shaft of the vehicle Š 781):
 $r = 0.0105m$, $l = 0.65m$, $E = 2.1 \cdot 10^{11}Pa$ and $\rho = 7.8 \cdot 10^3kg \cdot m^{-3}$. Using these parameters we will obtain:

$J = 9 \cdot 10^{-4}m^4$, $S = 3.46 \cdot 10^{-4}m^2$, $k = 3.3 \cdot 10^5Nm^{-1}$, $m = 0.88kg$ and $\Omega(0) = 591.9483rad \cdot s^{-1}$ (see Figure 5)

It is also possible to obtain analytical solution by solving following equation derived in [3], which is describing the model on the Figure 6

$$\frac{\partial^4 y}{\partial x^4} - \frac{\rho S r^2}{4EJ} \cdot \frac{\partial^4 y}{\partial x^2 \partial t^2} - \frac{\rho S r^2 \omega^2}{4EJ} \cdot \frac{\partial^2 y}{\partial x^2} + \frac{\rho S}{EJ} \cdot \frac{\partial^2 y}{\partial t^2} - \frac{\rho S \omega^2}{EJ} \cdot y = 0 \quad (6)$$

Solution of eq. 6 provide us relation between Ω and ω in form of:

$$\frac{\Omega^2}{R^2} + \frac{\omega^2}{R^2} = 1 \quad (7)$$

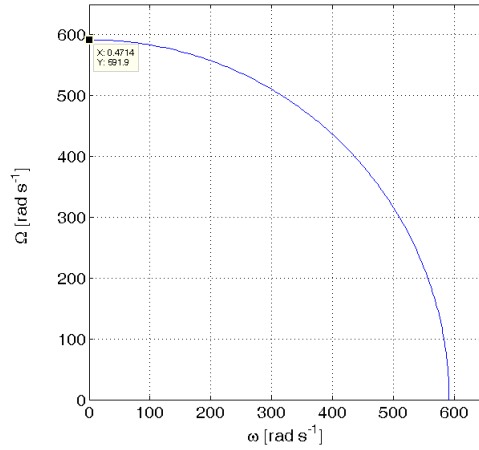


Figure 5: The natural frequency dependence of discrete model’s relative transverse vibration (shown in Figure 4) on the angular velocity of rotation

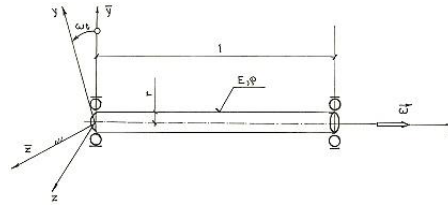


Figure 6: Test model for calculation of propeller shaft’s speed resonance

For our test model is the final analytic solution:

$$R = \frac{r}{2} \sqrt{\frac{E}{\rho}} \left(\frac{\pi}{l}\right)^2 \tag{8}$$

If we calculate R with testing parameters we obtain the value $R = 636.1432rad \cdot s^{-1}$ and by parametrizing with ω the graph 7.

5 Conclusion

We are able to define the mathematical model based on the physical discretization and used it for solving the problem of finding critical speed of rotations. This model was programmed as a script in GNU Octave. There

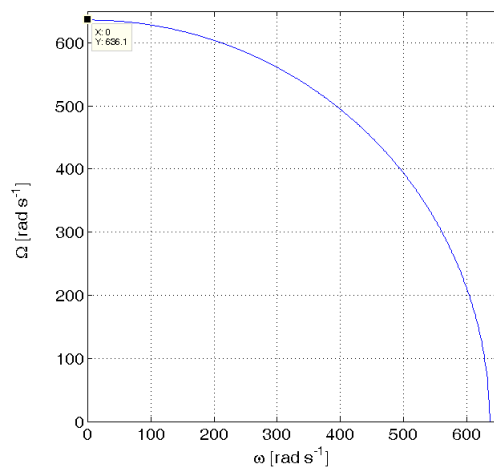


Figure 7: The graph functional dependence of the angular frequency (Ω) lateral vibrations relative to the angular speed of rotation (ω) of the propeller shaft's test model.

is also possibility of using analytical solution derived from equation 6. Both of these solutions gives us the circular dependency of Ω and ω (Equations 5, 7). As future work we would like to use also Finite element method for modelling propeller shaft and for calculation of critical speed.

References

- [1] E. Hájek, P. Reif, F. Valenta, The elasticity and strength I. , SNTL/ALFA. Prag, 1988. 04-224-88.
- [2] E. Hájek et al. The elasticity and strength II. ČVUT Publishing. Publication number - 3251. Prag, 1979.
- [3] P. Hrubý, Cardan coupling shaft vibrations in the rotating plane. The written work to the professional exam candidate. VŠSE. Plzeň, 1979.

The Randomized Non-Autonomous Scaled Logistic Differential Equation: Theory and Applications

J.-C. Cortés^b*, A. Navarro-Quiles^b,
J.-V. Romero^b and M.-D. Roselló^b.

(^b) Instituto Universitario de Matemática Multidisciplinar,
Universitat Politècnica de València, Spain.

November 30, 2017

1 Introduction

In this contribution we study the randomization of the classical logistic differential equation

$$X'(t) = K(t)(1 - X(t))X(t), \quad t > t_0 \in \mathbb{R}, \quad X(t_0) = X_0. \quad (1)$$

We will assume that the initial condition, X_0 , is an absolutely continuous real random variable (r.v.) and the diffusion coefficient, $K(t)$, is a stochastic process (s.p.) defined on a common complete probability space $(\Omega, \mathcal{F}, \mathbb{P})$. For the sake of convenience, it is assumed the equation is normalized, that is,

$$\mathbb{P}[\{\omega \in \Omega : 0 < X_0(\omega) < 1\}] = 1.$$

We compute the first probability density function (1-p.d.f.), $f_1(x, t)$, of the solution s.p. $X(t)$ to random initial value problem (1) in different scenarios.

*e-mail: jccortes@imm.upv.es

The computation of the 1-p.d.f. is advantageous since it permits to compute all one-dimensional statistical moments of the solution s.p.

$$\mathbb{E} [(X(t))^k] = \int_{-\infty}^{+\infty} (x(t))^k f_1(x, t) dx, \quad k = 0, 1, 2, \dots$$

As a consequence, the mean, $\mu_X(t) = \mathbb{E} [X(t)]$, and the variance, $\sigma_X^2(t) = \mathbb{V} [X(t)] = \mathbb{E} [(X(t))^2] - (\mu_X(t))^2$, are easily derived as particular cases. Furthermore, $f_1(x, t)$ allows us to compute the probability that the solution lies in specific sets of interest,

$$\mathbb{P} [\{\omega \in \Omega : a \leq X(t, \omega) \leq b\}], \quad -\infty \leq a < b \leq +\infty.$$

To conduct our study, two major techniques will be applied in a combined manner, namely, the so-called Karhunen-Loève expansion (KLE) and the Random Variable Transformation (RVT) method.

The KLE allows us to represent the second-order s.p. $K(t)$, i.e., $\mathbb{E} [K^2(t)] < +\infty$ for all t , that has a non-numerable degree of randomness as a function of a denumerable set of r.v.'s, say $\{\eta_i : i \geq 1\}$ having zero-mean, unit variance and uncorrelated, $\mathbb{E}[\eta_i] = 0$, $\mathbb{V}[\eta_i] = 1$ and $\mathbb{E}[\eta_i \eta_j] = 0$ for every $i, j \geq 1$, $i \neq j$. KLE constitutes a generalized Fourier-type spectral representation for second-order s.p.'s.

Theorem 1 (KLE expansion) [1, p.202]. *Let us consider the second-order s.p. $\{X(t) : t \in \mathcal{T}\}$ being $\mathcal{T} \subset \mathbb{R}$. Then,*

$$X(t, \omega) = \mu_X(t) + \sum_{j \geq 1} \sqrt{v_j} \phi_j(t) \eta_j(\omega), \quad \omega \in \Omega, \tag{2}$$

where this sum is mean square convergent and

$$\eta_j(\omega) := \frac{1}{\sqrt{v_j}} \mathbb{E} [(X(t) - \mu_X(t)) \phi_j(t)],$$

being $\{(v_j, \phi_j(t)) : j \geq 1\}$ the eigenpairs of the covariance $\Gamma_X(t, s)$ operator satisfying the integral equation

$$\lambda_j \phi_n(t) = \int_{\mathcal{T}} \Gamma_X(t, s) \phi_k(s) ds, \quad j \geq 1.$$

The RVT method is a powerful result that permits to obtain the joint p.d.f. of a random vector that results after mapping another random vector whose joint p.d.f. is known. This result is very useful in dealing with s.p.'s having a finite degree of randomness. In its multi-dimensional version, this result can be stated as follows

Theorem 2 (Multidimensional RVT method) [2, p.25]. *Let us consider $\mathbf{X} = (X_1, \dots, X_n)^\top$ and $\mathbf{Z} = (Z_1, \dots, Z_n)^\top$ two n -dimensional absolutely continuous random vectors defined on a probability space $(\Omega, \mathfrak{F}, \mathbb{P})$. Let $\mathbf{r} : \mathbb{R}^n \rightarrow \mathbb{R}^n$ be a one-to-one deterministic transformation of \mathbf{X} into \mathbf{Z} , i.e., $\mathbf{Z} = \mathbf{r}(\mathbf{X})$. Assume that \mathbf{r} is continuous in \mathbf{X} and has continuous partial derivatives with respect to each X_i , $1 \leq i \leq n$. Then, if $f_{\mathbf{X}}(\mathbf{x})$ denotes the joint probability density function of random vector \mathbf{X} , and $\mathbf{s} = \mathbf{r}^{-1} = (s_1(z_1, \dots, z_n), \dots, s_n(z_1, \dots, z_n))^\top$ represents the inverse mapping of $\mathbf{r} = (r_1(x_1, \dots, x_n), \dots, r_n(x_1, \dots, x_n))^\top$, the joint probability density function of random vector \mathbf{Z} is given by*

$$f_{\mathbf{Z}}(\mathbf{z}) = f_{\mathbf{X}}(\mathbf{h}(\mathbf{z})) |J|, \tag{3}$$

where $|J|$, which is assumed to be different from zero, is the absolute value of the Jacobian defined by the determinant

$$J = \det \left(\frac{\partial \mathbf{s}^\top}{\partial \mathbf{z}} \right) = \det \begin{pmatrix} \frac{\partial s_1(z_1, \dots, z_n)}{\partial z_1} & \dots & \frac{\partial s_n(z_1, \dots, z_n)}{\partial z_1} \\ \vdots & \ddots & \vdots \\ \frac{\partial s_1(z_1, \dots, z_n)}{\partial z_n} & \dots & \frac{\partial s_n(z_1, \dots, z_n)}{\partial z_n} \end{pmatrix}. \tag{4}$$

2 Study-cases

2.1 General case: Non-numerable degree of randomness

In a first step, we deal with the case that the diffusion coefficient $K(t)$ is an arbitrary second-order s.p. Then, we use a truncated KLE together the RVT method to construct the following sequence $\{f_1^N(x; t) : N \geq 1\}$, that is, the 1-p.d.f. of each truncation of the solution s.p., $X_N(t)$.

$$\begin{aligned}
 f_1^N(x;t) = & \int_{\mathcal{D}(\eta_1)} \cdots \int_{\mathcal{D}(\eta_N)} f_N \left(\frac{x \exp \left(- \int_{t_0}^t \left(\mu_K(s) + \sum_{j=1}^N \sqrt{v_j} \phi_j(s) \eta_j \right) ds \right)}{1 + x \left(-1 + \exp \left(- \int_{t_0}^t \left(\mu_K(s) + \sum_{j=1}^N \sqrt{v_j} \phi_j(s) \eta_j \right) ds \right) \right)}, \eta_1, \dots, \eta_N \right) \\
 & \times \frac{\exp \left(- \int_{t_0}^t \left(\mu_K(s) + \sum_{j=1}^N \sqrt{v_j} \phi_j(s) \eta_j \right) ds \right)}{\left(1 + x \left(-1 + \exp \left(- \int_{t_0}^t \left(\mu_K(s) + \sum_{j=1}^N \sqrt{v_j} \phi_j(s) \eta_j \right) ds \right) \right) \right)^2} d\eta_N \cdots d\eta_1,
 \end{aligned} \tag{5}$$

being $0 < x < 1$, $t > 0$, $f_N = f_{X_0, \eta_1, \dots, \eta_N}$ and $\mathcal{D}(\eta_i)$, $1 \leq i \leq N$, stands for the domain of r.v. η_i . Furthermore, we provide mild conditions in order to guarantee the convergence of this sequence to the 1-p.d.f. of the exact solution s.p.

This result is particularized in the significant case that $K(t) := W(t)$ is the brownian (or Wiener) s.p. for which the correlation function is $\Gamma_W(t, s) = \min(t, s)$ and the eigenpairs are $\left\{ \left(\frac{4T^2}{\pi^2(2j-1)^2}, \sqrt{\frac{2}{T}} \sin \left(\frac{(2j-1)\pi t}{2T} \right) \right) \right\}$ for a fixed interval $[0, T]$, $T > 0$. The numerical results obtained via the approximation $\{f_1^N(x;t) : N \geq 1\}$ are compared against the exact distribution which is known in this particular. So, this example acts as a test to account for the accuracy of the proposed technique.

2.2 Lognormal case

As a second example, we consider the case where $K(t) = \exp(W(t))$, that is the diffusion coefficient is a positive s.p., namely, the so-called Lognormal s.p.. In this case a sequence of approximations is constructed using the KLE for $W(t)$ and then we obtain approximations for $K(t) = \exp(W(t))$. This type of positive s.p.'s can play the role of the diffusion coefficient in dealing with the random logistic model, thus its theoretical and practical analysis has interest by itself right.

2.3 Numerable degree of randomness

The study is completed obtaining the 1-p.d.f. of the random IVP (1) in the case that the diffusion coefficient depends on a finite number of r.v.'s. In particular, we

consider the case $K(t) = A \exp(Bt)$ being A and B r.v.'s. An exact expression for the 1-p.d.f. of $X(t)$ is obtained take advantage of the RVT technique. Afterwards, the theoretical results are illustrated modelling the diffusion of a technology using real data. In this context, both A and B are assumed to have parametric probability distribution and then applying an inverse estimation technique the parameters of such distributions are adjusted. Once this has been done, the theoretical result is applied to construct punctual predictions (via the mean function) and probabilistic predictions (via confidence intervals) as well as further quantities of interest.

Acknowledgements

This work has been partially supported by the Ministerio de Economía y Competitividad grants MTM2013-41765-P. Ana Navarro Quiles acknowledges the doctorate scholarship granted by Programa de Ayudas de Investigación y Desarrollo (PAID), Universitat Politècnica de València.

References

- [1] Gabriel J. Lord, Catherine E. Powell, Tony Shardlow, An Introduction to Computational Stochastic PDEs. USA, Cambridge Text in Applied Mathematics, 2014.
- [2] T.T. Soong, Random Differential Equations in Science and Engineering. New York, Academic Press, 1973.

PROPOSAL OF A GRAPHIC MODEL FOR SOLVING DELAY TIME MODEL INSPECTION CASES OF REPAIRABLE MACHINERY

Fernando Pascual¹, Emilio Larrodé¹, Victoria Muerza²

¹UNIVERSITY OF ZARAGOZA. Dpto. de Ingeniería Mecánica. C/ María de Luna, 3 – 50018. Zaragoza (Spain). Tel: +34 976 762319. fpascual@unizar.es, elarrode@unizar.es

²ARAGON INSTITUTE OF ENGINEERING RESEARCH (i3A). Edificio de I+D+i, C/ Mariano Esquillor s/n – 50018, Zaragoza (Spain). Tel: +34 976 761888. vmuerza@unizar.es

1. INTRODUCTION

The maintenance of railway fleets is a problem of great relevance at present. An optimum maintenance has significant implications in society, both in terms of safety and economics.

The application of innovative methods and technologies to the railway maintenance has shown in real cases increases in productivity and service, with savings up to 23%, and investments that can be amortized in less than two years (González-Fernández, 2012).

The implementation of requirements for the calculation of the Life Cycle Cost (LCC) has driven the development of railway maintenance. In this regard, the European Standard UNE-EN 60300-3 defines the calculation of the LCC as an economic analysis process to determine the life cycle cost of the product during its life cycle or a part thereof. The life cycle is considered as the time interval between the conception of the product and its elimination, and the LCC is the accumulated cost of the product during its life cycle. The LCC procedure provides customer service and a clear competitive advantage (Dunk, 2004).

This paper focuses on the study of the optimization of the costs of railway maintenance under the philosophy of LCC, studying the main parameters of optimization of the maintenance plan from the perspective of the reliability engineering. For doing this, the Delay Time Model approach is adapted to the railway case and a proposal of graphic resolution method is presented.

2. CONCEPT OF DELAY TIME MODEL

The basic Delay Time Model for a complex system was developed by Christer and Waller (1984). It is based on the concept of the delay time h of a defect, which is the time that elapses since a defect can be detected by means of an inspection until the defect becomes a fault. The process is divided into two stages (see Figure 1), allowing the development of different delay time models for maintenance policy optimization (e.g. Wang (2002), Jardine et al. (2006)).

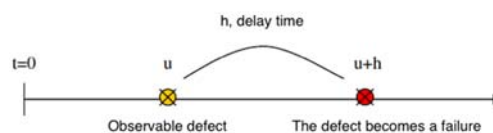


Figure 1. Time relationship between observable defect, failure and delay time

The main difficulty in this family of models lies in the determination of the initial time distributions u and the delay time h . This paper proposes an adaptation of the Delay Time Model by using graphic methods. This type of optimization method based on inspection with revealed failures is considered adequate for the optimization of the rail safety inspections.

Given u and h distributions, the inspection policy to be modelled is characterized according to the following hypotheses (H):

- H1. Inspections are carried out every T units of time with a cost C_i (currency unit), duration t_i , being $T \gg t_i$.

- H2. Inspections are perfect: (a) in case of any defect, it is detected; (b) the inspection does not contribute to degrade the system.
- H3. In case of any defect detection during the inspection, it is repaired in t_i at a CCM cost within the inspection period. It is considered enough resources to address repairs.
- H4. The repair is perfect (the component of the repaired system stays in the initial condition).
- H5. Defects follows a Homogenous Poisson Process with a rate of defects occurrence, λ , constant.
- H6. In case of failure, it is immediately repaired at a time d_p with a cost C_b , which comprises the repair cost and a penalty cost.
- H7. The repair time complies $d_p \ll T$.
- H8. The delay time H of a random defect is described by a probability density function $f(h)$ and a cumulative distribution function $F(H)$, independent of the initial point of occurrence of the defect U .
- H9. $C_b > C_{CM}$.
- H10. The probability density function of the delay time, $f(h)$, is known.

3. GRAPHIC MODEL PROPOSAL FOR THE DELAY TIME MODEL

It is selected a Delay Time Model formulation with exponential distributions for the occurrence of defects $u(t)$ and the delay time $h(t)$. The study considers a period with a single inspection and N defects. A number B of defects will not be detected, implying a penalty. The model is expressed as

$$C(T) = \frac{B(T) * C_b + C_{CM}(N(T) - B(T)) + C_i}{T + d_i} \quad (1)$$

where $C(T)$ is the total cost per unit of time in the cycle; C_b are the penalty costs, C_{CM} are the corrective maintenance costs, and C_i are the inspection costs ($C_b > C_{CM} > C_i$); T is the time of the periodic inspection cycle; d_i is the time required for a periodic inspection; N represents the total number of defects in a cycle. The defect detection rate is considered to follow an exponential distribution; the total number of failures in the period is given by

$$N(T) = \lambda * T \quad (2)$$

Considering an exponential distribution for the delay time, the number of failures per cycle $B(T)$ is expressed as

$$B(T) = \int_0^T \lambda * F(T - u) du = \int_0^T \lambda * (1 - e^{-\beta(T-u)}) du = \lambda * \left(\frac{e^{-\beta T} - 1}{\beta} + T \right) \quad (3)$$

Substituting the terms of Eq. (1), simplifying and taking into account that $T \gg d_i$ (in railway maintenance, safety inspections usually last minutes and inspection periods, months), it is obtained the following expression

$$C(T) = \frac{\lambda * \left(\frac{e^{-\beta T} - 1}{\beta} + T \right) * C_b - \lambda * \left(\frac{e^{-\beta T} - 1}{\beta} \right) * C_{CM} + C_i}{T} \quad (4)$$

This equation seeks to obtain the total cost per unit of time for a programmed inspection period. It can be observed that the result depends on three cost variables (C_i , C_b , C_{CM}) and two statistical variables (λ , β). The multiple dependence of the equation in this general form decreases its application usefulness, since in practice it is not intuitive understanding the variations of the final result in function of the precision of each of the available variables. This research intends to understand the weighting of each variable, while developing a simplified method for estimating the minimum cost inspection cycle. For doing this, certain algebraic manipulations are carried out.

If Eq. (4) is reordered by grouping terms according to their dependence on the inspection period, the following expression is obtained:

$$C(T) = \frac{\lambda * \left(\frac{e^{-\beta T} - 1}{\beta * T} + 1 \right) * C_b * T - \lambda * \left(\frac{e^{-\beta T} - 1}{\beta * T} \right) * C_{CM} * T + C_i}{T} = \lambda * C_b + \frac{C_i}{T} + \lambda * (C_b - C_{CM}) * \left(\frac{e^{-\beta T} - 1}{\beta * T} \right) \quad (5)$$

$$C(T) = \lambda * C_b + \frac{C_i}{T} + \lambda * (C_b - C_{CM}) * \left(\frac{e^{-\beta T} - 1}{\beta * T} \right) = \lambda * C_b + C_i * \left(\frac{1}{T} + \lambda * \frac{(C_b - C_{CM})}{C_i} * \left(\frac{e^{-\beta T} - 1}{\beta * T} \right) \right) \quad (6)$$

The corrected rate of failure is defined as

$$\Lambda = \lambda * \frac{(C_b - C_{CM})}{C_i} = \lambda * K \quad (7)$$

Owing $C_b > C_{CM} > C_i$ and $C_b > C_{CM} + C_i$, the cost ratio (K) is greater than 1 (Eq. (8)). These relationships must be fulfilled to make sense the program of inspections. Otherwise it would be carried out a replacement program based on schedule or age.

$$K = \frac{(C_b - C_{CM})}{C_i} > 1 \quad (8)$$

Thus, the corrected rate of failure (Λ) will be the failure rate of the equipment weighted by a factor that will usually raise its order of magnitude by one or two orders in the railway case. Substituting Λ into Eq. (6) it is obtained the following expression

$$C(T) = \lambda * C_b + C_i * \left(\frac{1}{T} + \Lambda * \left(\frac{e^{-\beta T} - 1}{\beta * T} \right) \right) \quad (9)$$

Observing Eq. (9) it is deduced the cycle cost is obtained as a sum of two terms:

- (i) $\lambda * C_b$, is the cost of a cycle in which no inspection is carried out. It represents the maximum cost, calculated as the number of failures in cycle λ multiplied by the cost that would imply all the failures be penalizable, C_b . This term does not depend on the inspection period and will be denominated as the maximum cost of cycle, C_{max} .
- (ii) The second term $C_i * \left(\frac{1}{T} + \Lambda * \left(\frac{e^{-\beta T} - 1}{\beta * T} \right) \right)$ represents the achievable savings through a policy of periodic inspections. It depends on the inspection period and is the term to be optimized.

Eq. (9) can also be expressed as (Eq. (10), Figure 2).

$$C(T) = C_{max} - A(T) \quad (10)$$

where $C_{max} = \lambda * C_b$, and $A(T) = -C_i * \left(\frac{1}{T} + \Lambda * \left(\frac{e^{-\beta T} - 1}{\beta * T} \right) \right)$

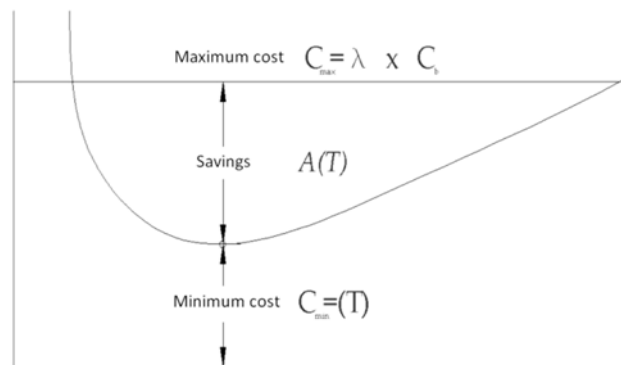


Figure 2. Costs per cycle based on the inspection period

4. USEFULNESS OF THE MODEL

Eq. (10) shows once the transformation of the starting model (Eq. 1) has been carried out, the saving term $A(T)$ is the only one dependent on the inspection period. In addition, the number of variables of the problem has been reduced from the initial five, to three: period, delay factor (β) and corrected rate of failure (Λ).

The utility of the graphic method presented (Figure 3) is the representation of the optimum period in which saving is maximum. In order to graph the results, it has only be considered the term which varies with the period, the function $\frac{A(T)}{-C_i} = -C_i * \left(\frac{1}{T} + \Lambda * \left(\frac{e^{-\beta T} - 1}{\beta * T} \right) \right)$

For doing this, it is intended to solve the equation in two domains, time and cost, according to the following objectives:

1. Obtain the optimal inspection period to maximize the saving function based on β and Λ ;
2. Obtain the maximum achievable saving A_0 for this optimal inspection period, based on β and Λ .

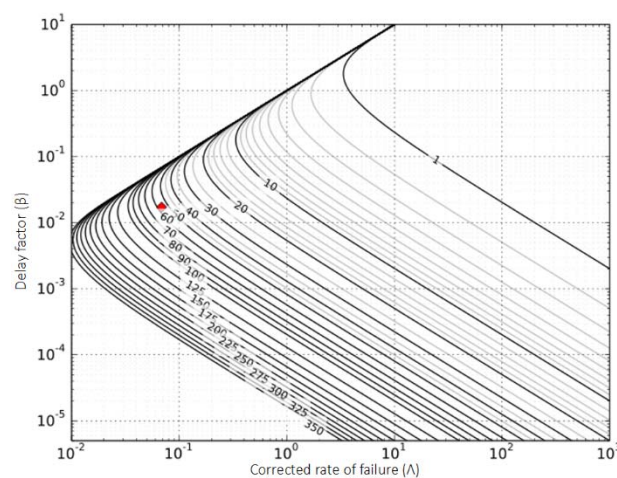


Figure 3. Optimum inspection period to obtain maximum savings per cycle based on Λ and β ($T > t_i$)

The need for an easy graphic representation of the model has involved a mathematical transformation that will be presented in the full version of the paper.

5. CONCLUSION

This paper presents a new model of the Delay Time Model with exponential distributions for its application in the railway maintenance. The objective is to speed up the calculation for its practical application in this type of operations. With this graphic model presented, a mathematical model can be applied for the calculation of the delay time in tasks of rail transport equipment and fleets maintenance in an agile and precise way, being this is the main usefulness of the model.

REFERENCES

- Christer, A. H., and Waller, W. M. (1984). Delay time models of industrial inspection maintenance problems. *Journal of the Operational Research Society*, 35(5), 401-406.
- González-Fernández, J. (2012). *Teoría y Práctica del mantenimiento industrial*. FC editorial, Madrid
- UNE EN 60300 (2009). *Gestión de la confiabilidad, parte 3-3: Guía de aplicación, Cálculo del coste del ciclo de vida*. Aenor.
- Dunk, A. S. (2004). Product life cycle cost analysis: the impact of customer profiling, competitive advantage, and quality of IS information. *Management Accounting Research*, 15(4), 401-414.
- Wang, H. (2002). A survey of maintenance policies of deteriorating systems. *European Journal of Operational Research*, 139(3), 469-489
- Jardine, A. K., Lin, D., & Banjevic, D. (2006). A review on machinery diagnostics and prognostics implementing condition-based maintenance. *Mechanical systems and signal processing*, 20(7), 1483-1510.

New insights on multiplex PageRank

F. Pedroche^{b,*}, R. Criado[‡], E. García[‡], Miguel Romance[‡]

(b) Institut de Matemàtica Multidisciplinària, Universitat Politècnica de València,
València. Espanya,

(‡) Department of Applied Mathematics, Rey Juan Carlos University,
and Center for Biomedical Technology (CTB), Technical University of Madrid
Madrid, Spain.

November 30, 2016

1 Introduction

Since the introduction of the PageRank algorithm - originally devised by the founders of Google [16]- to sort web pages, much research has been done in order to improve both the numerical method and the range of applications. In this respect, in the latest research papers one can find new numerical methods for computing PageRank (see, e.g., [21], [22], [20], [15], [9]) and a myriad of new applications (see, e.g., [1], [19], [12], [14], and the dedicated article [7]) including those applications related to the emerging topic of multiplex networks, like the studies in [2] and [5]. It is also worth noting the technique of extension of PageRank by using higher-order Markov chains (that is, chains that depend on previous states of the surfer), see [8] and the references therein.

We are interested in a particular feature of the PageRank algorithm: its capability of biasing the PageRank -and therefore the resulting ranking- to some particular nodes. This biasing is done by means of the so-called personalization vector, see [13], [3]. Given that the PageRank vector is the dominant unitary positive eigenvector of a stochastic matrix, and by using

*e-mail:pedroche@mat.upv.es

basic matrix algebra, it is easy to explicitly write the PageRank vector π , associated to a network of n nodes, as the product of a personalization vector v times a nonsingular matrix X . That is, in the form

$$\pi^T = v^T X \quad (1)$$

where X is a nonsingular $n \times n$ matrix, and $\pi, v \in \mathbb{R}^{n \times 1}$.

By using (1) and some properties of matrix X , one can obtain a useful result: giving a network, the value of the PageRank of each node can only attain values inside a precise subinterval of $(0, 1)$ depending on the entries of matrix X . In more detail, the bounds are defined by the minimum of each column of X and the values of the diagonal entries of X (in [6] it is shown precisely how this localization of the PageRank takes place). Consequently, we have that the biasing produced by the personalization vector v is limited.

In this talk, we present a result about the localization of a particular class of PageRank. We refer to this PageRank as the multiplex PageRank, that is, an ad-hoc PageRank that has been introduced to deal with the problem of multiplex graphs (graphs composed by several layers with the same number of nodes).

There are different ways to define multiplex PageRank (see, for example [10] and [4]), but we use the one introduced in [17]. According to this approach the multiplex PageRank is the unitary positive eigenvector of a stochastic matrix M_k associated to the multiplex equipped with k layers with n nodes on each layer. Matrix M_k is of the form

$$M_k = \frac{1}{k} \begin{pmatrix} B_{11} & B_{12} \\ B_{21} & B_{22} \end{pmatrix} \in \mathbb{R}^{2kn \times 2kn}, \quad (2)$$

where B_{11} gathers the information about the topology of the network, B_{22} takes into account the personalization vectors and B_{21} and B_{12} are diagonal matrices.

In this new formulation, personalization vectors are also considered. In fact, we consider one personalization vector for each layer. In the same manner as in the classic PageRank, the multiplex PageRank changes when there exists a change in the personalization vectors. Once again, this change is delimited and its magnitude can be precisely described. In the following we recall this result and show an example in a small multiplex.

2 Results

Given a multiplex with adjacency matrices A_1, A_2, \dots, A_k , we construct row stochastic matrices P_{A_i} by dividing each coefficient of A_i by the sum of the entries in its row. Let

$$\mathbb{P}_A = \begin{pmatrix} \alpha P_{A_1} & I_n & \cdots & I_n \\ I_n & \alpha P_{A_2} & \cdots & I_n \\ \vdots & \vdots & \ddots & \vdots \\ I_n & I_n & \cdots & \alpha P_{A_k} \end{pmatrix}, \quad \tilde{Y} = I_{kn} - \frac{1}{k} \mathbb{P}_A,$$

$$\tilde{Z} = \tilde{Y} - \frac{\alpha(1-\alpha)}{k} I_{kn}, \quad \tilde{B} = \frac{(1-\alpha)^2}{k(1+\alpha(k-1))} (\tilde{Y} \tilde{Z}^{-1} + \alpha \tilde{Z}^{-1}),$$

and

$$\begin{pmatrix} C_1 \\ C_2 \\ \vdots \\ C_k \end{pmatrix} = \tilde{B} \begin{pmatrix} I_n \\ I_n \\ \vdots \\ I_n \end{pmatrix}.$$

Then (see Theorem 4.4 in [18]) it holds that each component i -th of the Multiplex PageRank vector $\hat{\pi}_k$ lies in the interval $(c(i), d(i))$ where

$$c(i) = \min_j (C_1)_{ji} + \min_j (C_2)_{ji} + \dots + \min_j (C_k)_{ji}$$

and

$$d(i) = (C_1)_{ii} + (C_2)_{ii} + \dots + (C_k)_{ii}$$

for the matrices C_1, \dots, C_k defined above.

Example. Let us consider a multiplex with three layers defined by the adjacency matrices

$$A_1 = \begin{pmatrix} 0 & 0 & 1 & 1 \\ 0 & 0 & 1 & 0 \\ 0 & 0 & 1 & 0 \\ 0 & 0 & 1 & 0 \end{pmatrix}, \quad A_2 = A_3 = \begin{pmatrix} 0 & 1 & 0 & 0 \\ 1 & 0 & 0 & 0 \\ 0 & 0 & 1 & 0 \\ 1 & 0 & 0 & 0 \end{pmatrix}.$$

When taking the personalization vectors $\mathbf{v}_1 = \mathbf{v}_2 = \mathbf{v}_3 = \frac{1}{4}[1, 1, 1, 1]^T$, then the Multiplex PageRank results to be $[0.0370, 0.0332, 0.9166, 0.0131]^T$.

node	c(i)	d(i)
1	0.0000	0.0679
2	0.0000	0.0629
3	0.8825	1.0000
4	0.0000	0.0389

Table 1: Bounds for the Multiplex PageRank in the example with three layers and four nodes in each one.

The bounds for each component are shown in Table 1. We can observe that no matter the personalization vector, the node 3 always obtain the greatest value.

Let us compare the value of the Multiplex PageRank with that obtained by projecting all the layers into a single one with adjacency matrix

$$A_p = \begin{pmatrix} 0 & 1 & 1 & 1 \\ 1 & 0 & 1 & 0 \\ 0 & 0 & 1 & 0 \\ 1 & 0 & 1 & 0 \end{pmatrix}$$

In this case, by using the homogeneous personalization vector $\mathbf{v} = \frac{1}{4}[1, 1, 1, 1]^T$, one can obtain that the classic PageRank results to be

$$[0.0914, 0.0634, 0.7818, 0.0634]$$

and the bounds (computed by the formula given in [6]) are shown in Table 2. As we see, there can be differences in the results when one uses a single approach or a multiplex approach.

node	min	max
1	0.0000	0.1976
2	0.0000	0.1738
3	0.6905	1.0000
4	0.0000	0.1738

Table 2: Bounds for the classic PageRank in the example by using a projected single layer.

References

- [1] T. Agryzkov, L. Tortosa, and J. F. Vicent, New highlights and a new centrality measure based on the Adapted PageRank Algorithm for urban networks, *Applied Mathematics and Computation*, **291**, (2016), 14-29.
- [2] S. Boccaletti, G. Bianconi, R. Criado, C.I. del Genio, J. Gómez-Gardeñes, M. Romance, I. Sendiña-Nadal, Z. Wang and M. Zanin, The structure and dynamics of multilayer networks, *Physics Reports* **544**(1) (2014), 1-122.
- [3] P. Boldi, M. Santini and S. Vigna, PageRank: Functional Dependencies, *ACM Trans. Inf. Syst.* **27**(4) (2009), 19:1–19:23.
- [4] G.M. Del Corso and F. Romani, A multi-class approach for ranking graph nodes: Models and experiments with incomplete data, *Information Sciences*, 329, (2016) 619-637.
- [5] M. De Domenico, A. Solé-Ribalta, E. Omodei, S. Gmez, and A. Arenas Ranking in interconnected multilayer networks reveals versatile nodes, *Nature Communications* 6, Article number: 6868. (2015).
- [6] E. García, F. Pedroche and M. Romance, On the localization of the Personalized PageRank of Complex Networks, *Linear Algebra and its Applications*, **439**, 640 (2013).
- [7] D. Gleich PageRank beyond the web, *SIAM Rev.*, **57**, (2015), 321363.
- [8] D. F. Gleich, L-H. Lim, and Y. Yu. Multilinear PageRank, *Siam J. Matrix Anal. Appl.*, **36**, 4, (2015), 15071541.
- [9] C. Gu, and W. Wang, An Arnoldi-Inout algorithm for computing PageRank problems, *Journal of Computational and Applied Mathematics*, **309**, (2017), 219-229
- [10] A. Halu, R. J. Mondragón, P. Panzarasa, and G. Bianconi, Multiplex PageRank, *Plos One*, Vol. 8, issue 10, 2013.
- [11] G. Iván, and V. Grolmusz, When the Web meets the cell: using personalized PageRank for analyzing protein interaction networks, *Bioinformatics*, 27(3), (2011), 405-7.

- [12] Z. Jiang, J. Liu, and S. Wang, Traveling salesman problems with PageRank Distance on complex networks reveal community structure, *Physica A: Statistical Mechanics and its Applications*, **463**, (2016), 293-302.
- [13] A. Langville, and C. Meyer, Deeper inside PageRank, *Internet Math.*, 1 (3) (2005),335380.
- [14] C. Lodigiani, and M. Melchiori, A PageRank-based Reputation Model for VGI Data, *Procedia Computer Science*, **98**, 2016, 566-571.
- [15] H. Migallón, V. Migallón, J. A. Palomino, and J. Penadés, A heuristic relaxed extrapolated algorithm for accelerating PageRank, *Advances in Engineering Software*, Available online 22 February 2016.
- [16] L. Page, S. Brin, R. Motwani and T. Winograd, The PageRank citation ranking: Bridging order to the Web, *Tech.Rep.* **66**, *Stanford University*. 1998.
- [17] F. Pedroche, M. Romance, and R. Criado, A biplex approach to PageRank centrality: From classic to multiplex networks, *Chaos: An Interdisciplinary Journal of Nonlinear Science.* 26, 065301 (2016).
- [18] Pedroche, F., García, E., Romance, M, and Criado, R. Sharp estimates for the Personalized Multiplex PageRank *Journal of Computational and Applied Mathematics*, **330**, (2018), 1030-1040.
- [19] M. Scholz, J. Pfeiffer, and F. Rothlauf, Using PageRank for non-personalized default rankings in dynamic markets, *European Journal of Operational Research*, Available online 7 January 2017.
- [20] Z-L Shen, T-Z Huang, B. Carpentieri, X-M Gu, and C. Wen, An efficient elimination strategy for solving PageRank problems, *Applied Mathematics and Computation*, **298**, (2017), 111-122.
- [21] X. Tan, A new extrapolation method for PageRank computations, *Journal of Computational and Applied Mathematics*, **313**, (2017), 383 - 392
- [22] C. Wen, T-Z Huang, and Z-L Shen, A note on the two-step matrix splitting iteration for computing PageRank, *Journal of Computational and Applied Mathematics*, **315**, (2017), 87-97.

Simultaneous Smoothing and Sharpening of colour images

Cristina Pérez-Benito^b*, J. Alberto Conejero[†], Cristina Jordán[‡]
Samuel Morillas[†]

(^b) Instituto de Biomecánica de València, ([†]) Instituto Universitario de Matemática Pura y Aplicada

([‡]) Instituto Universitario de Matemática Multidisciplinar,
Universitat Politècnica de València, 46022 Valencia, Spain,

November 30, 2017

Abstract

We have proposed a new method able to improve and enhance the details of a color image at the same time that the noise is removed. The characterization based on graph theory allows us to distinguish different regions and to use each of them to achieve the simultaneous sharpening and denoising. With this method we solve the problems presented by the two-step application, getting to enhance the details without increasing the noise, and smoothing without losing too much information.

1 Introduction

Nowdays, the use of digital images is present in almost every area, from daily life use with digital cameras to medical applications or artificial intelligence. More and more fields make use of digital imaging for different purposes, which has led a great growth of the techniques able to improve the image visual quality and extract all kind information from it.

*e-mail: cripebe1@posgrado.upv.es

There are many factors that can affect the image quality, causing loss of information that makes difficult to process the image. Sensor malfunctions and poor acquisition conditions are the two most common causes of deterioration in the visual appearance of images. Sensor quality is closely related to the amount of noise in the image whereas the poor conditions during the acquisition process may limit the definition of image details. For this reason, it is both necessary to remove the image noise and enhance the texture and details.

In many applications we need to improve the image details, for example, for later segmentation or object detection. However, pristine images do not exist in the real world and almost all images contain noise to a greater or lesser extent. This noise hampers the work of enhancement techniques and therefore a previous smoothing step is required. This need has led to the development of methods that combine both pre-processing techniques.

The intuition could lead us to consider two different steps, first smoothing and then sharpening, or the other way around. However, these approach can lead to many problems since if we apply a smoothing technique there is the risk of losing details information that will not be recovered in the enhancement step. On the other hand, if we apply an enhancing method over a noisy image, we will amplify the noise preventing a suitable smoothing. In the Figure 1 we can see an example of this two-step approaches, using the well-known Bilateral Filter [1] for smoothing and CLAHE [2] for sharpening.

A more efficient solution to address this problem is a simultaneous perspective capable of sharpening image details while removing noise. However, this is not a simple task given the opposite nature of these two operations given both correspond to high frequencies. Some authors have tried to address this problem, by using different approaches [3]-[4]. Nevertheless the state of the art concerning smoothing or sharpening is very extensive, there are currently not many methods able to address with both methods in a simultaneous way [5].

We propose a new model which enable the noise removing at the same time that enhance the borders and details. A new graph-based model enables us to characterize a color image and operate properly to smooth or sharpen according to the pixel nature.

2 Simultaneous sharpening and denoising approach

We consider, for each image pixel F_0 , a window centered on it of size 3×3 . The rest of the neighbour pixels in the window are denoted as $\mathbf{F}_i, i = 1, \dots, N^2 - 1$. Each pixel \mathbf{F}_i is in

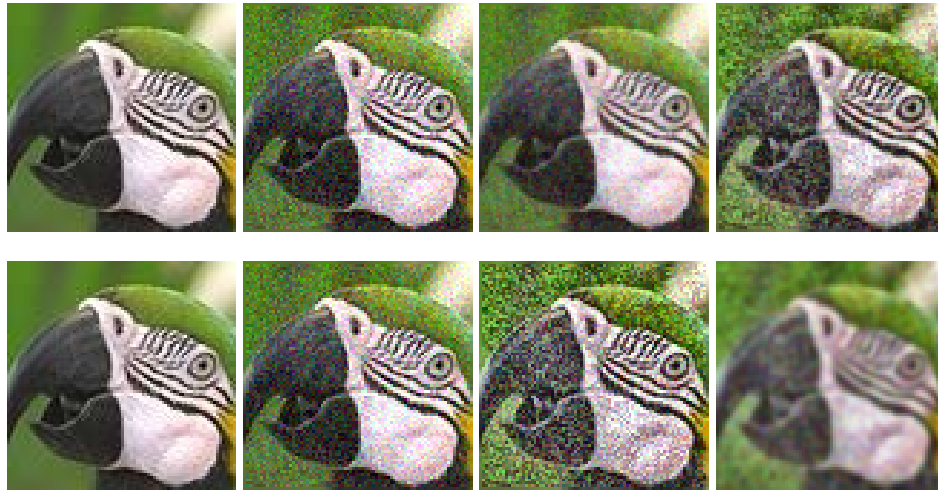


Figure 1: Example of the two-step approach. In the first row, from left to right, the noise-free image, the noisy image, the smoothed image and the result of enhancing over the smoothed image. In the second row, noise-free and noisy image, the enhanced image and finally, the result of smoothing over the enhanced image.

turn defined by the tern (F_i^R, F_i^G, F_i^B) of its three RGB colour components.

Given a pixel \mathbf{F}_0 , we define a local weighted graph $G_{\mathbf{F}_0}$ where the node set and the links set are given by

$$V(G_{\mathbf{F}_0}) = \{\mathbf{F}_i, i = 0, \dots, N^2 - 1\}$$

$$L(G_{\mathbf{F}_0}) = \{(\mathbf{F}_i, \mathbf{F}_j), i \neq j, \|\mathbf{F}_i - \mathbf{F}_j\|_2 < \mathcal{U}\}$$

That is, a link exists between pixel \mathbf{F}_i and \mathbf{F}_j , $i \neq j$, if the euclidean distance between their colour vectors is lower than a certain threshold \mathcal{U} . If such link exists, its weight is $w(\mathbf{F}_i, \mathbf{F}_j) = \|\mathbf{F}_i - \mathbf{F}_j\|_2$, where $\|\cdot\|$ stands for the Euclidean norm.

The principal role of the parameter \mathcal{U} is to determine the different connected components of the associated graph to each pixel that allow us to classify it into flat region or detail region, even in presence of noise. This classification allows us to process each pixel appropriately in function of its nature. We can see more details about the model as well as the setting of an optimal threshold in [6].

There is a lot of information that we can extract from the graph for an appropriate image processing. For example, in [6], the cardinal of the links set of the connected component that contain the central pixel is used for color image smoothing in an adaptative way. In this case, the main feature of these graphs that allows us to smooth and sharpen in a

simultaneous way are the different connected components of the graph since each of them represents a different region of the image.

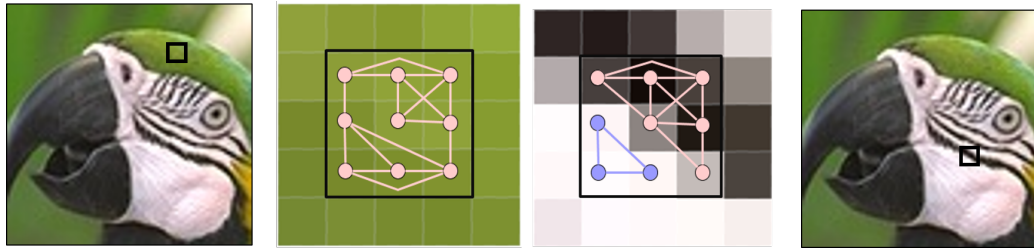


Figure 2: Examples of the associated graphs to a flat region and a detail region

In the Figure 2 we can see an example of the graph associated to a pixel that belongs to a flat and other to a detail one. In the first case all pixels are grouped in a single connected component while in the detail zone they are grouped into several components. This structure of the graph shows us that we are in a flat or border region.

Notice that a suitable classification requires a good setting of the threshold, otherwise we shall run the risk of classify a homogeneus region as a detail one, and therefore highlighting regions that do not interest us, or the other way around, classify as flat region a border or detail one and blurs it.

To achieve the simultaneous result we are looking for, we have defined a 3x3 adaptive kernel using the information provided by the model so that each kernel weight is determined by the membership of its associated node in a connected component. The pixels that belong to the connected component that contains the central pixel will be used for smoothing, corresponding to positive values in the kernel. On the other hand, the pixels that belongs to other connected components will be used for sharpening, corresponding to negative values in the kernel.

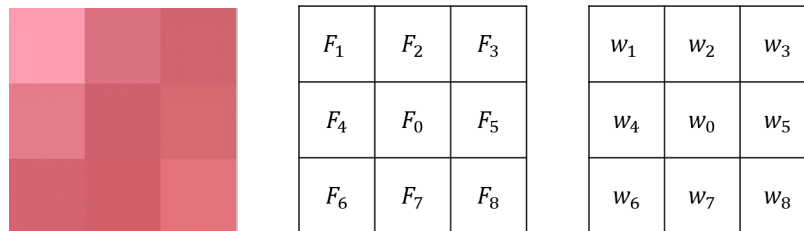


Figure 3: Illustration of the 3x3 pixel window, its notation and the asociated 3x3 kernel

Given a pixel F_0 and its associated neighborhood, we denote the corresponding 3x3 kernel in analogous way that in the neighborhood case in order to simplify the notation, see Figure 3.

And, the values w_i of the kernel are given by the following expressions

$$w_i = \begin{cases} \frac{\exp\left(-\frac{\|F_0-F_i\|}{2\alpha^2}\right)}{\sum_{i \in CC_{F_0}} \exp\left(-\frac{\|F_0-F_i\|}{2\alpha^2}\right)} (1 + \lambda) & \text{if } F_i \in CC_{F_0} \\ -\frac{\lambda}{\text{card}(CC_{\overline{F_0}})} & \text{if } F_i \notin CC_{F_0} \end{cases} \quad (1)$$

where $\alpha \neq 0$ is the parameter that controls the smoothing effect, λ is a parameter for controlling the sharpening effect, CC_{F_0} is the connected component that contains the central pixel and $\text{card}(CC_{\overline{F_0}})$ is the cardinal of the connected components that do not contain the central pixel.

In Figure 4 we can see an example of applying the proposed method over an image with White Gaussian Noise. Firstly the result of applying only smoothing, and then the result of the simultaneous sharpening and smoothing, where we can see that the noise has been removed and the details and borders of the image have been enhanced.



Figure 4: Example of the proposed method, firstly, the initial noisy image, then the result of applying only smoothing and finally the combination between smoothing and sharpening

3 Conclusions

Sharpening and denoising are two methods related to the improvement of the digital color images within the Computer Vision field. In many cases it is necessary to apply both methods for different purposes and their opposite nature makes their simultaneous application

still a challenge. We have proposed a new graph-based model that allows us to characterize a color image and use its local features for removing noise while improving image border and details.

References

- [1] Carlo Tomasi and Roberto Manduchi. Bilateral filtering for gray and color images. In *Computer Vision, 1998. Sixth International Conference on*, pages 839–846. IEEE, 1998.
- [2] Karel Zuiderveld. Contrast limited adaptive histogram equalization. In *Graphics gems IV*, pages 474–485. Academic Press Professional, Inc., 1994.
- [3] Vadim Ratner and Yehoshua Y Zeevi. Stable denoising-enhancement of images by telegraph-diffusion operators. In *Image Processing (ICIP), 2013 20th IEEE International Conference on*, pages 1252–1256. IEEE, 2013.
- [4] Sang Ho Kim and Jan P Allebach. Optimal unsharp mask for image sharpening and noise removal. *Journal of Electronic Imaging*, 14(2):023005–023005, 2005.
- [5] Cristina Pérez-Benito, Samuel Morillas, Cristina Jordán, and J Alberto Conejero. Smoothing vs. sharpening of colour images: Together or separated. *Applied Mathematics and Nonlinear Sciences*, pages 299–316, 2017.
- [6] Cristina Pérez-Benito, Samuel Morillas, Cristina Jordán, and J Alberto Conejero. A model based on local graphs for colour images and its application for gaussian noise smoothing. *Journal of Computational and Applied Mathematics*, 2017.

Numerical solution of nonlinear moving boundary problems for carbonation in reinforced concrete structures

M. A. Piqueras[†]*, R. Company[†], and L. Jódar[†]

([†]) Instituto de Matemática Multidisciplinar, Universitat Politècnica de València,
Camino de Vera s/n, 46022 Valencia, Spain.

November 30, 2017

1 Concrete carbonation problem and Front-fixing transformation

This work deals with the construction, analysis and computation of a numerical method to solve a moving boundary coupled nonlinear system of parabolic equations, arising in concrete carbonation problems, see [1]. By means of a front-fixing transformation, the domain of the problem becomes fixed, and the position of the moving carbonation front has to be determined together with the mass concentrations of the involved chemical species. Qualitative properties like positivity and stability of the numerical solution are established.

The mass concentrations of the species are represented by the following variables, where time takes values in the interval $0 \leq t \leq T$,

$$\begin{aligned} \bar{U}_1(x, t) &= [\text{CO}_2(aq)], & \bar{U}_2(x, t) &= [\text{CO}_2(g)], & \bar{U}_5(x, t) &= [\text{H}_2\text{O}], & 0 \leq x \leq S(t), \\ \bar{U}_3(x, t) &= [\text{Ca}(\text{OH})_2(aq)], & \bar{U}_6(x, t) &= [\text{H}_2\text{O}], & & S(t) \leq x \leq L, \\ \bar{U}_4(t) &= [\text{CaCO}_3(aq)], & & & & \end{aligned} \tag{1}$$

*e-mail: mipigar@cam.upv.es

where $T > 0$ is the time horizon.

Let us consider the suitable transformation of variables:

$$\hat{U}_i(x, t) = \phi\phi_\omega\bar{U}_i(x, t), \quad i \in \{1, 3\}, \tag{2}$$

$$\hat{U}_2(x, t) = \phi\phi_a\bar{U}_2(x, t), \quad \hat{U}_4(t) = \phi\phi_\omega\bar{U}_4(t), \tag{3}$$

$$\hat{U}_i(x, t) = \phi\bar{U}_i(x, t), \quad i \in \{5, 6\}, \tag{4}$$

where porosity of concrete is given by the parameter ϕ , while air and water fractions in pores are denoted by ϕ_a and ϕ_ω , respectively.

Under the new variables $\hat{U}_i(x, t)$, $i \in \{1, 2, 3, 5, 6\}$, $\hat{U}_4(t)$ and using Kronecker's symbol δ_{ij} , the continuous model proposed in [1, 2] is described by a coupled system of five partial differential equations (PDE) and one ordinary differential equation (ODE); together with the initial, boundary and transmission conditions and the velocity law of the moving front:

$$\begin{aligned} (\delta_{1i} + \delta_{2i} + \delta_{5i})\frac{\partial\hat{U}_i}{\partial t} - D_i\frac{\partial^2\hat{U}_i}{\partial x^2} &= (1 - \delta_{5i})(-1)^i P_i(\hat{U}_1 - Q_i\hat{U}_2), \\ 0 \leq x < S(t), \quad 0 < t < T, \quad i \in \{1, 2, 5\}, \end{aligned} \tag{5}$$

$$\frac{\partial\hat{U}_i}{\partial t} - D_i\frac{\partial^2\hat{U}_i}{\partial x^2} = \delta_{3i}(-S_{3,diss}(\hat{U}_3 - U_{3,eq})), \quad S(t) < x \leq L, \quad 0 < t < T, \quad i \in \{3, 6\}, \tag{6}$$

$$\frac{d\hat{U}_4}{dt} = \kappa(\phi\phi_\omega)^{1-p-q}[(\hat{U}_1)^p(\hat{U}_3)^q]_{\Gamma(t)}, \quad 0 < t < T. \tag{7}$$

The transformed initial conditions become $S(0) = S_0 > 0$ and

$$\begin{aligned} \hat{U}_1(x, 0) = \hat{U}_{10}(x) &= \phi\phi_\omega\bar{U}_{10}(x), \quad \hat{U}_2(x, 0) = \hat{U}_{20}(x) = \phi\phi_a\bar{U}_{20}(x), \\ \hat{U}_5(x, 0) = \hat{U}_{50}(x) &= \phi\bar{U}_{50}(x), \quad 0 < x < S_0, \end{aligned} \tag{8}$$

$$\hat{U}_4(0) = \hat{U}_{40} = \phi\phi_\omega\bar{U}_{40}, \tag{9}$$

$$\hat{U}_3(x, 0) = \hat{U}_{30}(x) = \phi\phi_\omega\bar{U}_{30}(x), \quad \hat{U}_6(x, 0) = \hat{U}_{60}(x) = \phi\bar{U}_{60}(x), \quad S_0 < x < L, \tag{10}$$

and the transformed boundary conditions are

$$\hat{U}_i(0, t) = \Lambda_i(t), \quad 0 < t < T, \quad i \in \{1, 2, 5\}, \tag{11}$$

$$\frac{\partial \hat{U}_i}{\partial x}(L, t) = 0, \quad 0 < t < T, \quad i \in \{3, 6\}. \tag{12}$$

Finally, the transformed interface conditions for $x = S(t)$, $0 < t < T$, become

$$- \left[D_i \frac{\partial \hat{U}_i}{\partial x} \right]_{\Gamma(t)} = (\delta_{5i} - \delta_{1i})(\phi\phi_\omega)^{-p-q}\eta_\Gamma(\hat{U}_1, \hat{U}_3) + S'(t)[\hat{U}_i]_{\Gamma(t)}, \quad i \in \{1, 2, 5\}, \tag{13}$$

$$\left[D_i \frac{\partial \hat{U}_i}{\partial x} \right]_{\Gamma(t)} = -(\delta_{3i})(\phi\phi_\omega)^{-p-q}\eta_\Gamma(\hat{U}_1, \hat{U}_3) + S'(t)[\hat{U}_i]_{\Gamma(t)}, \quad i \in \{3, 6\}, \tag{14}$$

and the velocity law is

$$S'(t) = \alpha\kappa(\phi\phi_\omega)^{1-p-q}[(\hat{U}_1)^p(\hat{U}_3)^{q-1}]_{\Gamma(t)}. \tag{15}$$

For the sake of simplicity, and taking advance of the fact that $(S^2(t))' = 2S(t)S'(t)$, in the following we will consider as unknown the square of the free boundary $R(t)$ instead of the free boundary itself $S(t)$ in order to obtain a more simplified PDE system, i.e. $R(t) = S^2(t)$.

In order to transform the PDE problem with moving domain into a fixed domain one, let us consider the following change of spatial variable inspired by the well known Landau transformation:

$$z(x, t) = \begin{cases} (x/\sqrt{R(t)}) - 1, & 0 \leq x < \sqrt{R(t)}, \quad 0 \leq t \leq T, \\ 0, & x = \sqrt{R(t)}, \quad 0 \leq t \leq T, \\ (x - \sqrt{R(t)})/(L - \sqrt{R(t)}), & \sqrt{R(t)} < x \leq L, \quad 0 \leq t \leq T. \end{cases} \tag{16}$$

2 Positive and stable numerical scheme

In this section we construct a finite difference scheme for solving numerically the coupled system after applying Landau front-fixing transformation. Let M and N be positive integers, so that the domain $[-1, 1] \times [0, T]$ is partitioned in $(2M + 1) \times (N + 1)$ mesh points denoted by (z_j, t^n) , where $z_j = jh$, $-M \leq j \leq M$ and $t^n = nk$, $0 \leq n \leq N$. Here the step sizes discretizations h and k verify $hM = 1$ and $kN = T$, respectively. Numerical approximations of the involved variables are denoted by $u_{i,j}^n \approx U_i(z_j, t^n)$, $i \in \{1, 2, 3, 5, 6\}$, $u_4^n \approx U_4(t^n)$, $r^n \approx R(t^n)$, while we denote $\lambda_i^n = \Lambda_i(t^n)$, $i \in \{1, 2, 5\}$.

Partial derivatives at the interior points are approximated using forward in time and centered in space finite difference expressions. With respect to the discretization of the first derivatives of the transformed transmission conditions at the carbonation front $z = 0$, we use one side second order finite difference approximations.

The solutions at the interior points at time level $n + 1$ are given by:

$$u_{i,j}^{n+1} = a_{i,j}^n u_{i,j-1}^n + b_{i,j}^n u_{i,j}^n + c_{i,j}^n u_{i,j+1}^n + \delta_{1i} k P_1 Q_1 u_{2,j}^n + \delta_{2i} k P_2 u_{1,j}^n, \quad (17)$$

$$-M + 1 \leq j \leq -1, \quad 0 \leq n \leq N - 1, \quad i \in \{1, 2, 5\},$$

$$u_{i,j}^{n+1} = a_{i,j}^n u_{i,j-1}^n + b_{i,j}^n u_{i,j}^n + c_{i,j}^n u_{i,j+1}^n + \delta_{3i} k S_{3,diss} u_{3,eq}^n, \quad (18)$$

$$1 \leq j \leq M, \quad 0 \leq n \leq N - 1, \quad i \in \{3, 6\},$$

where

$$a_{i,j}^n = \begin{cases} \frac{D_i k}{h^2 r^n} - \frac{1+z_j}{4h} \Delta_1^n, & i \in \{1, 2, 5\}, \\ \frac{D_i k}{h^2 \Delta_3^n} + \frac{z_j-1}{4h} r^n \frac{\Delta_1^n \Delta_2^n}{\Delta_3^n}, & i \in \{3, 6\}, \end{cases} \quad (19)$$

$$b_{i,j}^n = \begin{cases} 1 - \frac{2D_i k}{h^2 r^n} - \delta_{1i} k P_1 - \delta_{2i} k P_2 Q_2, & i \in \{1, 2, 5\}, \\ 1 - \frac{2D_i k}{h^2 \Delta_3^n} - \delta_{3i} k S_{3,diss}, & i \in \{3, 6\}, \end{cases} \quad (20)$$

$$c_{i,j}^n = \begin{cases} \frac{D_i k}{h^2 r^n} + \frac{1+z_j}{4h} \Delta_1^n, & i \in \{1, 2, 5\}, \\ \frac{D_i k}{h^2 \Delta_3^n} + \frac{1-z_j}{4h} r^n \frac{\Delta_1^n \Delta_2^n}{\Delta_3^n}, & i \in \{3, 6\}, \end{cases} \quad (21)$$

and

$$\Delta_1^n = \frac{r^{n+1}}{r^n} - 1, \quad \Delta_2^n = \frac{L}{\sqrt{r^n}} - 1, \quad \Delta_3^n = \left(L - \sqrt{r^n} \right)^2, \quad 0 \leq n \leq N - 1. \quad (22)$$

Finally, the concentration of $\text{CaCO}_3(\text{aq})$ in the carbonation front at the step $n + 1$ is given by

$$u_4^{n+1} = u_4^n + k\kappa(\phi\phi_\omega)^{1-p-q}(u_{1,0}^n)^p(u_{3,0}^n)^q, \quad 0 \leq n \leq N - 1. \tag{23}$$

We assume the hypothesis:

$$Q_1\tilde{G}_2 \leq \tilde{G}_1, \quad \tilde{G}_1 \leq Q_2\tilde{G}_2, \tag{24}$$

where \tilde{G}_1 is the upper bound of $[\text{CO}_2(\text{aq})]$ and \tilde{G}_2 is the upper bound of $[\text{CO}_2(\text{g})]$, for both at the exposed boundary and in the carbonated zone at the initial time, together with the condition on the equilibrium concentration of $\text{Ca}(\text{OH})_2(\text{aq})$:

$$u_{3,\text{eq}}^n \leq \tilde{G}_3. \tag{25}$$

We also assume the existence of an upper bound \tilde{G}_5 for the water content for both at the exposed boundary and in the carbonated region at the initial time, and that $[\text{Ca}(\text{OH})_2(\text{aq})]$ and water content are upper-bounded by \tilde{G}_3 and \tilde{G}_6 , respectively, at the initial time, see [2], Section 3, pp. 239-240.

Taking small enough values of h and imposing the following condition on the temporal step size

$$k < k_0 = \min\{k_i\}, \quad 1 \leq i \leq 6, \quad i \neq 4, \tag{26}$$

where

$$k_1 \leq \frac{h^2r^0}{2D_1 + h^2r^0P_1}, \quad k_2 \leq \frac{h^2r^0}{2D_2 + h^2r^0P_2Q_2}, \quad k_5 \leq \frac{h^2r^0}{2D_5}, \quad i \in \{1, 2, 5\}, \tag{27}$$

$$k_3 \leq \frac{h^2L^2(1 - \beta)^2}{2D_3 + h^2L^2(1 - \beta)^2S_{3,\text{diss}}}, \quad k_6 \leq \frac{h^2L^2(1 - \beta)^2}{2D_6}, \quad i \in \{3, 6\}, \tag{28}$$

the following theorem shows that the numerical solution obtained from the scheme (17)-(18) and (23), preserves the qualitative properties of the theoretical solution obtained in Section 3 of [2]:

Theorem 1. *Under hypotheses (24)-(25), for small enough values of the step size h together with the condition (26), the following conclusions hold true:*

- i) Concentration solutions $u_{i,j}^n$, $i \in \{1, 2, 5\}$ of the scheme (17) in the carbonated zone, concentration solutions $u_{i,j}^n$, $i \in \{3, 6\}$ of the scheme (18) in the uncarbonated region, and concentrations $u_{i,0}^n$, $1 \leq i \leq 6$, $i \neq 4$, at the carbonation front are positive and uniformly bounded for $0 \leq n \leq N$.*
- ii) The solution u_4^n of the scheme (23) for the calcium carbonate concentration is positive, increasing and bounded, for $0 \leq n \leq N$.*
- iii) The carbonation front is positive and increasing, $0 < r^0 < r^1 < \dots < r^N$.*

As a consequence of the boundedness of the mass concentrations, scheme (17)-(23) is $\|\cdot\|_\infty$ -stable under assumptions (24)-(25), for small enough values of h and conditions (26).

References

- [1] A. Muntean, M. Böhm, J. Kropp, "Moving carbonation fronts in concrete: A moving-sharp-interface approach", *Chemical Engineering Science*, 66 (2011), no. 3, 538-547.
- [2] A. Muntean, M. Böhm, "A moving-boundary problem for concrete carbonation: Global existence and uniqueness of weak solutions", *Journal of Mathematical Analysis and Applications*, 350 (2009), 234-251.

MODELING THE DEPRECIATION RATE OF CONSTRUCTION MACHINERY. AN ORDINARY LEAST- SQUARES APPROACH AND QUANTILE REGRESSION APPROACH.

*David Postiguillo**, *Ana Blasco*** and *Fco. Javier Ribal****

Department of Economics and Social Science, Universitat Politècnica de València,
Valencia, Spain

ABSTRACT

The development of information and communication technologies has had an impact on the economic, political, social and cultural perspectives. After the world economic crisis and subsequent recession, several economic sectors have decreased their activity profoundly. In Spain, the construction industry has been the most affected by the economic crisis. As a consequence of the decrease in the public construction, part of the machinery used in that activity has been put on sale in the secondary market. Currently, a large amount of information is available on the internet, which allows studying the behavior of the price (endogenous variable) of these assets based on several variables (exogenous variable). This research uses ordinary least-squares regression from three perspectives, linear, exponential and power. The main goal is to determine the depreciation rate at which these assets are depreciated as a function of their age, that is, it relates the asking price in the secondary market with the machine age. Furthermore, this research shows the difference between each level of asking price and its depreciation rate for each group of assets. This relationship is the first basic parameter of the depreciation of a productive asset. Finally, these rates are contrasted with the minimum and maximum percentages proposed by the accounting regulations in Spain.

Keywords: *quantile regression, MAD, depreciation, machinery, construction.*

INTRODUCTION

The variety of construction machinery that is commercialized at the moment is extensive. In general terms, different asset families are established to carry out the analysis: machinery used for earthmoving, excavation and thrust, excavation and loading, loading and hauling, compaction and hoisting machinery.

* Email: daposgar@upvnet.upv.es

** Email: ablascor@upvnet.upv.es

*** Email: frarisan@esp.upv.es

The economic crisis has deeply affected the construction sector, and consequently public construction. This caused a downturn in the demand of this type of services, and led to an underutilization of the productive capacity of the sector. According to the Central Business Directory of Spain (CBDS) from 2008 to 2016 the construction sector has decreased by-34.63%. The cessation/stoppage of activity of a large part of the companies in the industry entailed the liquidation of their assets, and this caused a decrease of the market prices of public construction machinery. Its supply in the secondary market increased sharply while the demand was reduced or almost disappeared.

The mechanization of the construction industry has allowed gaining competitiveness, reducing production costs and increasing earnings. Labor costs have been gradually reduced, nevertheless, machinery costs have been increased, particularly due to the evolution of fuel prices, insurance, repairs, maintenance and depreciation. The depreciation methods legally established and accepted by the accounting principles are theoretical models. Nevertheless, these models do not assure the real imputation of the depreciation that the assets have suffered.

In the United States there are several studies that show this situation, as reflected by Peacock and Brake (1970), McNeil (1979), Leatham and Baker (1981), Reid and Bradford (1983), Perry et al. (1990), Hansen and Lee (1991), Cross and Perry (1995) and Unterschultz and Mumey (1996). Some of them used regression methods to estimate the residual value of the machinery taking into account variables such as age and technical characteristics. In Spain, some studies have also been developed, as shown by Fenollosa and Guadalajara (2007), in the case of the agricultural machinery industry.

The extensive number of machines in the market together with the growing data availability on the internet makes it possible to study the machinery depreciation with samples larger than ever. Therefore the main goal of the chapter is to determine empirical depreciation rates and models for construction machinery.

METHODS

Data Gathering

The information to carry out this chapter has been obtained by means of web-scraping techniques. Specifically, sale listings of used construction machinery in Spain were gathered from www.europa-mop.com on August, 2015.

For each machinery type the listings provided some descriptive information (brand and model of the asset, location and other secondary information), machine age, operation hours and sale price (asking price).

For this research the information of operating hours has been deemed insufficient since many of the sale references do not provide it. Furthermore the accounting systems implemented in Spanish Small and Medium Enterprises (SMEs) do not track the number of operating hours of their machines. Thus, it is difficult to apply a depreciation coefficient as a function of the number of operating hours.

The research focuses on the analysis of the following groups of assets: a) *Bulldozers*, b) *Compactors*, c) *Track excavators*, d) *Wheel excavators*, e) *Mini excavators*, f) *Graders*.

Regression models

This research focuses on analyzing the relationship between the age of the machines from several groups of assets and their market price. To do this a regression model, based on ordinary least squares, is proposed.

The general expression of a regression model for a total of k explanatory variables is:

$$Y = a + b_1 \cdot x_1 + b_2 \cdot x_2 + \dots + b_n \cdot x_n + U \quad [1]$$

Where 'Y' is the endogenous variable, ' x_i ' are the exogenous variables, and the parameters ' b_i ' are parameters that quantify the relationship between the endogenous variable and each exogenous variable, ' a ' represents the interception in the regression model and ' U ' is the model's error.

In this case, the model is based on relating the asking price (exogenous variable) with the age of the machine (endogenous variable). It is not a valuation model since it is not used to value but to obtain the depreciation rate. Three different approaches have been developed in order to determine the depreciation rate following models from literature.

The model uses asking price as the endogenous variable since sale listings are the main data source. However, the goal of the research is to model depreciation which should be related with market value. Therefore the asking price is used as the best proxy of market value although some bargaining discounts can be expected, Peña (2000).

In some cases, an exponential relationship can be found between t (age) and V (asking price):

$$V = a \cdot e^{bt} \quad [3]$$

By applying the neperian logarithm, equation [3] can be linearized:

$$\ln(V) = b \cdot t + \ln(a) \quad [4]$$

Finally, the relation between t (age) and V (asking price) can be logarithmic.

$$V = a \cdot t^b \quad [5]$$

it can be transformed into:

$$\log(V) = b \cdot \log(t) + \log(a) \quad [6]$$

Quantile regression

Since the data sample are made of machine types each sample includes different brands and models which brand new price can be totally different. This fact raises the question whether expensive and economical machines should use the same depreciation rate. That is to say, is the depreciation behavior the same within each machinery group?

To answer this question quantile regression will be used. The quantile regression offers the possibility of creating different regression lines for different quantile levels for the dependent variables. For this research sample, the relationship between quantile machinery prices and age could be worked out. Koenker and Basset (1978) explain that quantile regression is suited for those cases of heteroscedasticity, presence of outliers or structural change.

In order to determine the coefficient of determination of each quantile the Pseudo-R or R_1 has been used (Koenker and Machado, 1999).

Outliers treatment. Median Absolute Deviation (MAD)

In a database obtained from public sale listings errors, mistakes and non-realistic values are bound to exist. Therefore an strategy to deal with outliers is needed. Considering the number of machine groups and the number of machines in each group an automated strategy has been applied.

Specifically, the median absolute deviation (MAD) has been used. The MAD relies on the use of the deviations around the median. The median (M) is, like the average, a measure of the central tendency but offers an advantage, it is less sensitive to the presence of outliers. An example of this lack of sensitivity would be the “breaking point” (Donoho & Huber, 1983). MAD would be defined, according to Huber (1981) as:

$$MAD = b M_i(|x_i - M_j(x_j)|) \quad [7]$$

Where x_j is the original number of observations and M_i is the median of the series. The parameter $b = 1.4826$ is usually a constant, assumed from the normality of the data, against the abnormality induced by the outliers (Rousseeuw & Croux, 1993). The MAD has been applied recursively to each machine group until no outlier is found.

RESULTS

The R programming language has been used for processing and modeling. Table 1 summarizes the coefficients obtained by applying the least-squares regression models in their linear, exponential and potential approaches. The column ‘n0’ expresses the number of initial data for each group of assets. Nevertheless, when outlier data are detected, MAD technique is used to remove them. In this way, the variable ‘n1’ provides the information corresponding to the final data for each group.

Table 1. Summary of statistical parameters.

			OLS Linear Model (M1)		
Type of asset	n0	n1	Coef. A	Coef. B	R ²
Wheel excavators	451	407	52,413.43	-1,841.7224	0.5145

			OLS Exponential Model (M2)		
Type of asset	n0	n1	Coef. A	Coef. B	R ²
Wheel excavators	451	407	1,109.69	-0.0753	0.6163

Type of asset	n0	n1	OLS Power Model (M3)		
			Coef. A	Coef. B	R ²
Wheel excavators	451	407	1,235.30	-0.9044	0.5475

Among the three linear least squares regression models, Linear (Model 1), Exponential (Model 2) and Power (Model 3), Model 2 shows the higher R² coefficient for any type of productive assets. Compactors are the only exception, Model 2 offers an R² of 0.0181, while Model 3 equals 0.0322. Nevertheless, in both cases, this R² indicates that the model does not have a significant goodness-of-fit.

The R² explains how much of the variability of a factor can be caused or explained by its relationship to another factor, i.e. the quality of the model when calculating the value of the type of productive asset as a function of the explanatory variable (age). Compactors have a low R², in all of the three models proposed. This implies that the explanatory variable 'age' is not representative to determine the price of this type of assets. The closer to 1 is, the greater the adjustment, and therefore the less possibility that there are significant deviations between the calculated value and the value that can be found in the market.

At this point it should be noted that the purpose of this research is not to establish a model to carry out the valuation of productive assets. On the other hand, the market depreciation rate is analyzed in order to determine the rates of depreciation according to the market behavior and to compare it with the coefficients established by official bodies (such as the Public Finance). Developing this chapter we can observe that Model 2, exponential regression, has the highest R², which belongs to the group of Wheel Excavators (R² = 61.63%).

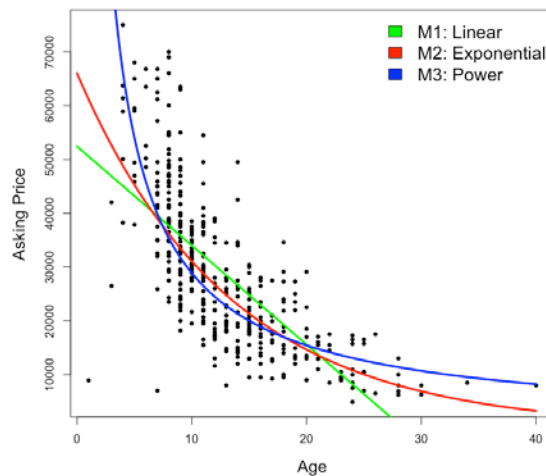


Figure 1. Regression models $f(\text{Price}, \text{Age})$ Wheel Excavators. R software.

The exponential model presents a path of productive assets subject to accelerated depreciation, greater depreciation in the initial stage of the asset's useful life, and then a moderate depreciation rate. For the first years, the exponential model slope is less steeper than the potential model one (see Figure 1). The R² of Model 3 is 54.71%. Thus, we proceed with the calculation and presentation of the depreciation coefficients for each asset group based on the three models analyzed (Table 2).

Table 2. Summary of depreciation coefficients.

	Model 1. Linear	Model 2. Exponential	Model 3. Power
Wheel excavators	-0.035	0.927	-0.904

In Model 1, it can be seen that for all asset groups, the depreciation rate goes from 0.7% (compactors) to 3.8% (mini excavators) following a straight-line. Wheel Excavators would depreciate at 3.5% annual rate. That is, they would have a maximum useful life of approximately 28 years.

Through Model 2, it can be concluded that the assets with the highest depreciation coefficient are the ones corresponding to the excavators (track, wheels and mini excavators). Compactors would have a longer lifespan. In general, the exponential regression exhibits a higher depreciation in the first years; and a milder depreciation in the medium/long term. E.g., in the fifth year the Wheel Excavators have been depreciated by 31.38% of their market value. By age 28, the accumulated depreciation reaches 89.56%.

Finally, Model 3 shows the extremely fast depreciaton of the assets in the first years. Wheel Excavators value would deteriorate by almost 76.67% in five years of use.

According to the Spanish corporate tax regulation machinery should be depreciated by means of straight-line method with a depreciation rate within in the range 5.55% - 12%. The secondary market, on the other hand, implicitly recognizes that these productive assets have a longer life than the legal or accounting life. This extension of the useful life is determined by updates and maintenance, which improves and increases the state of conservation of the machinery. There are several variables from which regression analysis can be established (brand, model, hours of operation, etc.), however, the approach developed in this chapter aims to establish a basic depreciation rate, based on the age of the assets.

These coefficients would apply to all assets of the same typology, nevertheless, there may be a difference in the behavior of the depreciation rate as a function of the value of the assets.

Thus, by applying the quantile regression on the exponential model for the “Wheel excavator”, the realized quantile partition is shown in Figure 2.

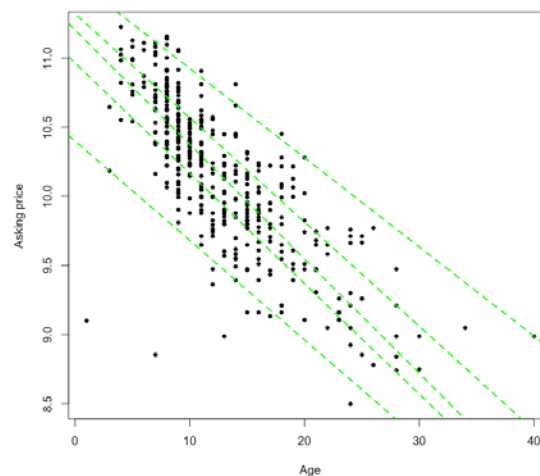


Figure 2. Quantile exponential regression model $f(\text{Price}, \text{Age})$ Wheel Excavators. R software.

Results show that the depreciation rate is in the range 0.92 – 0.94 for all the quantiles. This means that in 30 years the residual value would be in the 9 – 14.5 %.

In other words, the cheapest Wheel excavators have a slower rate of depreciation.

Table 3. Depreciation coefficients by quantile regression (Exponential model).

		tau= 0.025	tau= 0.25	tau= 0.50	tau= 0.75	tau= 0.975
Wheel excavators	Dep. rate	0.93058421	0.923259251	0.920539692	0.927396572	0.937452789
	Pseudo R2	9.95%	34.07%	43.08%	42.23%	37.62%

The same quantile analysis has been carried out for the rest of the machinery groups. In all of them the depreciation rates are not affected by the machine asking price.

CONCLUSIONS

This chapter allows two main conclusions to be drawn:

- The data availability in the machinery secondary market makes possible to determine that these machines do not follow a straight line depreciation. The best fit is reached by means of an exponential or semi-log relationship. This relationship implies that the depreciation is higher in the early years.
- Economical machines do not depreciate differently than expensive machines.

This work makes up a good example of how the increasing Internet information can help to improve analysis and decisions in business environments. It also highlights the differences between fiscal and accounting regulations, and market behavior.

REFERENCES

- Cross. T.L. Perry G.M.. (1995) "Depreciation patterns for agricultural machinery". Am J Agr Econ 77. 194-204.
- Donoho. D.L. y Huber. P.J. (1983) "The notion of breakdown point". en P. J. Bickel. K.A. Doksum y J. L. Hodges (eds.). Festschrift for Erich L. Lehmann. Wadsworth. Belmont. California
- Fenollosa Ribera. M.L.. Guadalajara Olmeda. N. (2007) "An empirical depreciation model for agricultural tractors in Spain" Spanish Journal of Agricultural Research. 5(2). 130 – 141 ISSN: 1695-971-X
- Hansen L.. Lee. H.. (1991) "Estimating farm tractor depreciation: tax implications". Can J Agr Econ 39. 463-479
- Huber. P. J. (1981) "Robust Statistics". Wiley. New York
- Koenker. R. y Basset. G. (1978). "o" en Econometrica. Vol. 46. nº 1. pp. (33-50).
- Koenker. R y Machado, J.A. (1999). "Goodness of Fit and Related Inference Processes for Quantile Regression". Journal of the American Statistical Association, Vol. 94, No. 448. (Dec., 1999), pp. 1296-1310.
- Leatham D.J.. Baker T.G. (1981) "Empirical estimates of the effects of inflation on salvage values. cost and optimal replacement of tractors and combines". N C J AgrEcon 3 (2). 109-117
- Ley 26/2014. de 27 de noviembre. por la que se modifican la Ley 35/2006. de 28 de noviembre. del Impuesto sobre la Renta de las Personas Físicas. el texto refundido de la Ley del Impuesto

-
- sobre la Renta de no Residentes. aprobado por el Real Decreto Legislativo 5/2004. de 5 de marzo. y otras normas tributarias.
- McNeill. R.C. (1979) "Depreciation of farm tractors in British Columbia" *Can J Agr Econ* 27. 53-8
- Peacock D.L., Brake. J.R. (1970) "What is used farm machinery worth?" Michigan StateUniversity. *AgrExpSta. Res Rep* 109
- Peña. D. (2000) "Estadística y Modelos y Metodos" V.2. Alianza Editorial. Madrid.
- Reid. D.W., Bradford. G.L. (1983) "On optimal replacement of farm tractors". *Am J Agr Econ* 65 (2). 326-331.
- Rousseuw. P. J. y Croux. C. (1993) "Alternatives to the Median Absolute Deviation". *Journal of the Americian Statistical Association*. pp: 1273 - 1283
- Unterschultz J., Mumey G.. (1996) "Reducing investment risk in tractors and cabins with improved terminal asset value forecast". *Can J Agr Econ* 44(3). 295-309.

Mathematical modeling of the suicidal risk in Spain.

De la Poza, Elena^{*a}; Jódar, Lucas^b and Durá, Daniel^b

^aFaculty of Business and Management. Center of Economic Engineering, Universitat Politècnica de València, Building 7J, Camino de Vera s/n, 46022, Valencia, Spain.

^bInstituto Universitario de Matemática Multidisciplinar, Universitat Politècnica de València, Building 8G, 2nd floor, Camino de Vera s/n, 46022, Valencia, Spain.

*Corresponding author e-mail: elpopla@esp.upv.es

Abstract

Suicide is one of the leading causes of death for all ages of the general population, but its relevance seems to be hidden by several reasons (Hawton, *et al.*, 2013; Leadholm *et al.*, 2014). In fact, western media coverage minimizes their writing about the subject and calls the public attention to alternative issues; this pattern tries to prevent “social contagion” (Werther effect), but also it responds to an initial lack of evidence about the problem.

Contrary to popular assumption, suicidal behavior does not only occur in countries with bad weather, or limited sunshine; it also takes place in countries such as Spain, where international media links us to tourism and happiness, ignoring an increasingly hidden problem (Miret *et al.*, 2014). In fact, in Spain the suicide is the second non-natural death, beneath the traffic mortal accidents.

One of the reasons that explains the hidden nature of the problem is the undetermined level of suicidal intend cases that leads police investigations and medico-legal examinations to non- conclusive results for a large number of deaths (by poisoning, drawings...), which are classified as accidents.

In recent years, associations preventing from suicide have emerged, but they have not captured massive public attention. This social problem has in common characteristics with other mental disorders such as drugs addiction, depression; thus, suicidal behavior is a kind of mental disorder, (Gea *et al.*, 2013).

In fact, the fatal event of a person taking his/her own life, affects their close neighborhood (family and friends) by the experienced loss as well as society due to the loss of productivity and health care costs (Dias de Mattos Souza, *et al.*, 2016).

The neglect of this phenomenon stems from a lack of measure, which is uncontrolled and hence can not be improved. Thus, sizing the population at risk of suicide has an undoubted social interest.

The quantification of the general population to the risk of attempting suicide is not an easy task. It is also controversial due to the multidisciplinary nature of the problem. In fact,

previous studies tackling the suicidal behavior have not agreed on an approach to determine the magnitude of the problem.

In this paper we address the quantification of the Spanish population at risk of attempting suicide aged among the interval [16, 78] during the period of time July 2015 to January 2021. Thus, a discrete mathematical model will be created to quantify the level of risk of attempting suicide of Spanish population by taking into account demographic, cultural, and socio-economic factors.

Keywords

Risk, suicide, Spain, dynamic compartment model, economy, mental illness, stress.

1. Introduction

Suicide is the action of killing oneself intentionally. In fact, nobody talks openly about it but about 4,000 people suicided in Spain in 2014, (SIS, Spanish Institute of Statistics, 2016). Moreover, suicide is the top rank violent death in Spain causing more deaths than traffic accidents.

Apart from the official data about suicides, there is a relevant number of suicides that have been classified as “natural” or as domestic or work accidents. Actually, the number of suicides is uncertain and hidden. Thus, official statistics about suicide victims reflect just a small proportion of total number of fatal events, but from 20 attempts of suicide, just 1 succeeds (hypothesis assumed by experts). In addition, in 90% of suicides the victim was suffering some mental disease, (bipolar disorder, schizophrenia, personality disorder).

Suicide is a social problem that needs attention for its direct effects, but also for the indirect effects causing that for each suicide, 6 people life is socio-economically and psychologically impacted in the close environment of the fatal event. Also, there is a relevant loss of labor productivity and growth of healthcare expenditure that justifies the need of public resources to treat not only physical citizen illnesses but also mental ones.

In fact, many depressive people never become suicidal, and many non-diagnosed but depressed people commit suicide, (Solomon, 2015). Suicide varies inversely with the degree of integration of the individual to the social groups of which belongs (family; religion; politics), (Durkheim, 1995 (1896)). The person who suffers from depression, does not understand what happens to him/her but feels the urgency to isolate himself/herself to carry this burden. Also, the individual has no information but society neither about the depression. In conclusion, it can be stated that depression is something that can affect any of us, (Rojas, 2016).

2. Methods

a. Hypothesis of the study

The model was built under several hypotheses that is important to detail. The **first one** consist of the assumption about the suicide is not an unpredictable event, since there is an evolution on people’s behaviour towards this fatal event. This drives us to the **second**

hypothesis about how individual behaviour is not predictable but the aggregated might be, (Raafat *et al.*, 2009). Thus, the **third** hypothesis was made under the assumption that the Spanish population can be classified according to their risk to commit suicide. Following this hypothesis a rating to classify Spanish population according to their level of risk to commit suicide was built. We considered 4 levels of risk to commit suicide :

- No risk subpopulation, (Z): individuals who have none indicator suggesting a relation to the problem. In fact, it is assumed that a proportion of them (F^*) will never transit.
- Pre-risk subpopulation, (P): individuals that due to their personality traits (LGTBI, post-traumas), and or having experienced episodes of violence, and/ or due to their labor have access to weapons and suffer from labor stress.
- Low risk population, (L): those who have ideated/planed a suicide.
- High risk population, (H): those attempting to suicide at least once in their life combined with those who suicide.

The **forth** hypothesis assumes individuals transit from one category to another in one semester period, what has been called the “one jump principle”. The subpopulation transits can occur to higher but also to lower risk categories (recovery).

The **fifth** hypothesis relies on the bases that individual behaviour is affected by different drivers. The combination of those drivers makes a proportion of each subpopulation evolve (jump) from one category to another. Following the factors impacting on individuals’ behaviour are detailed:

- Demographic factor (Birth & death rates; emigration), (SIS, 2016)
- Economic factor (Poverty rate indicator), (SIS, 2016)
- Social contagion factor (Christakis & Fowler, 2009),
- Behaviour patterns, (Raafat *et al.*, 2009),
- Alcohol abuse and drugs consumption, (SIS, 2016)
- Emotional slow-down, (Rojas, 2016)

i. Population of study

The Spanish population $S(0)=37,075,000$ aged [16, 78] in July 2015 ($n=0$) is classified at one of the subpopulations according to the reports and previous studies:

- $Z(0) = 31,603,000$, non risk population is the 85.24% of $S(0)$.
- $P(0) = 4,925,000$, pre-risk subpopulation is the 13.28% of $S(0)$.
- $L(0) = 450,000$, low risk subpopulation is the 1.21% of $S(0)$.
- $H(0) = 97,500$, high risk subpopulation is the 0.26% of $S(0)$.

b. Transition Coefficients Modelling

There are four types of transit coefficients: demographic, economic, social contagion and drugs and alcohol abuse consumption. Those are denoted by α when the transit expresses an increase in the level of risk to commit suicide, β meaning a transit to lower risk

compartments. Then, neutral demographic factor at semester n is denoted by $b_i(n)$, where $1 \leq i \leq 4$.

The demographic factor $b_i(n)$, represents the net balance among newcomers and out-comers to the system. The newcomers of the system are those individuals becoming 16 years old, while the outcomers are those who become 79 years old at semester n and those who are deceased at semester n , (excluding those who suicide according to official data, (INE, 2015)).

The transit from $Z(n)$ to $P(n+1)$ can be due to the contagion effect ($\alpha_c^*(n)$), and/or the economic stress, ($\alpha_p^*(n)$). The $\alpha_c^*(n)$ is explained as follows:

$$\alpha_c^*(n) = 0.9 \cdot \left[\frac{1}{10} \cdot \left(\left(\frac{P(n) - P(n-1)}{Z(n)} \right) + \left(\frac{L(n) - L(n-1)}{Z(n)} \right) \right) \right] \quad (1)$$

where 10% are “immune against depression”, (Spanish Ministry of Education, Culture and Sports, 2015).

The economic stress, ($\alpha_p^*(n)$) is expressed as:

$$\alpha_p^*(n) = 0.9 \cdot \alpha_p(n) = \begin{cases} 0.45 \cdot (\rho(n) - \rho(n-1)), & \rho(n) \geq \rho(n-1) \\ 0, & \rho(n) < \rho(n-1) \end{cases} \quad (2)$$

where $\rho(n)$ is the Spanish poverty risk rate (based on the household income), [2015, 2017], INE. Also, 10% $Z(0)$ are not affected by the economy. 3,700,000 people.

The transit from $P(n)-H^*$ to $L(n+1)$ is due to the combination of at least three factors (α_1^*) impacting on individual behavior. Where H^* represents the amount of people that due to physical and psychical conditions will not transit to $L(n+1)$. $\alpha_1^* = 0.03 \cdot 0.9 = 0.027$.

The transit from $L(n)$ to $H(n+1)$ is explained by the impulse coefficients α_{AD}^2 . This transit coefficient is explained by the abuse of drugs and alcohol of population already at risk ($L(n)$). $(\alpha_{AD}^2)^* = \alpha_{AD}^2 \cdot 0.9 = 0.1225 \cdot 0.9 = 0.11025$.

Finally, the population at risk is susceptible to recover transiting to lower levels of risk. However, it is assumed the recovery (β_{ri} , where $1 \leq i \leq 4$) will be easier for those individuals at lower risk levels. Thus, the recovery from $P(n)$ to $Z(n+1)$ is modeled as $\beta_{r1} = \rho(n-1) - \rho(n)$, if $\rho(n) < \rho(n-1)$, where $\rho(n)$ is the Spanish poverty risk rate, (SIS, 2016). While β_{r2} is based on psychotherapy/drug prescription (Rojas, 2016) and β_{r3} is the recovery by endogenous reasons (physical illness/mental disorders) but it is a slow long process, (Rojas, 2016). For the period of study considered $\beta_{r1} = 0.01$; $\beta_{r2} = 0.02$; $\beta_{r3} = 0.0025$.

c. Mathematical model

$$Z(n+1) = Z(n) - \alpha_c^*(n) (Z(n)-F^*) - \alpha_p^*(n) (Z(n)-F^*) + \beta_{r1}(P(n)) + b_1$$

$$P(n+1) = P(n) - \alpha_1^*(P(n)-H^*) + \alpha_p^*(n) (Z(n)-F^*) + \alpha_c^*(n) (Z(n)-F^*) - \beta_{r1}(P(n)) + \beta_{r2}(L(n)) + b_2$$

$$L(n+1) = L(n) - (\alpha_{AD}^2)^*(L(n)) + \alpha_1^*(P(n)-H^*) - \beta_{r2}(L(n)) + \beta_{r3}(H(n)) + b_3$$

$$H(n+1) = H(n) + (\alpha^2_{AD})*(L(n)) - \alpha_s(H(n)) - \beta_{r3}(H(n)) + b_4, \tag{3}$$

Then, solving the difference system of equations of the model the subpopulations Z(n),P(n), L(n), and H(n) are computed for each semester forecasting those at the end of the period of study, January 2021.

3. Results

Table1 shows the trend of subpopulations for the period of study. Table 2 shows the initial proportions of each supopulation (n=0) and the subpopulations at n=13.

Table 1. Forecast of subpopulations for the period of study

Semester	Z	P	L	H
July 2015	31,603,000	4,925,000	450	97,5
January 2016	30,665,955	5,616,305	489,99	143,31
July 2016	30,481,404	5,537,251	543,961	192,339
January 2017	30,354,971	5,406,077	589,443	246,064
July 2017	30,239,481	5,268,411	626,06	303,406
January 2018	30,132,378	5,128,201	654,71	363,272
July 2018	30,031,227	4,986,398	676,285	424,700
January 2019	29,935,754	4,843,873	691,597	486,856
July 2019	29,844,523	4,701,260	701,378	549,017
January 2020	29,757,132	4,559,201	706,29	610,565
July 2020	29,672,625	4,418,193	706,931	670,970
January 2021	29,590,591	4,278,705	703,839	729,785

Table 2. Proportions of the subpopulations at n=0 and n=13.

	Z	P	L	H
July 2015	85.24%	13.28%	1.21%	0.26%
January 2021	83.82%	12.12%	1.99%	2.07%

4. Conclusions

This paper models and quantifies the suicidal risk growth in the Spanish population aged [16, 78] during the period July 2015–January 2021. For this purpose, it has been necessary to identify and quantify the main drivers of this social problem. Thus, we have identified the population on risk to ideate and commit suicide and we have proposed a model to rate their level of risk.

By forecasting the number of future suicides, we can provide recommendations to reduce and prevent the growth of this social problem. The main action should be focused on avoiding individual isolation; this requires the promotion of social integration and the elimination of marginalization, favouring the growth of values. Also, it is recommended to include the study of humanities and educate youth on how to employ their leisure time.

References

- Christakis & Fowler, *Connected: The Surprising Power of Our Social Networks* (2009), Little, Brown and Company, Hachette Book Group, New York, USA.
- Diaz de Mattos Souza, L., Lopez Molina, M., Azevedo da Silva, R., & Jansen, K. (2016). History of childhood trauma as risk factors to suicide risk in major depression. *Psychiatry Research*, (April), 0– 1. <http://doi.org/10.1016/j.psychres.2016.11.002>

- Durkheim, E. *The Suicide*, Akal, Madrid, 1995.
- Gea, A., Beunza, J. J., Estruch, R., Sánchez-Villegas, A., Salas-Salvadó, J., Buil-Cosiales, P., ... Martínez- González, M. a. (2013). Alcohol intake, wine consumption and the development of depression: the PREDIMED study. *BMC Medicine*, 11, 192. <http://doi.org/10.1186/1741-7015-11-192>
- Hawton, K., Casañas I Comabella, C., Haw, C., & Saunders, K. (2013). Risk factors for suicide in individuals with depression: A systematic review. *Journal of Affective Disorders*. <http://doi.org/10.1016/j.jad.2013.01.004>
- Leadholm, A. K. K., Rothschild, A. J., Nielsen, J., Bech, P., & Stergaard, S. D. (2014). Risk factors for suicide among 34,671 patients with psychotic and non-psychotic severe depression. *Journal of Affective Disorders*, 156, 119–125. <http://doi.org/10.1016/j.jad.2013.12.003>
- Miret, M., Caballero, F. F., Huerta-Ramírez, R., Moneta, M. V., Olaya, B., Chatterji, S., Haro, JM., Ayuso-Mateos, J. L. (2014). Factors associated with suicidal ideation and attempts in Spain for different age groups. Prevalence before and after the onset of the economic crisis. *Journal of Affective Disorders*, 163, 1–9. <https://doi.org/10.1016/j.jad.2014.03.045>
- Raafat, R. M., Chater, N., & Frith, C. (2009). Herding in humans. *Trends in Cognitive Sciences*, 13, 420-428.
- Rojas, E. *Adios Depresión*, E: Temas de Hoy, 2006, Madrid.
- Solomon, A. *The Noonday Demon. An Atlas of the Depression*, (In Spanish). Madrid: Debate, 2015.
- Spanish Statistics Institute, 2016.
- Sportive Habits Survey. Spanish Ministry of Education, Culture and Sports, 2015.

Coupling internal nozzle flow turbulence features to DNS of sprays primary atomization

F.J. Salvador^b *; Marco Crialesi-Esposito^b,
J.-V. Romero[†], and M.-D. Roselló[†],

(^b) CMT-Motores Térmicos, Universitat Politècnica de València
Camino de Vera, s/n, Edificio 6D, 46022 Valencia, España

([†]) Instituto de Matemática Multidisciplinar, Universitat Politècnica de València
Camino de Vera, s/n, Edificio 8G, 2o, 46022 Valencia, España

November 30, 2017

1 Introduction

In the last couple of decades, sprays have been a central point of investigation for Internal Combustion Engines (ICE). In fact, spray atomization is of fundamental relevance in combustion process and pollutant formation. As regulation on pollutant emission and energy efficiency are becoming more and more restrictive, the scientific community has invested considerable time and resources addressing the combustion process from both a theoretical and a practical standpoint, both with numerical and experimental techniques. In this context, it is nowadays evident that the actual knowledge on sprays, primary and secondary atomization as well as coalescence in the injection process is far from been complete as it becomes more and more relevant for applied research, especially in a complex frame as the ICE application, where the combination of injection velocities, pressures and characteristic length is quite unique and difficult to replicate and study with experimental technique on the appropriate length scale.

*fsalvado@mot.upv.es

In this work, Direct Numerical Simulation (DNS) is used to provide a detailed description of the very first millimetres downstream the nozzle: this area is of fundamental importance in the formation of the spray, as it presents the regions in which the atomization begins ([7]) due to the combination of aerodynamic drag forces and air/liquid turbulence interaction. As a simulation environment, the code Paris-Simulator, developed in [1], is been chosen. In order to accurately represent turbulence properties of the velocity outgoing the nozzle, a Large Eddy Simulation was performed in OpenFOAM.

The results provided up to now with DNS for the Near-Field region have reportedly simulate low injection velocity, therefore pressure conditions unrealistic for Diesel ICE and rare for Gasoline Direct Injection ICE. Currently, only Lebas et al. [4] have simulated turbulence at the outlet of the nozzle, accounting for the turbulence generated by the fluid inside the nozzle duct. Many studies have related cavitating [5] and non-cavitating conditions [6] inside the nozzle with non negligible effects on the turbulence distribution at the nozzle outlet. Furthermore, it has been proved in previous works [3] that the higher the turbulence at the injector outlet is, the more the atomization affects the spray shape, as the intact core length reduces significantly and the atomization process starts earlier.

As appears evidently, still large improvement in the understanding of turbulent atomization can be achieved. This work investigate how the nozzle turbulence features (such as distribution and lengthscale) effects the spray's shape, turbulence and formation, while reproducing the inlet turbulence with a methodology derived in [3] and applied to circular jet. In order to do so, a comparison between the case .

2 Main results

In order to get the correct turbulence features for the case studied here, a LES simulation of a periodic pipe has been performed in order to assess the turbulence distribution and the turbulence length scale.

In Fig. 1 a cross section of the pipe velocity field is showed. As it can be observed, the mesh used is significantly finer at the pipe wall, in order to capture the boundary layer dynamics. The results have been validated against DNS from [2] and theoretical data and the comparison is represented in Fig. 2. Here is clear how, even with lower grid resolution in comparison with DNS simulations, the LES is clearly capable of capturing the turbulence

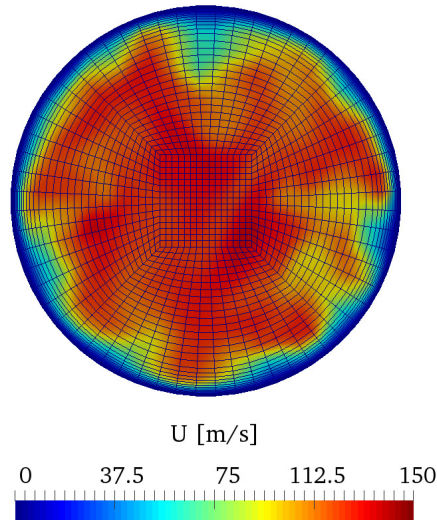
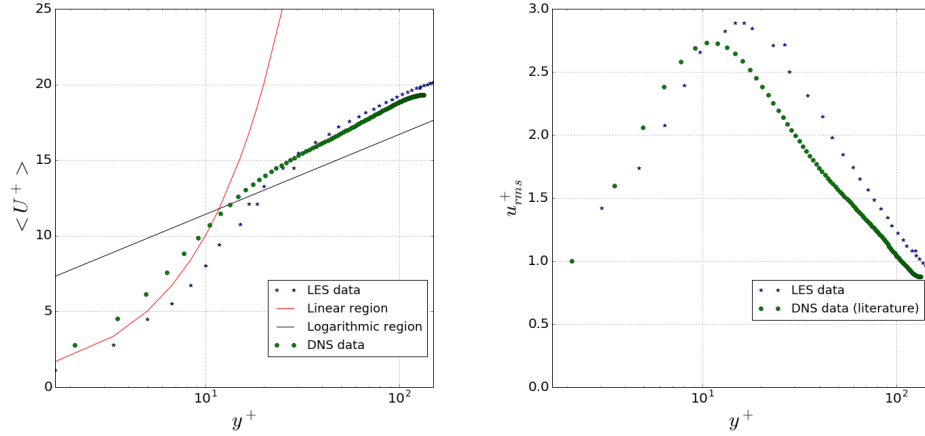


Figure 1: Instantaneous velocity field in the periodic pipe in the middle section

behaviour of the pipe flow. therefore, the turbulence coherent structures have been analysed and the parameters to be used as inputs for the synthetic boundary conditions have been isolated.

Fig. 3 shows the external aspect of the spray at $t = 20\mu s$. As it can be clearly noted, the higher the turbulence induced, the sooner the atomization process starts, shortening the *external non-perturbed length*. The penetration in the two cases is significantly different due to the different axial Reynolds number, that is justified by the behaviour of the velocity profile in the turbulent case, shown in Fig. 2(a). The atomization process is significantly promoted by the nozzle turbulent, as it can be demonstrated by the significant higher number of droplets in the turbulent case. Furthermore, the typical mushroom tip is no more visible in the turbulent cases, showing once again the chaotic behaviour introduced by the atomization process.



(a) Mean velocity profile at the pipe wall (b) Velocity rms at the pipe wall

Figure 2: Validation of LES results

The different behaviour among the cases can be quantified by means of the mass concentration (m_c), calculated as :

$$m_c = \frac{\rho_l \cdot C}{\rho_l \cdot C + \rho_g \cdot (1 - C)} \quad (1)$$

where ρ_l is the liquid density, ρ_g is the gas density and C is the color function defined in [1]. Figure 4 shows the time-averaged mass concentration in the spray axis. Once the spray is stabilized for the both cases, m_c is used to characterize the *intact core length*, which is directly related to the atomization intensity. It can be noticed that while the case without turbulent boundary condition do not reach the axial breakup (and therefore the drop in the axial mass concentration), the case with the synthetic turbulence at the inlet shows a more realistic behaviour and drop to a mass concentration under 95% within the simulation domain. Fig. 4 can be viewed also as a further quantification of the increased atomization regime for the case with the synthetic turbulence.

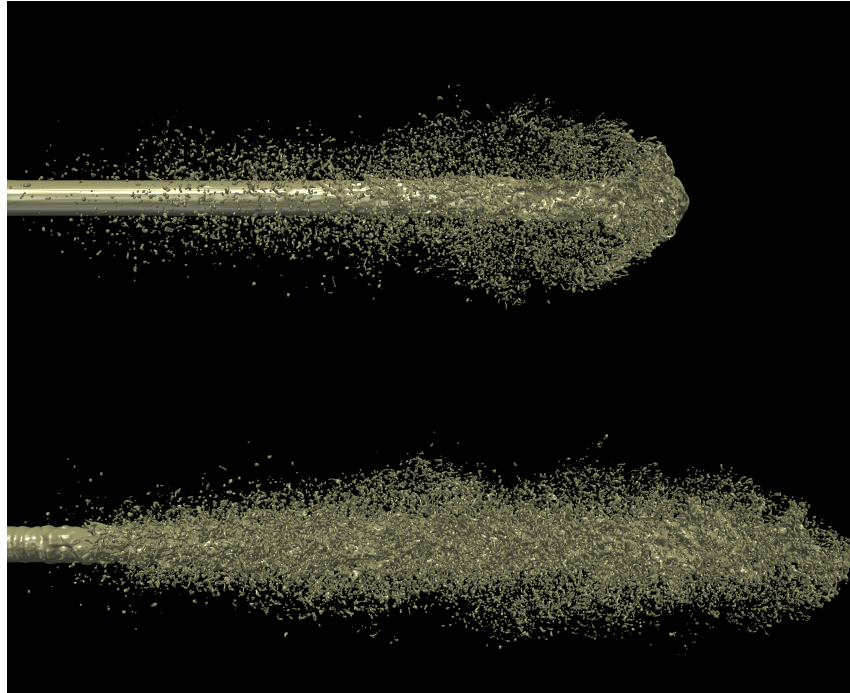


Figure 3: External aspect of the injected spray at $t = 20\mu s$

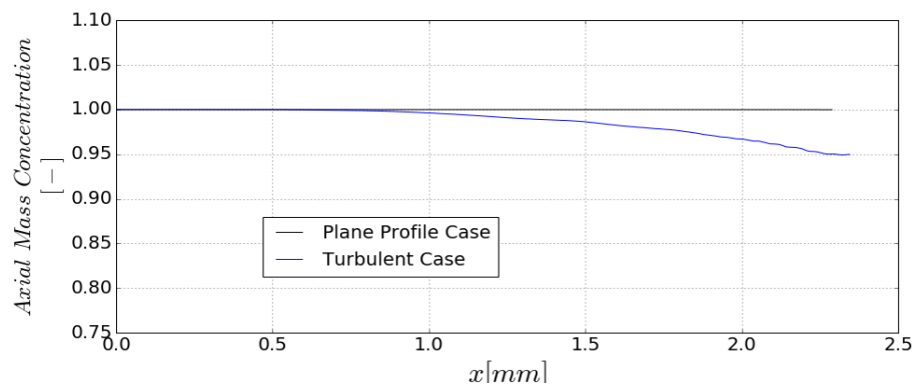


Figure 4: Axial mass concentration

Acknowledgements

This work was partly sponsored by “Ministerio de Economía y Competitividad”, of the Spanish Government, in the frame of the Project “Estudio de la interacción chorro-pared en condiciones realistas de motor”, Reference TRA2015-67679-c2-1-R. Authors thankfully acknowledge the computer resources at MareNostrum and the technical support provided by Barcelona Supercomputing Center (RES-FI-2016-3-0031).

References

- [1] Gilou Agbaglah, Sébastien Delaux, Daniel Fuster, Jérôme Hoepffner, Christophe Josserand, Stéphane Popinet, Pascal Ray, Ruben Scardovelli, and Stéphane Zaleski. Parallel simulation of multiphase flows using octree adaptivity and the volume-of-fluid method. *Comptes Rendus Mécanique*, 339(2-3):194–207, 2011.
- [2] J. G. M. Eggels, F. Unger, M. H. Weiss, J. Westerweel, R. J. Adrian, R. Friedrich, and F. T. M. Nieuwstadt. Fully developed turbulent pipe flow: a comparison between direct numerical simulation and experiment. *Journal of Fluid Mechanics*, 268:175–210, 1994.
- [3] M. Klein, A. Sadiki, and J. Janicka. A digital filter based generation of inflow data for spatially developing direct numerical or large eddy simulations. *Journal of Computational Physics*, 186(2):652–665, 2003.
- [4] R. Lebas, T. Menard, P.A. Beau, A. Berlemont, and F.X. Demoulin. Numerical simulation of primary break-up and atomization: DNS and modelling study. *International Journal of Multiphase Flow*, 35(3):247–260, mar 2009.
- [5] Francisco Javier Salvador, Jorge Martínez-López, J. V. Romero, and M. D. Roselló. Computational study of the cavitation phenomenon and its interaction with the turbulence developed in diesel injector nozzles by Large Eddy Simulation (LES). *Mathematical and Computer Modelling*, 57(7-8):1656–1662, 2013.
- [6] Francisco Javier Salvador, Santiago Ruiz, Jaime Gimeno, and Joaquin De la Morena. Estimation of a suitable Schmidt number range in diesel sprays

at high injection pressure. *International Journal of Thermal Sciences*, 50(9):1790–1798, 2011.

- [7] J. Shinjo and A. Umemura. Simulation of liquid jet primary breakup: Dynamics of ligament and droplet formation. *International Journal of Multiphase Flow*, 36(7):513–532, jul 2010.

Numerical mode matching for sound propagation in silencers with granular material

E.M. Sánchez-Orgaz^b, F.D. Denia^{b*}, L. Baeza[†], and R. Kirby[‡]

(b) Centro de Investigación en Ingeniería Mecánica, Universitat Politècnica de València
Camino de Vera s/n, 46022, Valencia, Spain

(†) Institute of Sound and Vibration Research, University of Southampton
Southampton, SO17 1BJ, United Kingdom

(‡) Centre for Audio, Acoustics and Vibration, University of Technology Sydney
Broadway, Sydney, NSW, Australia.

November 30, 2017

1 Introduction

Multidimensional methods are widely used for the acoustic modelling of automotive exhaust silencers [1]. Accurate predictions of the sound attenuation performance at mid and high frequencies require the consideration of three dimensional waves corresponding to higher order modes. Numerical approaches such as the boundary element method (BEM) and the finite element method (FEM) are usual design tools, although the associated computational expenditure of these fully numerical schemes can be considerable as the number of degrees of freedom increases [2, 3]. Thus, an effort has been made in the last two decades with a view to develop alternative modelling techniques that provide improved computational efficiency without sacrificing accuracy. Some of these techniques are based on hybrid approaches [4-11] that combine analytical and numerical aspects of the wave propagation. For example, in silencers with irregular but axially uniform cross section, a numerical approach can be used to model the transversal governing eigenequation [7]. The complete solution of the acoustic field in a particular silencer subdomain is obtained by considering the contribution of the axial propagating terms analytically. Finally, the acoustic coupling of all the subdomains involved is achieved through enforcing suitable compatibility conditions of acoustic pressure and axial velocity across the geometrical discontinuities. Bibliography tends to favour the point collocation technique and mode matching method as techniques to enforce these conditions [4, 11-13]. In general, for small dimensions mode matching has been

*fdenia@mcm.upv.es

shown to have some advantages in terms of speed and accuracy, due in part to symmetry properties, orthogonality of the transversal modes, the sensitivity of point collocation to the grid chosen and acoustic scattering at particular locations [4, 12, 13].

On the other hand, absorbent granular materials are studied here, from an acoustical point of view, as a potential alternative to the traditional fibrous materials used in dissipative silencers. As shown in earlier studies, sound propagation in granular materials can be modelled through complex and frequency dependent density and speed of sound [14]. Their acoustic properties can be predicted through models available in the bibliography [15, 16], which will be used in the context of the current investigation.

In this work, a mathematical approach based on a numerical version of the mode matching method [8, 9] is presented to compute the transmission loss of silencers with granular material. Multidimensional sound propagation is taken into account in configurations with arbitrary, but axially uniform, cross section. Transversal material heterogeneities are included in the model [3, 11]. Also, the possibility of using different filling levels of granular material gives rise to cross sections with an abrupt change of properties and the existence of a transition between air and material involving a remarkable change in porosity (see Figure 1). The computational requirements of a full numerical scheme such as FEM are reduced through a method that combines analytical axial propagation terms with numerical transversal eigensolutions of the silencer heterogeneous cross section. Numerical mode matching [8, 9] is then used to couple the modal expansions associated with each silencer component and to obtain the complete solution of the wave equation. To this end, the compatibility conditions of the acoustic fields (pressure and axial acoustic velocity) at the geometric discontinuities between the silencer chamber and the inlet and outlet pipes are taken into account. Transmission loss predictions show good agreement with experimental results obtained for a particular configuration. Also, the results obtained with the proposed approach are compared favourably with general three-dimensional finite element computations, offering a reduction in the computational effort. Finally, a number of silencer geometries with granular material have been considered. The effect of several parameters on the acoustic attenuation has been assessed, including filling level, grain size and porosity. The results are not presented here for the sake of brevity.

2 Overview of the mathematical approach

The governing equation for the sound propagation is common for the chamber containing air and granular material (see Figure 1), and it can be written as [3, 11]

$$\nabla \left(\frac{1}{\rho_{a/gr}} \nabla P_{a/gr} \right) + \frac{k_{a/gr}^2}{\rho_{a/gr}} P_{a/gr} = 0 \quad (1)$$

where subscripts *a* and *gr* are related to the air and the granular material domains, respectively. *P* is the acoustic pressure, *k* the wavenumber and ρ the

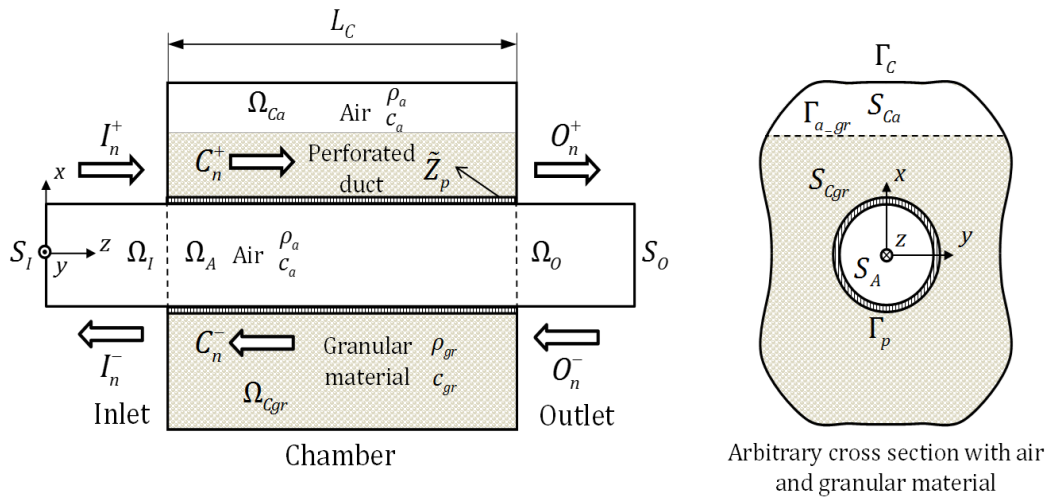


Figure 1: Scheme of silencer with granular material.

density (notice that ρ_a is the air density, while ρ_{gr} is the equivalent density of the granular material [14]). Taking into account that the silencer presents an axially uniform cross section and following a separation of variables procedure, the pressure amplitud can be expressed as [7, 8]

$$P_{a/gr}(x, y, z) = \Psi_{a/gr}^{xy}(x, y)e^{-jk_z z} \quad (2)$$

where Ψ^{xy} is the transversal acoustic pressure and k_z is the axial wavenumber. Now, a 2D FE discretization can be considered and applying the weighting residuals method, together with Green's theorem and Galerkin's approach [11], the procedure leads to

$$\int_{S_{a/gr}} \frac{1}{\rho_{a/gr}} \nabla_{xy}^T \mathbf{N} \nabla_{xy} \mathbf{N} dS \{ \Psi_{a/gr} \} + \int_{S_{a/gr}} \frac{1}{\rho_{a/gr}} (k_z^2 - k_{a/gr}^2) \mathbf{N}^T \mathbf{N} dS \{ \Psi_{a/gr} \} = \int_{\Gamma_{a-gr} \cup \Gamma_p} \frac{1}{\rho_{a/gr}} \mathbf{N}^T \frac{\partial \Psi_{a/gr}}{\partial n} d\Gamma \quad (3)$$

where \mathbf{N} are vectors that contain the nodal shape functions of each subdomain, S_a refers to S_A and S_{Ca} , and S_{gr} represents S_{Cgr} . Then, the coupling conditions at interface Γ_{a-gr} are related to continuity of pressure and normal acoustic velocity, the latter being

$$\frac{1}{\rho_a} \frac{\partial \Psi_a}{\partial n} = -\frac{\phi}{\rho_{gr}} \frac{\partial \Psi_{gr}}{\partial n} \quad (4)$$

where ϕ is the porosity of the granular material. Regarding the porosity of the perforated duct (with boundary Γ_p), it is assumed high enough (near 100%) so that, in practical terms, its acoustic impedance can be neglected and the transition between the air and the granular material can be modelled in the same way as the interface Γ_{a-gr} . Now, by introducing Eq. (4) in the system

represented by expression (3), the following assembled FE system of equations can be obtained

$$\int_{S_a} \frac{1}{\rho_a} (\nabla_{xy}^T \mathbf{N} \nabla_{xy} \mathbf{N} + (k_z^2 - k_a^2) \mathbf{N}^T \mathbf{N}) dS \{\Psi_a\} + \int_{S_{gr}} \frac{\phi}{\rho_{gr}} (\nabla_{xy}^T \mathbf{N} \nabla_{xy} \mathbf{N} + (k_z^2 - k_{gr}^2) \mathbf{N}^T \mathbf{N}) dS \{\Psi_{gr}\} = \{0\} \quad (5)$$

Then, the solution of the system provides the axial wavenumbers and pressure modes associated with the cross section of the chamber. Finally, the continuity of the acoustic fields (pressure and axial acoustic velocity) is taken into account at the geometric discontinuities (expansion/contraction) between the chamber and the inlet/outlet ducts. These acoustic fields can be written in terms of a modal expansion, containing both the incident and reflected waves. The corresponding expressions for the continuity of the acoustic pressure, in compact form, are

$$\int_{S_I} P_I \Psi_{iI}^n(x, y) dS_I = \int_{S_A} P_A \Psi_{iI}^n(x, y) dS_A \quad (6)$$

$$\int_{S_A} P_A \Psi_{iO}^n(x, y) dS_A = \int_{S_O} P_O \Psi_{iO}^n(x, y) dS_O \quad (7)$$

where A is referred to the central duct section within the chamber and I/O , to the inlet/outlet duct sections at coordinates $z = L_I$ and $z = L_I + L_C$ (L_I and L_C being the length of the inlet duct and the chamber), respectively. The weighting function chosen is $\Psi_{iI/O}$, given by the eigenfunction associated with the incident wave at the inlet/outlet sections. In addition, the weighted axial acoustic velocity conditions can be written as

$$\int_{S_I} U_I \Psi_{iC}^n(x, y) dS_I = \int_{S_C} U_C \Psi_{iC}^n(x, y) dS_C \quad (8)$$

$$\int_{S_C} U_C \Psi_{iC}^n(x, y) dS_C = \int_{S_O} U_O \Psi_{iC}^n(x, y) dS_O \quad (9)$$

$S_C = S_A \cup S_{Ca} \cup S_{Cgr}$ being the integration domain related to the whole chamber cross section (including the air central duct S_A , see Figure 1), while Ψ_{iC} is the the weighting function associated with the incident wave at the chamber [7]. Then, weighting integrals are numerically evaluated after truncating the number of unknown wave amplitudes at n modes. Equations are simultaneously solved to obtain the modal amplitudes, considering a unity amplitude for the incident wave at the inlet section and an anechoic termination of the silencer [7, 8-13]. Further details about the methodology can be found at [17].

3 Granular material model

The granular material can be modelled by means of its equivalent properties, e. g. complex density and bulk modulus. According to Umnova *et al.* [15] the equivalent density of the granular material can be expressed as

$$\rho_{gr} = \rho_a q \left(1 - \frac{j\mu\sigma}{\omega\rho_a c_a q} \sqrt{1 + \frac{\omega\rho_a 4q^2 k_p^2}{-j\mu\Lambda^2\sigma^2}} \right) \quad (10)$$

where c_a is the air sound speed, μ the dynamic viscosity, σ the volumetric porosity (different from the surface porosity previously defined), q the tortuosity, k_p the steady state thermal permeability, and Λ the viscous characteristic length.

In addition, the bulk modulus can be written as [16]

$$K_{gr} = \gamma P_0 \left(\gamma - (\gamma - 1) \left(1 + \frac{8\mu}{j\omega\rho_a N_{Pr}\Lambda^2} \sqrt{1 + \frac{j\omega\rho_a N_{Pr}\Lambda'^2}{16\mu}} \right)^{-1} \right)^{-1} \quad (11)$$

γ being the specific heat capacity ratio, P_0 the atmospheric pressure, N_{Pr} the Prandtl number, ω the angular frequency and Λ' the thermal characteristic length. Once the complex density and the bulk modulus are known, the characteristic impedance of the granular material can be obtained as $Z_{gr} = \sqrt{K_{gr}\rho_{gr}}$. More details about the material model can be found at [15-17].

4 Results

The mode matching model previously developed for a silencer containing granular material is validated for a circular configuration. The material is composed of spherical particles of 0.00595 m in diameter, while its porosity is 39.9%. The dimensions of the geometry under study are defined by the radii of the inlet/outlet ducts, $R_I = R_O = 0.0268$ m, and the radius and length of the central chamber, $R_C = 0.091875$ m and $L_C = 0.3$ m, respectively. The air properties at 21.4°C are $\rho_a = 1.1979$ kg/m³ and $c_a = 344.13$ m/s. Two different cases have been studied: (I) The chamber of the silencer has been filled up to approximately 0.02 m below the bottom of the inlet/outlet ducts; (II) the chamber is filled until the spheres reach the bottom of the inlet/outlet ducts.

The results computed with the mode matching method (using 40 modes) for filling cases I and II are compared in Figure 2a and 2b, respectively, showing a good agreement with those obtained from experimental measurements as well as an analysis carried out with the FE commercial software Comsol Multiphysics[®]. However, in filling case II (see Figure 2b) the discrepancies between the experimental measurement and the numerical models are slightly higher, probably due to a stronger effect of the material model inaccuracy as the amount of spheres increases. The use of granular material increases the attenuation achieved by the silencer in the mid and high frequency range due to sound energy dissipation, as expected [3].

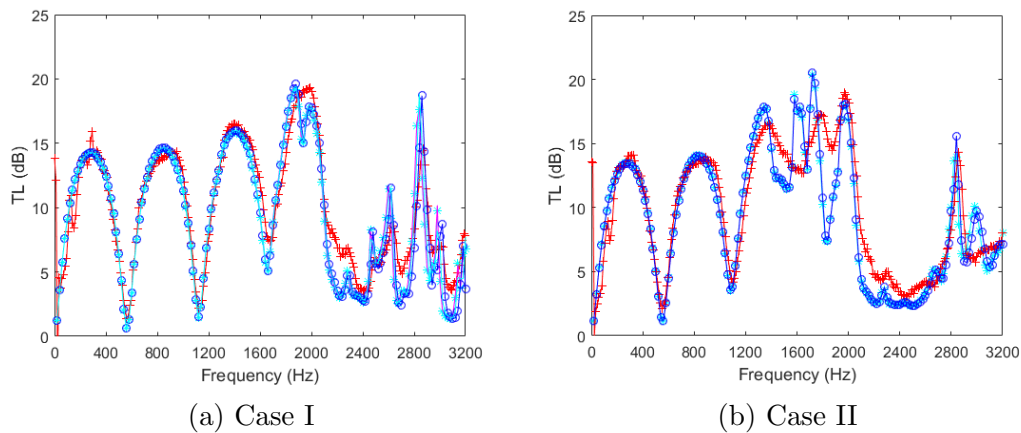


Figure 2: TL of a silencer partially filled with granular material: $+++$, experimental measurement; $***$, mode matching method; ooo , Comsol Multiphysics[®].

5 Conclusions

A numerical model based on the mode matching technique has been presented in this work to assess the acoustic behaviour of silencers with an arbitrary uniform cross section containing granular material. The approach proposed in this work has been shown to provide accurate predictions of the attenuation performance while reducing the computation time of a traditional FEM calculation. The model for the granular material has also been proved to be accurate enough. However, some discrepancies appear as the amount of spheres within the chamber increases.

6 Acknowledgement

Project supported by a 2016 BBVA Foundation Grant for Researchers and Cultural Creators. The BBVA Foundation takes no responsibility for the opinions, remarks or content included in the project and/or the results thereof, which are the sole responsibility of the authors.

References

- [1] M.L. Munjal. *Acoustics of Ducts and Mufflers*, Wiley, New York, 2014.
- [2] T.W. Wu. *Boundary Element Acoustics*, WIT Press, Southampton, 2000.
- [3] F.D. Denia, E.M. Sánchez-Orgaz, J. Martínez-Casas, and R. Kirby. Finite element based acoustic analysis of dissipative silencers with high temperature and thermal-induced heterogeneity. *Finite Elements in Analysis and Design*, 101(1):46–57, 2015.

- [4] R.J. Astley. FE mode-matching schemes for the exterior Helmholtz problem and their relationship to the FE-DtN approach. *Communications in Numerical Methods in Engineering*, 12(4):257–267, 1996.
- [5] R. Glav. The point-matching method on dissipative silencers of arbitrary cross-section. *Journal of Sound and Vibration*, 189(1):123–135, 1996.
- [6] R. Glav. The transfer matrix for a dissipative silencer of arbitrary cross-section. *Journal of Sound and Vibration*, 236(4):575–594, 2000.
- [7] R. Kirby. Transmission loss predictions for dissipative silencers of arbitrary cross section in the presence of mean flow. *Journal of the Acoustic Society of America*, 114(1):200–209, 2003.
- [8] R. Kirby. A comparison between analytic and numerical methods for modelling automotive dissipative silencers with mean flow. *Journal of Sound and Vibration*, 325(3):565–582, 2009.
- [9] Z. Fang, and Z.L. Ji. Numerical mode matching approach for acoustic attenuation predictions of double-chamber perforated tube dissipative silencers with mean flow. *Journal of Computational Acoustics*, 22(2), Article number 1450004, 2014.
- [10] L. Yang, Z.L. Ji, and T.W. Wu. Transmission loss prediction of silencers by using combined boundary element method and point collocation approach. *Engineering Analysis with Boundary Element*, 61(1):265–273, 2015.
- [11] F.D. Denia, E.M. Sánchez-Orgaz, L. Baeza, and R. Kirby. Point collocation scheme in silencers with temperature gradient and mean flow. *Journal of Computational and Applied Mathematics*, 291(1):127–141, 2016.
- [12] Kirby R. Modeling sound propagation in acoustic waveguides using a hybrid numerical method. *Journal of the Acoustic Society of America*, 124(4):1930–1940, 2008.
- [13] F.D. Denia, J. Martínez-Casas, J. Carballeira, E. Nadal, and F.J. Fuenmayor. Computational performance of analytical methods for the acoustic modelling of automotive exhaust devices incorporating monoliths. *Journal of Computational and Applied Mathematics*, 330(1):995–1006, 2018.
- [14] J.F. Allard, and N. Atalla, *Propagation of Sound in Porous Media: Modelling of Sound Absorbing Materials*, Wiley, New York, 2009.
- [15] O. Umnova, K. Attenborough, and K.M. Li. A cell model for the acoustical properties of packing of spheres. *Acta Acustica united with Acustica*, 87(2):226–235, 2001.
- [16] J. Li, S. Zhao, and K. Ishibara. Study on acoustical properties of sintered bronze porous material for transient exhaust noise of pneumatic system. *Journal of Sound and Vibration*, 322(11):2721–2734, 2013.
- [17] E.M. Sánchez-Orgaz, F.D. Denia, J. Martínez-Casas, and L. Baeza. Efficient approaches for the acoustic modelling of automotive exhaust devices. Application to configurations incorporating granular materials and monoliths. *24th International Congress on Sound and Vibration*, London, UK, 2017.

Modal Method for the Efficient Analysis and Design of Microwave Filters based on Multiple Discontinuities

Juan R. Sánchez *, Carmen Bachiller, María Juliá
and Héctor Esteban

Instituto de Telecomunicaciones y Aplicaciones Multimedia,
Universitat Politècnica de València.
Camino de Vera, s/n, 46021 Valencia, Spain.

November 30, 2017

1 Introduction

Microwave filters are essential components in high frequency communication systems. So far, for designing these filtering structures, different technologies are used. One of them are rectangular or circular metallic waveguides, which present low insertion losses, ability to carry out high power signals and high quality factor [1]. However, metallic waveguides are heavy, big, expensive and difficult to integrate with planar technology. Lately Substrate Integrated Waveguide (SIW) technology has appeared to solve these problems [2]. It integrates a rectangular waveguide into a planar substrate, obtaining devices much smaller, significantly cheaper and easier to manufacture.

For all technologies, the coupled cavities H-plane filters are the most used. Their design combines cavity resonators and impedance inverters. These impedance inverters are implemented by coupling windows, whose widths change depending on the desired impedance value [3]. However, there is

*e-mail:juasncm1@upv.es

a new alternative to this scheme consisting on filling the waveguide with dielectric material by sections, keeping the width of the whole structure.

There are several commercial tools like Ansys HFSS and CST Studio Suite based on numerical methods that enable to carry out the analysis and design of these structures, but they require a very high computational time during the analysis process. This affects negatively to the automated design of these devices, since the optimization process of the design requires a huge number of iterations of the analysis of the structure.

In this paper, the authors propose an efficient and accurate analysis method by following a multimodal analysis of the device. The device is considered as a waveguide with N different sections of length $l^{(i)}$ and $N - 1$ dielectric discontinuities as shown in Fig. 1. The sections filled with a dielectric material (odd sections in the figure, except the first and the last one) behave as resonant cavities and the empty sections (even ones in the figure) are the coupling windows.

For the analysis, the input and output normalized electric and magnetic fields are defined for each section and mode. At each discontinuity, the continuity of electric and magnetic transverse fields is forced for the M modes, obtaining $2(N - 1)$ equations for each mode. These equations are solved recursively obtaining the cross relation between the input and output voltages of the first and last section. The relations of these normalized voltages determine the scattering matrix (\mathbf{S}) of the whole device.

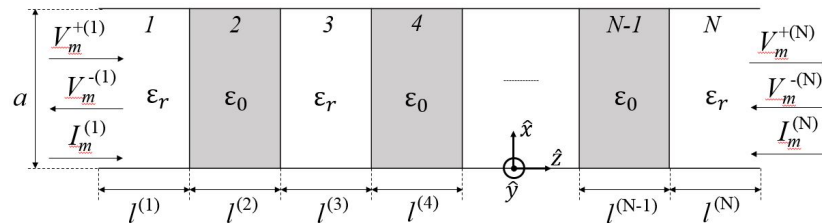


Figure 1: Multiple discontinuities waveguide filter and its reference system. Gray sections are the coupling windows. White sections are the resonant cavities.

Since both the geometry and the excitation are invariant in height (dimension y), for the analysis, only TE_{m0} modes are considered. Furthermore, although there are infinite modes, only the first M modes are selected.

2 Results

The analysis tool is implemented in MatLab and integrated into a Computer Aided Design (CAD) tool based on the theoretical synthesis of a starting point, in order to calculate the physical parameters of the structure, i.e. the lengths of the resonant cavities and the coupling windows. Once the starting point has been calculated, the next step is the optimization of these design dimensions to get a frequency response as much similar as possible to the ideal response.

The optimization process is based on several iterations of the analysis of the structure: in each iteration the analysis tool calculates the electromagnetic response of the structure, then it is compared to the desired response, if the difference between them does not reach a predefined minimum, the structure parameters are slightly changed and the process is repeated. Obviously, the strategy for changing these physical dimensions is not random, but a set of optimizations algorithms are used. The whole process is described in [4], where its efficiency and robustness are improved by using the adequate combination of algorithms.

In order to evaluate the effectiveness (computational time) and the accuracy (frequency response) of the analysis tool, several filters with different number of cavities have been designed and afterward analyze. The responses of two of them are presented.

Figure 2 shows the frequency response of a filter of two cavities when it is analyzed with the analysis tool and a commercial software (CST). Both modal and numerical analysis are compared to the ideal response of a two cavities Chebysev filter. It is observed that there is a very good agreement between all of them. It means that the developed analysis tool is accurate.

Figure 3 shows the same comparison that the previous figure but for a filter of four cavities. In this case, it is also observed the very good agreement between all the frequency responses. The analysis tool can be used for filters of different orders.

Once the accuracy of the tool is checked, the effectiveness is also tested. The computational time for the analysis of filters from two to ten cavities is shown in Table 2 for the Modal Method and CST commercial software. This time is calculated under the same conditions for both: computing processor, start and stop frequencies and number of sample points. The obtained times are plotted in Figure 4. It is observed that the computational time of the commercial software based on numerical methods increases linearly with a

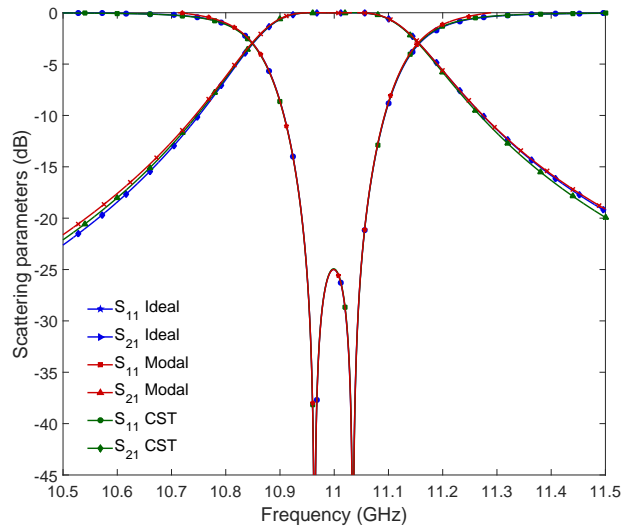


Figure 2: Comparison of frequency responses for a filter of two cavities.

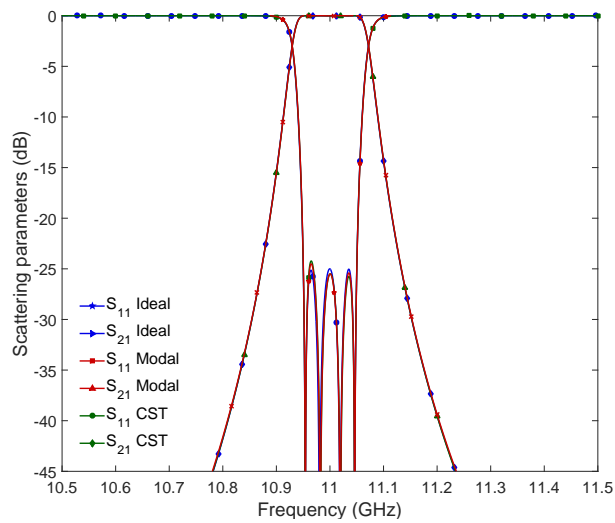


Figure 3: Comparison of frequency responses for a filter of four cavities.

sharp slope when the number of cavities increases. However, in the case of the developed modal method the time increases very slowly. It shows the

advantage of the new method versus the commercial one.

Cavities	Modal Method	CST
2	2.70 s	40.00 s
4	4.28 s	80.00 s
6	5.79 s	130.00 s
8	7.15 s	160.00 s
10	8.85 s	194.00 s

Table 1: Computational time for the analysis of the filter.

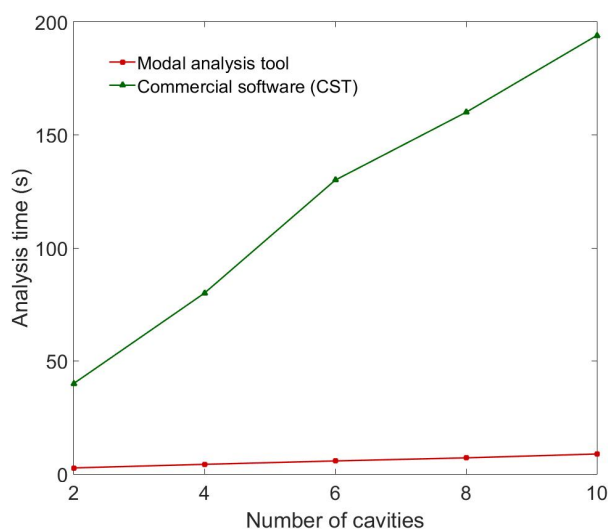


Figure 4: Computational time comparison between both methods.

3 Conclusion

A modal method for the efficient analysis of microwave waveguide filters based on multiple discontinuities has been developed and assessed. Its performance shows that the method is more efficient and accurate compared to numerical methods commercial software. This makes the new approach very competitive for its usage in the automatic design of such devices.

Acknowledgment

This work was partially founded by the Generalitat Valenciana research project PROMETEOII/2015/005, by the Ministerio de Educación, Cultura y Deporte (Spain) under the Fellowship Program for Training University Professors FPU14/00150 and by Ministerio de Economía y Competitividad (Spain) under R&D project TEC2016-75934-C4-R.

References

- [1] G. Matthaei and E. Jones and L. Young. *Microwave Filters Impedance-Matching Networks, and Coupling Structures*. Artech House Publishers. February, 1980.
- [2] D. Deslandes and K. Wu, Integrated microstrip and rectangular waveguide in planar form, *IEEE Microw. and Wireless Components Letters*, vol. 11, no. 2, pp. 68-70, February 2001.
- [3] I. Hunter *Theory and Design of Microwave Filters*. London: The Institution of Electrical Engineers, 2001.
- [4] E. Diaz and J. V. Morro and H. Esteban and V. E. Boria and C. Bachiller and A. Belenguer, *Simulation-Driven Design Optimization and Modeling for Microwave Engineering*. Singapore: Imperial College Press, 2013, ch. Simulation-Driven Design of Microwave Filter por Space Applications.

Introducing Covariates in Reliability Models by Markovian Arrival Processes

C. Santamaría[†]*, B. García-Mora[†], and G. Rubio[†]

([†]) Instituto Universitario de Matemática Multidisciplinar,
Universitat Politècnica de València

November 30, 2017

1 Introduction and Objectives

We are interested in studying processes which generate events repeatedly over time, as multiple recurrences of a tumor that occur in the same subject (*Survival analysis*) or multiple failures of a device (*Reliability*). A **correlation** between the recurrent relapse or failure times within the same unit (patient or device) may exist due to either the *heterogeneity* among the individuals or devices and the *event dependence*. This situation leads us to have *correlated* and *not identically distributed* inter-failure times. In this study we consider a device with three failures and so with three inter-failure times (Figure 1 and 2). We assume that after each failure the device is repaired immediately and the repair time is negligible. It is simulated a sample of operational random times for 300 independent devices with inter-failure times, T_1 , T_2 and T_3 , each one as we indicate in the following table

	T_1	T_2	T_3
<i>device (1)</i>	$t_1^{(1)}$	$t_2^{(1)}$	$t_3^{(1)}$
<i>device (2)</i>	$t_1^{(2)}$	$t_2^{(2)}$	$t_3^{(2)}$
<i>device (3)</i>	$t_1^{(3)}$	$t_2^{(3)}$	$t_3^{(3)}$
\vdots	\vdots	\vdots	\vdots
<i>device (300)</i>	$t_1^{(300)}$	$t_2^{(300)}$	$t_3^{(300)}$

*e-mail: crisanna@imm.upv.es

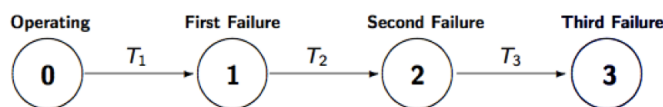


Figure 1: one device with three failures

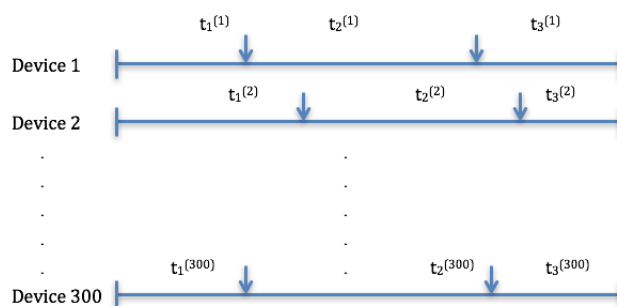


Figure 2: Simulated data of 300 devices

The most common assumptions in the literature is that **events** occur *independently* and with the *same distribution*. For it the *Poisson process* with specific arrival rate is the usual arrival process used to model this situation. When these two assumptions fail, we need models to fit correctly to data with *correlated inter-failure times and with a different distribution*. Moreover, the introduction of *covariates* that identify the different characteristics of the devices is of great interest in the modelization process. Then, in order to obtain more accurate predictions, our aim is to model correlated and not identically distributed inter-failure times taking into account covariates.

2 Simulated data

The inter-failure times are simulated using Weibull distributions where the dependence is performed modifying the shape parameter of this distribution. Let T_k be the random variable representing *the operational time between the*

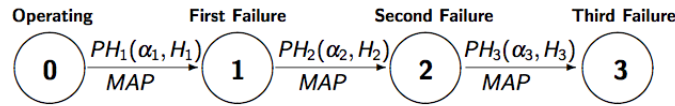


Figure 3: Mixture of two Erlang distributions in each transition

$(k-1)$ -th failure and the k -th failure. In our case, T_1 , T_2 and T_3 are correlated and not identically distributed (Figure 1).

The following step consists of selecting a suitable probability model family $F_{ij}(t|\theta_{ij})$ for each waiting time distribution in each transition. We compute the empirical distributions and approximate them by means of the mixture of two Erlang distributions, a class of Phase-Type distribution ([1],[2]). The Erlang distribution $E[r, \mu]$ has a representation (α, H) as a PH-distribution, with $\alpha = (1, 0, \dots, 0)_{1 \times r}$ a row r -vector and

$$H = \begin{pmatrix} -\mu & \mu & & & \\ & -\mu & \mu & & \\ & & \ddots & \ddots & \\ & & & -\mu & \mu \\ & & & & -\mu \end{pmatrix}_{r \times r}$$

a square matrix of order r representing a distribution time associated to a Markov process with generator

$$Q = \begin{pmatrix} H & -H\mathbf{e} \\ 0 & 0 \end{pmatrix},$$

with \mathbf{e} denoting a column vector with all components equal to one. The distribution function is $F(t) = 1 - \alpha \exp(Ht)\mathbf{e}$, $t \geq 0$.

The parameters α_i and H_i for $i = 1, 2, 3$ of each transition (mixture of two Erlangs) are calculated by minimizing $\|F_{ij}(t) - PH_i(t|\alpha_i, H_i)\|$ where $F_{ij}(t)$ is the empirical Kaplan-Meier estimator for the transition $i \rightarrow j$ and $PH_i(t|\alpha_i, H_i)$ is the mixture distribution for the same transition (Figure 3).

The Cumulative Distribution Functions for the variables T_1 , T_2 and T_3 are represented in the Figure 4.

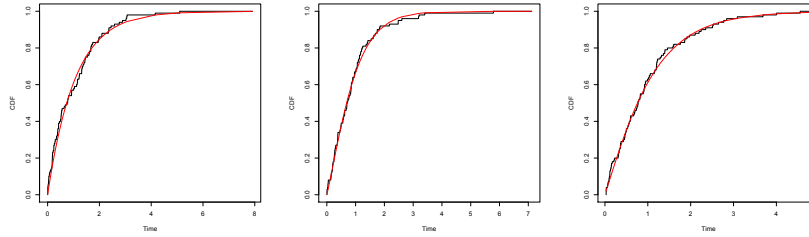


Figure 4: Erlang mixture (*smooth line*) and empirical distribution (*step function*) for the transitions $0 \rightarrow 1$, $1 \rightarrow 2$ and $2 \rightarrow 3$ respectively.

3 The Markov Arrival Process (MAP) with covariates

The Markov Arrival Process (MAP) is a matrix generalization of the Poisson point process for dealing with *correlated inter-failures times and not identically distributed* ([3], [4], [5], [6]). A MAP (π, D_0, D_1) is an irreducible Markov chain with a finite state space S , initial vector π and a generator matrix Q which is represented as $Q = D_0 + D_1$ where,

- $D_1 \geq 0, D_1 \neq 0$
- $D_0(i, j) \geq 0$ for $i \neq j$
- (π, D_0) is a phase-type distribution [6].

The idea is to make up a MAP (π, D_0, D_1) for modeling this process $0 \rightarrow 1 \rightarrow 2 \rightarrow 3$ of three failures for 300 devices. The *joint density function* for the three dependent interarrival times $(t_1^{(i)}, t_2^{(i)}, t_3^{(i)})$ of each device is

$$f_i(t_1^{(i)}, t_2^{(i)}, t_3^{(i)}) = \pi e^{D_0 t_1^{(i)}} D_1 e^{D_0 t_2^{(i)}} D_1 e^{D_0 t_3^{(i)}} D_1 \mathbf{e}$$

Then we simulate two covariates for each device: *age*, continuous variable (using a Normal distribution: X_1) and *device class*, variable of two levels (using a Bernoulli distribution: X_2).

We consider the matrix D_0 as the mean of the three matrices: H_1, H_2 and H_3 of the Phase-Type distributions fitted before (Figure 3). We introduce the effect of the covariates multiplying by

$$D_0 * e^{\beta_1 * X_1 + \beta_2 * X_2} = D_0 * e^{\vec{\beta} \vec{X}}$$

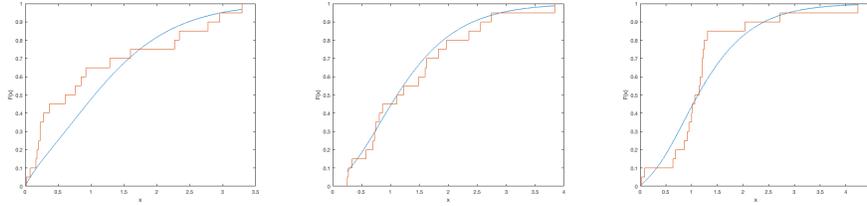


Figure 5: $F_{T_1}(t)$, $F_{T_2}(t)$, $F_{T_3}(t)$ (smooth line) and empirical distribution (step function) for the transitions $0 \rightarrow 1$, $1 \rightarrow 2$ and $2 \rightarrow 3$ respectively. Group: age of device 12 years old and material class 0. *P-value* Kolmogorov–Smirnov test=0.12, 0.93 and 0.11 respectively for the three transitions.

with $\vec{\beta}$ the vector of coefficients to estimate, where $(\pi, D_0 * e^{\vec{\beta}\vec{X}})$ is a phase-type distribution [7].

In a second step the matrix D_1 is fitted by maximizing the *likelihood function* for the 3 interarrival operational times $(t_1^{(i)}, t_2^{(i)}, t_3^{(i)})$ of 300 devices.

$$\prod_{i=1}^{300} f_i(t_1^{(i)}, t_2^{(i)}, t_3^{(i)})$$

Then $D_0 * e^{\vec{\beta}\vec{X}} + D_1$ will represent the matrix generator of a Markov process $J(t)$, with stationary vector ϕ , that is calculated as

$$\phi P^* = \phi$$

where P^* is the transition probability matrix given by $P^* = (-D_0 * e^{\vec{\beta}\vec{X}})^{-1} D_1$. The cumulative density function (CDF) of the *variables* T_1, T_2 and T_3 are defined by these expressions

$$F_{T_k}(t) = 1 - \pi_k e^{D_0 * e^{\vec{\beta}\vec{X}} t} \mathbf{e}$$

where $\pi_k = \pi(P^*)^{k-1}$ and $T_k \sim PH\{\pi_k, D_0 * e^{\vec{\beta}\vec{X}}\}$, different phase-type distributions for the correlated variables T_1, T_2 and T_3 (Figure 5).

4 Concluding Remarks

- Realistic contexts in biomedical and engineering fields need to deal with correlated and not identically distributed data. Taking into account covariates is a fundamental issue. Markovian Arrival Processes (MAPs) are a useful tool to manage this type of data.

- We have proposed an easy set-up method to take into account covariates in the MAP methodology.
- Our approach is extensible in a natural way to allow us to incorporate censored data, another typical feature of real life.

References

- [1] Rubio G, García-Mora B., Santamaría C. and Pontones J.L. Incorporating multiple recurrences in a Flowgraph model for bladder carcinoma. International Work-Conference on Bioinformatics and Biomedical Engineering, IWBBIO 2015. 15–17 April, 2015. Granada (Spain).
- [2] Pérez-Ocón R. and Segovia M.C. Modeling lifetimes using phase-type distributions. In: Aven, T., Vinnem, J.E. (eds.) Risk, Reliability and Societal Safety, Proceedings of the European Safety and Reliability Conference 2007 (ESREL), Taylor & Francis, 3rd edition (2007).
- [3] Rodríguez J., Lillo R.E. and Ramírez-Cobo P. Failure modeling of an electrical N -component framework by the non-stationary Markovian arrival process. *Reliability Engineering and System Safety*, (134): 126–133, 2015.
- [4] Santamaría C., García-Mora B., Rubio G. and Pérez-Ocón R. Managing dependence in Flowgraphs models. An application to Reliability Engineering. Modelling for Engineering & Human Behaviour 2015, Valencia, Instituto Universitario de Matemática Multidisciplinar, 2015.
- [5] Rubio G., García-Mora B., Santamaría C. Modeling dependence in multistate processes. International Work-Conference on Bioinformatics and Biomedical Engineering, IWBBIO 2016. 20–22 April, 2016. Granada (Spain).
- [6] Neuts M. F. Matrix-Geometric Solutions in Stochastic Models: An Algorithmic Approach., John Hopkins University Press, 1981.
- [7] García-Mora B., Santamaría C., Rubio G. and Pontones J.L. Bayesian Prediction for flowgraph models with covariates. An application to bladder carcinoma., *Journal of Computational and Applied Mathematics*, (291): 85-93, 2016.

Including a human happiness index in a social well-being model

Joan C. Micó^a, David Soler^a, María T. Sanz^{b*}, Antonio Caselles^c

^a *Institut Universitari de Matemàtica Multidisciplinar*

Universitat Politècnica de València

Camí de Vera s/n, 46022 València, Spain

^b *Departament de Didàctica de la Matemàtica*

Universitat de València

Avda. Tarongers 4, 46022 València. Spain

^c *Departament de Matemàtica Aplicada*

Universitat de València

Dr. Moliner 50, 46100 Burjassot, Spain.

1. Introduction

Most people believe that happiness is the basis of a meaningful life [1], and for this reason, the intention to measure the happiness is increasing. The literature reflects two different ways to measure this concept. On the one hand, authors who try to measure the happiness of the people. George Gallup created the Gross National Well-Being (GNW), also known as the Gross National Happiness Index (GNH Index). It consists of 7 dimensions: economic, environmental, physical, mental, work, social, and political. The Scale of Life Satisfaction (SWLS) [2] is a short 5-item instrument designed to measure global cognitive judgments of satisfaction with one's life, and the Scale of Subjective Happiness [3] asks four questions to measure the happiness on a scale from 1 to 7. On the other hand, there are authors that try to measure the happiness of a country, as The Happy Planet Index (*HPI*), which captures the degree to which long and happy lives are achieved per unit of environmental impact. It is calculated [4] through life expectancy at birth, well-being and progress in life, and ecological footprint. Finally, in the Overall Life Satisfaction Index, used in [5], subjective well-being questions are involved about health, wealth, and access to basic education.

The index presented here is calculated through the terms studied by Caselles [6]. He considered that human dignity (from now on Happiness Index) could be calculated from five fundamental concepts (see Fig. 1). He also showed a list of variables (qualitative and quantitative) that could be related with them.

This paper has two objectives. First, obtaining a generic formula to measure the happiness of a country/region with quantitative variables. The term “generic” is introduced because this formula could be extrapolated to any country, although in this work this new index has been calculated only for 13 EU countries in 2013, because the information is not available for all countries in the different database. Second, adding this index to a dynamic mathematical model through the demographic rates [7,8].

2. Happiness Index

As mentioned before, we consider happiness as a disaggregation of the five fundamental concepts: Development, Solidarity, Justice, Peace and Freedom, but in order to evaluate it, we must find quantitative variables that allow us to get closer to its meaning.

* Email: m.teresa.sanz@uv.es

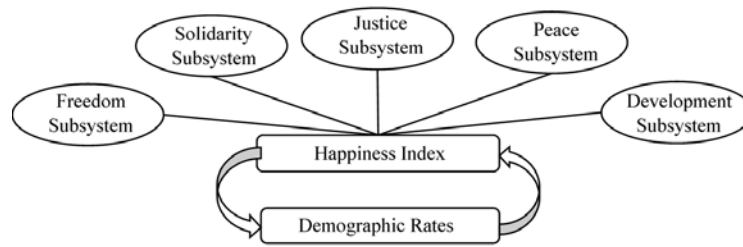


Fig 1. Causal diagram of the Happiness Index.

Our theoretical reference has been [6], and data have been obtained from Eurostat and World Data Bank in the 2001-2015 period. The methodology to obtain the Happiness Index is the one used in UNDP Reports. Minimum and maximum values (values limits) are determined to transform the real variables into variables with values between 0 and 1. In this way, all variables can be used in the same formula because they have the same dimension. Due to the limitation on the number of pages, it is impossible to show all the equations here. For this reason, the fundamental concepts are only explained and the chosen quantitative variables are presented.

Development: *Options of survival and self-fulfilment. It includes: life/health, social progress (education, culture, etc.) and standard of life (economic resources, comforts, etc.).*

It is related with the Gender Development Index (*GDI*) [5]. Note that the education quality is not computed in *GDI*, therefore it is included through the following four variables: a) primary school teachers trained to teach, b) performance of 15-year-old students in reading, mathematics and science, c) the average number of pupils per teacher in primary education in a given school year and d) public expenditure on education.

Freedom: *Non-restrictions to self-fulfilment. This would be the total freedom that, obviously, in a group must be limited by the dignity of the other members of the group.* The variables used in this subsystem are: a) Net migration rate, b) Stock of immigrants, c) International inbound tourists, d) Mobile phone subscriptions, e) Exports and imports and f) Research and development expenditure.

Peace: *Absence of violence, coercion and fear.* The corresponding quantitative variables to measure this concept are the prison population and the homicide rate.

Solidarity: *It is considered synonymous of brotherhood, that is, mutual aid.* The information to create the Solidarity Index are a) at-risk-of-poverty rate, b) share of total population living in a dwelling, and c) material deprivation rate.

Justice: *Mechanisms of prevention, protection and compensation for individuals or groups face to possible damages or benefits.* The variables considered in this case are, a) the police officers, b) the professional judges, c) the prison population. and d) crimes and violence.

Finally, the Happiness Index (*HAIN*) is calculated through Eq. (1). The geometric mean is used because it is considered the best option to calculate indices [5].

$$HAIN(t) = \sqrt[5]{development * freedom * peace * solidarity * justice} \quad (1)$$

To validate this new index, we have compared it with the Overall Life Satisfaction Index (Fig. 2), calculated in the Human Development Reports [5].

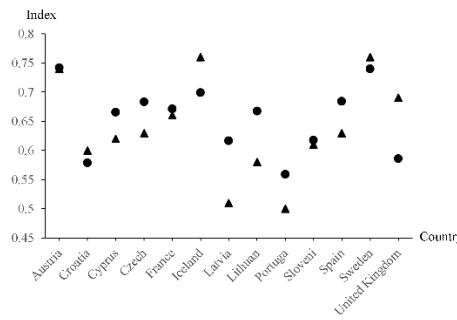


Fig 2. Happiness Index (circle) and Overall Life Satisfaction Index (triangle) in 2013 year. R²=0.5027.

3. Demographic Model

The starting point of the demographic model is the model presented by [9] without age structure where all variables depend on time $t \in [t_0, \infty[$, $i=1$ refers to male and $i=2$ refers to female,

$$\frac{dPOPL_i(t)}{dt} = RFER_i(t) \cdot POPL_2(t) - RDEF_i(t) \cdot POPL_i(t) + (RINM_i(t) - REMM_i(t)) \cdot POPL_i(t) \quad (2)$$

where, $POPL_i$ is the total population, $RFER_i$ is the birth rate, $RDEF_i$ is the death rate, $RINM_i$ and $REMM_i$ are, respectively, the immigration and emigration rates.

In previous studies, birth and death rates depended on the well-being variables [7,10] or the environmental variables [8]. A goal of this paper is to introduce the Happiness Index in all demographic rates: birth, death and migration rates (emigration and immigration). The model, with this change, would be the following,

$$\begin{aligned} \frac{dPOPL_i(t)}{dt} = & RFER_i(xhdi, equi, hain) \cdot POPL_2(t) - \\ & RDEF_i(xhdi, equi, hain) \cdot POPL_i(t) + (RINM_i(xhdi, equi, hain) - \\ & REMM_i(xhdi, equi, hain)) \cdot POPL_i(t) \end{aligned} \quad (3)$$

Where, HDI , $EQUI$ and $HAIN$ are, respectively, the Human Development Index [11], the Environmental Quality Index [11] and the Happiness Index.

To do this, the input variables of the Happiness Index must be fitted by the time through a software (*Regint*) [12,13]. Regarding the Environmental Index, an extension of the temporal period is made, since in [8] the construction is for a time series from 2000 to 2007 and is needed until 2015. Finally, the Human Development Index is defined by the UN Human Development Reports [11] and there is a time series 2010-2014. In [5] there are values since 1980 but every 5 years. To have the time series analogous to the previous ones, the temporal trend is observed and it is fitted as a logistic function with a determination coefficient, $R^2 = 0.99964$.

The mathematical structure considered for the demographic rates are described as functions of the *three indices* as follows:

$$a0 + \frac{b0}{1 + \text{Exp}\left[\left(-b1 + \frac{xhdi-hain}{equi}\right)/b2\right]} + \frac{c0}{1 + \text{Exp}\left[\left(-c1 + \frac{xhdi-hain}{equi}\right)/c2\right]} \quad (4)$$

Logistic functions have the property that they can be interpreted in saturation of resources, and their use in demography has been proved to be very useful [14]. To introduce the Happiness Index in the fertility and mortality rates [8], the rates tendency with the new index is observed and it reveals direct relation. In the migration rates case, they are fitted with the same independent variable and with the same mathematical structure. Finally, the specific structures have been found by a trial and error process with the fitter tool *Regint* [12,13]. The fitted process is considered successful for three reasons: the R^2 are very high: female fertility rate $R^2=0.683692$, male fertility rate $R^2=0.705732$, female mortality rate $R^2=0.61328$, male mortality rate $R^2=0.809224$, female emigration rate $R^2=0.86737$, male emigration rate $R^2=0.887952$, female immigration rate $R^2=0.888557$ and male immigration rate $R^2=0.899601$. The

randomness of the residuals has been verified and the Kolmogorov-Smirnov test is chosen to prove the data normality.

4. Validation

The historical data used in this article to fit the model have been obtained from the Spanish National Statistics Institute database [15] in 2001-2015 period. The software tool used for the model verification is *SIGEM* [13].

The validation is considered successful for three reasons: the visual evaluation of the graphic overlapping of the historical data and the calculated data is satisfactory, the determination coefficients, R^2 , are very high and the randomness of the residuals is verified by the maximum relative error, which do not exceed the 5%. As an example, Fig. 3 shows the female mortality and the male immigration.

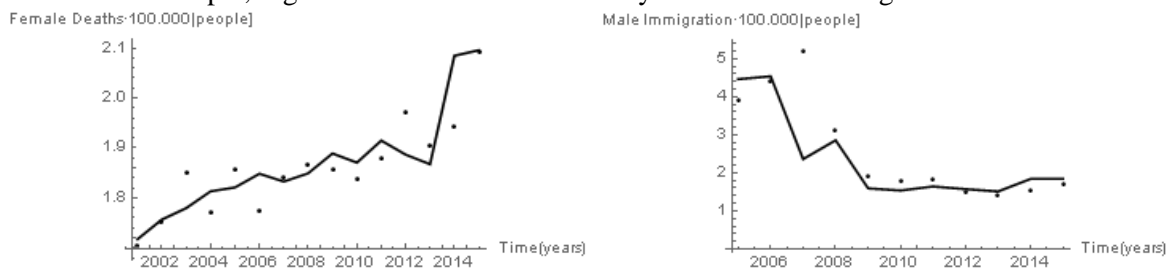


Figure 3. Left: Spanish Female Mortality, $R^2= 0.70961$. Right: Spanish Male Immigration, $R^2= 0.55873$. Real data (points), Fitted data (line), in 2001-2015 period.

5. Conclusion

A dynamic demographic model by sex has been presented where the birth, death and migration rates are calculated through variables related with well-being, environmental and happiness. The well-being and environmental variables have been presented in previous works [7,8] but the happiness variables are built in this work. A general formula is obtained from a Happiness Index. It is calculated through five fundamental concepts: solidarity, development, justice, peace and freedom. This formula provides similar values to those obtained with the Overall Life Satisfaction Index [5] in the case of 13 countries in 2013.

The mathematical structures of the demographic rates are logistic function with a specific dependent variable ($\frac{x_{hdi-hain}}{equi}$). Finally, the study has been performed with a deterministic model and has been fitted and verified with the corresponding criteria and real data from Spain in the 2001-2015 period.

Nowadays we are working on the design of the different strategies and scenarios to obtain a demographic sustainability with this model.

References

- [1] N. Extremera, P. Fernández-Berrocal, The Subjective Happiness Scale: Translation and preliminary psychometric evaluation of a Spanish version, *Soc Indicators Res.* 119(1) (2014) 473-81
- [2] E. Diener, R.A. Emmons, R.J. Larsen, S. Griffin, The Satisfaction with Life Scale, *J. Pers. Assess.*, 49 (1985) 71-75.
- [3] S. Lyubomirsky, H. Lepper, A Measure of Subjective Happiness: Preliminary Reliability and Construct Validation. *SOCI*, 46 (1999) 137-155.
- [4] <http://www.gallup.com/home.aspx> (accessed 24.03.2017)
- [5] UNDP, Human Development Report 2014. Oxford University Press. New York, Oxford, 2014.
- [6] A. Caselles, Trying to evaluate the human dignity in a social group. In: 9th Congress of the European Union of Systems (UES-EUS). Valencia (Spain), 2014.

- [7] M.T. Sanz, J.C. Micó, A. Caselles, D. Soler, A stochastic model for population and well-being dynamics. *J. Math. Sociol.*, 38 (2) (2014) 75-94.
- [8] M.T. Sanz, A. Caselles, J.C. Micó, D. Soler, Including an environmental quality index in a demographic model, *Int. J. Glob. Warm.*, 9(3) (2016) 362-396.
- [9] J.C. Micó, A. Caselles, D. Soler, Age-Structured Human Population Dynamics, *J. Math. Sociol.*, 30 (2006) 1-31.
- [10] A. Caselles, D. Soler, M.T. Sanz, J.C. Micó, Simulating Demography and Human Development Dynamics, *Cybernet. Syst.*, 45 (6) (2014) 465-485.
- [11] UNDP, Human Development Report. New York: Oxford University Press, 2010.
- [12] A. Caselles, A tool for discovery by complex function fitting. In *Cybernetics and Systems Research'98*. R. Trappl (ed.), Austrian Society for Cybernetic Studies, (1998) 787-792.
- [13] A. Caselles, *Modelización y simulación de sistemas complejos (Modeling and simulation of complex systems)*. Valencia (Spain). Ed. Universitat de València, 2008. (Available in <http://www.uv.es/caselles> (accessed 24.03.2017) as well as SIGEM).
- [14] C. Marchetti, P. S. Meyer, J. H. Ausubel, Human Population Dynamics Revisited with the Logistic Model: How Much Can Be Modeled and Predicted? *Technological Forecast. Soc. Chang.*, 52 (1996) 1-30.
- [15] <http://www.ine.es/> (accessed 24.03.2017)

Numerical solution of the Burgers' equation by splitting methods using Crank-Nicolson schemes

M. Seydaođlu^b *, S. Blanes[†] ,

(b) Department of Mathematics, Faculty of Art and Science,
Muş Alparslan University, 49100, Muş, Turkey.

(†)(b) Instituto de Matemática Multidisciplinar,
Universitat Politècnica de València. 46022 Valencia, Spain.

November 30, 2017

1 Introduction

Consider one-dimensional Burgers' equation

$$\frac{\partial u}{\partial t} + \frac{\partial}{\partial x} \left(\frac{u^2}{2} \right) = \nu \frac{\partial^2 u}{\partial x^2}, \quad (x, t) \in D \times [0, \infty), \quad (1.1a)$$

with the initial condition

$$u(x, 0) = u_0(x), \quad 0 \leq x \leq 1, \quad (1.2a)$$

and the boundary conditions

$$u(0, t) = u_1(t), \quad u(1, t) = u_2(t), \quad t \geq 0, \quad (1.3a)$$

where $D = [0, 1]$, t and x represent time and space variable respectively, $\nu > 0$ is the coefficient of kinematic viscosity defined by $\nu = 1/Re$, Re is the

*e-mail:m.seydaoglu@alparslan.edu.tr

Reynolds number and the given function $u_0(x)$ is sufficiently smooth. The steady state solutions of the nonlinear partial differential equation (1.1) are first time presented by Bateman in [1]. In 1948, Burger [2] used this equation in a mathematical modeling of turbulence, therefore it is known as “Burgers’ equation”. This equation arise in different areas of applied mathematics, physics, and engineering, containing gas dynamics, modeling of shock waves, traffic flows, heat conduction, elasticity and continuous stochastic processes, etc [3, 4]. The purpose of the present paper is to present the numerical integration of Burgers’ equation using splitting methods tailored for near-integrable systems.

2 Splitting methods for near-integrable systems

One dimensional Burgers’ equation (1.1) involves small viscosity parameter ν . Thus it is possible to consider splitting methods for near-integrable systems to obtain accurate solutions of the Burgers’ equation. Consider the nonlinear separable PDE of the form

$$\frac{du}{dt} = A(u(t)) + \epsilon B(u(t)), \quad u(0) = u_0, \tag{2.1}$$

$u(x, t) \in \mathbb{R}^D$, where ϵ is small parameter, i.e $|\epsilon| \ll 1$, and the (possibly unbounded) operators A , B and $A + \epsilon B$ are infinitesimal generators of C_0 semi-groups for positive t on a finite or infinite Banach space. For simplicity, the nonlinear equation can be written in the (apparently) linear form

$$\frac{du}{dt} = L_{A(u(t))}u(t) + \epsilon L_{B(u(t))}u(t), \tag{2.2}$$

where L_A, L_B are the Lie operators acting on $u(t)$ of A and B respectively, i.e.

$$L_{A(u(t))} \equiv A(u(t)) \frac{\partial}{\partial u}, \quad L_{B(u(t))} \equiv B(u(t)) \frac{\partial}{\partial u}. \tag{2.3}$$

The key idea behind splitting methods to approximately solve (2.2) is to construct of an approximate solution by concatenating the solutions of the two subproblems

$$\frac{du}{dt} = A(u(t)) \quad \text{and} \quad \frac{du}{dt} = \epsilon B(u(t)). \tag{2.4}$$

On the other hand, one can replace the formal solution of the (2.2), $e^{t(L_A+\epsilon B)}$, by the flow map $\Phi_t^{(L_A+\epsilon B)}$ in the nonlinear case. Now we define the exact h -flows for each problem in (2.4) to be $\Phi_h^{L_A}, \Phi_h^{\epsilon L_B}$ (or $e^{hL_A}, e^{h\epsilon L_B}$) respectively, where h is sufficiently small time step. Approximation at any order can be constructed with arbitrary coefficients in the pattern ABA with $b_{p+1} = 0$

$$\Psi(h) = e^{ha_{p+1}L_A} e^{hb_p\epsilon L_B} \dots e^{ha_2L_A} e^{hb_1\epsilon L_B} e^{ha_1L_A}, \tag{2.5}$$

or pattern BAB with $a_{p+1} = 0$ [5]

$$\Psi(h) = e^{hb_{p+1}\epsilon L_B} e^{ha_pL_A} \dots e^{hb_2\epsilon L_B} e^{ha_1L_A} e^{hb_1\epsilon L_B}. \tag{2.6}$$

On the other hand, if one considers the second order symmetric methods of effective order $(2s, 2)$, then can obtain methods with positive and real coefficients by considering the terms of order h^{2l+1} for $l = 1, 2, \dots, s$ to be zero. These methods are well defined for non-reversible systems such as Burgers' equation and their error is of order $\mathcal{O}(\epsilon h^{2s+1} + \epsilon^2 h^3)$ [6].

2.1 Splitting methods for Burgers' equation

Consider the one-dimensional Burgers' equation (1.1) and split it into sub-problems

$$u_t = -uu_x, \tag{2.7a}$$

$$u_t = \nu u_{xx}. \tag{2.7b}$$

The splitting method for Burgers' equation (1.1) can be applied by concatenating the solutions (exact or numerical) of the separate problems (2.7a) and (2.7b). Let the exact solution (or a sufficiently accurate numerical approximation) of the (2.7a), (2.7b) to be maps $\Phi_h^{L_A}, \Phi_h^{\epsilon L_B}$ respectively. Then, the approximate solutions of (1.1) can be obtained as $u(x, h) = \Psi_h u_0(x)$, where Ψ_h is (2.5)(or 2.6) for sufficiently small h .

2.2 Methods for the Subproblems

We consider the Picard's approximation for the equation (2.7a) and then numerically solve the discretized form of the linearized version of the equation (2.7a) and the linear equation (2.7b) by the Crank-Nicolson finite difference method. Picard's approximation for the equation (2.7a) reads as

$$u_t^{(n+1)} = -(uu_x)^{(n)}, \quad n = 0, 1, 2, \dots, \tag{2.8}$$

where the value of u at the n th iteration defined by $u^{(n)}$ with the initial data $u^{(0)}$. The solution domain $\{(x, t) : x \in [0, 1], t \in [0, \infty)\}$ is discretized into a uniform grid with the grid point (x_m, t_j) where $x_m = m\tau, m = 0, 1, 2, \dots, N, t_j = jk, j = 0, 1, 2, \dots, M, \tau$ is spatial mesh size and k is time step. The exact and numerical values of u at the grid point (x_m, t_j) denoted as $u_{m,j}$ and $U_{m,j}$ respectively. Following [7], Crank-Nicolson finite difference approximation to equation (2.7a) is given by

$$U_{m,j+1}^{(n+1)} - U_{m,j}^{(n_j)} = \frac{-k}{4\tau} [U_{m,j+1}^{(n)} (U_{m+1,j+1}^{(n)} - U_{m-1,j+1}^{(n)}) + U_{m,j}^{(n_j)} (U_{m+1,j}^{(n_j)} - U_{m-1,j}^{(n_j)})], \tag{2.9}$$

where the n_j represents the final number of iteration needed to approximate the value of $U_{m,j}$ by considering following criterion [7]

$$\max_m |U_{m,j}^{(n+1)} - U_{m,j}^{(n)}| \leq 10^{-8}, \quad 1 \leq m \leq N. \tag{2.10}$$

On the other hand, Crank-Nicolson scheme for equation (2.7b) reads

$$aU_{m,j+1} - b(U_{m+1,j+1} + U_{m-1,j+1}) = (a - 4b)U_{m,j} + b(U_{m+1,j} + U_{m-1,j}), \tag{2.11}$$

where $a = \frac{1}{k} + \nu \frac{1}{\tau^2}$ and $b = \nu \frac{1}{2\tau^2}$.

3 Numerical Results

In order to illustrate the efficiency and accuracy of the present methods, we have applied it to a test example whose exact solutions and numerical results available in the literature. Even one uses the unconditionally stable methods, this problem will produce oscillations and nonlinear instabilities for the small viscosity ν . Thus, one should care about these properties. One can reduce the effect of these oscillations and instabilities by using proper filtering procedure. In this work, we have considered the filtering technique presented in [7] which suggest to approximate U_m^j in the nonlinear term as

$$U_{m,j} = \frac{U_{m+1,j} + \gamma U_{m,j} + U_{m-1,j}}{2 + \gamma}, \tag{3.1}$$

where $\gamma = \frac{4\nu - \tau}{\tau - 2\nu}$.

Table 1: Comparison of the approximate solutions with the exact solution of example 1 at different times with $v = 0.01$, $N = 80$ and $k = 0.01$.

x	T	[8]	[9]	[10], $k = 0.0001$	Mc(10,2) [6]	Exact Solution
0.25	0.4	0.34229	0.34267	0.34819	0.34187	0.34191
	0.6	0.26902	0.26908	0.27536	0.26894	0.26896
	1.0	0.18817	0.18806	0.19375	0.18818	0.18819
	3.0	0.07511	0.07505	0.07754	0.07511	0.07511
0.50	0.4	0.66797	0.67588	0.66543	0.66065	0.66071
	0.6	0.53211	0.53678	0.53525	0.52937	0.52942
	1.0	0.37500	0.37671	0.38047	0.37439	0.37442
	3.0	0.15018	0.15022	0.15362	0.15017	0.15018
0.75	0.4	0.93680	0.95424	0.91201	0.91032	0.91026
	0.6	0.77724	0.79252	0.77132	0.76721	0.76724
	1.0	0.55833	0.56535	0.56157	0.55601	0.55605
	3.0	0.22485	0.22528	0.22874	0.22485	0.22481

Example 1 The first problem corresponds the (1.1) on space domain $[0, 1]$ with the initial condition

$$u(x, t = 0) = \sin(\pi x), \tag{3.2}$$

and the following boundary conditions

$$u(x = 0, t) = u(x = 1, t) = 0, \quad t > 0. \tag{3.3}$$

The exact solution of this problem can be obtained by using the Hopf-Cole transformation.

In Table 1 numerical solutions generated by effective order Mc(10, 2) [6] method have been tabulated at different times and compared with results presented in [8, 9] for $v = 0.01$, $h = 0.0125$, $k = 0.01$ and also compared with [10] where the time step taken as $k = 0.001$. In Table 1 the superiority of the effective order Mc(10, 2) method is manifest.

References

- [1] H. Bateman. Some recent researchers on the motion of fluids. *Mon. Weather Rev.*, 43:163–170, 1915.
- [2] J. M. Burger. A mathematical model illustrating the theory of turbulence. *Adv. App. Mech.*, 1:171–199, 1948.
- [3] L. Acedo. On the gravitational instability of a set of random walkers. *Europhys. Lett.*, 73:698–704, 2006.
- [4] A. Franques A. Cordero and J. R. Torregrosa. Numerical solution of turbulence problems by solving burgers' equation. *Algorithms*, 8:224–233, 2015.
- [5] S. Blanes and F. Casas. *A concise introduction to geometric numerical integration*, volume 23. CRC Press, 2016.
- [6] R. I. McLachlan. Composition methods in the presence of small parameters. *BIT*, 35:258–268, 1995.
- [7] L. Iskandar and A. Mohsen. Some numerical experiments on the splitting of burgers' equation. *Numer. Meth. Part. Differ. Equat.*, 8:267–276, 1992.
- [8] M. K. Kadalbajoo and A. Awasthi. A numerical method based on crank-nicolson scheme for burgers' equation. *Appl. Math. Comput.*, 182:1430–1442, 2006.
- [9] L. Verma K. Pandey and A. K. Verma. On a finite difference scheme for burgers' equation. *Appl. Math. Comput.*, 215:2206–2214, 2009.
- [10] A. Esen S. Kutluay and I. Dag. Numerical solutions of the burgers' equation by the least-squares quadratic b-spline finite element method. *J. Comput. Appl. Math.*, 167:21–33, 2004.

Infectious Disease Expansion: a discrete approach to the

Kermack and McKendrick model

Maria Teresa Signes^{1*}, Higinio Mora*, Antonio Cortés**

(*) Departamento de Tecnología Informática y Computación
Universidad de Alicante.

Ctra. San Vicente del Raspeig s/n., Alicante, Spain.

(**) Facultad de Informática
Universidad de Panamá, Panamá

1. Introduction

Mathematical modelling is helpful for prevention and control of emerging infectious diseases. It provides both information to health workers about the vaccination needed to protect a population and help to the public health decision making when new diseases potentially emerge on a large scale, such as Bird flu, measles, malaria, influenza and Ebola over the past few years [1]. After Bernouilli presented the first model for an infectious disease in 1760 [2], Kermack and McKendrick published papers on epidemic models and obtained the threshold that has to be exceeded for an epidemic outbreak can occur [3, 4]. Their model includes three states, the S (susceptible), I (Infectious) and R (Recovered) instead of the two, S and I, of the Bernouilli's model [5]. In the nineties, new paradigms spread out to better understand and model the impact of numerous variables that go beyond the micro host-pathogen level, such as ecological, social, economic, and demographic factors. Multidisciplinary approach is suitable for rapid assessment of urgent pandemic situations. The case of HIV/AIDS is a good example [6-9].

This paper presents a model to approach the dynamics of infectious diseases expansion. The spread of the disease is performed by binary rules that are tailored to model different situations such as Susceptible, Infected, Recovered, with or without capability to infect further. The capability of the rules to perform the expansion depends on the neighbourhood relationship between individuals. Following the introduction, in Section 2 our model is detailed and compared with the Susceptible-Infectious-Recovered (SIR) model solved by ordinary differential equations (ODE). Section 3 promotes a discussion concerning the link between both approaches. Finally, Section 4 presents some concluding remarks.

¹ E-mail: teresa@dtic.ua.es

2. Method

2.1 Our model

Our model is based on both, a concrete connection pattern provided by a particular neighbourhood (4-neighbours or Von Neuman, 8-neighbours or Moore, chess horse jumping) which fixes the possible contacts between individuals, and a local rule which defines whether the contact is infective or not. This rule is implemented by a binary operation to define the results of the contacts between 0 and 1, 1 and 0, 0 and 0, 1 and 1, see [10-12]. Without loss of generality, we consider a two-dimensional square grid where every cell represents a susceptible person (value 0) except the one at the centre, which locates an infected one (value 1). When the infected person contacts with his/her neighbours, he/she can spread the disease. The new infected people have then in turn the capability to infect their neighbours, a time later. When infected people recover from their illness they can no longer infect nor transmit the illness because they immunize. As follows, Figure 1 represents the number of Susceptible, Infected and Recovered people in the case of different neighbourhood patterns, for a 10x10 grid (100 people) and for a concrete binary rule. The chosen rule defines the result of the contacts as follows: (1, 0) = 1; (1, 1) = 1; (0, 1) = 1 and (0, 0) = 0. The first and second conditions depict the contagion mode triggered by the value 1 (in bold), which changes 0 to 1 and has no effect on 1. The third and fourth conditions mean the value 0 (in bold) has no effect on 0 nor 1. Obviously, $2^4=16$ different rules can be defined.

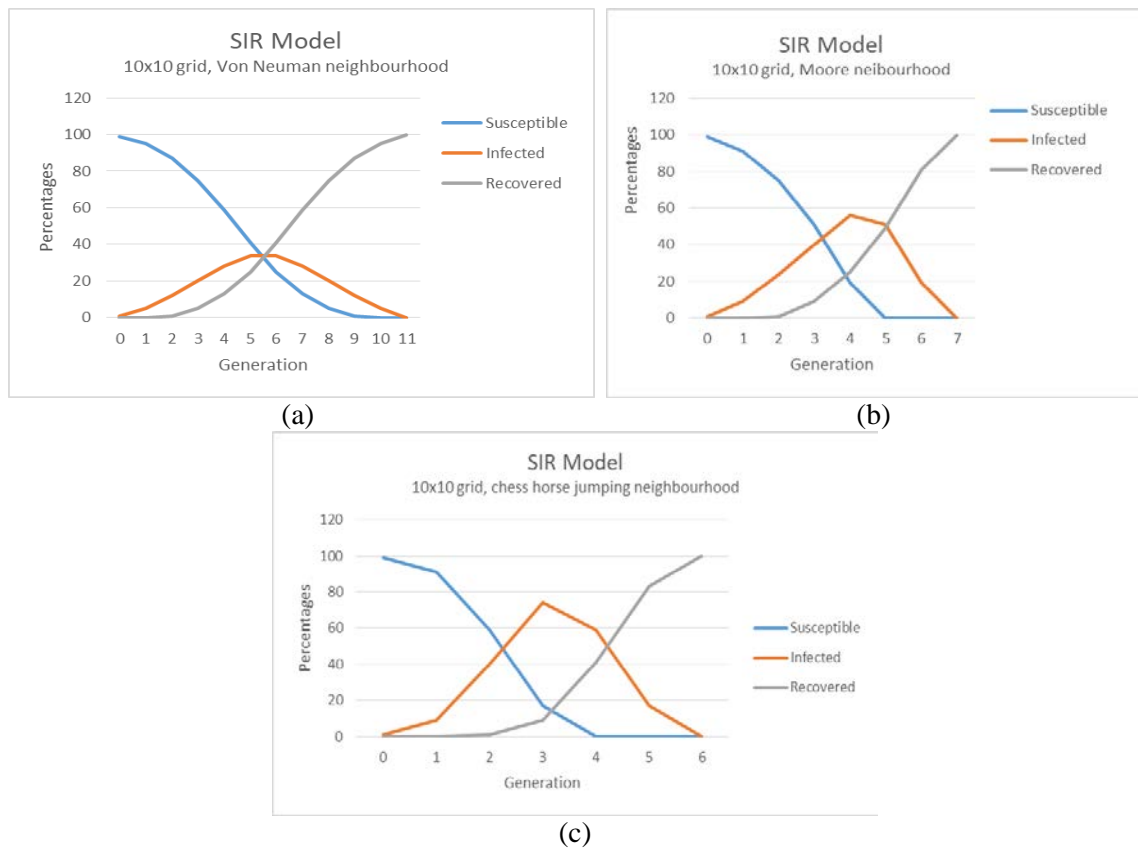


Figure 1. Simulation of our SIR model for different neighbourhood patterns.

Figure 1 represents the simulation of our SIR model for three different neighbourhoods. Horizontal axis stands for the time (generations), vertical axis stands for the number of individuals (percentages, here equivalent to the number of individuals). We observe a symmetric evolution of S and I. The plotting presents a crossing point for S and R at the same time as a maximum value for I occurs. In this experiment we have fixed the disease duration in two generations, but it can be variable depending of the concrete disease we have to model.

2.2 The deterministic SIR model

The Kermack-McKendrick or SIR model concerns a number of people infected with a contagious illness in a closed population over time. The model assumes that the population size, N , is fixed (i.e., no births, deaths due to disease, nor deaths by natural causes) and incubation period of the infectious agent is instantaneous. The population is divided into three health states: Susceptible, Infected and Recovered. The SIR model provides immunity, so recovered people are no more able to infect nor transmit the disease. The model is depicted by a system of ODE shown in (1). Although the system has no analytical solution, in practice it can numerically be solved (Euler, Runge-Kutta). The rate at which susceptible hosts become infected is a product of the number of contacts each host has per unit time, r , and the probability of transmission of infection per contact, β . The recovery rate is γ (or, in other words, the mean infective period is $1/\gamma$). The total population size is $N = S + I + R$. Figure 2 represents a generic simulation of the SIR model equations. Horizontal axis stands for the time, vertical axis stands for the number of individuals.

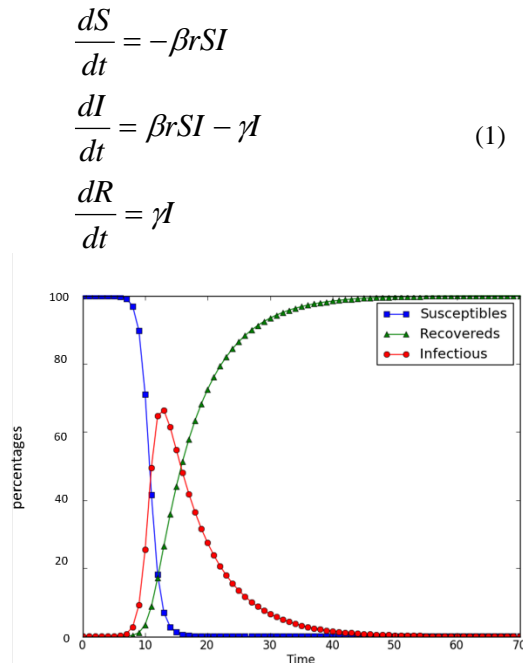


Figure 2. The generic deterministic SIR model simulation (Wikipedia)

3. Discussion

Our model establishes a link between traditional simulation of the Susceptible-Infectious-Recovered (SIR) model of disease expansion based on ODE, and a very simple approach, based on both connectivity between people and elementary binary rules that define the result of these

contacts. Our model identifies the connectivity pattern (neighbourhood + rule), with the parameter βr (number of effective infections per time unit), and the delay (generations between contagion and healing) with the parameter $1/\gamma$. We have assumed “time = generation” in order to allow flexibility for parameter fitting in real cases. We have also set $10 \times 10 = 100$ people in the grid to obtain the percentages of Susceptible, Infectious and Recovered people for an easier comparison between different study cases. We observe some similarities between our graphics in Figure 1 and the generic simulation in Figure 2. In Table 1 we analyse the main results provided by the different models.

Model	Time / gener. for equilibrium in Susceptible	Time /gener. for equilibrium in Recovered	Time /gener. for crossing point between S and R	(Time; height) or (Gener.; height) for the peak of Infected
ODE (Figure 2)	15	40	13	(13; 65)
V.N. neighbourhood Figure 1 (a)	9	11	5,5	(5,5; 32)
M. neighbourhood Figure 1 (b)	7	7	4	(4; 55)
H.J. neighbourhood Figure 1 (c)	4	6	3	(3;75)

Table 1. Comparison between the results provided by the different models.

Table 1 shows the timing for equilibrium in Susceptible and Recovered, and for crossing point between Susceptible and Recovered (the timing is estimated in generations in our model). The fourth column shows the coordinates of the peak of Infected in all the cases. It appears that in ODE simulation, the time for equilibrium in Susceptible (15) and for crossing (13) is very similar, and the time for equilibrium in Recovered is about three times greater and the peak of Infected reaches 65% of the population. On the contrary, in our model, we observe less similarity between time for equilibrium in Susceptible and crossing, as well as more similarity between time for equilibrium for Susceptible and Recovered. The peak of Infected has a variable height depending on the considered neighbourhood.

A more careful study based on real cases is crucial to succeed in an accurate approximation, just as we do when simulating with the traditional ODE model. The Susceptible-Infectious (SI) deterministic compartmental model and the Susceptible-Infectious-Susceptible (SIS) model have already been analysed and successfully modelled by our method in the case of different connectivity patterns [11, 12].

4. Conclusions

Our proposal presents an alternative to the ODE conventional approach of the SIR model for infectious disease expansion. The method is based on both a connectivity pattern, which determines the possible contacts between people, and a local rule, which defines whether the contacts are

infective or not. We have considered three connectivity patterns (4-neighbours or Von Neumann, 8-neighbours or Moore, chess horse jumping) and a concrete rule among 16 different possible rules.

References

- [1] Bailey NJT. *The Mathematical Theory of Infectious Diseases and its Application*. Griffin, London, 1957.
- [2] Siettos, C.I. & Russo, L. Mathematical modeling of infectious disease dynamics Virulence (2013) May 15; 4(4): 295–306.
- [3] Kermack, W.O & McKendrick, A.G. A contribution to the mathematical theory of epidemics, *Proc. R. Soc. Lond.* 115 (1927), 700-721.
- [4] Isea, R & Lonngren, K.E. On the Mathematical Interpretation of Epidemics by Kermack and McKendrick. *Gen. Math. Notes*, Vol. 19, No. 2, December 2013, pp. 83-87.
- [5] Van den Driessche, P. *Deterministic Compartmental Models: Extension of Basic Models*. Lecture Notes in Mathematics, Mathematical Epidemiology, Springer, 2008.
- [6] Culshaw, R.V. *Mathematical Modeling of AIDS Progression: Limitations, Expectations, and Future Directions*. Ph.D. *Journal of American Physicians and Surgeons*, Vol 11, N°4, Winter 2006.
- [7] Marshall, Brandon D. L. et al. A Complex Systems Approach to Evaluate HIV Prevention in Metropolitan Areas: Preliminary Implications for Combination Intervention Strategies. *PLOS ONE*, Vol.7, (9), 2012.
- [8] Naresh, R. et al. Modelling and analysis of the spread of AIDS epidemic with immigration of HIV infectives. *Mathematical and Computer Modelling*, Vol. 49, Issues 5–6, March 2009, pp. 880–892.
- [9] Cassels, S. & Goodreau, S.M. Interaction of mathematical modeling and social and behavioral HIV/AIDS research. *Curr Opin HIV AIDS*. 2011 Mar; 6(2): 119–123.
- [10] Signes Pont, M.T. et al. A Computational Approach of the French Flag Model to Connect Growth and Specification in Developmental Biology, *Cognitive Computation*, September 2016.
- [11] Signes Pont, M.T. et al. The Susceptible-Infectious Model of disease expansion analysed under the scope of connectivity and neighbour rules. *Proceedings of the CSITA conference, Computer Science & Information Technology (CS & IT) 7 (1): 1-10 (January 2017)*.
- [12] Signes Pont, M.T. et al. A discrete approach of the Susceptible-Infectious-Susceptible (SIS) Model of Disease Expansion. *International Journal of Computers*, Volume 2, 2017.

On Legendre Transformation for Hamiltonian Systems Corresponding to Second Order Lagrangians

D. Smetanová^b *

(b) Institute of Technology and Business,

Department of Informatics and Natural Sciences, Okružní 10, České Budějovice, Czech Republic.

November 30, 2017

1 Introduction

The work is devoted to an extension of classical Hamilton-Cartan variational theory on fibered manifolds to the case of class second order Lagrangians. The aim of this paper is to announce some recent results in case of second order Lagrangians corresponding to 2nd and 3rd Euler-Lagrange form. We are interested in second order Lagrangians which give rise to Euler-Lagrange equations of the 3rd order or non-affine 2nd order. All these Lagrangians are singular in the standard Hamilton-De Donder theory and do not have Legendre transformation. For such Lagrangian we find appropriate set of Legendre equivalents (resp. family of Hamilton equations) which admit a generalized Legendre transformation. We note that the generalized momenta p_{ij}^σ satisfy $p_{ij}^\sigma \neq p_{ji}^\sigma$. The generalized Legendre transformation and its properties are illustrated on examples. We consider Hamiltonian systems for concrete above mentioned Lagrangians.

Throughout the paper all manifolds and mappings are smooth and summation convention is used. We consider a fibered manifold (i.e., surjective submersion) $\pi : Y \rightarrow X$, $\dim X = n$, $\dim Y = n + m$, its r -jet prolongation

*e-mail: smetanova@mail.vstecb.cz

$\pi_r : J^r Y \rightarrow X$, $r \geq 1$ and canonical jet projections $\pi_{r,k} : J^r Y \rightarrow J^k Y$, $0 \leq k \leq r$ (with an obvious notations $J^0 Y = Y$). A fibered char on Y (resp. associated fibered chart on $J^r Y$) is denoted by (V, ψ) , $\psi = (x^i, y^\sigma)$ (resp. (V_r, ψ_r) , $\psi_r = (x^i, y^\sigma, y_i^\sigma, \dots, y_{i_1 \dots i_r}^\sigma)$).

A vector field ξ on $J^r Y$ is called π_r -vertical (resp. $\pi_{r,k}$ -vertical) if it projects onto the zero vector field on X (resp. on $J^k Y$).

Recall that every q -form η on $J^r Y$ admits a unique (canonical) decomposition into a sum of q -forms on $J^{r+1} Y$ as follows [4]:

$$\pi_{r+1,r}^* \eta = h\eta + \sum_{k=1}^q p_k \eta,$$

where $h\eta$ is a horizontal form, called the *horizontal part of η* , and $p_k \eta$, $1 \leq k \leq q$, is a *k-contact part of η* .

We use the following notations:

$$\omega_0 = dx^1 \wedge dx^2 \wedge \dots \wedge dx^n, \quad \omega_i = i_{\partial/\partial x^i} \omega_0, \quad \omega_{ij} = i_{\partial/\partial x^j} \omega_i,$$

and

$$\omega^\sigma = dy^\sigma - y_j^\sigma dx^j, \quad \dots, \quad \omega_{i_1 i_2 \dots i_k}^\sigma = dy_{i_1 i_2 \dots i_k}^\sigma - y_{i_1 i_2 \dots i_k j}^\sigma dx^j$$

For more details on fibered manifolds and the corresponding geometric stuctures we refer e.g. to [9].

2 Hamiltonian systems of 3rd order.

In general, a second order Lagrangian gives rise to an Euler–Lagrange form on $J^4 Y$. We shall consider second order Lagrangians λ which satisfy one of the following conditions

1) The corresponding Euler–Lagrange form is of order 3, i.e. the Lagrangians satisfy the conditions

$$\left(\frac{\partial^2 L}{\partial y_{ij}^\sigma \partial y_{kl}^\nu} \right)_{Sym(ijkl)} = 0, \tag{1}$$

where $Sym(ijkl)$ means symmetrization in the indicated indices,

2) The Euler–Lagrange expressions λ of are of the second order, “non-affine” in the second derivatives

$$\frac{\partial^2 E_\sigma}{\partial y_{kl}^\nu \partial y_{ij}^\kappa} \neq 0. \tag{2}$$

In what follows, we shall study Hamiltonian systems corresponding to a special choice of a Lepagean equivalent of such Lagrangians, namely, α of order 3, $\alpha = d\rho$, where

$$\begin{aligned} \rho = & L\omega_0 + \left(\frac{\partial L}{\partial y_j^\sigma} - d_k \frac{\partial L}{\partial y_{jk}^\sigma} \right) \omega^\sigma \wedge \omega_j + \frac{\partial L}{\partial y_{ij}^\sigma} \omega_i^\sigma \wedge \omega_j + \bar{\mu} \\ & + a_{\sigma\nu}^{ij} \omega^\sigma \wedge \omega^\nu \wedge \omega_{ij} + b_{\sigma\nu}^{kij} \omega^\sigma \wedge \omega_k^\nu \wedge \omega_{ij} \\ & + c_{\sigma\nu}^{klj} \omega^\sigma \wedge \omega_{kl}^\nu \wedge \omega_{ij}, \end{aligned} \tag{3}$$

with an arbitrary at least 3-contact n -form $\bar{\mu}$ and functions $a_{\sigma\nu}^{ij}$, $b_{\sigma\nu}^{kij}$, $c_{\sigma\nu}^{klj}$ dependent on variables x^k , y^κ , y_k^κ , y_{kl}^κ and satisfying the conditions

$$\begin{aligned} a_{\sigma\nu}^{ij} &= -a_{\sigma\nu}^{ji}, \quad a_{\sigma\nu}^{ij} = -a_{\nu\sigma}^{ij}; \quad b_{\sigma\nu}^{kij} = -b_{\sigma\nu}^{kji}; \\ c_{\sigma\nu}^{klj} &= c_{\sigma\nu}^{lkj}, \quad c_{\sigma\nu}^{klj} = -c_{\sigma\nu}^{klji}. \end{aligned} \tag{4}$$

Proposition *Let $\dim X \geq 2$. Let $\lambda = L\omega_0$ be a second order Lagrangian with the Euler–Lagrange form (1) or (2), and $\alpha = d\rho$ with ρ of the form (3), (4), be its Lepagean equivalent. Assume that the matrix*

$$P_{\sigma\nu}^{ijkl} = \left(\frac{\partial^2 L}{\partial y_{ij}^\nu \partial y_{kl}^\sigma} + 2 c_{\nu\sigma}^{klj} \right)_{Sym(jkl)}, \tag{5}$$

with mn^3 rows (resp. mn columns) labelled by σjkl (resp. νi) has maximal rank equal to mn and matrix

$$Q_{\sigma\nu}^{ijkl} = \left(\frac{\partial^2 L}{\partial y_{ij}^\sigma \partial y_{kl}^\nu} - 2c_{\sigma\nu}^{klj} \right), \tag{6}$$

with mn^2 rows (resp. mn^2 columns) labelled by σij (resp. νkl) has maximal rank equal to $mn(n+1)/2$. Then the Hamiltonian system $\alpha = d\rho$ is regular (i.e. every Dedecker–Hamilton extremal is of the form $\pi_{3,2} \circ \delta_D = J^2\gamma$, where γ is an extremal of λ).

If moreover $\bar{\mu}$ is closed then the Hamiltonian system $\alpha = d\rho$ is strongly regular (i.e. every Hamilton extremal is of the form $\pi_{3,2} \circ \delta = J^2\gamma$, where γ is an extremal of λ).

The Hamiltonian systems admitting Legendre transformation are studied. By the Legendre transformation we understand the coordinates transformation onto J^3Y .

Writing the Lepagean equivalent ρ (3), (4) in the form of a noninvariant decomposition we get

$$\begin{aligned} \rho &= -H\omega_0 + p_\sigma^j dy^\sigma \wedge \omega_j + p_\sigma^{ij} dy_i^\sigma \wedge \omega_j + 2c_{\sigma\nu}^{klj} y_j^\sigma dy_{kl}^\nu \wedge \omega_i \\ &+ a_{\sigma\nu}^{ij} dy^\sigma \wedge dy^\nu \wedge \omega_{ij} + b_{\sigma\nu}^{kij} dy^\sigma \wedge dy_k^\nu \wedge \omega_{ij} \\ &+ c_{\sigma\nu}^{klj} dy^\sigma \wedge dy_{kl}^\nu \wedge \omega_{ij} + \bar{\mu}, \end{aligned} \quad (7)$$

where

$$\begin{aligned} H &= -L + \left(\frac{\partial L}{\partial y_i^\sigma} - d_j \frac{\partial L}{\partial y_{ij}^\sigma} \right) y_i^\sigma + \frac{\partial L}{\partial y_{ij}^\sigma} y_{ij}^\sigma - 2a_{\sigma\nu}^{ij} y_i^\sigma y_j^\nu \\ &- 2(b_{\sigma\nu}^{kij})_{Sym(ki)} y_i^\sigma y_{kj}^\nu - 2(c_{\sigma\nu}^{klj})_{Sym(klj)} y_i^\sigma y_{klj}^\nu, \\ p_\sigma^j &= \frac{\partial L}{\partial y_j^\sigma} - d_i \frac{\partial L}{\partial y_{ij}^\sigma} + 4a_{\sigma\nu}^{ij} y_i^\nu + 2(b_{\sigma\nu}^{kij})_{Sym(ki)} y_{ki}^\nu + 2(c_{\sigma\nu}^{klj})_{Sym(kli)} y_{kli}^\nu, \\ p_\sigma^{ij} &= \frac{\partial L}{\partial y_{ij}^\sigma} + 2b_{\nu\sigma}^{ijk} y_k^\nu. \end{aligned} \quad (8)$$

If moreover the matrix

$$\begin{pmatrix} \frac{\partial p_\sigma^i}{\partial y_{kl}^\nu} & \frac{\partial p_\sigma^i}{\partial y_{klm}^\nu} \\ \frac{\partial p_\sigma^{ij}}{\partial y_{kl}^\nu} & \frac{\partial p_\sigma^{ij}}{\partial y_{klm}^\nu} \end{pmatrix}, \quad (9)$$

has maximal rank then

$$(x^i, y^\sigma, y_i^\sigma, p_\sigma^i, p_\sigma^{ij})$$

is part of coordinate system.

3 Conclusion

A regularization (by different methods) of some interesting singular physical fields (the Dirac field, the Electromagnetic field and Scalar Curvature

Lagrangians) has been studied in [2], [3] and [5], some second order Lagrangians have been discussed also in [8]. The multisymplectic approach has been proposed in [1], [7] and [11].

Note that an alternative approach to the study of “degenerated” Lagrangians (singular in standard sense) is the constraint theory in mechanics (see [10]) and in the field (c.f. [6]).

In the paper [8] properties (e.g., regularity, Legendre transformation) of Hamilton p_2 -equations for second order Lagrangian affine in second derivatives are studied. The Hamilton p_2 -equations for second order Lagrangian are created from Lepagean equivalents whose order of contactness is maximal 2.

This paper is generalization of the paper [8] to Hamilton equations whose arise from Lepagean equivalent more than 2-contact. The case of second order Lagrangians affine in second derivatives is generalized to case of Lagrangians satisfying the conditions (1) and (2).

References

- [1] Cantrijn, F., Ibort, A., De León, M. On the geometry of multisymplectic manifolds *Journal of the Australian Mathematical Society*, Volume 66 (3): 303–330, 1999.
- [2] Dedecker, P. On the generalization of symplectic geometry to multiple integrals in the calculus of variations, *Lecture Notes in Math. 570* (Springer, Berlin) 395–456, 1977.
- [3] Hořava, P. On a covariant Hamilton-Jacobi framework for the Einstein-Maxwell theory, *Classical and Quantum Gravity*, Volume 8(11): 2069–2084, 1991.
- [4] D. Krupka, Some geometric aspects of variational problems in fibered manifolds, *Folia Fac. Sci. Nat. UJEP Brunensis*, Volume (14): 1–65, 1973.
- [5] Krupková, O., Smetanová, D. Legendre transformation for regularizable Lagrangians in field theory, *Letters in Math. Phys.* Volume (58): 189–204, 2001.

- [6] Krupková, O., Volný, P. Euler-Lagrange and Hamilton equations for non-holonomic systems in field theory, *Journal of Physics A: Mathematical and General* Volume 40(7): 8715–8745, 2005.
- [7] Prieto - Martínez, P.D., Román - Roy, N. A new multisymplectic unified formalism for second order classical field theories, *Journal of Geometric Mechanics*, Volume 7(2): 203–253, 2015.
- [8] Smetanová, D. On Hamilton p_2 -equations in second-order field theory, in: *Steps in Differential Geometry, Proc. of the Coll. on Diff. Geom., Debrecen 2000* (University of Debrecen, Debrecen, 2001), 329–341, 2001.
- [9] D. J. Saunders, *The Geometry of Jets Bundles*, Cambridge University Press, Cambridge, 1989.
- [10] Swaczyna, M., Volný, P. Uniform motions in central fields, *Journal of Geometric Mechanics*, Volume 9(1): 91 - 130, 2017.
- [11] Vey, D. Multisymplectic formulation of vielbein gravity: I. De Donder-Weyl formulation, Hamiltonian (n - 1)-forms . *Classical and Quantum Gravity*, Volume 32 (9): 50 pp., 2015.

Using Integer Linear Programming to study the relationship between the main variables involved in the construction of an external wall

Andrea Salandin*, David Soler^{1**}, Joan C. Micó**

(*) Centro de Tecnologías Físicas,
Universitat Politècnica de València, Camí de Vera s/n 46022, València, Spain

(**) Instituto Universitario de Matemática Multidisciplinar,
Universitat Politècnica de València, Camí de Vera s/n 46022, València, Spain

1. Introduction

Linear Programming, and particularly its cases with all integer variables (ILP) and with both integer and continuous variables, are increasingly applied in the field of energy and buildings to solve optimization problems, mainly to improve the energy efficiency of a building [1-4].

Thermal transmittance U ($Wm^{-2}K^{-1}$) ([5]) is a key magnitude to assess the energy efficiency of a building, and measures the rate of heat flow through the elements of the building envelope [5]. The external wall is one of the most relevant parts of this envelope, and its thermal transmittance must abide by the current legislation [6] depending on the climate zone.

After an exhaustive research, we realized that there is no work in the scientific literature relating the thermal transmittance of an external wall to be built, from the constructor's or designer's point of view, beyond the standards of the legal regulations. The aim of this paper is to present an ILP approach that takes into account some restrictions involved in the building process of a wall: current legislation with respect to thermal transmittance, budget, total thickness of the wall, number of layers, availability of materials and thicknesses for the different layers, workforce, time limits, final cost, etc. Among thousands of combinations of materials and thicknesses for the different layers of the wall, the aim of this paper is to choose the best one to optimize one of the involved variables without violating any restriction to be taken into account by the construction company. In particular, in this paper we deal with the problem of minimizing the thermal transmittance of the wall, but other variables, like cost or thickness, can be optimized in a similar way. This magnitude has been chosen due to the fact that the housing stock represents 24.8% of the final energy consumption in the EU [7] and due to an increased demand of a more sustainable and healthy indoor environment that helps reducing the carbon footprint.

¹ E-mail: dsoler@mat.upv.es

Nomenclature

n	Number of layers of the wall
s	Total surface in m^2 of the wall
m	Number of different materials
h_{int}	Standard internal conductivity
h_{ext}	Standard external conductivity
w_j	Number of different thicknesses for material j
e_{jk}	Thickness corresponding to material j with type of thickness k
c_{ijk}	Cost of placing in layer i $1m^2$ of material j with type of thickness k
t_{ijk}	Time of placing in layer i $1m^2$ of material j with type of thickness k
e_{min}	Lower bound for the thickness of the wall
e_{max}	Upper bound for the thickness of the wall
s_{max}^{jk}	Maximum number of m^2 available of material j with thickness of type k
b_{max}^{jk}	Maximum budget for the installation of the material j with thickness of type k
t_{max}	Maximum time required to construct the wall
b_{max}	Maximum budget to construct the wall
U	Thermal transmittance
U_{max}	Maximum thermal transmittance allowed for the wall
λ_j	Thermal conductivity corresponding to material j

2. Definition of the ILP problem

Taking into account the nomenclature given above, the variables of the ILP problem are x_{ijk} , whose values are 1 if layer i is made with material j and thickness k , or 0 otherwise, $i \in \{1, \dots, n\}$, $j \in \{1, \dots, m\}$, $k \in \{1, \dots, w_j\}$. It is important to stress that k does not indicate the measure of the thickness but the type of thickness. Note also that layers will be enumerated from outside to inside.

The thermal transmittance of the wall, as described in [5], is therefore given by Eq. (1):

$$U = \frac{1}{\frac{1}{h_{int}} + \sum_{i=1}^n \sum_{j=1}^m \sum_{k=1}^{w_j} \frac{e_{jk}}{\lambda_j} x_{ijk} + \frac{1}{h_{ext}}} \quad (1)$$

Since U is not a linear function of variables x_{ijk} , it cannot be the objective function of the ILP problem. However, h_{int} , h_{ext} , e_{jk} and λ_j are constant for all the involved subscripts, and minimizing U is equivalent to maximizing the triple summation given in the denominator of U , which is certainly a linear function of binary variables x_{ijk} . Therefore, our ILP problem will maximize this triple summation. The restriction set of the ILP problem is open, in the sense that the set of restrictions presented represents the most usual conditions imposed to a constructor to build an external wall. But this set can be expanded, reduced or modified, according to the particular conditions or interest of each building in construction or refurbishment, to adjust as much as possible the mathematical model to the real problem.

The ILP formulation of the problem studied here is given through Eqs. 2 to 12:

$$\text{Maximize } \sum_{i=1}^n \sum_{j=1}^m \sum_{k=1}^{w_j} \frac{e_{jk}}{\lambda_j} x_{ijk} \quad (2)$$

s.t.:

$$\sum_{i=1}^n \sum_{j=1}^m \sum_{k=1}^{w_j} \frac{e_{jk}}{\lambda_j} x_{ijk} \geq \frac{1}{U_{max}} - \frac{1}{h_{int}} - \frac{1}{h_{ext}} \quad (3)$$

$$e_{min} \leq \sum_{i=1}^n \sum_{j=1}^m \sum_{k=1}^{w_j} e_{jk} x_{ijk} \leq e_{max} \quad (4)$$

$$\sum_{i=1}^n \sum_{j=1}^m \sum_{k=1}^{w_j} c_{ijk} x_{ijk} \leq b_{max} \quad (5)$$

$$\sum_{j=1}^m \sum_{k=1}^{w_j} x_{ijk} = 1 \quad \forall i \in \{1, \dots, n\} \quad (6)$$

$$\sum_{i=1}^n \sum_{j=1}^m \sum_{k=1}^{w_j} st_{ijk} x_{ijk} \leq t_{max} \quad (7)$$

$$\sum_{i=1}^n sx_{ijk} \leq s_{max}^{jk} \quad \forall j \in \{1, \dots, m\}, k \in \{1, \dots, w_j\} \quad (8)$$

$$\sum_{i=1}^n sc_{ijk} x_{ijk} \leq b_{max}^{jk} \quad \forall j \in \{1, \dots, m\}, k \in \{1, \dots, w_j\} \quad (9)$$

$$x_{ijk} = 0 \quad \forall ijk - \text{incompatible} \quad (10)$$

$$x_{ijk} + x_{(i+1)j'k'} \leq 1 \quad \forall (ijk - (i+1)j'k') - \text{incompatible} \quad (11)$$

$$x_{ijk} \in \{0, 1\} \quad \forall i \in \{1, \dots, n\}, j \in \{1, \dots, m\}, k \in \{1, \dots, w_j\} \quad (12)$$

In this formulation:

- Eq. (3) ensures that the obtained thermal transmittance meets the legal upper bound U_{max} according to the climate zone.
- Eq. (4) guarantees that the total thickness of the wall belongs to the interval $[e_{min}, e_{max}]$.
- Eq. (5) forbids that the cost per m^2 of the wall exceeds the budgeted cost b_{max} .
- Eq. (6) guarantees that each layer is composed by exactly one material with a specific thickness.
- Eq. (7) forbids to exceed the established time limit t_{max} to build a m^2 of the wall.
- Eq. (8) takes into account the available quantity of each material with its respective thicknesses.
- Eq. (9) forbids to spend more money than budgeted for each material and thickness.
- Eq. (10) forbids to place a given material j with a given thickness k in a given layer i (this fact is denoted by “ ijk -incompatibility”). For instance, it does not make sense to put a waterproof extruded face brick in an intermediate layer. But even if some options make sense, the conditions imposed on the constructor may forbid these options.
- Eq. (11) forbids to place a material j' with thickness k' in the next layer to the one (layer i) containing the material j with thickness k (this fact is denoted by $(ijk - (i+1)j'k')$ -incompatibility). Therefore, at most one of the two materials with the given thickness will appear in the corresponding layer. For instance, it does not make sense to put solid concrete block as a layer, with the next layer (to the interior) made by pressed face brick.

- Eq. (12) defines variables x_{ijk} as binary.

3. Case study and best achieved solution

Our case study consists on a façade of 6 layers. This façade is a common but representative constructive solution for an external wall. Its composition is described in Table 1.

Table 1. Composition of the layer of the case study

Layer	Function	Material	Thickness	Fixing solution
Layer 1	External coating	2 plaster types, plates, absence.	Up to 4 thicknesses	
Layer 2	External panel	Solid brick, concrete block, face brick, 2 pressed face brick	Depending on the dimension of the brick or block	
Layer 3	Air chamber	Light ventilated, not ventilated, absence	3 thicknesses	
Layer 4	Thermal insulation	Cork Mineral wool Extruded polystyrene Expanded polystyrene Wood chips Sandwich panel	Up to 6 thicknesses	3 fixing methods
Layer 5	Internal panel	Solid brick Air brick perforated brick	Depending on the dimension of the brick	
Layer 6	Internal coating	Plaster	Up to 4 thicknesses	

In all cases costs are taken from the cost generator website of CYPE Ingenieros [8]. Costs always include materials, staff and site facilities. With these options, a total amount of 671,328 combinations for this external wall are possible. Furthermore, the recommended thermal resistance for the air layers close to the external and internal surfaces are: $1/h_{ext} = 0,04 \text{ m}^2\text{KW}^{-1}$ and $1/h_{int} = 0,13 \text{ m}^2\text{KW}^{-1}$ as indicated in the Spanish Technical Act (CTE), Basic Document of Energy Saving (DB_HE) [6].

We have considered that the total thickness of the wall can vary between 0.24 and 0.69 m in intervals of 1 cm. We have also considered a budget to construct 1 m^2 of wall limited to an amount ranging between €85 and €190, with intervals of €5. The aim is to find the lowest thermal transmittance wall for each combination of wall thickness and budget. As there are 45 intervals of 1 cm and 22 budgets, 990 ILP problems have been solved using *Mathematica* 10.4 [9].

As expected trend, given a fixed thickness, the thermal transmittance decreases as the budget increases. Another expected trend is that given a budget, the thermal transmittance also decreases as the thickness increases, but once a certain thickness is exceeded, the problem becomes impossible.

The lowest possible U value for an external wall is $0.2035 \text{ Wm}^{-2}\text{K}^{-1}$, which is achieved for a cost of 166.89 €/m^2 and a thickness of 0.664m . Note that this U value is very small and therefore is useful for every climate zone. Figure 1 represents the best solution.

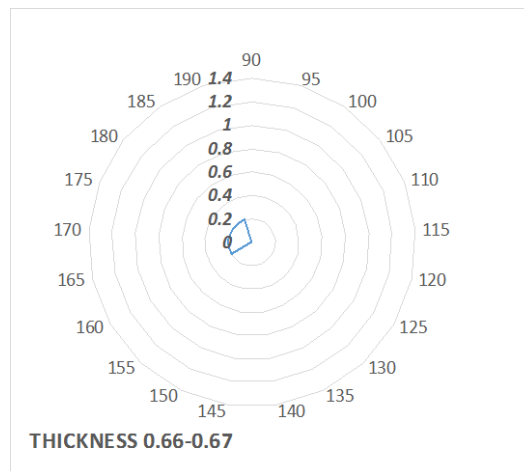


Figure 1. Lowest U vs Thickness and cost.

References

- [1] G. Privitera, A.R. Dayb, G. Dhesic, D. Long, Optimising the installation costs of renewable energy technologies in buildings: A Linear Programming approach, *Energy Build.* 43 (2011) 838-843.
- [2] A. Ashouri, S.S. Fux, M.J. Benz, L. Guzzella, Optimal design and operation of building services using mixed-integer linear programming techniques, *Energy* 59 (2013) 365-376.
- [3] K.B. Lindberg, G. Doorman, D. Fischerc, M. Korpås, A. Ånestad, I. Sartori, Methodology for optimal energy system design of Zero Energy Buildings using mixed-integer linear programming, *Energy Build.* 127 (2016) 194-205.
- [4] A.S.O. Ogunjuyigbe, T.R. Ayodele, O.E. Oladimeji, Management of loads in residential buildings installed with PV system under intermittent solar irradiation using mixed integer linear programming, *Energy Build.* 130 (2016) 253-271.
- [5] R. McMullan, *Environmental Science in Building*, Ed. Palgrave Macmillan, Basingtoke, 2012.
- [6] CTE. Código Técnico de la Edificación (Spanish Technical Building Act). Documento Básico de Ahorro de Energía (Basic Document for Energy Saving). Version of 2013 with comments of 2016. <http://www.codigotecnico.org/images/stories/pdf/ahorroEnergia/DccHE.pdf> (2017).
- [7] EUROSTAT, Consumption of energy, http://ec.europa.eu/eurostat/statistics-explained/index.php/Consumption_of_energy (2017).
- [8] Generador de precios de la construcción. España. CYPE Ingenieros, S.A., <http://www.generadordeprecios.info> (2017)
- [9] Wolfram, Mathematica, <http://www.wolfram.com/mathematica> (2017).

Metamaterial Acoustics on the (2+1)D Schwarzschild Plane

Michael M. Tung^{b*} and Ewa B. Weinmüller[†]

(^b) Instituto de Matemática Multidisciplinar,

Universitat Politècnica de València,

Camino de Vera, s/n, 46022 Valencia, Spain,

([†]) Institute for Analysis and Scientific Computing,

Vienna University of Technology,

Wiedner Hauptstrasse 8–10/1152, 1040 Wien, Austria.

November 30, 2017

1 Introduction

Metamaterials are artificially manufactured materials which by far surpass the properties of conventional materials found in nature. With their help researchers and engineers alike are presented with unique possibilities for the development of novel artificial devices with extraordinary characteristics. This does not merely entail a simple and gradual improvement of devices with already known features, but involves a paradigm shift, *e.g.* with optical metamaterials it has become possible to construct devices with negative refractive index [1]—a concept which was traditionally regarded as impossible, although already hypothesized in the late 1960's [2].

For almost two decades researchers now have focussed on optical metamaterials, whereas the manipulation of sound waves via acoustic metamaterials only recently has come under their spotlight [3–6]. Acoustic metamaterials allow to model sophisticated acoustic phenomena with curved background

*e-mail: mtung@imm.upv.es

spacetimes and make predictions for future laboratory experiments. Apart from the interesting technical applications, these models may also help to settle fundamental questions with far-reaching impact.

One of the first—and remarkably simple—solutions of Einstein’s equations for the curved spacetime of the gravitational field with underlying static and spherical symmetry is the Schwarzschild solution [7]. In the beginning considered to be a mathematical curiosity and only of academic interest, it has now in the age of high-precision GPS navigation and black-hole astronomy become the center stage of many practical and important applications.

In order to implement 2D artificial black holes for acoustic waves, several experimental and theoretical pathways have been studied and proposed in the literature [8–11]. In the present work, we employ a different approach to model acoustic wave propagation on a curved spacetime, which is based on a variational principle within the powerful framework of differential geometry [12–14].

The Schwarzschild geometry is both a mathematically and physically intriguing non-euclidean geometry and as such a fascinating candidate for the implementation and study of an acoustic metamaterial. In general, for the $(n + 1)$ D case, it represents a modification of flat Minkowski spacetime which imposes full spherical symmetry for the n -dimensional spatial part.

First, we will briefly review the field formulation of acoustics and its variational principle. Then, before beginning the discussion on the modelling of acoustic wave propagation on the Schwarzschild plane, we examine the feasibility of Schwarzschild-type geometries in $(2+1)$ spacetime dimensions. Next, we outline how to derive within this framework the partial differential equation for the acoustic potential which simulates wave propagation on the Schwarzschild plane. Finally, we will comment on the design and implementation of such a spacetime with acoustic metadevices. Employing the constitutive equations [12] will enable us to connect the Schwarzschild geometry with the acoustic parameters of the model.

2 Field formulation of acoustics and variational principle

This outline on the field formulation of acoustics and its variational principle closely follows Refs. [12, 14]. The importance of variational principles in

classical and field mechanics, including optics and electrodynamics, lies in defining concisely and in a coordinate-independent manner the fundamental laws which they describe, *i.e.* they remain invariant with respect to arbitrary transformations of the coordinates. The equations of motion that fully determine the physical behaviour of the system correspond to the extremal solutions of the action integral \mathcal{A} for a given scalar Lagrange function \mathcal{L} . This Lagrangian approach allows to easily reveal the underlying symmetries and conservation laws of the theoretical model via Noether's theorem. Furthermore, physical laws will have their equivalent in equations of motion with self-adjoint differential operators acting on the related field variables [15]. In principle, this yields separable partial differential equations which are Sturm-Liouville problems for one of the field variables with analytical or at least semi-analytical solutions.

Let acoustics be described by the acoustic potential $\phi : M \rightarrow \mathbb{R}$, where M is a smooth spacetime endowed with a Lorentzian metric \mathbf{g} having negative signature, *i.e.* $g = \det \mathbf{g} < 0$. Then, we postulate that the following action integral is stationary with respect to variations of the potential [12]:

$$\mathcal{A}[\phi] = \int_{\Omega} d\text{vol}_g \mathcal{L}(x, \phi, \nabla \phi) = 0 \quad \text{so that} \quad \frac{\delta}{\delta \phi} \mathcal{A}[\phi] = 0. \quad (1)$$

The integration domain $\Omega \subseteq M$ is a bounded, closed set of spacetime and the invariant volume element is denoted by $d\text{vol}_g = \sqrt{-g} dx^0 \wedge \dots \wedge dx^3$, where $x \in M$. Here, in general, the Lagrangian is a function $\mathcal{L} : TM \rightarrow \mathbb{R}$, where TM is the tangent bundle of coordinate space M . The form of \mathcal{L} is severely constrained by fundamental symmetry requirements: energy-momentum conservation, locality, and free-wave propagation. Its simplest possible choice is [12]

$$\mathcal{L}(\phi, \mu) = \frac{1}{2} \mathbf{g}(\nabla \phi, \nabla \phi) = \frac{1}{2} g^{\mu\nu} \phi_{,\mu} \phi_{,\nu}. \quad (2)$$

Note that if \mathbf{v} denotes the local fluid velocity, p the acoustic pressure, ϱ_0 the density, and $c > 0$ the time-independent wave speed of the acoustic metamaterial, the gradient or covariant derivative¹ appearing in Eq. (2) will

¹Greek tensor indices indicate the full range of spacetime components, whereas Latin indices will only refer to the spatial components. Comma and semicolon are standard notation for partial and covariant derivatives, respectively. For a scalar ϕ it always holds $\phi_{;\mu} = \phi_{,\mu}$.

be

$$\phi_{,\mu} = \begin{pmatrix} p/c\varrho_0 \\ -\mathbf{v} \end{pmatrix}. \tag{3}$$

This expression encapsulates elementary relations of acoustics [16] and is valid within a fixed laboratory frame.²

After substituting Eq. (2) into Eq. (1), we obtain the Euler-Lagrange equation for the acoustic potential. This equation directly gives the wave equation of the acoustic system for the spacetime (M, \mathbf{g}) under investigation. In the laboratory (*physical space*), the acoustic engineer who wishes to implement spacetime (M, \mathbf{g}) has to calibrate the mass-density tensor ϱ and bulk modulus κ relating them to their magnitude in the corresponding space with known acoustic wave propagation (*virtual space*). For convenience, we will denote all quantities in virtual by an overbar. In explicit form, both of these spaces are linked by the *constitutive relations* [12]. The underlying symmetry for the $(n + 1)$ D Schwarzschild geometry obviously implies $SO(n)$ symmetry for the n spatial coordinates. This group symmetry obviously reflects itself in the constitutive relations, and for $n = 2$ we have

$$\kappa = \frac{\sqrt{\gamma}}{\sqrt{\bar{\gamma}}} \bar{\kappa}, \quad \rho_0 \rho^{ij} = \frac{\sqrt{\gamma}}{\sqrt{\bar{\gamma}}} \bar{g}^{ij}, \tag{4}$$

where we have employed the usual shorthand notation $\gamma = \det(g^{ij})$ for the determinant of the spatial metric components.

3 Schwarzschild-type spacetime geometries

In $(n + 1)$ D spacetime geometry, the static and spherically symmetric metric of Schwarzschild-type takes the following form

$$\mathbf{g} = -h(r) c^2 dt \otimes dt + h^{-1}(r) dr \otimes dr + r^2 d\Omega_{n-1} \otimes d\Omega_{n-1}, \tag{5}$$

where t and r are the local time and radial coordinates, respectively. It is a generalized form of the Friedmann-Lemaître-Robertson-Walker (FLRW) metric with positive curvature including the radial fudge factor $h(r)$. For $h \equiv 1$, one recovers the FLRW form in hyperspherical coordinates. Here, as

²Obviously the four-vector $\phi_{,\mu}$ cannot be fully relativistic but transforms with a subgroup of the Lorentz group.

usual, the solid angle Ω_n comprises all n angles φ_i of the hypersphere S^n , and it is defined by

$$d\Omega_n^2 = d\varphi_1^2 + \sin^2\varphi_1 d\varphi_2^2 + \cdots + \left(\prod_{i=1}^{n-1} \sin^2\varphi_i \right) d\varphi_n^2, \quad (6)$$

where $\varphi_1 \in [0, 2\pi[$ and $\varphi_i \in [0, \pi[$ for $i = 2, 3, \dots, n$.

The radial function implies the inverse correlation between relativistic time dilation and space contraction, and thus it will satisfy $0 < h(r) \leq 1$ for all $r > 0$. The specific solution for $h(r)$ will depend on dimension n and the physical conditions imposed. For $n = 3$ the vacuum solution yields the conventional Schwarzschild metric. O'Neill [17] introduced the toy model with the geometry of Eq. (5) for $n = 1$, which is conformally flat, and thus all solutions are automatically vacuum solutions. Here, we will propose the considerably richer case $n = 2$, a spacetime which we term the $(2 + 1)D$ *Schwarzschild plane*, and will discuss its admissible solutions.

Rewriting the metric Eq. (5) for $n = 2$ in terms of the nonholonomic basis 1-forms θ^μ , we obtain

$$\mathbf{g} = -(\underbrace{\sqrt{h(r)} c dt}_{\theta^0}) \otimes (\underbrace{\sqrt{h(r)} c dt}_{\theta^0}) + \frac{dr}{\sqrt{h(r)}} \otimes \underbrace{\frac{dr}{\sqrt{h(r)}}}_{\theta^1} + \underbrace{(r d\varphi)}_{\theta^2} \otimes \underbrace{(r d\varphi)}_{\theta^2}. \quad (7)$$

In the nonholonomic frame $(\theta^0, \theta^1, \theta^2)$ local flatness and orthogonality hold, such that $\eta = -\theta^0 \otimes \theta^0 + \theta^1 \otimes \theta^1 + \theta^2 \otimes \theta^2$, with η being the Minkowski metric, and Cartan's structure equations enable us to compute the curvature 2-form Ω in a straightforward manner.

Explicit calculation of the curvature yields only three non-vanishing results: $\Omega^0_1 = (-h''/2) \theta^0 \wedge \theta^1$, $\Omega^0_2 = (-h'/2r) \theta^0 \wedge \theta^2$, and $\Omega^1_2 = (-h'/2r) \theta^1 \wedge \theta^2$. From $\Omega^i_j = \hat{R}^i_{jij} \theta^i \wedge \theta^j$ (no summation implied), the independent components of the Riemann tensor \hat{R}^i_{jkl} in the Cartan frame can easily be obtained. Next, contraction immediately gives the Ricci tensor \mathbf{R} and then the curvature scalar

$$R = -h'' - \frac{2h'}{r}, \quad (8)$$

which themselves imply the following Einstein tensor

$$\hat{\mathbf{G}} = \hat{\mathbf{R}} - \frac{1}{2}R\eta = \begin{pmatrix} -\frac{h'}{2r} & 0 & 0 \\ 0 & \frac{h'}{2r} & 0 \\ 0 & 0 & \frac{1}{2}h'' \end{pmatrix}. \quad (9)$$

The Einstein tensor Eq. (9) has to vanish in all frames due to the vacuum condition. Hence, there exists only one trivial solution exactly then when $h(r) = C_1$ is a constant, and the corresponding metric is Minkowski flat (all $\hat{R}^i_{jkl} = 0$). After selecting the appropriate time scale $h \equiv 1$, the metric agrees with the FLRW metric. Consequently, black holes are forbidden to exist on the conventional 2D plane, and it would not make much sense either to try implementing the acoustic analogue.

A necessary requirement for Schwarzschild-type spacetimes is that the Ricci curvature scalar R must be constant. Upon integrating Eq. (8), we obtain

$$h(r) = C_1 + \frac{C_2}{r} - \frac{R}{6}r^2, \quad (10)$$

and we note again that $C_2 = 0$ and $R = 0$ (Ricci flatness) is the only possible solution. However, Eq. (7) with Eq. (10) represents the Kottler metric [18,19]. It is well-known to be the only spherically symmetric solution of Einstein's vacuum field equation with a cosmological constant Λ : $\hat{\mathbf{G}} + \Lambda\eta = \mathbf{0}$. In three spacetime dimensions one has $\Lambda = R/6$. Furthermore, since $\hat{G}_{00} = -\hat{G}_{11}$ in Eq. (9), we require for consistency that $C_2 = 0$. Altogether this gives for Eq. (10):

$$h(r) = 1 - \Lambda r^2, \quad \Lambda \neq 0. \quad (11)$$

Choosing the natural length scale $\ell > 0$, we may identify

$$\Lambda = \pm \frac{1}{\ell^2}, \quad (12)$$

which for the positive sign gives *de Sitter spacetime* (dS_{2+1}) with positive scalar curvature. Similarly, for a negative sign it gives *anti-de Sitter spacetime* (AdS_{2+1}) with negative scalar curvature (see *e.g.* [19]). This leaves us with two possible spacetime candidates in (2+1)D for implementing and simulating the acoustic analogues of black holes.

4 Acoustic wave simulation of black holes

A description of wave propagation for acoustic black holes in dS_{2+1} and AdS_{2+1} spacetime is readily obtained by applying the variational principle, Eq. (1), with the Lagrangian function, Eq. (2), where the metric \mathbf{g} explicitly contains $h(r) = 1 \pm r^2/\ell^2$ [*viz.* Eqs. (11)–(12)]. The resulting wave equation is

just the Euler-Lagrange equation and involves the Laplace-Beltrami operator for either the dS_{2+1} or the AdS_{2+1} manifold M :

$$\Delta_M = \frac{1}{r} \left(r g^{\mu\nu} \phi_{,\mu} \right)_{,\nu} \phi = 0. \tag{13}$$

This is a self-adjoint partial differential equation for coordinates $x^0 = ct$, $x^1 = r$, and $x^2 = \varphi$. The standard procedure is to use the separation of variables method and assume

$$\phi(t, r, \varphi) = \phi_0(t) \phi_1(r) \phi_2(\varphi). \tag{14}$$

The time dependence $\phi_0(t)$ will display a simple harmonic behaviour. It will also be reasonable to study concentric wave propagation, so that $\phi_2(\varphi) \equiv 1$.

Therefore, only the radial dependence $\phi_1(r)$ remains to be examined and completely determines the nontrivial behaviour for the wave propagation. A detailed calculation yields the following differential equations for the AdS_{2+1} potential $\phi_1^-(r)$, and the dS_{2+1} potential $\phi_1^+(r)$:

$$AdS_{2+1} : \quad r \left(1 + \frac{r^2}{\ell^2} \right)^2 \phi_1^{-''} + \left(1 + \frac{r^2}{\ell^2} \right) \left(1 + 3 \frac{r^2}{\ell^2} \right) \phi_1^{-'} + \lambda r \phi_1^- = 0, \tag{15}$$

$$dS_{2+1} : \quad r \left(1 - \frac{r^2}{\ell^2} \right)^2 \phi_1^{+''} + \left(1 - \frac{r^2}{\ell^2} \right) \left(1 - 3 \frac{r^2}{\ell^2} \right) \phi_1^{+'} + \lambda r \phi_1^+ = 0. \tag{16}$$

Figures 1 and 2 illustrate the radial behaviour of prototype waves probing AdS_{2+1} and dS_{2+1} spacetime, respectively. The numerical estimates were carried out with MATHEMATICA and the SBVP solver under MATLAB [20].

The analogous acoustic space is implemented by a suitable choice of the physical parameters ϱ and κ . For this we only require the components of metric \mathbf{g} , immediately read off from Eq. (7) with Eqs. (11)–(12), and the constitutive equations, Eqs. (4). Thus, we obtain the following simple prescription for the acoustic analogue of Schwarzschild-deSitter black holes and Schwarzschild-AdS spacetime:

$$\kappa = \frac{\bar{\kappa}}{\sqrt{1 \pm r^2/\ell^2}}, \quad \rho_0 \rho^{ij} = \sqrt{1 \pm r^2/\ell^2} \begin{pmatrix} 1 & 0 \\ 0 & 1/r^2 \end{pmatrix}, \tag{17}$$

where it is clear that only the quantities with a negative sign (dS_{2+1}) will give rise to a spacetime geometry with an event horizon.

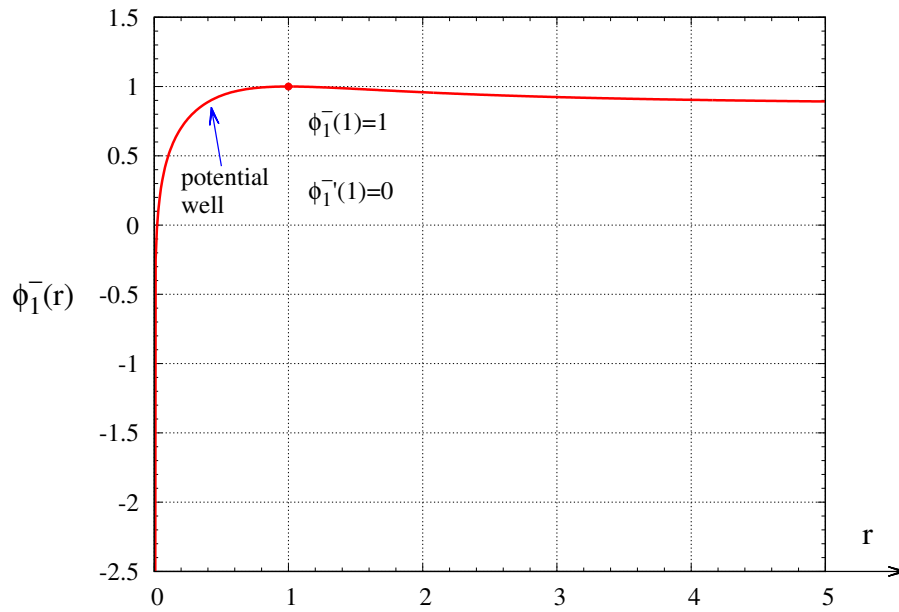


Figure 1: Simulation of acoustic AdS_{2+1} spacetime. Numerical estimates for the nontrivial radial dependence $\phi_1^-(r)$ obeying Eq. (15), with scale $\ell = 1$ and boundary conditions $\phi_1^-(1) = 1$, $\phi_1^-'(1) = 0$. A potential well is observed while any event horizons are absent.

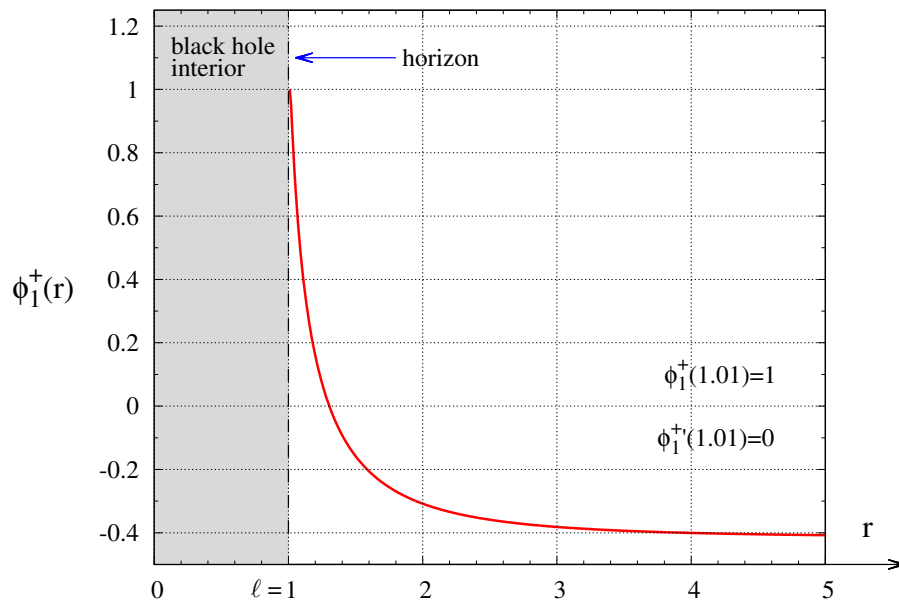


Figure 2: Simulation of acoustic dS_{2+1} black hole. Numerical estimates for the nontrivial radial dependence $\phi_1^+(r)$ obeying Eq. (16), with scale $\ell = 1$ and boundary conditions $\phi_1^+(1.01) = 1$, $\phi_1^{+'}(1.01) = 0$. A typical event horizons emerges as r approaches $\ell = 1$.

The concentric wave solution $\phi(t, x, y)$ for Eq. (13) displays a harmonic dependence in the time variable t . All of the non-trivial propagation behaviour occurs in the radial direction, as expected. Standard techniques may yield useful approximate solutions for the nontrivial r -dependence of Eq. (13) in terms of the Bessel functions J_n and Y_n .

5 Conclusions

Our closer examination of (2+1)D Schwarzschild black holes naturally led us to spacetimes with a non-vanishing cosmological constant, since conventional Schwarzschild solutions on the plane are forbidden. The dS_{2+1} or Schwarzschild-deSitter black hole is also mathematically very intriguing, because there is no comparable solution with a noncompact event horizon in asymptotic Minkowski space. On the other hand, AdS_{2+1} solutions have no event horizons. However, we have seen that their radial potential takes the form of a potential well.

The acoustic analogues of both spacetimes are therefore particularly interesting. In order to derive the corresponding wave equation for the acoustic potential, we have employed a covariant variational principle, and in principle we have arrived at a unified description of acoustic wave phenomena on the (2+1)D Schwarzschild plane.

It is our hope that the variational spacetime approach to transformation acoustics and the corresponding constitutive relations supply a powerful tool for the study and design of acoustic metadevices and may help to open up new research pathways in this field.

Acknowledgements

M. M. T. wishes to thank the Spanish *Ministerio de Economía y Competitividad* and the European Regional Development Fund (ERDF) for financial support under grant TIN2014-59294-P.

References

- [1] R. A. Shelby, D. R. Smith, and S. Schultz. Experimental verification of a negative index of refraction, *Science*, **292**:77–79, 2001.

- [2] V. G. Veselago. The electrodynamics of substances with simultaneously negative values of ε and μ , *Sov. Phys. Uspekhi*, **10**(4):509–514, 1967.
- [3] S. A. Cummer, Transformation Acoustics. *Acoustic Metamaterials*, R. V. Craster, S. Guenneau (eds.), Springer Series in Materials Science **166**, pp. 197–218. Berlin, Springer Verlag, 2013.
- [4] S. A. Cummer. A sound future for acoustic metamaterials, *J. Acoust. Soc. Am.*, **141**(5):3451, 2017.
- [5] M. Haberman and M. Guild. Acoustic metamaterials, *Physics Today*, **69**(6):42–48, 2016.
- [6] G. Ma and P. Sheng. Acoustic metamaterials: From local resonances to broad horizons, *Sci. Adv.*, **2**:e1501595, 16 pp., 2016.
- [7] K. Schwarzschild. On the gravitational field of a mass point according to Einstein's theory, *Sitzungsber. Preuss. Akad. Wiss. Berlin (Math. Phys.)*, pp. 189–196, 1916.
- [8] A. Climente, D. Torrent, and J. Sanchez-Dehesa, Noise reduction by perfect absorbers based on acoustic metamaterials, in *Proceedings of the ASME 2011 International Mechanical Engineering Congress & Exposition*, Denver, CO, 2011.
- [9] R. Q. Li, X. F. Zhu, B. Liang, Y. Li, X. Y. Zou, and J. C. Cheng. A broadband acoustic omnidirectional absorber comprising positive-index materials, *Appl. Phys. Lett.*, **99**(19):193507, 2011.
- [10] L. Zigoneanu, Design and Experimental Applications of Acoustic Metamaterials. PhD thesis, Department of Electrical and Computer Engineering, Duke University, 2013.
- [11] S. Hossenfelder. A relativistic acoustic metric for planar black holes, *Phys. Lett. B*, **752**, pp. 13–17 (2016).
- [12] M. M. Tung. A fundamental Lagrangian approach to transformation acoustics and spherical spacetime cloaking, *Europhys. Lett.*, **98**:434002–34006, 2012.
- [13] M. M. Tung, E. B. Weinmüller. Gravitational Frequency Shifts in Transformation Acoustics, *Europhys. Lett.*, **101**:54006–54011, 2013.

- [14] M. M. Tung, Modelling acoustics on the Poincaré half-plane, *J. Comput. Appl. Math.*, in press, <http://doi.org/10.1016/j.cam.2017.10.037>, 2017.
- [15] C. Lanczos, *The Variational Principles of Mechanics*, p. 351. New York, Dover Publications, 1970.
- [16] F. P. Mechel, *Formulas of Acoustics*. Berlin, Springer Verlag, 2002.
- [17] B. O'Neill, Semi-Riemannian Geometry, *Series in Pure and Applied Mathematics*, **103**, pp. 152–153, San Diego, Academic Press, 1983.
- [18] F. Kottler, Über die physikalischen Grundlagen der Einsteinschen Gravitationstheorie, *Ann. Phys.*, **4**(56):401–462, 1918.
- [19] V. Perlick, Gravitational lensing from a spacetime perspective, *Living Rev. Rel.*, **7**(9), p. 66, <http://doi.org/10.12942/lrr-2004-9>, 2004.
- [20] W. Auzinger, G. Kneisl, O. Koch, and E. Weinmüller, A collocation code for singular boundary value problems in ordinary differential equations, *Numer. Algorithms*, **33**:27–39, 2003.

On the solution of different eigenvalue problems associated with the neutron transport using the finite element method

A. Vidal-Ferràndiz^b, S. González-Pintor[†], D. Ginestar[‡]*,
G. Verdú^b and C. Demazière[§]

(b) Instituto de Seguridad Industrial: Radiofísica y Medioambiental,
Universitat Politècnica de València, Camino de Vera s/n, 46022, València, Spain,

(†) Department of Mathematical Sciences

Chalmers University of Technology, Maskingränd 2, SE-412 58 Göteborg, Sweden

(‡) Instituto de Matemática Multidisciplinar.

Universitat Politècnica de València, Camino de Vera s/n, 46022, València, Spain.

(§) Subatomic and Plasma Physics, Department of Physics Chalmers University of Technology

Chalmers University of Technology, Maskingränd 2, SE-412 58 Göteborg, Sweden.

November 30, 2017

1 Introduction

High-fidelity neutronic simulations of nuclear systems are an important goal to ensure the efficient and safe operation of nuclear reactors. The steady-state neutron transport equation [1] predicts the quantity of neutrons in every region of the reactor and thus, the number of fissions and nuclear reactions. The neutron transport equation for three-dimensional problems is an equation defined in a support space of dimension 6, and this makes that high-fidelity simulations using this equation can only be done using

*e-mail: dginesta@mat.upv.es

super computers. Different approximations have been successfully used for deterministic neutron transport, eliminating the energy dependence of the equations by means of the multi-group approximation, and using a special treatment to eliminate the dependence on the direction of the incident neutrons. The angular discretization of the neutron transport equation chosen in this work has been the Discrete Ordinates method (S_N), which is a collocation method based on a set of quadrature points for the unit sphere, [1], obtaining equations depending only on the spatial variables. The spatial discretization used in this work, has been a high-order discontinuous Galerkin finite element method. After the spatial discretization, a large algebraic generalized eigenvalue problem with rank deficient matrices is obtained, which can be formulated in different ways.

The eigenvalue problem arising from the different approximations to the deterministic neutron transport equations is classically solved with the power iteration method. However, Krylov methods are becoming increasingly popular. These methods permit to solve the eigenvalue problem faster when the power iteration convergence decreases due to high dominance ratios. It also allows to compute more eigenvalues than the largest one. We study the advantage of using a Krylov subspace method such as the Krylov-Schur method for these generalized eigenproblems, compared to the use of simpler solvers as the power iteration method.

2 The Discrete Ordinates Method

The energy multigroup neutron transport equation can be written as

$$\mathcal{L}_g \psi_g = \sum_{g'=1}^G \left(\mathcal{S}_{g,g'} + \frac{1}{\lambda} \chi_g \mathcal{F}_{g'} \right) \psi_{g'}, \quad g = 1, \dots, G, \quad (1)$$

where the group dependent operators of transport, \mathcal{L}_g , scattering, $\mathcal{S}_{g,g'}$ and fission $\mathcal{F}_{g'}$ are defined by

$$\begin{aligned} \mathcal{L}_g \psi_g &= \Omega \cdot \nabla \psi_g + \Sigma_{t,g} \psi_g, & \mathcal{S}_{g,g'} \psi_{g'} &= \int_{(4\pi)} \Sigma_{s,gg'} \psi_{g'} d\Omega', \\ \mathcal{F}_{g'} \psi_{g'} &= \frac{1}{4\pi} \nu_{g'} \Sigma_{f,g'} \int_{(4\pi)} \psi_{g'} d\Omega', \end{aligned}$$

and $\Sigma_{t,g}$, $\Sigma_{s,gg'}$ and $\Sigma_{f,g'}$ are the total, scattering and fission cross sections. ψ_g is the angular neutron flux for the group g .

This equation is discretized in the angular variable by means of a collocation method on a set of quadrature points of the unit sphere, $\{\Omega_n\}_{n=1}^N$ with their respective weights $\{\omega_n\}_{n=1}^N$. This method is referred as the *Discrete Ordinates* method, S_N [1].

Using the angular discrete ordinates quadrature set the discrete ordinates equation is written as

$$\begin{aligned} \mathcal{L}_{g,n}\psi_{g,n} &= \mathcal{M}_n \sum_{g'=1}^G \mathcal{S}_{g,g'} \mathcal{D}\psi_{g'} + \frac{\chi_g}{\lambda} \sum_{g'=1}^G \mathcal{F}_{g'} \phi_{g'}^0, \\ g &= 1, \dots, G, \quad n = 1, \dots, N, \end{aligned} \quad (2)$$

where the transport and fission operators are redefined by

$$\begin{aligned} \mathcal{L}_{g,m}\psi_{g,n} &= \Omega \cdot \nabla \psi_{g,n} + \Sigma_{t,g}\psi_{g,n}, \\ \mathcal{F}_{g'}\psi_{g'} &= \frac{1}{4\pi} \nu_{g'} \Sigma_{f,g'} \psi_{g'} d\Omega'. \end{aligned}$$

\mathcal{M} is the projector moment-to-direction operator and \mathcal{D} is the direction-to-moment operator. Generally, $\mathcal{L} \neq \mathcal{M}^{-1}$.

A discontinuous Galerkin finite element method for the S_N approximation of the transport equation is used leading to the following algebraic generalized eigenvalue problem.

$$\mathbf{L}\Psi = \mathbf{M}\mathbf{S}\mathbf{D}\Psi + \frac{1}{\lambda}\mathbf{X}\mathbf{F}\mathbf{D}\Psi \quad (3)$$

where each matrix is the result of the energetic, angular and spatial discretization of the S_N approximation and Ψ is the vector of weights for the polynomials expansion of the angular neutron flux. A similar discontinuous Galerkin discretization for the neutron diffusion equation was developed in [2].

3 Eigenvalue Calculation

Equation (3) can be arranged into an ordinary eigenvalue problem of the form

$$\mathbf{A}\Phi = \lambda\Phi, \quad (4)$$

where $\mathbf{A} = \mathbf{D}\mathbf{H}^{-1}\mathbf{X}\mathbf{F}$, $\mathbf{H} = \mathbf{L} - \mathbf{M}\mathbf{S}\mathbf{D}$ and $\Phi = \mathbf{D}\Psi$. In particular, the solution of the system involving \mathbf{H} is performed as $\mathbf{H}^{-1}v = (\mathbf{I} - \mathbf{L}^{-1}\mathbf{M}\mathbf{S}\mathbf{D})^{-1}\mathbf{L}^{-1}v$, which greatly reduces the number of iterations needed to solve the system, where \mathbf{L}^{-1} is the most costly operation known as the *transport sweep*.

To solve the ordinary eigenvalue problem (4) only the multiplication by the matrix \mathbf{A} is available. Each multiplication is usually called an outer iteration. The matrices \mathbf{L} , \mathbf{M} and \mathbf{D} are block diagonal where each block corresponds to the transport equation for a particular energy group. If a problem does not have upscattering, the \mathbf{S} is block lower diagonal. In that case, the action of the operator \mathbf{H} on a vector is calculated by block forward substitution for each group from high to low energy in a sequence. Each forward substitution requires solving the spatially discretized S_N equations for a single energy group, which is called the source problem [3]. This source problem is usually solved by using a Krylov iterative method preconditioned with a *diffusion synthetic acceleration*. The iterations used to solve each source problem are called inner iterations.

3.1 Power Iteration method

The power iteration method to solve the eigenvalue problem (4) reads as the iterative procedure

$$\Phi^{i+1} = \frac{1}{\lambda_1} \mathbf{A}\Phi^i, \quad (5)$$

where λ_1 is updated at each iteration according to the Rayleigh quotient

$$\lambda^{(i+1)} = \lambda^{(i)} \frac{\Phi^{(i)T} \mathbf{X}\mathbf{F}\Phi^{(i+1)}}{\Phi^{(i)T} \mathbf{X}\mathbf{F}\Phi^{(i)}}, \quad (6)$$

where $\Phi^{(i)} = \mathbf{D}\Psi^{(i)}$.

Power iteration will converge to the eigenvalue of largest magnitude, k_{eff} . However, if more than one eigenvalue is requested a deflation technique should be used. In other words, it can be computed one harmonic at a time while decontaminating the subspace of the computed eigenvalue. The convergence rate is determined as by the dominance ratio $\delta = |\lambda_2|/|\lambda_1|$, where λ_2 is the next largest eigenvalue in magnitude. Convergence of the power iteration method slows as $\delta \rightarrow 1.0$.

Table 1: Performance results without upscattering for the MOX fuel slab.

δ	Method	m	O	I	Time (s)
0.895	Power Iteration	-	31	2410	9.5
	Krylov-Schur	3	25	3771	14.0
	Krylov-Schur	5	14	2129	8.1
	Krylov-Schur	10	10	1509	5.6
0.946	Power Iteration	-	48	3722	14.6
	Krylov-Schur	3	31	4542	17.0
	Krylov-Schur	5	17	2484	9.3
	Krylov-Schur	10	15	2144	8.1
0.971	Power Iteration	-	100	7447	29.2
	Krylov-Schur	3	53	7876	28.8
	Krylov-Schur	5	23	3364	12.7
	Krylov-Schur	10	20	2914	10.8

3.2 Krylov-Schur

The Krylov-Schur method is an Arnoldi method which uses an implicit restart based on a Krylov-Schur decomposition. In this work, the Krylov-Schur method algorithm has been using the eigenvalue problem library SLEPc [4]. The Arnoldi method is based on the creation of a Krylov subspace of dimension m ,

$$\mathcal{K}_m(A, \Phi^{(0)}) = \text{span}\{\Phi^{(0)}, \mathbf{A}\Phi^{(0)}, \dots, \mathbf{A}^{m-1}\Phi^{(0)}\}. \quad (7)$$

4 Numerical Results

To test the results some numerical benchmarks are solved. Table 1 displays the performance results for a MOX fuel slab problem of the C5G7 benchmark. It is shown the number of outer, O , and inner iterations, I , using the eigenvalue solvers for the different problems with different dominance ratio that have been defined. For problems with high dominance ratio Krylov-Schur method can be from 1.5 to 6 times faster than the usual power iteration method. For these high dominance ratio problems the Krylov subspace dimension, m , must be high to achieve a better performance.

5 Conclusions

In this work, a S_N method based on a Discontinuous Galerkin method has been presented and is used to approximate the Lambda modes problem associated to the neutron transport equation. The generalized algebraic eigenvalue problem resulting from the energy, angles and spatial discretization is very large and has been implemented using a matrix-free methodology. Two eigenvalue solvers have been considered, the usual power iteration method and the Krylov-Schur method and the performance of both methods have been evaluated solving different problems with different dominance ratios. From the obtained results it can be concluded that only for problems with high dominance ratios it is worth the while to use the Krylov subspace method with a large Krylov subspace dimension. Otherwise it is better to use the simpler power iteration method to compute the dominant eigenvalue and its corresponding eigenfunction for a reactor core.

Acknowledgements

The work is partially supported by the Ministerio de Economía y Competitividad under projects ENE 2014-59442-P and MTM2014-58159-P, Generalitat Valenciana under PROMETEO II/2014/008 and Universitat Politècnica de València under FPI-2013. It is also financed by the Swedish Research Council (VR-Vetenskapsrådet) within the framework DREAM4SAFER, research contract C0467701.

References

- [1] Lewis, E.E. and W.F. Miller, Computational methods of neutron transport. New York, USA, John Wiley & Sons, Inc., 1984.
- [2] Vidal-Ferràndiz, A., S. González-Pintor, D. Ginestar, G. Verdú, M. Asadzadeh and C. Demazière. Use of discontinuity factors in high-order finite element methods *Annals of Nuclear Energy*, Volume(87): 728–738, 2016.
- [3] Warsa, J. S., T. A. Wareing, J. E. Morel, J. M. McGhee and Lehoucq R. B. Krylov subspace iterations for deterministic k-eigenvalue calculations *Nuclear Science and Engineering*, Volume(147): 26–42, 2004.
- [4] Hernandez V., Roman J.E. and Vidal V. SLEPc: A Scalable and Flexible Toolkit for the Solution of Eigenvalue Problems *ACM Trans. Math. Software*, Volume(31): 351–362, 2005.

Finding multiple roots of nonlinear equations using eighth-order optimal iterative methods

Fiza Zafar^b*, Alicia Cordero[†], Sana Sultana^b,
and Juan R. Torregrosa[†]

(b) Centre for Advanced Studies in Pure and Applied Mathematics,
Bahauddin Zakariya University, Multan 60800, Pakistan

(†) Instituto de Matemáticas Multidisciplinar, Universitat Politècnica de València,
Camino de Vera, s/n, 46022-Valencia, Spain

November 30, 2017

1 Introduction

Newton's method has been widely used to investigate simple or multiple zeros of a non-linear equation. If the given function involves only one numerical zero, then Newton's method converges quadratically to the exact solution provided that a proper initial guess is selected close enough to the exact solution. However, Newton's method has a drawback: it converges linearly when a given function has repeated (multiple) roots. For a non-linear equation $f(x) = 0$, which involves repeated roots with multiplicity $m > 1$ a priori, modified Newton's method [1] is given as:

$$x_{n+1} = x_n - m \frac{f(x_n)}{f'(x_n)}, \quad n = 0, 1, 2, \dots \quad (1)$$

It efficiently locates the desired multiple zero with quadratic order of convergence. The numerical scheme (1) is a second-order, one-point, optimal

*e-mail: fizazafar@gmail.com, acordero@mat.upv.es, sanasultana8877@gmail.com, jr-torre@mat.upv.es

method on the basis of Kung-Traub's conjecture [2] which states that any multipoint method without memory can reach its convergence order of at most 2^{r-1} for r function evaluations per iteration. In the recent past, many researchers from all over the world like Li et al. [3] in 2009 and Sharma and Sharma [4] in 2010, Zhou et al. [5] in 2011, Sharifi et al. [6] in 2012, Soleymani et al. [7] in 2013 and Hueso et al. [8] in 2015 have presented optimal fourth order iterative methods for multiple zeros. Recently, in [9] Behl et al. have developed a family optimal eighth order iterative methods.

Motivated by the need to present a family of optimal higher order convergent methods for finding simple as well as multiple roots, we construct an optimal eighth order convergent method involving weight functions for finding multiple roots. Section 2 provides the methodology and some special cases of new scheme. Section 3 includes the numerical experiments using test functions. Finally, conclusions are given in Section 4.

2 Construction of optimal scheme with eighth-order convergence

Let us consider the following scheme involving univariate weight functions for solving the root-finding problem:

$$\begin{aligned} y_n &= x_n - m \frac{f(x_n)}{f'(x_n)}, \\ z_n &= y_n - m u_n H(u_n) \frac{f(x_n)}{f'(x_n)}, \\ x_{n+1} &= z_n - u_n P(u_n) G(v_n) L(w_n) \frac{f(x_n)}{f'(x_n)}, \quad n \geq 0 \end{aligned} \quad (2)$$

where the weight functions $H_f : \mathbb{C} \rightarrow \mathbb{C}$, $P_f : \mathbb{C} \rightarrow \mathbb{C}$, $G_f : \mathbb{C} \rightarrow \mathbb{C}$ and $L_f : \mathbb{C} \rightarrow \mathbb{C}$ are analytic functions in a neighborhood of 0 with $u_n = \left(\frac{f(y_n)}{f(x_n)}\right)^{\frac{1}{m}}$, $v_n = \left(\frac{f(z_n)}{f(y_n)}\right)^{\frac{1}{m}}$ and $w_n = \left(\frac{f(z_n)}{f(x_n)}\right)^{\frac{1}{m}}$. In the next result, we show that the order of convergence of the proposed scheme will reach at optimal eight without using additional function evaluations.

Theorem 1 *Let $x = \gamma$ be a multiple zero with multiplicity $m > 1$ of the involved function f . In addition, we assume that $f : \mathbb{C} \rightarrow \mathbb{C}$ is an analytical function in the region enclosing a multiple zero γ . The proposed*

scheme defined by (2) has an optimal eight-order convergence, satisfying $H_0 = H(0) = 1$, $H_1 = H'(0) = 2$, $H_2 = H''(0)$, $H_3 = H'''(0)$ are free real numbers and

$$\begin{aligned} P_0 &= P(0), L_0 = L(0), P_1 = P'(0) = 2P_0, P_2 = P''(0) = P_0(2 + H_2), \\ L_1 &= L'(0) = 2L_0, P_3 = P'''(0) = P_0(-24 + 6H_2 + H_3), \\ G_0 &= G(0) = 0, G_1 = G'(0) = \frac{m}{L_0P_0}, G_2 = G''(0) = \frac{2m}{L_0P_0}, \end{aligned}$$

where P_0, L_0 are also free real numbers. The error equation is given as:

$$\begin{aligned} x_{n+1} &= \frac{1}{48m^8}c_1 (c_1^2(m - H_2 + 9) - 2mc_2) [\{14m^3 - G_3L_0P_0(H_2 - 9)\}^2 \\ &\quad - m^2(G_3L_0P_0 + 12H_2 - 144) \\ &\quad + 2m(161 - 48H_2 + 3H_2^2 + 4H_3 - 9G_3L_0P_0 + G_3H_2L_0P_0)\}c_1^4 \\ &\quad - 4m\{12m^2 + G_3(H_2 - 9)L_0P_0 - m(-72 + 6H_2 + G_3L_0P_0)\}c_1^2c_2 \\ &\quad + 4m^2(6m - G_3L_0P_0)c_2^2 + 24m^3c_1c_3]e_n^8 + O(e_n^9). \end{aligned} \tag{3}$$

Now, we discuss some special cases of our suggested method (2) by using different types of weight functions P, H, G and L . These special cases are as follows:

Iterative Method S1: When all the weight functions are polynomials:

$$\begin{aligned} H(u_n) &= 1 + 2u_n + \frac{H_2}{2}u_n^2 + \frac{H_3}{6}u_n^3, \\ P(u_n) &= P_0 + 2P_0u_n + \left(1 + \frac{H_2}{2}\right)P_0u_n^2 + \left(-4 + H_2 + \frac{H_3}{6}\right)P_0u_n^3, \\ G(v_n) &= \frac{m}{L_0P_0}v_n + \frac{m}{L_0P_0}v_n^2 + G_3\frac{v_n^3}{6}, \\ &\text{and} \\ L(w_n) &= L_0 + 2L_0w_n + L_2\frac{w_n^2}{2} + L_3\frac{w_n^3}{6}, \end{aligned} \tag{4}$$

so for $H_2 = H_3 = G_3 = L_2 = L_3 = 0$ the method (2) becomes:

$$\begin{aligned} y_n &= x_n - m\frac{f(x_n)}{f'(x_n)}, \\ z_n &= y_n - mu_n(1 + 2u_n)\frac{f(x_n)}{f'(x_n)}, \end{aligned}$$

$$x_{n+1} = z_n - mu_n v_n \frac{f(x_n)}{f'(x_n)} \left[(1 + 2u_n + u_n^2 - 4u_n^3) \right. \\ \left. (1 + v_n) (1 + 2w_n) \right]. \tag{5}$$

Iterative Method S2: When the combination of polynomial and rational functions are used:

$$H(u_n) = \frac{1}{6} \left(\frac{-24 - 48u_n + 6H_2u_n - 4u_n^3H_3 + 3u_n^3H_2^2}{-4 + H_2u_n} \right), \\ P(u_n) = \frac{1}{6} \frac{P_0(-24 - 36u_n + 6H_2u_n + 108u_n^3 - 12H_2u_n^3 + 3H_2^2u_n^3 - 4H_3u_n^3)}{-4 + 2u_n + H_2u_n}, \\ G(v_n) = \frac{m}{L_0P_0}v_n + \frac{m}{L_0P_0}v_n^2 + G_3 \frac{v_n^3}{6}, \\ L(w_n) = -\frac{2(-3L_2 + 24L_0 + L_3w_n - 12L_2w_n + 48L_0w_n)L_0^2}{6L_0L_2 - 48L_0^2 - 2L_0L_3w_n + 12L_0L_2w_n - 3L_2^2w_n^2 + 4L_3L_0w_n^2}.$$

For $L_2 = G_3 = 0, H_2 = H_3 = L_0 = L_3 = 1$ the method (2) becomes:

$$y_n = x_n - m \frac{f(x_n)}{f'(x_n)}, \\ z_n = y_n - mu_n \frac{1}{6} \left(\frac{-24 - 42u_n - u_n^3}{-4 + u_n} \right) \frac{f(x_n)}{f'(x_n)}, \\ x_{n+1} = z_n - mu_n v_n \frac{f(x_n)}{f'(x_n)} \left[\frac{1 - 24 - 30u_n + 95u_n^3}{6} \right. \\ \left. (1 + v_n) \left(\frac{24 + 49w_n}{24 + w_n - 2w_n^2} \right) \right]. \tag{6}$$

In a similar way, we can find new optimal eight order convergence iterative schemes for multiple zero by simply assigning different values of $P_0, L_0, G_3, L_2, L_3, H_2, H_3$ or by considering new weight functions which satisfy all the conditions of Theorem 1.

3 Numerical Experiments

In this section, we will demonstrate the efficiency, convergence behavior and effectiveness of our suggested scheme. For this purpose, we consider some

special cases of our proposed scheme namely, (5) and (6), denoted by $S1$ and $S2$ respectively. We choose two test problems and we test our methods on the basis of residual errors in the function $|f(x_n)|$, iteration error $|x_n - \gamma|$, asymptotic error constant and computational order of convergence ρ_n . All computations have been performed using Maple 16, with multiple precision arithmetic. We have done our calculations with a minimum of 1000 significant digits. Further, the meaning of $a(\pm b)$ is a $a \times 10^{(\pm b)}$ in the Table. We use the formula given by Jay [10]:

$$\rho_n \approx \frac{\log |f(x_{n+1})/f(x_n)|}{\log |f(x_n)/f(x_{n-1})|},$$

in order to calculate COC.

Example 1 Let us consider $f_1(x) = [\cos(\frac{\pi x}{2}) + x^2 - \pi]^5$. This function has a multiple zero at $\gamma \approx 2.03472489627912661035$ of multiplicity $m = 5$; we use the initial guess $x_0 = 2.5$.

Example 2 Let us suppose another standard test function $f_2(x) = (\sin^2 x - x^2 + 1)^2$. The function f_2 has multiplicity $m = 2$, multiple zero at $\gamma = 1.40449164821534122603$ and initial guess $x_0 = 2$.

Table 1: Results for Selected New Methods

$f_i(x)$	n	x_n	$ f(x_n) $	$ x_n - \alpha $	$ e_n/e_{n-1}^8 $	ρ_n
f_1	0	2.5				
S1	1	2.034847775	3.470811790(-17)	1.228789153(-4)		
	2	2.034724896	1.729229137(-153)	6.745130071(-32)	5.606819161(-2)	7.423159330
	3	2.034724896	6.612246055(-1244)	5.565313341(-250)	1.297691254	7.999977075
f_2	0	2.0				
S2	1	1.406320394	2.066902234(-5)	1.828746306(-3)		
	2	1.404491648	1.518564168(-41)	1.569755717(-21)	1.185049311(-1)	6.742817383
	3	1.404491648	1.364389398(-330)	4.7052712778(-166)	1.254886302(1)	7.999319213

4 Conclusion

In this paper, we have proposed a family of iterative methods for solving nonlinear equations for multiple roots with known multiplicity. The family of methods include univariate weight functions involving function-to-function ratio. The methods involve only one derivative evaluation. The selection of weight functions yield optimal eighth order convergent methods for multiple roots. In addition, Table 1 shows that the proposed methods S1 and S2 perform efficiently to approximate a multiple root of a function.

References

- [1] L.B. Rall. Convergence of Newton's process to multiple solutions, *Numer. Math.*, 9: 23–37, 1966.
- [2] J.F. Traub. Iterative methods for the solution of equations, Prentice-Hall, Englewood Cliffs, 1964.
- [3] S. Li, X. Liao, and L. Cheng. A new fourth-order iterative method for finding multiple roots of nonlinear equations, *Appl. Math. Comput.*, 215: 1288–1292, 2009.
- [4] J.R. Sharma, and R. Sharma. Modified Jarratt method for computing multiple roots, *Appl. Math. Comput.*, 217: 878–881, 2010.
- [5] X. Zhou, X. Chen, and Y. Song. Constructing higher-order methods for obtaining the multiple roots of nonlinear equations, *J. Comput. Math. Appl.*, 235: 4199–4206, 2011.
- [6] M. Sharifi, D.K.R. Babajee, and F. Soleymani. Finding the solution of nonlinear equations by a class of optimal methods, *Comput. Math. Appl.*, 63: 764–774, 2012.
- [7] F. Soleymani, D.K.R. Babajee, and T. Lofti. On a numerical technique for finding multiple zeros and its dynamic, *J. Egypt. Math. Soc.*, 21: 346–353, 2013.
- [8] J.L. Hueso, E. Martínez and C. Teruel. Determination of multiple roots of nonlinear equations and applications, *J. Math. Chem.*, 53: 880–892, 2015.
- [9] Ramandeep Behl, Alicia Cordero, Sandile S. Motsa and Juan R. Torregrosa, An eighth-order family of optimal multiple root finders and its dynamics, *Numer. Algor.*, In Press, 2017.
- [10] L.O. Jay. A note on Q-order of convergence. *BIT Numer. Math.*, 41: 422–429, 2001.

SPATIAL MODELLING OF DIABETES PATIENTS IN THE REGION OF VALENCIA

J. Díaz-Carnicero¹, D. Vivas-Consuelo¹, N. Guadalajara-Olmeda¹, V. Caballer-Tarazona¹

¹ INECO Centro de Investigación de Ingeniería Económica
Universitat Politècnica de Valencia

1 INTRODUCTION

Diabetes is a metabolic condition that affects the glucose levels due to problems associated with the insulin. Depending on the affection's origin, we consider different types, principally Type 1, in which there has been a complete destruction of the β cells in the pancreas, causing the absence of insulin; and Type 2, related to the deficit or resistance to this hormone. We can find as well other minor types, such as the LADA or gestational ones.

To contextualize the situation of the diabetes in Spain, we will take as reference the results of the 'di@bet.es' study about the patients affected of Type 2 diabetes. We can find alarming data pointing out that this pathology affects the 13,8% of the population older than 18, and the 43% of these people (near 2.3 millions) have not been diagnosed. In addition, the 12,6% of the population presents glucose intolerance, a previous stage that can lead to the presence of the diabetes [1].

Attending to this data, it can be seen the importance of the disease, and the great impact that it has and will have in the National Health Service. For this reason, it is significantly important to take into account the consumption of resources associated with the diabetes process, seeking to maximize the efficiency as the assistance quality improves.

One of the main factors in the attendance of diabetes patients is the pharmacological treatment. Attending to the recommendations provided by the American Diabetes Association (ADA) related to this fact, there are four different stages in the treatment, starting with the use of metformine, a medicine with a moderated cost that in further steps is combined with one or several second-generation compounds, ending up in the higher therapy level where the use of injected insulin is required [2]. The importance of this classification goes beyond the patients attendance, as the cost of the treatment also raises as we move on the different stages.

The objective for the present work is to analyse the diabetes type 2 farmaceutical trataments in the Valencia Region, modelling the spatial distribution of the prevalence and cost of drugs used.

2 MATERIAL AND METHODS

A database is available containing all the prescriptions made in the primary health centres and hospitals in the different health distrits in the Valencia Region in 2015. The study carried out finds the spatial distribution of the variables, represented in maps, as well as the linear regression model associated [3].

The process starts clustering the initial information of the patient's data by primary health centre. With these aggregated data and the total population related to each health centre, it is possible to develop a calculation of both the prevalence and the average cost per patient for each health centre. Finally, the spatial mapping is carried out with the prepared variables, and the linear regression model is proposed [4-5].

3 MODELLING

To quantify the level of spatial dependence in the data we will use the Moran's I index, which formula can be found below, and will offer a value between 0 and 1, been 1 the complete spatial correlation and values close to 0 the correspondent to a random spatial distribution. To generate the nodes weights matrix required, a threshold distance was established, warranting the existence of at least one neighbour for each node.

$$I = \frac{N}{\sum_i \sum_j w_{ij}} \frac{\sum_i \sum_j w_{ij} (X_i - \bar{X})(X_j - \bar{X})}{\sum_i (X_i - \bar{X})^2}$$

$X \rightarrow$ Measured variable
 $W \rightarrow$ Coefficient in weight matrix

Figure 1: Moran's I index formula

For the result visualization, LISA (Local Indicator of Spatial Association) maps are available, in which there will be shown the clustering areas of high and low values, as well as the distribution outliers.

The modelling of the variables studied will be carried out employing a lineal regression model where different demographic and socioeconomically parameters will be essayed. We distinguish in the regression residuals one part as corresponding to the spatial dependence of the variable, which estimation will be considered as it has been said employing the Moran's I index.

$$Y = \beta_0 + \beta_1 X_1 + \beta_2 X_2 + \dots + \varepsilon_s + \varepsilon$$

$Y \rightarrow$ Independent variable
 $X_n \rightarrow$ Explanatory variables
 $\beta_n \rightarrow$ Parameters
 $\varepsilon_s \rightarrow$ Spatial residuals
 $\varepsilon \rightarrow$ General residuals

Figure 2: General lineal regression model proposed

4 RESULTS

Prevalence

While calculating the Moran's I test in the conditions explained, we obtain a value of 0,2941, showing that whereas there is a certain spatial dependence in the prevalence results, the correlation is not high.

Analysing the LISA maps, we can see that half of the health centres presents significant values that can be distinguished into two different cluster types: on one hand, the

metropolitan zones of the province capitals, as well as in most of the Alicante region, there are low value clusters. On the other hand, the interior zones of Valencia and Castellon, Southern coast of Valencia and little interior areas of Alicante presents high values. In addition, we find significant outliers principally in the capitals, where some health centres raises beyond the values expected by the location.

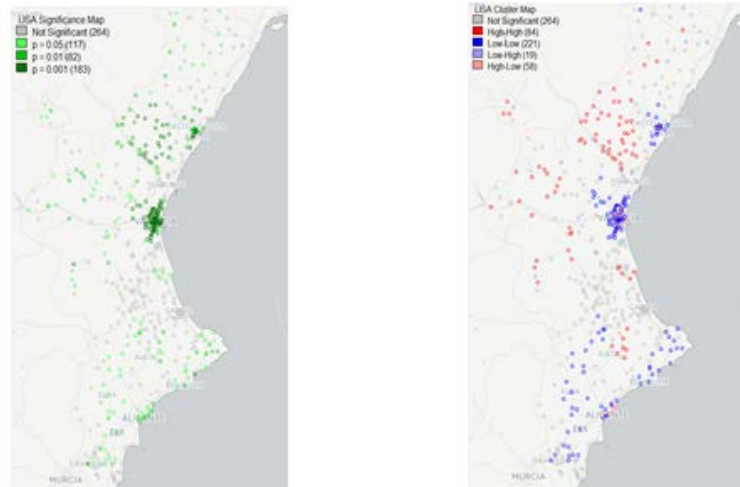


Figure 3: LISA maps of statistical significance (left) and clustering (right) for the prevalence

When trying to generate a regression model valid to explain the prevalence values, according to the nature of the disease that often takes place related to others as it was commented in the introduction, we decided to add a well-known comorbidity index that have been studied, the Clinical Risk Groups (CRG) values. If we represent the spatial distribution of the average CRG value of the primary health centres, we can find a mapping similar to the prevalence one, matching the clusters in general.

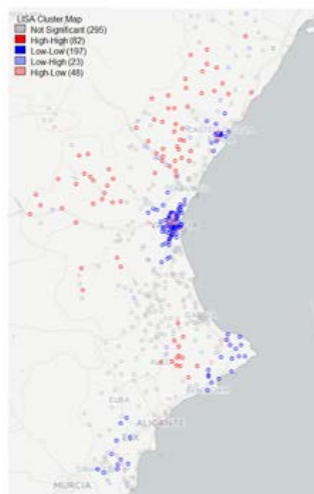


Figure 4: LISA clustering map of the average value of CRG

This way we find a regression model for the prevalence that shows a great relation with the state of health quantified in the CRG values, as well as with the average age of the patients. An Ordinary Least Squares adjust is obtained, with an R^2 value of 0.6401 for these two variables. If we take into account the spatial dependence reflected in the Moran's I index, we can consider that the majority of the variability in prevalence values can be explained.

Variable	Coefficient	Std. Error
Constant	-0.01902	0.00347
CRG - Weight	0.00109	0,00005
Average age	0,00094	0,00009

Total pharmacological cost

As for the prevalence, we start the study with the Moran's I test, taking a high value of 0.6825. This result is indicative of the presence of a high spatial dependence in the complete pharmacological cost.

Attending to the LISA maps results, we can clearly observe that the majority of the health centres present significant values, and while clustering them there is clear evidence of the dependence that the Moran's I index showed. We can find high values in the southern half of the community, especially in Alicante province, as well as in the northern part of Castellon. On the opposite, we find the Valencia province and the southern part of Castellon clustering with low values. The outliers can be found mainly in capital, Valencia City, where some centres presents higher values than the neighbour cluster.

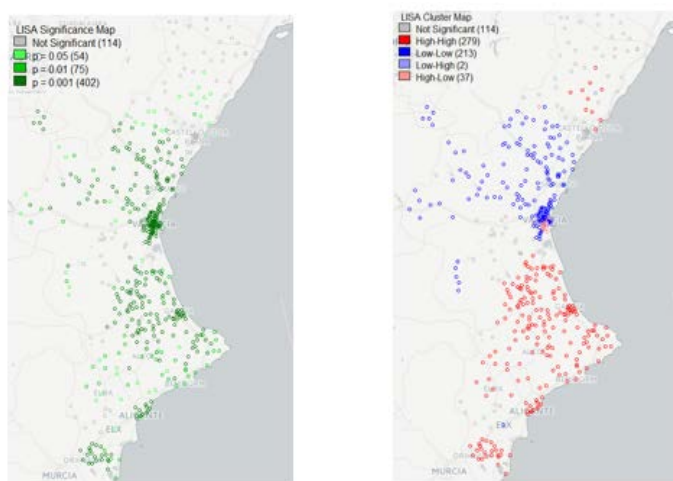


Figure 5: LISA maps of statistical signification (left) and clustering (right) for the complete pharmacological cost

When proposing a regression model, we find that variables that in a first approach we can assume as explicative, such as the prevalence itself previously studied, or the state of health measured in the comorbidity index, are not statistically significant for the model. As the Moran's I test showed in advance, the pharmacological cost presents a spatial dependence stronger than with any of the variables studied, as they are not able to explain the distribution satisfyingly.

5 CONCLUSIONS

Taking into account the results obtained in the study, we can affirm that there is a spatial dependence in the variables that have been studied, been significantly higher for the pharmacological cost over the prevalence. For this one, a regression model can be obtained using demographic information and related to the state of health of the population. Adding knowledge about the spatial distribution allows having a correct explanation of the values.

On the other hand, for the pharmacological cost the high spatial dependence is alarming, for the preponderance over medical and demographical aspects. This is indicative of a high variability in the use of resources that does not follow the criteria of ADA. The development and put into practice of clinical guidelines according to professional studies and publications could be a great tool to correct the mentioned variability.

REFERENCES

- [1] International Diabetes Federation Guideline Development Group, *Global guideline for type 2 diabetes.*, vol. 104, no. 1. 2014.
 - [2] S. E. Inzucchi, R. M. Bergenstal, J. B. Buse, M. Diamant, E. Ferrannini, M. Nauck, A. L. Peters, A. Tsapas, R. Wender, and D. R. Matthews, "Management of Hyperglycemia in Type 2 Diabetes, 2015: A Patient-Centered Approach: Update to a position statement of the american diabetes association and the european association for the study of diabetes," *Diabetes Care*, vol. 38, no. 1, pp. 140–149, 2015.
 - [3] C. Sancho-Mestre, D. Vivas-Consuelo, L. Alvis-Estrada, M. Romero, R. Usó-Talamantes, and V. Caballer-Tarazona, "Pharmaceutical cost and multimorbidity with type 2 diabetes mellitus using electronic health record data," *BMC Health Serv. Res.*, vol. 16, no. 1, pp. 1–8, 2016.
 - [4] S. Coly, M. Charras-Garrido, D. Abrial, and A.-F. Yao-Lafourcade, "Spatiotemporal Disease Mapping Applied to Infectious Diseases," *Procedia Environ. Sci.*, vol. 26, pp. 32–37, 2015.
 - [5] A. B. Lawson, *Statistical methods in spatial epidemiology*. Wiley, 2013.
-

Modeling Plant Virus Propagation with Seasonality

M. Jackson^b and B. Chen-Charpentier^{† *}

(b)(†) Department of Mathematics, University of Texas at Arlington,
Arlington, TX 76019-0408.

November 30, 2016

1 Introduction

Plants are a food source for man and many species. They also are sources of medicines, fibers for clothes, and are essential for a healthy environment. But plants are subject to diseases many of which are caused by viruses. These viruses often kill the plant. Specific examples can be seen in [4], [5], [10]. As a result, billions of dollars are lost every year because of virus related crop loss [9]. Most of the time, virus propagation is done by an insect vector. Insect vectors typically have a seasonal behavior. For example, aphids, a vector that transmits plant viruses, are more active in the growing season than other times of the year [6]. In general, vectors are very active in the warm months and not very active, almost dormant, in the cool or wet months. To combat the vectors, chemical insecticides are commonly used as a control. Unfortunately, these chemicals have toxic effects on humans, animals and the environment in general. An alternative is to introduce a predator, or just increase the number of a naturally present one, to prey on the insects. To understand the dynamics, we will use a mathematical model of differential equations.

Mathematical models have been used to model plant virus propagation [2], [3], [4], [8], [11]. However, these models do not take into consideration

*e-mail: bmchen@uta.edu

of the periodic nature of the vectors. In this paper, we extend the work in [3] to include this fact by introducing periodic coefficients to the model. We will consider a Holling Type 1 interaction. To analyze the model, the basic reproductive number R_0 is used. This is the number of secondary infections an infected individual generates. If $R_0 < 1$, the disease will die out as $t \rightarrow \infty$, but if $R_0 > 1$, an endemic will occur. For autonomous systems, the authors in [?] developed a method to determine basic reproductive number using the next generation approach. For nonautonomous systems, there have been several approaches to determining R_0 . The authors in [7], and [13] used a time average approach by replacing the periodic coefficients with their long time averages. This approach works in some specific cases, but can overestimate or underestimate R_0 in others. In [1], the authors defined R_0 for periodic case and presented some numerical methods to determine R_0 . The authors in [12] established the basic reproductive number to a large class of compartmental models using linear operators.

2 Mathematical model

We consider 6 populations: susceptible plants $S(t)$, infected plants $I(t)$, recovered plants $R(t)$, susceptible insect vectors $X(t)$, infected insect vectors $Y(t)$, and predators $P(t)$. Each variable describes its respective population at time t . Susceptible plants do not have the disease but could contract the disease if infected with the virus. The infected plants have the virus but cannot directly transmit the virus to susceptible plants. Infected plants can either die from the disease or recover. Additionally, since the infected plants can die from the viral infection their death rate is higher than that of plants that do not have the virus. We also assume that as soon as a plant dies either from the infection or from a natural death, it is immediately replaced with a new susceptible plant by a farm worker. Thus it is reasonable to assume that the plant population remains fixed and the total plant population will be denoted by K . This assumption has the modeling advantage that $K = S(t) + I(t) + R(t)$ can be used to eliminate the recovered population from the system of equations. The susceptible insects do not have the virus but can obtain the virus if they come in contact with a infected plant. Infected insects can transmit the virus to susceptible plants upon contact. We assume no vertical transmission of the virus with neither plants nor vectors. Moreover, we assume that the virus does not harm the vector and thus the vector

does not defend against the virus and it retains the virus for the rest of its life. Additionally, contact rate between insect and plant changes depending on the season. Contact rates are higher in warmer months than cooler ones. Thus, we first assume the contact rates to be yearly periodic. The predators use this energy from feeding on the vectors to grow the predator population. We also assume that even if a predator consumes an infected insect, it will not become infected with the virus. Since the insects do not show signs of being infected, the predators cannot differentiate between healthy and infected insects. Thus, we assume that the predators consume both infected and healthy insects at the same rate. The interaction between vector and plant as well as that of predator and vector are assumed to have a limitation of the form of predator-prey Holling type 1. The parameters for the model are:

Parameter	Description	Value
K	Total plant host population	63
β	biting rate of plants due to vectors	0.01-0.1
β_1	biting rate of vectors due to plants	0.01-0.1
μ	natural death rate of plants	.01
m	natural death rate of vectors	.2974
γ	recovery rate of plants	0.01
Λ	replenishing rate of vectors	10
d	death rate of infected plants due to the disease	0.2
c	contact rate between predators and healthy insects	0.05
δ	natural death rate of predators	0.05
α_4	conversion rate of predators due to insects	0.01

The model with the contact rates periodic is

$$\begin{aligned}
 \frac{dS}{dt} &= \mu(K - S) + dI - \beta(t)YS \\
 \frac{dI}{dt} &= \beta(t)YS - \omega I \\
 \frac{dX}{dt} &= \Lambda - \beta_1(t)IX - cXP - mX \\
 \frac{dY}{dt} &= \beta_1(t)IX - cYP - mY \\
 \frac{dP}{dt} &= \alpha_4cXP + \alpha_4cYP - \delta P.
 \end{aligned}
 \tag{1}$$

where

$$\beta(t) = \beta(1 + h \cos(\frac{2\pi t}{365})) \quad \beta_1(t) = \beta_1(1 + h \cos(\frac{2\pi t}{365})). \quad (2)$$

The system of equations has a couple of meaningful equilibrium points

$$S^* = K, \quad I^* = 0, \quad X^* = \frac{\delta}{c\alpha_4}, \quad Y^* = 0, \quad P^* = \frac{-m}{c} + \frac{\Lambda\alpha_4}{\delta}$$

$$S^* = K, \quad I^* = 0, \quad X^* = \frac{\Lambda}{m}, \quad Y^* = 0, \quad P^* = 0.$$

We focus our attention to the first disease free equilibrium point (DFE) since second DFE is not as meaningful as there are no predators in the system. There are other equilibrium points but due to the complexity of their formulas it is not possible to determine whether they make physical sense. The local stability of the equilibrium points of the system of ODE's is established by linearizing the system about the equilibrium point and determining whether the eigenvalues of the Jacobian matrix have positive real parts. However, this can be difficult since the eigenvalues are periodic. Instead we use the basic reproductive number. There are two approaches to calculating this number time average method [7] and linear operator method [12]. When time average method is used, R_0 is underestimated, whereas when the linear operator method is used, the true R_0 is obtained.

3 Periodic Immigration and Death Rates

Immigration rates and death rates change due to the season. This is because insects more active in warmer months, less active in cooler months. Therefore, we are now going to consider Λ and m , the immigration and natural death rates respectively, to be periodic. We also assume that the betas remain periodic as before. The following are the changes made to the system:

$$\begin{aligned} \frac{dX}{dt} &= \Lambda(t) - \beta_1(t)IX - cXP - m(t)X \\ \frac{dY}{dt} &= \beta_1(t)IX - cYP - m(t)Y \end{aligned} \quad (3)$$

$$m(t) = m(1 + A \cos(\frac{2\pi t}{365})) \quad \Lambda(t) = \Lambda(1 + A \cos(\frac{2\pi t}{365})) \quad (4)$$

We use the linear operator method to determine the basic reproductive number from this system. We find that it is different than the first model, when the same parameters are used.

4 Conclusion

Making contact, death and immigration rates periodic makes model more realistic, with the tradeoff being that R_0 is more difficult to calculate. R_0 calculated by taking average value periodic coefficients is not as accurate as linear operator method. R_0 calculated by linear operator method is more difficult to implement, but we only need to know if $R_0 > 1$ or not. Having a more accurate R_0 is crucial in epidemiological models. If R_0 is underestimated, then enough predators to control the vectors will not be introduced meaning an epidemic is likely to occur. If R_0 is overestimated, the number of predators needed will be higher than necessary according to the model. This means a higher cost to farmers who are purchasing the predators for control.

When immigration and death rates are made periodic in addition to the periodic contact rates, the system becomes more difficult to analyze, however it is more realistic. Additionally, R_0 changes for when the immigration and death rates are periodic. In the first model, when $\beta = \beta_1 = .018186$, $R_0 = 1$ but in second model when $\beta = \beta_1 = 0.0186371$, $R_0 = 1$. This means the contact rates from the first model yield a lower R_0 in the second, more realistic model. This means that we would underestimate R_0 using the contact rates from the first model.

References

- [1] N. Bacaer. Approximation of the Basic Reproduction Number R_0 for Vector-Borne Diseases with a Periodic Vector Population. *Bulletin of Mathematical Biology* 69: 10671091 (2007)
- [2] M. Jackson, B. Chen, Modeling plant virus propagation with delays, *Journal of Computational and Applied Mathematics*. 309 611–621.(2016)

- [3] M. Jackson, B. Chen, A model of biological control of plant virus propagation with delays, *Journal of Computational and Applied Mathematics*. (2017)
- [4] M.J. Jeger, J. Holt, F. van den Bosch, L.V. Madden, 2004. Epidemiology of insect-transmitted plant viruses: modelling disease dynamics and control interventions. *Physiol. Entomol.* 29, 291304.
- [5] D. Jones, Plant viruses transmitted by whiteflies. *European Journal of Plant Pathology* 109: 195219, (2003).
- [6] S. Kirchner, et al., Seasonal Phenology and Species Composition of the Aphid Fauna in a Northern Crop Production Area. *PLOS One*. (2013)
- [7] J. Ma and Z. Ma. Epidemic threshold conditions for seasonally forced SEIR models. *Math Biosci. Eng.*, 3(1):161-172, (2006)
- [8] X. Meng and Z. Li, The dynamics of plant disease models with continuous and impulsive cultural control strategies, *Journal of Theoretical Biology*, vol. 266, no. 1, pp. 2940, 20
- [9] V. Nicaise, Crop immunity against viruses: outcomes and future challenges, *Front. Plant Sci.* 5(660), (2014)
- [10] M. Roossinck, *Plant Virus Ecology*, PLOS (2013).
- [11] R. Shi, H. Zhao, S. Tang, Global Dynamic Analysis of a Vector-Borne Plant Disease Model, *Advances in Difference Equations*. 59 (2014).
- [12] W. Wang and X. Zhao. Threshold dynamics for compartmental epidemic models in periodic environments. *J. Dyn. Diff. Equat.*, 20:699-717, (2008).
- [13] C. Wesley, L. Allen The basic reproduction number in epidemic models with periodic demographics, *Journal of Biological Dynamics*, 3:2-3, 116-129, (2009)